

Millisecond pulsars in the era of sensitive telescopes

Dissertation

zur

Erlangung des Doktorgrades (Dr. rer. nat.)

der

Mathematisch–Naturwissenschaftlichen Fakultät

der

Rheinischen Friedrich–Wilhelms–Universität Bonn

von

Tasha GAUTAM

aus

Delhi, India

Bonn, 2022

Angefertigt mit Genehmigung der Mathematisch-Naturwissenschaftlichen Fakultät der
Rheinischen Friedrich–Wilhelms–Universität Bonn

1. Gutachter: Prof. Dr. Michael Kramer
2. Gutachter: Prof. Dr. Norbert Langer
3. Gutachter: Prof. Dr. Ian C Brock
4. Gutachter: Prof. Dr. Klaus Greve

Tag der Promotion: 19.12.2022

Erscheinungsjahr: 2023

Abstract

by Tasha Gautam

for the degree of

Doctor rerum naturalium

Pulsars are highly magnetised rotating neutron stars (NS) that emit beams of electromagnetic radiation along their magnetic axes. They are dense compact remnants of Supernova explosion of massive stars. Since their spin axes are usually misaligned with their magnetic axes, their emissions are visible to us as pulsations. Millisecond pulsars (MSPs) are a class of recycled pulsars (formed by accretion of matter in a binary system) that rotate with exceptionally small spin periods, typically < 20 ms. They are extremely stable in their rotation which makes them exceptional probes to a plethora of multifaceted applications to science. These include understanding the nature of dense matter, probing the gravitational potential and magnetic fields of their local environments such as Galactic field or Globular Clusters (GCs), understanding stellar binary formation and evolution, testing theories of gravity, and many more.

This thesis focuses on two crucial aspects of exploiting science with MSPs: a) discovering exotic MSP binaries (Chapters 3, 4) and b) studying known MSPs with long-term radio pulsar timing to exploit their potential for tests of gravity theories (Chapter 5) and measuring NS masses (Chapter 6).

The pulsar search surveys presented in the first half of this thesis are targeted on GCs. These are gravitationally bound groups of tens of thousands of stars concentrated over a few parsec in spherically condensed structures. Their large stellar densities create environments of increased stellar interaction rates that lead to a higher number of two- and three-body stellar encounters. This results not only in the formation of a large number of MSP binaries, but also in the formation of MSP binaries with unconventional properties. Some of these binaries might provide precise NS mass measurements and precise tests of gravity theories.

In Chapter 1, I provide an introduction to different class of pulsars and various interstellar effects acting on their pulsations, followed by their diverse scientific applications. In Chapter 2, I review the methods and techniques used for the data analysis carried out in this thesis, which broadly include three different categories: search for pulsars in time-domain, imaging GCs, and timing analysis of pulsar binaries.

In Chapter 3, I discuss the pulsar search survey carried out with the Giant Meterwave Radio Telescope (GMRT) on eight GCs at low frequencies (400 MHz and 650 MHz). This survey resulted in the discovery of an MSP, NGC 6652B that rotates every 1.83 ms. We present a phase-connected timing solution for the pulsar derived through long-term timing. The pulsar is in a ~ 1.2 day binary with a Helium WD companion having a median mass of $0.21 M_{\odot}$. We also discuss several low-frequency properties (such as flux, spectral index, and scattering timescales) of the pulsars re-detected in the data. In this survey, we also looked for steep spectrum radio sources in the images of all the GCs observed. We found four such previously un-identified sources that may likely be pulsars.

Chapter 4 discusses the first pulsar search survey performed with the MeerKAT radio telescope. In this survey we targeted nine GCs in the southern hemisphere at 1.4 GHz. The discovery and timing analysis of eight MSPs (of which five are in binary systems) are discussed. This survey corroborates the existing divide in the pulsar population of core-collapse and non core-collapse GCs: the former have a relatively larger population of isolated pulsars and the small fraction of MSP binaries that exist have highly unconventional properties.

The second half of this thesis focus on timing two previously known MSP binaries. Chapter 5 presents the timing analysis of PSR J1952+2630, for which continued timing observations have been carried out with the Arecibo radio telescope. Apart from refining the orbital and kinematic parameters, we detected three relativistic effects in this system: the advance of periastron, the orbital decay caused by the emission of gravitational waves, and the Shapiro delay, caused by the relativistic deformation of space-time near compact objects. Using these measurements we measured the pulsar mass to $1.20^{+0.28}_{-0.29} M_{\odot}$ and its companion mass to $0.97^{+0.16}_{-0.13} M_{\odot}$. This chapter also discusses the future potential of this system in testing GR and constraining alternative theories of gravity. Chapter 6 discusses the timing analysis of PSR J1012–4235 with the MeerKAT radio telescope. We detect a strong Shapiro delay signature in this system and determined that the binary has a high inclination of $88.06^{+0.28}_{-0.25}$ deg. We measured the pulsar and its companion’s mass to $1.44^{+0.13}_{-0.12} M_{\odot}$ and $0.27^{+0.016}_{-0.015} M_{\odot}$, respectively. Lastly, in Chapter 7, I summarise the results and discuss the potential future work for the projects presented in this thesis.

To papa, because all the strength came from you.

"Our passion for learning, evident in the behaviour of every toddler, is the tool for our survival"

Carl Sagan
Cosmos

Acknowledgements

This thesis wouldn't have been possible without the constant help and support from many people.

I would like to start by thanking my direct supervisor, Paulo Freire. His excellent guidance has helped me grow both academically and personally. His deep passion and curiosity for pulsars have kept me motivated and passionate all these years. I am grateful for his kindness and patience in supporting me through some of the most difficult times that I faced in my life and for making my PhD journey a stress-free experience. His advice and comments on improving this thesis have been invaluable.

I want to thank my official supervisor, Michael Kramer for making our fundi group as amazing as it is. Even when the entire world was struggling through loneliness (during Covid times), he managed to find a way to keep us all motivated and connected. His weekly emails were all that I needed to make sure everything was alright (or at least is going to be). I thank him for providing many great advice along the way and for proofreading this thesis. I still don't understand how he manages to find time to help us all in the way he does, but we are all extremely grateful for it.

Next, I want to thank Alessandro Ridolfi for being both a great guide and a friend, throughout. Without his support, I would not have been at this stage. I thank him for helping me through the initial years of my PhD and for his many great pieces of advice along the way (also thanks for those prompt skype calls that kept me motivated).

I would like to thank my senior colleagues who have helped me in my research projects and made me grow as a researcher: Yashwant Gupta, Robert Wharton, Robert Main, Vivek Venkatraman Krishnan, Federico Abate, Jason Wu, David Champion, Norbert Wex, Gregory Desvignes, Ewan Barr, Sarrvesh Sridhar, and Aditya Parthasarathy.

Thanks to all my wonderful friends and colleagues in our MPIfR fundi group. Even their presence (or background laughs and chit-chats) was enough to remember that the world is a kind and happy place. I would especially like to thank Arunima, who even though came in the final year of my PhD, became a close friend. She somehow managed to make me smile in all the difficult moments. Our lunches in Ferdinando and many coffee and chai sessions helped me keep my sanity during the writing phase. Special thanks to Jompoj, Timea, and Weiwei, for the lively chats and discussions around the corridor. Thanks to Mary, Natasha, and Kristen, for the delicious cakes and many cheerful times together. I would also like to thank other friends and colleagues at the institute (in no particular order): Jonah, Huanchen, Surya, Shilpa, Jaswant, Livia, Ferdinand, Miquel, Shalini, Marlon, Alexander, Tim, Joscha, Vishnu, Prajwal, Tilemachos, Jackie. The lunches, random discussions, coffees, pizzas, and many birthday celebrations, I enjoyed every single moment spent in the institute because of you all.

Next, I would like to thank Kira Kühn, Tuyet-Le Tran, Barbara Menten, and Frau Schneider for helping me with the administration-related tasks throughout my time here, and for making the complicated paperwork seem so easy.

Completing my PhD wouldn't have been possible without the emotional support from my

friends and family.

I want to especially thank Richa, right from picking me up from the central station on my 1st day in Germany to submitting my thesis, she has been there in all the big and small moments of this journey. Thanks for those idli and sambar nights! Arunima (you deserve another mention), thanks for cheering up any situation with your cute gestures! Geetam, from our gossip sessions with coffee to our trips to Cologne and Schwarzwald, thanks for some of the most wonderful memories I made in my PhD. Shashi, I am forever grateful to you for being there in the most difficult time of my life and for selflessly caring for me when I was in my most vulnerable state. Jayender, although your time in Bonn was short, it was one of my most cherished times in Bonn, thanks for all those philosophical and political discussions.

I would like to especially thank Gaurav ♡, I don't have words to express the support he has given to me through these years. Thanks for being there in all the good and bad times, and for always inspiring me to do the right thing.

Lastly, I would like to thank my family for their exceptional support and patience throughout. Mumma, thank you for calming me down in uncountable anxious moments and "always" having a solution to my problems. Didaa (my paara mumma), thank you for cheering me up when I needed it the most and telepathically knowing when to call. Dadi, thank you for providing me with the strength to deal with any situation in life, talking to you in the evening every day was what kept me motivated to keep going. And finally, Papa, wish you were here to see your Tashi beta finishing her PhD. Wherever you are, I know you must be very proud of me, whistling and dancing for me. You have made me the person I am today, thank you for providing me with the courage to pursue my dreams and for always believing in me. This was as much your dream as mine. The poem you taught me is forever etched in my mind "Veer tum badhe chalo, dheer tum badhe chalo".

List of publications

Related to this thesis

1. *Upgraded GMRT survey for pulsars in globular clusters. I: Discovery of a millisecond binary pulsar in NGC 6652.*
T. Gautam, A. Ridolfi, P. C. C. Freire, R. S. Wharton, Y. Gupta, S. M. Ransom, L. S. Oswald, M. Kramer, and M. E. DeCesar, *Astronomy & Astrophysics*, 664, A54 (2022).
DOI: <https://doi.org/10.1051/0004-6361/202243062>
2. *Eight new millisecond pulsars from the first MeerKAT globular cluster census.*
A. Ridolfi, **T. Gautam**, P. C. C. Freire, S. M. Ransom, S. J. Buchner, A. Possenti, V. Venkatraman Krishnan, M. Bailes, M. Kramer, B. W. Stappers, F. Abbate, E. D. Barr, M. Burgay, F. Camilo, A. Corongiu, A. Jameson, P. V. Padmanabh, L. Vleeschower, D. J. Champion, W. Chen, M. Geyer, A. Karastergiou, R. Karuppusamy, A. Parthasarathy, D. J. Reardon, M. Serylak, R. M. Shannon and R. Spiewak, *Monthly Notices of the Royal Astronomical Society*, 504 (1), 1407–1426 (2021)
DOI: <https://doi.org/10.1093/mnras/stab790>
3. *Relativistic effects in a mildly recycled pulsar binary: PSR J1952+2630.*
T. Gautam, P. C. C. Freire, A. Batrakov, M. Kramer, C. C. Miao, E. Parent, and W. W. Zhu, submitted to *Astronomy & Astrophysics*.
4. *Detection of Shapiro delay in the highly inclined millisecond pulsar binary PSR J1012–4235*, in prep.
Preliminary list of authors: **T. Gautam**, P. C. C. Freire, J. Wu, V. Venkatraman Krishnan, M. Kramer, F. Camilo, MeerTime relbin members et al.

Other co-authored publications

1. *TRAPUM discovery of 13 new pulsars in NGC 1851*
A. Ridolfi, P. C. C. Freire, **T. Gautam**, S. M. Ransom, E. D. Barr, S. Buchner, M. Burgay, F. Abbate, V. Venkatraman Krishnan, L. Vleeschower, A. Possenti, B. W. Stappers, M. Kramer, W. Chen, P. V. Padmanabh, D. J. Champion, M. Bailes, L. Levin, E. F. Keane, R. P. Breton, M. Bezuidenhout, J.-M. Grießmeier, L. Künkel, Y. Men, F. Camilo, M. Geyer, B. V. Hugo, A. Jameson, A. Parthasarathy and M. Serylak, *Astronomy & Astrophysics*, 664, A27 (2022).
DOI: <https://doi.org/10.1051/0004-6361/202143006>
2. *Four pulsar discoveries in NGC 6624 by TRAPUM using MeerKAT*
F. Abbate, A. Ridolfi, E. D. Barr, S. Buchner, M. Burgay, D. J. Champion, W. Chen, P. C. C. Freire, **T. Gautam**, J. M. Grießmeier, L. Künkel, M. Kramer, P. V.

- Padmanabh, A. Possenti, S. Ransom, M. Serylak, B. W. Stappers, V. Venkatraman Krishnan, J. Behrend, R. P. Breton, L. Levin and Y. Men, *Monthly Notices of the Royal Astronomical Society*, 513 (2), 2292–2301 (2022)
DOI: <https://doi.org/10.1093/mnras/stac1041>
3. *Burst properties of the highly active FRB20201124A using uGMRT*
V. R. Marthi, S. Bethapudi, R. A. Main, H.-H. Lin, L. G. Spitler, R. S. Wharton, D. Z. Li, **T. Gautam**, U.-L. Pen and G. H. Hilmarsson, *Monthly Notices of the Royal Astronomical Society*, 509 (2), 2209–2219 (2022)
DOI: <https://doi.org/10.1093/mnras/stab3067>
4. *The relativistic binary programme on MeerKAT: science objectives and first results*
M. Kramer, I.H. Stairs, V. Venkatraman Krishnan, P. C. C. Freire, F. Abbate, M. Bailes, M. Burgay, S. Buchner, D. J. Champion, I. Cognard, **T. Gautam**, M. Geyer, L. Guillemot, H. Hu, G. Janssen, M. E. Lower, A. Parthasarathy, A. Possenti, S. Ransom, D. J. Reardon, A. Ridolfi, M. Serylak, R. M. Shannon, R. Spiewak, G. Theureau, W. van Straten, N. Wex, L. S. Oswald, B. Posselt, C. Sobey, E. D. Barr, F. Camilo, B. Hugo, A. Jameson, S. Johnston, A. Karastergiou, M. Keith, S. Osłowski, *Monthly Notices of the Royal Astronomical Society*, 504 (2), 2094–2114 (2021)
DOI: <https://doi.org/10.1093/mnras/stab375>
5. *Detection of 15 bursts from the fast radio burst 180916.J0158+65 with the upgraded Giant Metrewave Radio Telescope*
V. R. Marthi, **T. Gautam**, D. Z. Li, H–H Lin, R. A. Main, A. Naidu, U–L Pen, R. S. Wharton, *Monthly Notices of the Royal Astronomical Society: Letters*, 499 (1), L16–L20 (2020)
DOI: <https://doi.org/10.1093/mnrasl/slaa148>
6. *The MeerKAT telescope as a pulsar facility: System verification and early science results from MeerTime*
M. Bailes, A. Jameson, F. Abbate, E. D. Barr, N. D. R. Bhat, L. Bondonneau, M. Burgay, S. J. Buchner, F. Camilo, D. J. Champion, Ismaël Cognard, P. B. Demorest, P. C. C. Freire, **T. Gautam**, M. Geyer, J-M Griebmeier, L. Guillemot, H. Hu, F. Jankowski, S. Johnston, A. Karastergiou, R. Karuppusamy, D. Kaur, M. J. Keith, M. Kramer, J. van Leeuwen, M. E. Lower, Y. Maan, M. A. McLaughlin, B. W. Meyers, S. Osłowski, L. S. Oswald, A. Parthasarathy, T. Pennucci, B. Posselt, A. Possenti, S. M. Ransom, D. J. Reardon, A. Ridolfi, C. T. G. Schollar, M. Serylak, G. Shaifullah, M. Shamohammadi, R. M. Shannon, C. Sobey, X. Song, R. Spiewak, I. H. Stairs, B. W. Stappers, W. van Straten, A. Szary, G. Theureau, V. Venkatraman Krishnan, P. Weltevrede, N. Wex, T. D. Abbott, G. B. Adams, J. P. Burger, R. R. G. Gamatham, M. Gouws, D. M. Horn, B. Hugo, A. F. Joubert, J. R. Manley, K. McAlpine, S. S. Passmoor, A. Peens-Hough, Z. R. Ramudzuli,

A. Rust, S. Salie, L. C. Schwardt, R. Siebrits, G. Van Tonder, V. Van Tonder, M. G. Welz, *Publications of the Astronomical Society of Australia (PASA)*, Volume 37, e028 (2020)

DOI: <https://doi.org/10.1017/pasa.2020.19>

Contents

1	Introduction to Pulsars	3
1.1	Dawn of Pulsar astronomy	4
1.2	Formation of a Neutron star	5
1.3	Composition and Characteristics	6
1.4	Pulsars: The rotating lighthouse model	8
1.5	Ensemble of pulsars - the $P - \dot{P}$ characterisation	10
1.5.1	Young/Canonical pulsars	11
1.5.2	Binary Pulsars	13
1.5.3	Recycled pulsars	13
1.6	Pulsars in Globular Clusters	16
1.7	Interstellar Effects	20
1.7.1	Dispersion	20
1.7.2	Faraday Rotation	21
1.7.3	Scattering	22
1.7.4	Scintillation	24
1.8	Science with Pulsars	24
1.8.1	Direct detection of GWs	24
1.8.2	Tests of gravity theories	25
1.8.3	Mass measurements and NS EOS	27
1.8.4	Science with GC pulsars	28
1.9	Thesis Outline	29
2	How to search, time and image a Pulsar?	31
2.1	Data acquisition with radio telescopes	32
2.1.1	Reflectors	32
2.1.2	Front-end	33
2.1.3	Back-end	34
2.2	Time domain searches	36
2.2.1	Interference mitigation	37
2.2.2	De-dispersion	37
2.2.3	Periodicity search	38
2.2.4	Acceleration and jerk searches	39
2.2.5	Candidate selection and confirmation	40
2.3	Image domain searches in globular clusters	41
2.3.1	Interferometric data acquisition	42
2.3.2	Flagging and calibration	43
2.3.3	Imaging	45
2.4	Orbital parameter estimation	48

2.5	Timing a pulsar	49
2.5.1	TOA creation	49
2.5.2	Timing Model	50
2.5.3	Residual fit and parameter estimation	53
3	Upgraded GMRT survey for pulsars in globular clusters. I: Discovery of a millisecond binary pulsar in NGC 6652 (Summary)	55
3.1	Context	55
3.2	Aims	56
3.3	Methods	56
3.4	Results and conclusions	57
4	Eight new millisecond pulsars from the first MeerKAT globular cluster census (Summary)	63
4.1	Context	63
4.2	Aims	64
4.3	Methods	64
4.4	Results and conclusions	66
5	Relativistic effects in a mildly recycled pulsar binary: PSR J1952+2630	69
5.1	Abstract	70
5.2	Introduction	70
5.3	Observations and data reduction	73
5.3.1	Observations	73
5.3.2	Data Reduction	74
5.3.3	Timing analysis and binary models	75
5.4	Results	77
5.4.1	Polarisation Calibration	77
5.4.2	Timing Solution	79
5.4.3	Astrometry	80
5.4.4	Kinematic Effects on the spin and orbital periods	80
5.4.5	Advance of periastron	82
5.4.6	Shapiro delay	82
5.4.7	Orbital Period Derivative	84
5.5	Mass measurements	84
5.6	PSR J1952+2630 as a gravitational laboratory	87
5.6.1	Simulations	88
5.6.2	Constraints on DEF gravity	91
5.6.3	Additional orbital parameters	95
5.7	Summary and conclusions	96

6	Detection of Shapiro delay in the highly inclined millisecond pulsar binary PSR J1012-4235	99
6.1	Introduction	99
6.2	MeerKAT observations	101
6.3	Data reduction	102
6.4	Polarisation calibration	103
6.5	Timing analysis	104
6.5.1	Binary models	104
6.5.2	Results from radio timing	105
6.5.3	Mass constraint from the Shapiro delay detection	105
6.5.4	Kinematic effects on the spin and orbital period	110
6.6	Gamma and radio profiles	112
6.7	Conclusion	112
7	Conclusion and future work	115
7.1	Summary and conclusion	115
7.2	Future work	119
7.2.1	TRAPUM GC pulsar survey	119
7.2.2	Imaging GCs to search for pulsars	119
7.2.3	Single pulse study of eclipsing binaries	120
7.2.4	Timing pulsar binaries for gravity tests	121
A	Paper titled “Upgraded GMRT survey for pulsars in globular clusters. I: Discovery of a millisecond binary pulsar in NGC 6652”	123
B	Paper titled “Eight new millisecond pulsars from the first MeerKAT globular cluster census”	143
	Bibliography	165

List of Figures

1.1	Mass-Radius relationships from different EOSs theorised for various type of matter inside a NS. The constrains put up by the mass measurements of two pulsars (PSR J0740+6620 and PSR J0348+0432) are shown as horizontal bars with 68.3% confidence limits for the two most massive neutrons stars known yet. Credit: Norbert Wex	7
1.2	Schematic representation of the pulsar lighthouse model with open field lines making up the region of radio beam emission. Picture taken from Lorimer & Kramer 2012	9
1.3	A $P - \dot{P}$ diagram of the pulsar population. Different classes of pulsar population are shown in different colors and shapes. The dashed-dot and dashed lines represent characteristic age and surface magnetic fields respectively. Black line shows the <i>death line</i> assuming multipolar magnetic field configuration from Zhang et al. 2000.	12
1.4	Schematic representation of binary pulsar formation scenarios taken from Stairs (2004). Case A shows binaries with low-mass companions, cases B and C show binaries with intermediate-mass companions while case D shows the MSP evolution with high-mass companions.	14
1.5	Left: Schematic representation of two types of exchange encounters. Right: Schematic representation of a tidal capture event (Figure taken from Mardling (1996)).	17
1.6	Histogram of fraction of different kinds of pulsar population in GCs and galactic field respectively. The difference in the abundances of MSP and binary pulsar population in GCs can be clearly seen.	18
1.7	Histogram of pulsar population in Globular clusters. Two pulsars (M3C and NGC 6749B) are likely real but need confirmation. Credit: Alessandro Ridolfi	19
1.8	Left: Schematic representation of the thin-screen model showing multi-path propagation of light due to turbulent ISM. The initially coherent pulsar signal is distorted due to ISM irregularities. Right: Measured scattering in PSR J1807-2459A profile observed in the GMRT dataset at different frequencies. The scattering timescale, τ increases with decreasing frequency (see legend). Black line is the smooth fitted profile and gray line is the observed profile. Figure credit: Lucy Oswald	23
1.9	Mass-mass diagram for the double pulsar showing measurement of six PK parameters and the mass ratio, R . Figure taken from Kramer et al. (2021)	26

1.10	NS mass measurements from radio pulsar timing. The letter C in parentheses to pulsar name indicate a NS companion to a pulsar that is itself not a pulsar. The blue names are the companion sources which could either be a NS or a massive WD. Right side of the plot shows the histogram of the masses. Credit: Vivek V. Krishnan.	28
2.1	Schematic of components of a typical radio telescope’s front-end and back-end. Figure taken from Cameron (2018)	33
2.2	Power spectrum for a 3ms pulsar, for three different cases: isolated pulsar showing one single peak (left), binary pulsar with large orbital period such that $P_{\text{orb}} > 10t_{\text{obs}}$ (center), and binary pulsar with compact orbit such that $P_{\text{orb}} \sim t_{\text{obs}}$ (right). Credit: Scott Ransom.	39
2.3	Diagnostic plot created by <code>prepfold</code> for PSR J1701–3006G (or M62 G) discovered in the GC survey performed with the MeerKAT radio telescope (discussed in Chapter 4.)	41
2.4	Representation of CLEAN algorithm implemented in CASA’s <code>tclean</code> . Figure taken from Taylor et al. (2014)	46
2.5	Radio image of NGC 6652 created from the GMRT visibility data recorded simultaneously with the time-domain data. Source 1 coincides with the timing position of NGC 6652B while sources 2, 3, and 4 are bright point-like sources within the tidal radii of the cluster.	47
2.6	Period-Acceleration plot for a near-circular orbit of PSR J1835–3259B discovered in GC survey carried out with GMRT presented in Chapter 3 (left) and for a simulated eccentric binary with $e = 0.9$ (right) (taken from Freire et al. 2001)	47
2.7	<code>fit_circular_orbit.py</code> ’s period vs time plot for PSR J1835–3259B.	48
2.8	Representation of residuals as a function of time. Panel <i>a</i> shows post-fit residuals when timing solution accounts for all the trends in the data, while rest of the panels show residuals with characteristic patterns for unaccounted parameters that need to be fit in the data, such as frequency derivatives (panel <i>b</i>), position (panel <i>c</i>), and proper motion (panel <i>d</i>). Figure taken from Lorimer & Kramer (2012)	53
3.1	Residuals obtained with phase-connected solution of NGC 6652B. Grey points are ToAs derived from the data taken with uGMRT at frequencies below 1000 MHz, while orange points represent GBT ToAs derived from L-band data within 1000-1700 MHz, and blue points show GBT S-band data above 1700 MHz.	57

3.2	Intensity profiles as function of rotational phase of NGC 6652B obtained with Band-3 receiver of uGMRT at 400 MHz, Band-4 receiver of uGMRT at 650 MHz, and L-band receiver of GBT at 1500 MHz. Flux number on y-axis is relative. The horizontal bars show the time resolution of the system for the DM of the pulsar. For the GBT profile, this is merely the adopted bin size of the profile. The profiles were visually aligned.	58
3.3	Radio images of NGC 6652 and NGC 6539 GCs observed with the uGMRT. X and Y axis represent RA (hh:mm:ss) and DEC ($^{\circ}$: $'$: $''$), respectively. The cyan-coloured circle shows the core radius, and the dashed cyan circle shows the half-mass radius.	59
3.4	Comparison of flux density estimates from radio images and folded profiles at 400 MHz for pulsars NGC 1851A, NGC 6544A, NGC 6544B, NGC 6652B, and NGC 6539A, and at 650 MHz for the rest. Blue points represent binary systems, while magenta points represent isolated systems. Pulsars in eclipsing binary systems are marked with black circles, and pulsars with large duty cycles are marked with squares. Points in grey represent the upper limits for pulsars with no measured flux in imaging. The dashed line represents the linear expected trend. The only factor correlating with an imaging flux excess is the large duty cycle.	60
4.1	Integrated pulse profiles of the eight MSPs discovered, with their spin period and DM indicated. The horizontal section of the tiny bars on the top-right of each panel shows the sampling time of the native-resolution (sampling time of $9.57 \mu\text{s}$) MeerTime search-mode data.	65
4.2	Mass-inclination and mass-mass diagram for Ter 5 an. The main square panels depict the $\cos i$ - M_c and M_c - M_p planes. The red lines depict the masses consistent with the measurement of $\dot{\omega}$ and its ± 1 - σ uncertainties, under the assumption that this effect is dominated by the GR contribution and that GR is the correct theory of gravity. The contours include 68.3 and 95.4% of a 2-D PDF derived from the χ^2 of TEMPO fits that assumed all GR effects to be according to the masses and orbital inclination at each point. The side panels show the PDF of $\cos i$ (top left), M_p (top right) and M_c (right) derived by marginalizing the aforementioned 2-D PDFs. The estimated median pulsar mass is $2.13 M_{\odot}$ and median companion mass is $0.75 M_{\odot}$	66

4.3	MeerTime L-band tied array beams, shown through their contours as solid grey lines at their 50 percent level of power, for one sample observation of GC Terzan 5 and NGC 6752F. We show the size of the beam for the top edge frequency (inner ellipse), center frequency (middle ellipse) and bottom edge frequency (outer ellipse). For both the clusters, we show the core radius (dashed blue line) as well as all the pulsars with a precisely determined position (black dots for the previously known pulsars, red dots for the discoveries presented here).	67
5.1	The total intensity is shown in black, while linear and circular polarisation is shown in red and blue, respectively, as a function of longitude. Top panel shows the polarisation angle (PA) swing across the rotational phase.	78
5.2	Post-fit residuals of ToAs from Arecibo data (with Mock and PUPPI backends) and FAST data (with ROACH backend) as a function of year (below) and orbital phase of pulsar (top). Different colors show residuals for different backends. Points labelled Mock-1 and Mock-2 show different set of timing observations with Mock spectrometers (see Table 5.1).	79
5.3	Total kinematic contribution to the observed orbital decay, $\dot{P}_{b,\text{gal}}$ is shown as a function of distance to the pulsar in the blue curve. Red, orange, and green curves represent individual contributions due to galactic disc acceleration, galactic rotation (or differential) acceleration, and proper motion of the pulsar, respectively, with errors in R_0 and θ_0 providing negligible contributions. The vertical black line marks the DM distance from the NE2001 model with 20% uncertainty in the model shown as dashed black lines. Grey lines show an estimate of the DM distance from the YMW16 model. The maximum uncertainty in total kinematic contribution is 5.1fs s^{-1}	83
5.4	Constraints on the M_c , M_p , and $\cos i$ derived from the measurement of three relativistic PK parameters are shown. Black dashed line shows the maximum M_c constraint of $1.48 M_\odot$. Colored dashed lines depict the 1σ uncertainty on the measurements. Black contours show the likelihood or 2-D PDFs at 68 % (inner) and 95 % (outer) confidence from the χ^2 maps on $\cos i - M_c$ and $M_p - M_c$ grids, derived from the DDGR fit. The corner plots represent the marginalised 1-D PDFs of each of these measurements and vertical lines on these mark the median, 1σ , and 2σ estimates. The black crosses indicate the best masses from the DDGR solution and the best inclination derived from the mass function using those masses.	85

5.5	1D Probability density function of $\dot{P}_{b,x}$ derived from the best fit χ^2 of DDGR solution. Blue dots represent the grid points over which the TEMPOfit was done and blue curve shows the interpolated function. Black vertical lines represent the median and 1σ values and gray lines show the 2σ constraint. We get 1σ estimate of $\dot{P}_{b,x}$ as $-6_{-68}^{+58} \times \text{fss}^{-1}$.	86
5.6	Representation of measurements of three PK parameters in future assuming timing campaigns with FAST until year 2039, which is when the mass uncertainties reach kinematic precision. Dashed lines show 1σ uncertainties, gray dashed lines represent the kinematic limit on \dot{P}_b measurement coming from distance uncertainty.	89
5.7	\dot{P}_b uncertainty variation with simulated orbital campaigns are shown for campaigns once (blue) and four (green) times every year. The precision of \dot{P}_b predicted by GR as $\dot{\omega}$ uncertainty decreases over the years is shown with orange and red points. The grey point shows the present value, and the dashed line represents the limit due to kinematic uncertainty.	90
5.8	$\Delta\chi^2$ map in Damour-Esposito-Farèse (DEF) gravity space $\{\alpha_0, \beta_0\}$ for the simulated dataset (2023-2032) with four campaigns every year. The tests are performed using the DDSTG timing model and assuming stiff MPA1 EOS. The solid lines correspond to the 68% CL limits ($\Delta\chi^2 \simeq 2.28$). Limit with the blue line is based on the existing TOAs. The blue shade and the orange line are the results for the simulated TOAs not accounting for the Galactic uncertainty in $\dot{P}_{b,x}$. The green line shows the corrected limit, with $\dot{P}_{b,x}$ taken at its 1σ limit. The grey dashed line is the limit from the Solar System Cassini experiment ($\alpha_0^2 \lesssim 1.15 \times 10^{-5}$).	92
5.9	Comparison of existing limits placed on DEF gravity space $\{\alpha_0, \beta_0\}$ by radiative tests from different pulsars to the predictions for J1952+2630. All limits are taken for 68% CL and assume MPA1 EOS. The limit for J1952+2630 is predicted by the DDSTG timing model based on the simulated data set for observations from 2023 till 2032 with four campaigns every year. The limits for other pulsars are calculated by the traditional PK method based on the current measured PK parameters published in the literature (see Table 5.4). We do not include the limit from the Triple System PSR J0337+1715 because of its non-radiative origin despite being more restrictive in the large range of β_0 .	93
6.1	MeerKAT L-Band profile integrating total 13.2 hr of data. Top: Intensity vs rotation phase, bottom: Frequency vs rotation phase. Number of phase bins are 1024 and SNR is 977.	101

6.2	Polarisation calibrated profile of PSR J1012–4235 formed from MeerKAT L-band data. The red color shows linear polarisation and the blue color shows circular polarisation across the rotational phase. Upper panel shows the polarisation angle swing across the rotational phase.	103
6.3	(a) Post fit residuals for PSR J1012–4235 showing TOAs from Parkes, GBT, and MeerKAT data, with error bars representing 1σ uncertainty in TOAs. (b) Residuals of MeerKAT TOAs excluding the fit for Shapiro delay effect but fixing all the other system and orbital parameters obtained from full fit. The orbital phase is measured from periastron and the peak in the Shapiro delay signature occurs around the phase of superior conjunction of the pulsar.	106
6.4	Constraints on the M_c , M_p , $\cos i$ derived from the measurement of Shapiro delay. Colored dashed lines depict the 1σ uncertainty on the measurement. Black contours show the likelihood or 2-D PDFs at 39 % (inner) and 85 % (outer) confidence ellipse from the χ_{red} maps on $\cos i - M_c$ and $M_p - M_c$ grids, derived from the ELL1 binary model fit. The corner plots represent the marginalised 1-D PDFs of each of these measurements and vertical lines on these mark the median, 1σ , and 2σ estimates. The black crosses indicate the best masses fit by the DDGR solution and the best inclination derived from the mass function using those masses.	109
6.5	Acceleration contributions to orbital period derivative due to kinematic effects as a function of distance. Orange and green curves show the vertical and differential accelerations from galactic disc while red curve shows the contribution from proper motion of the pulsar. Blue curve represents the total acceleration contribution. Distance uncertainty of 20% is assumed on the DM distance predictions from NE2001 (black vertical lines) and YMW16 model (cyan vertical lines) while 1σ uncertainty is shown for the parallax measurement from timing (purple vertical lines).	111
6.6	Comparison of the gamma-ray pulse profile (red) with the radio profile (black) of PSR J1012–4235. The profile is formed using a phase connected solution (ephemerides) such that both the folds take the same reference epoch as the start of the profile.	113

List of Tables

5.3	Timing solution of PSR J1952+2630 with DDGR and ELL1H+ models. Values in brackets are 1σ uncertainties, and values without uncertainties are derived from the corresponding binary model. Values in square brackets are not fit but derived assuming GR. ^a Assumed value derived from $\sin i$ parameter in the DDGR solution. ^b Assuming NE2001 distance and uncertainty	81
5.4	Binary pulsar systems used for comparing constraints on the DEF theory in Figure 5.9. The measured PK parameters published in the literature along with other information are used for calculating limits. M_c and the mass ratio q for J1738+0333 are measured from the optical observations of the companion. Value in bracket is expected to be measured in the future.	95
6.2	Phase-connected timing solution for PSR J1012–4235 using the ELL1H+ binary model.	107
6.3	Derived parameters for PSR J1012–4235.	108

Nomenclature

Acronyms used in this thesis

BAT	Baryctric Arrival Time	NANOgrav	North American Nanohertz Observatory for Gravitational Waves
BB	Binary Barycentre	NIST	National Institute of Standards and Technology
BIPM	Bureau International des Poids e Mesures	NS	Neutron Star
BT	Blandford & Teukolsky binary model	OPM	Orthogonal Polarized Mode
DADA	Distributed Acquisition and Data Analysis format	ONeMg WD	Oxygen-Neon-Magnesium White Dwarf
DFT	Discrete Fourier Transform	PA	Linear Polarization Position Angle
DM	Dispersion Measure	PFB	Polyphase Filterbank
DNS	Double Neutron Star	PK	Post-Keplerian
EoS	Equation of State	PPTA	Parkes Pulsar Timing Array
EPTA	European Pulsar Timing Array	PTA	Pulsar Timing Array
FAST	Five-hundred-meter Aperture Spherical Telescope	PUPPI	Puertorican Ultimate Pulsar Processing Instrument
FFT	Fast Fourier Transform	RFI	Radio Frequency Interference
FT	Fourier Transform	RM	Rotation Measure
FWHM	Full Width at Half Maximum	RVM	Rotating Vector Model
GC	Globular Cluster	S/N	Signal-to-Noise ratio
GPS	Global Positioning System	SAT	Site Arrival Time
GPU	Graphics Processing Unit	SI	International System of Units
GR	General Relativity	SKA	Square Kilometre Array
GW	Gravitational Wave	SN	Supernova
HA	Hour Angle	SNR	Supernova Remnant
He WD	Helium White Dwarf	SSB	Solar System Barycentre
HMXB	High-Mass X-ray Binary	TAI	International Atomic Time
HPC	High-Performance Computer	TCB	Barycentric Coordinate Time
IAU	International Astronomical Union	TDB	Barycentric Dynamic Time
ICRS	International Celestial Reference System	tMSP	Transitional Millisecond Pulsar
IEEE	Institute of Electrical and Electronics Engineers	ToA	Time of Arrival
IMBH	Intermediate-Mass Black Hole	TT	Terrestrial Time
IMXB	Intermediate-Mass X-ray Binary	UTC	Universal Coordinated Time
IPTA	International Pulsar Timing Array	VLBI	Very-Long-Baseline interferometry
ISM	Interstellar Medium	WAPP	Wideband Arecibo Pulsar Processors
JPL	Jet Propulsion Laboratory	WD	White Dwarf
LIGO	Laser Interferometer Gravitational-wave Observatory		
LMXB	Low-Mass X-ray Binary		
LNA	Low-Noise Amplifier		
LO	Local-Oscillator		
MJD	Modified Julian Date		
MS	Main Sequence		
MSP	Millisecond Pulsar		

Numerical Constants

π 3.14159265358979323846264338327950288419716939937510
 e 2.71828182845904523536028747135266249775724709369995

Physical and Astronomical Constants

Speed of light	c	299792458 m s ⁻¹
Newton constant of gravitation	G	6.67408(31) × 10 ⁻¹¹ m ³ kg ⁻¹ s ⁻²
Planck constant	h	6.626070040(81) × 10 ⁻³⁴ J s
Elementary charge	e	1.6021766208(98) × 10 ⁻¹⁹ C
Electron mass	m_e	9.10938356(11) × 10 ⁻³¹ kg
Proton mass	m_p	1.672621898(21) × 10 ⁻²⁷ kg
Boltzmann's constant	k_B	1.38064852(79) × 10 ⁻²³ erg deg ⁻¹
Astronomical unit	AU	149 597 870 700 m
Parsec	pc	30856775814913673.513720652 m
Julian year	yr	31557600 s
Solar mass	M_\odot	1.98855(25) × 10 ³⁰ kg
Nominal solar radius	R_\odot	695700 m
Solar mass in units of time	$T_\odot = GM_\odot/c^3$	4.9254909476412675 × 10 ⁻⁶ s

Introduction to Pulsars

Contents

1.1 Dawn of Pulsar astronomy	4
1.2 Formation of a Neutron star	5
1.3 Composition and Characteristics	6
1.4 Pulsars: The rotating lighthouse model	8
1.5 Ensemble of pulsars - the $P - \dot{P}$ characterisation	10
1.5.1 Young/Canonical pulsars	11
1.5.2 Binary Pulsars	13
1.5.3 Recycled pulsars	13
1.6 Pulsars in Globular Clusters	16
1.7 Interstellar Effects	20
1.7.1 Dispersion	20
1.7.2 Faraday Rotation	21
1.7.3 Scattering	22
1.7.4 Scintillation	24
1.8 Science with Pulsars	24
1.8.1 Direct detection of GWs	24
1.8.2 Tests of gravity theories	25
1.8.3 Mass measurements and NS EOS	27
1.8.4 Science with GC pulsars	28
1.9 Thesis Outline	29

This chapter discusses briefly the nature and characteristics of pulsar systems that have been observed until now. The formation and composition of a pulsar is discussed in Sections 1.2 and 1.3. Varied types of pulsar population are discussed in Section 1.5. The effects of the interstellar medium on the pulsar signal are discussed in Section 1.7. The application of pulsars in astronomy and their role in deepening our knowledge of fundamental physics are discussed in Section 1.8. Lastly, the structure of this thesis is stated in Section 1.9.

1.1 Dawn of Pulsar astronomy

First discovered in 1967 (Hewish et al., 1968) by then-graduate student Jocelyn Bell, pulsars are highly magnetized rotating neutron stars (NS). Their non-pulsating radio beams pass our line of sight with each rotation they make, generating apparent radio “pulses”. These radio beams are highly polarised and originate from the plasma streaming along open magnetic field lines of NS.

In 1934, soon after the discovery of neutrons, the existence of NSs was theorised by W. Baade and F. Zwicky in a series of papers (Baade & Zwicky, 1934a; Baade & Zwicky, 1934b) where they coined the term “Supernova” (SN). These rare and violent explosions occur when a massive star runs out of nuclear fuel (as explained in detail in Section 1.2), with its core collapsing on its own gravity to form a NS, while the outer layers shed in an expanding fireball with maximum luminosity reaching as much as the luminosity of the whole “nebulae” in which they originate (in today’s terminology, the host galaxy).

Four years later, Landau (Landau, 1938) proposed that even though the neutronic state of matter is usually endothermic and is much less energetically favoured than the electronic state, a massive star that has immense self-gravity can still create conditions to form neutrons in a stable reaction. Hence, it was proposed that the end product of a SN is a cold, dense, and compact neutron star that is mostly made of neutrons. Its size decreases significantly in the process of collapse making it as compact as the size of a small city (~ 12 km).

In 1939, Oppenheimer & Volkoff (1939) studied the structure of the NS and constrained its maximum mass (similar to Chandrasekhar’s limit on the mass of a white dwarf) assuming it to be entirely made of degenerate cold Fermionic gas of neutrons. Considering a more realistic equation of state that assumes nuclear forces between neutrons, this limit is estimated as $3 M_{\odot}$. In 1964, Woltjer (1964) proposed that due to the magnetic flux conservation, a star with such extraordinary densities will have amplified magnetic field strength going up to 10^{14} to 10^{16} G.

The first identification of a SN with a nebula was in 1939 by Nicholas Mayall (Mayall, 1939) (and soon after by Walter Baade (Baade, 1942) and others) who recognised that the Crab nebula was associated with a SN remnant (the SN was recorded as a bright “guest” star by Chinese astronomers in 1054).

The first pulsar, PSR B1919+21 (Hewish et al., 1968), then known as CP1919 (Cambridge Pulsed source at an RA of 19h 19m) was discovered in the survey carried out at Mullard Radio Astronomy Observatory in Cambridge (UK). The survey was conducted to study the scintillation of the interplanetary medium at a frequency of 81.5 MHz. Jocelyn Bell Burnell discovered extremely stable periodic radio pulses in those data. The pulses arrived at an interval of ~ 1.337 s with a dispersion sweep across the 1-MHz frequency band, confirming that the source was non-terrestrial. Soon after, three other similarly pulsating sources were discovered (Pilkington et al., 1968).

Several theories on the origin of these sources were proposed at that time. Hewish

et al. (1968) had proposed that these could arise either from the radial oscillations of a white dwarf or a neutron star, or from the orbital motion of a close binary (also proposed by Burbidge & Strittmatter 1968) or either from a rotating neutron star, while Ostriker & Hartwick (1968) hypothesized its origin to hot spots on rotating white-dwarf, and Gold (1969) proposed its origin from a rotating neutron star. In 1967, Franco Pacini theorised that the source of the energy of a SN could be a fast-rotating and highly magnetised neutron star (Pacini, 1967), a scenario later explored for Crab Nebula (Pacini, 1968). Soon after which followed the discovery of the Crab pulsar in this nebula (Staelin & Reifenstein, 1968) whose fast periodic pulsations of 33 ms provided a compelling argument that the source of observed radio pulsations are rotating neutron stars (Comella *et al.*, 1969). Secular variation over longer timescales in the pulse period provided additional evidence that the pattern in the pulsations is a result of a decrease in rotational speeds (as predicted by Gold 1969) instead of source oscillations (from WD or NS). These initial discoveries marked the dawn of pulsar astronomy which has consistently enlightened our understanding of fundamental physics since then.

1.2 Formation of a Neutron star

In its entire evolutionary cycle, a star spends the longest time in a stable stage known as the main-sequence. In this stage, it is in a stable equilibrium balanced by the force of gravity pulling inwards and the radiation pressure and thermal expansion of the gas pushing outwards. This outward pressure is produced by the thermonuclear fusion of Hydrogen via a proton-proton chain reaction to form Helium (Vogt, 1926; Russell, 1931). The time span of this stage depends on the mass of the star. A more massive star exerts higher pressure on the core; this increases its temperature and the rate of fusion reactions (and resulting luminosity). These reactions increase, as a function of stellar mass, at a rate much faster the stellar mass itself. This means that more massive stars spend much shorter times in the main-sequence stage.

Once all the Hydrogen is exhausted, the decrease in thermal pressure causes the star to shrink, this raises the internal temperature of the star and, in turn, promotes the burning of Helium to form Carbon. An increased release of energy from Helium fusion causes the star to leave the main sequence, expanding and becoming a giant. This stage sustains only until enough Helium is available to provide energy via fusion. Once Helium has been depleted, if the star is massive enough, a similar process is continued where Carbon burns to form Oxygen.

In the case where the progenitor star is not massive enough ($M < 8 M_{\odot}$), the increase in temperature after the collapse may not be enough to form heavier elements via nuclear fusion, this leaves behind a degenerate core: either a Helium (He), a Carbon-Oxygen (CO) or an Oxygen-Neon-Magnesium (ONeMg) white dwarf star (WD) (based on the progenitor's mass). The WD formed is sustained by the electron degeneracy pressure, caused by the fact that the electrons obey the exclusion principle

and their energy is described by Fermi-Dirac statistics.

In contrast, if the progenitor star has a mass ranging from 8 to 20 M_{\odot} , the burning of elements continues until Iron, ^{56}Fe is formed. Since fusion of ^{56}Fe is an endothermic process and requires an enormous amount of energy, the star can no longer sustain the gravitational pressure and thus collapse under its own gravity resulting in a violent explosion – core-collapse Supernovae (CCSNe or Type II). In this process, if the resulting core has mass above Chandrasekhar’s limit ($M_{\text{ch}} \sim 1.44 M_{\odot}$) (Chandrasekhar & Milne, 1931; Chandrasekhar, 1935), the Fermi pressure of electrons becomes so high that it is energetically more favourable for electrons to combine with protons and form neutrons. This happens via the inverse beta decay reaction in a process called *neutronisation*: $p + e^{-} \longrightarrow n + \nu_e$. The neutrino outbursts produced as a result of this reaction create shock waves in the outer layers, which then shed outwards releasing energies up to $\sim 10^{53}$ ergs. Nearly 99% of the gravitational binding energy of the newly formed NS is released in the form of neutrino outburst and only a small fraction of it creates the observed SN explosion. The NS is held against implosion mostly because of the Fermi pressure of neutrons. Due to angular momentum conservation, the slowly rotating massive progenitor star turns into an extremely fast rotating NS, with rotations up to a fraction of a second. Densities in the core of NSs can reach up to and higher than $\sim 10^{14} \text{g cm}^{-3}$, which is the density of nuclear matter. Core-collapse is thought to be the most common formation mechanism of an NS.

An alternative NS formation mechanism is through CO WD binaries with either a main-sequence star, a low-mass giant or a helium star companion (Wang & Han, 2012). If the CO WD accretes enough mass to reach M_{ch} then the WD can explode in a Type Ia supernovae (Hoyle & Fowler (1960); Nomoto et al. (1984)) and leave behind a NS. Additional formation channel from ONeMg WD binary has also been proposed. At the end stage of an MS star’s life cycle, the WD accrete material from the star and fills its Roche lobe. If the accreted mass exceeds M_{ch} , the WD’s core can reach high ignition temperatures assisting electron capture reactions of Mg and Ne, this would make the WD implode and form a neutron star. This mechanism is commonly known as accretion-induced collapse (AIC) (Tauris et al., 2013). Since both the above scenarios involve WD binaries, they are proposed to be more common in globular clusters (GCs) (Boyles et al., 2011). This is because the high rate of stellar interactions provides a higher chance of formation of such binaries.

1.3 Composition and Characteristics

The unknown microscopic composition of NS yields its equation of state (EOS) which is the relation of its pressure and density. The exact EOS of the internal structure directly relates to the macroscopic properties of NSs such as mass, radius, and moment of inertia. Since NSs have degenerate neutrons, their EOS need to be relativistic. It is calculated via the relativistic hydrostatic equilibrium equations known as Tolmann-Oppenheimer-Volkoff (TOV) equations that are derived from general relativity (Op-

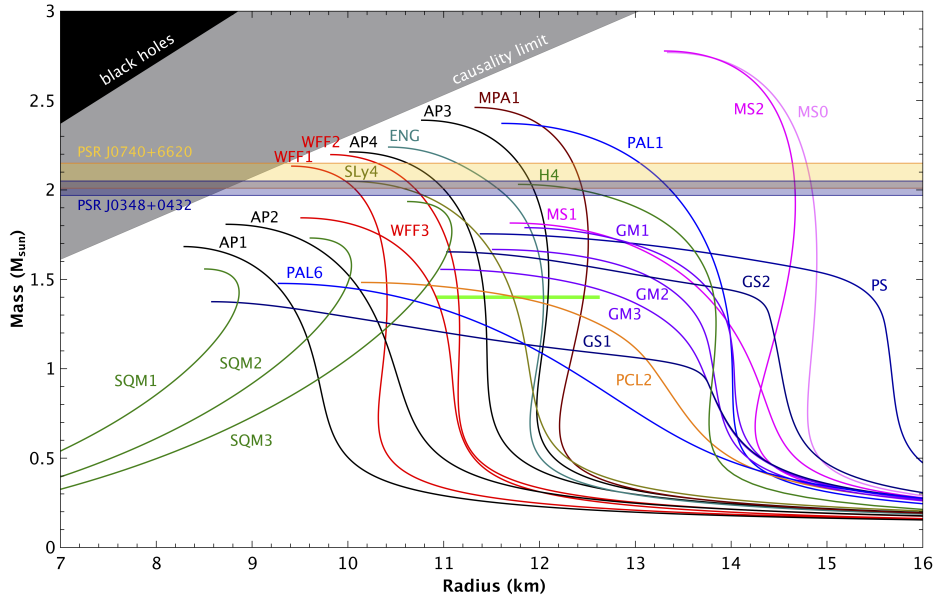


Figure 1.1: Mass-Radius relationships from different EOSs theorised for various type of matter inside a NS. The constrains put up by the mass measurements of two pulsars (PSR J0740+6620 and PSR J0348+0432) are shown as horizontal bars with 68.3% confidence limits for the two most massive neutrons stars known yet. Credit: Norbert Wex

penheimer & Volkoff, 1939; Tolman, 1939). Assuming a simple EOS with only neutron degeneracy pressure, the maximum mass of the NS was first predicted to be only $0.7 M_{\odot}$, hence it was clear that additional repulsive forces should to be considered for a NS as heavy as $1-2 M_{\odot}$ to remain stable against the gravitational collapse (Harrison et al., 1965). Since then, many different models have predicted various EOSs (see Sauls 2019 for a recent review). Most of these models propose a layered structure for the NS: comprising different states of matter (with their respective EOSs) at various levels of densities, going from the outer crust to the inner core. Observational studies of pulsars are crucial to determine their exact composition because the immensely dense (denser than atomic nuclei) yet relatively cold matter present inside the NS can not be recreated in a laboratory on Earth while maintaining low temperatures. Such EOSs must therefore be inferred theoretically.

Each proposed theoretical model for an EOS predict a different mass-radius relationship having a distinct limiting mass for the NS, above which, it will become unstable against its gravitational pull (see Figure 1.1). We can constrain several of these EOSs by measuring a large NS mass that can eliminate several EOSs, for instance, the horizontal bars in Figure 1.1 show constraints from the mass measurement of PSR J0740+6620 (Fonseca et al., 2021) and PSR J0348+0432 (Riley et al., 2021; Antoniadis et al., 2013).

1.4 Pulsars: The rotating lighthouse model

Pulsars are rapidly rotating highly magnetised neutron stars, we categorise them as a subset of NSs whose combination of rotation and magnetic fields allow for a strong emission of electromagnetic beams that are visible to us. In what follows, we will concentrate mostly on radio pulsars. Even though the their true structure and the phenomenology behind the radio pulse emission is rather intricate (as discussed in Section 1.3) and still heavily debated, a relatively simple toy model commonly known as the “lighthouse model” can nevertheless explain many of their observational properties to a sufficiently good level. For a rotating NS with a purely dipolar magnetic field, \mathbf{B} in a direction misaligned with the spin axis, \mathbf{S} . The radio emission comes mostly from, and is directed mostly along, directions near the magnetic axis of the pulsar. Distant observers will observe an apparent radio pulse every time the regions close to the spin axis are aimed in their direction, in a fashion similar to a lighthouse. The pulse period is therefore the rotation period of the pulsar, P . The field lines are divided into a set of open and closed field lines. The emission beam of a pulse is defined by the extent of the open field line region around the direction of the pulsar’s magnetic axis (see Figure 1.2). The cylindrical region limited by the last closed field line characterizes the pulsar’s magnetosphere. This is the region within which the plasma particles are bound to the magnetic fields and co-rotate with the rotation of the NS. The radius of this cylinder, R_{LC} is defined as the region where these particles reach a limiting speed of light, c and is given by:

$$R_{LC} = \frac{c}{\Omega} = \frac{cP}{2\pi} \sim 4.77 \times 10^4 \text{km} \left(\frac{P}{\text{s}} \right), \quad (1.1)$$

where Ω is the angular frequency of the pulsar. A coherent beam of accelerated charged particles generate in the direction of open magnetic field lines from a region called *polar gap* which is just above the magnetic poles on the surface. For a more realistic approach to pulse emission physics, we refer the readers to [Graham-Smith \(2003\)](#); [Harding \(2018\)](#).

Over time the pulsar lose its rotational kinetic energy, also referred as *spin-down luminosity* which is given as:

$$\dot{E} = \frac{d}{dt} (I\Omega^2/2) = -I\Omega\dot{\Omega} = 4\pi^2 I \dot{P} P^{-3}, \quad (1.2)$$

where I is the moment of inertia of the NS and $\dot{P} = dP/dt$ is the spin-down rate. The moment of inertia is defined as $I = km_p R^2$, where k is a constant based on the EOS, and m_p and R are the mass and radius of the NS. Since this information is generally unavailable, a value of for I of 10^{45}g cm^2 is commonly assumed, as it has the same order of magnitude as most detailed NS models.

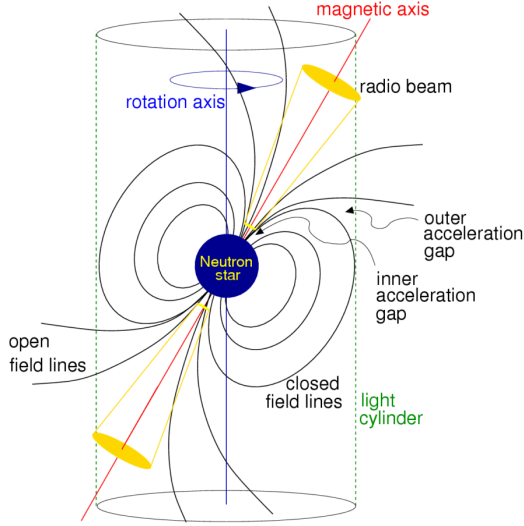


Figure 1.2: Schematic representation of the pulsar lighthouse model with open field lines making up the region of radio beam emission. Picture taken from [Lorimer & Kramer 2012](#)

A majority of spin down is due to energy loss in the form of magnetic dipole radiation and through high energy emission and pulsar winds. Only a small portion of this energy ($\sim 10^{-5} - 10^{-6}$) is lost in the form of radio emission. Assuming the NS as simply a rotating magnetic dipole, the energy loss in the form of electromagnetic waves can be given as ([Jackson, 1962](#)):

$$\dot{E}_{\text{dipole}} = \frac{2}{3c^3} |\mathbf{m}|^2 \Omega^4 \sin^2 \alpha \text{ erg s}^{-1}, \quad (1.3)$$

where α is the misalignment angle between spin and magnetic axis, and \mathbf{m} is the magnetic dipole moment. Attributing all the energy loss \dot{E} to magnetic dipole radiation, we will get a relation between Ω and $\dot{\Omega}$:

$$\dot{\Omega} = - \left(\frac{2|\mathbf{m}|^2 \sin^2 \alpha}{3Ic^3} \right) \Omega^3. \quad (1.4)$$

This implies a power law-like relation between the pulsar spin-down ($\dot{\nu}$) and its rotation (ν): $\dot{\nu} = -K\nu^n$, where n is the *breaking index* and K is the proportionality constant. Following our assumption above, if the rotating energy is only dissipated through magnetic dipole radiation, n is 3 (from Equation 1.4). Realistically, the pulsar magnetosphere is not in vacuum and instead filled with energetic plasma, thus contributions from other radiation processes such as outward flowing winds of particles or quadrupolar radiation can deviate this number. By differentiating the above equation, we can calculate n as follows:

$$n = \nu \ddot{\nu} / \dot{\nu}^2, \quad (1.5)$$

where ν , $\dot{\nu}$, and $\ddot{\nu}$ can be measured through radio pulsar timing. In practice, measuring $\ddot{\nu}$ is challenging (e.g. see [Espinoza 2018](#)) as it can get contaminated from a) timing irregularities, b) due to the low spin-down rates in older pulsars, it can go well below $10^{-20} \text{ Hz s}^{-2}$ making its measurement difficult, or c) because of the presence of glitches in young pulsars (mentioned in Section 1.5.1) (e.g. [Lower et al. 2021](#)) its value can change sporadically. Assuming a population of only young pulsars we get n from 1.2 to 3 ([Espinoza et al., 2017](#)), this clearly indicates $n=3$ assumption is generally not correct and other contributions are needed to explain the spin down (or breaking index).

A pulsar's age can also be estimated by integrating the above relation (Lorimer & Kramer, 2012):

$$T = \frac{P}{(n-1)\dot{P}} \left[1 - \left(\frac{P_0}{P} \right)^{n-1} \right], \quad (1.6)$$

where P is the current pulsar spin period and P_0 is its spin period at birth. Assuming pure magnetic dipole braking ($n=3$) and considering $P_0 \ll P$, we get the characteristic age of the pulsar τ_c as:

$$\tau_c \equiv \frac{P}{2\dot{P}} \simeq 15.8 \text{Myr} \left(\frac{P}{\text{s}} \right) \left(\frac{\dot{P}}{10^{-15}} \right)^{-1}. \quad (1.7)$$

Note that this equation is not valid for very young pulsars (such as Crab Pulsar or PSR J1801-2451) or milli-second pulsars where the assumption of $P_0 \ll P$ and $n=3$ breaks.

An estimate of the surface magnetic field of the pulsar can also be determined from the measurement of ν and $\dot{\nu}$. Since a dipolar magnetic field is proportional to the dipole moment and inversely proportional to the distance: $|\mathbf{m}|/r^3$, Equation 1.3 can be used to derive the surface magnetic field (B_s) of an NS of radius R :

$$\begin{aligned} B_s &\equiv \sqrt{\frac{3c^3}{8\pi^2} \frac{I}{R^6 \sin^2 \alpha} P \dot{P}} \\ &\simeq 10^{12} \text{G} \left(\frac{\dot{P}}{10^{-15}} \right)^{1/2} \left(\frac{P}{\text{s}} \right)^{1/2}, \end{aligned} \quad (1.8)$$

where the relation assumes $R \sim 10$ km, $I \simeq 10^{45}$ g cm², and $\alpha = 90^\circ$. Magnetic field in the range $\sim 10^{11} - 10^{13}$ G is estimated from the above relation for typical NSs. These align very well with the measurements from X-ray spectra of both isolated and binary pulsars (Bignami et al., 2003; Ebbens, 2020).

1.5 Ensemble of pulsars - the $P - \dot{P}$ characterisation

There are 3321 confirmed pulsars at the time of writing this thesis ¹. Of these, 258 pulsars are in globular clusters, and 31 are in the Small and Large Magellanic Cloud (LMC) combined. There is a wide variety in the observational properties of these systems, which depict several different classes with distinct evolutionary histories. One crucial way of classifying the pulsar population is to divide them based on their spin parameters, i.e. their spin periods, P and spin period derivative, \dot{P} . Since the release of rotational energy of a pulsar increases its spin period over time, classifying pulsars based on their P and \dot{P} can help us predict both its present stage and its evolutionary passage in its life cycle. From the relationships discussed in Section 1.4, one can also estimate the magnetic fields and characteristic ages of each pulsar and use these to

¹<https://www.atnf.csiro.au/research/pulsar/psrcat/>

classify pulsars on the $P - \dot{P}$ plane. Figure 1.3 shows all the pulsars for which these properties have been estimated. We can see that there exist different “islands” of the pulsar population.

The population at the top right corner are “magnetars”: isolated neutron stars with very high magnetic field strengths ($> 10^{13}$ G) and long spin periods ($\sim 2 - 12$ s). Their emission mechanism is powered by the decay of their ultra-strong magnetic field, hence they are known to emit mostly in Gamma-ray and X-rays. Of 30 known Magnetars ² at the time of writing, only six have been detected in Radio waves (Olausen & Kaspi, 2014). We do not discuss these in detail as this thesis work does not study magnetars (see Kaspi & Beloborodov 2017 for review).

Below we discuss in detail each of the broad categories of the diverse pulsar population and how they differ from each other.

1.5.1 Young/Canonical pulsars

The largest island towards right in Figure 1.3 shows the young or canonical pulsar population. Young pulsars, as the name suggests, are the class of pulsars that have recently formed in SN (as discussed in Section 1.1). Pulsars that are found to be associated with supernova remnants (SNRs) usually have characteristic ages of less than 100 kyrs. These pulsars are mostly found isolated, as the binary (even if present initially) gets disrupted due to violent SN. They have small rotational periods (~ 20 ms) that increase over time as they lose their rotational kinetic energy and high spin-down rates ($> 10^{-15} \text{ s s}^{-1}$) implying a high spin-down luminosity. They have strong surface magnetic fields, $B_s \sim 10^{12} - 10^{14}$ G (Johnston & Karastergiou, 2017). An interesting application of studying such pulsars is that they can be associated with their progenitor SNR, which are yet to achieve equilibrium with the surrounding medium. The young age of such pulsars thus not only allow us to study their birth properties such as their luminosities, spin periods, and kick velocities (imparted by the asymmetric SN), but also assist in understanding their progenitor’s evolution history that led to the SN.

A common characteristic observed in young pulsars is that they occasionally experience sudden spin-up events interrupting their otherwise smooth spin-down process. This phenomenon is called a “glitch” and was first observed in the Vela pulsar (Radhakrishnan & Manchester, 1969). A glitch in the period is sometimes also accompanied by a sudden jump in the spin-down rate. A commonly favoured physical mechanism associated with their cause is the rapid transfer of angular momentum to the crust of the NS when it interacts rapidly with pinned and unpinned vorticity regions in the neutron superfluid region present in its core (Anderson & Itoh, 1975; Ruderman, 1976; Alpar et al., 1981).

As young pulsars evolve and loose their energies, they create a population of so-called normal or “canonical pulsars” with a reduced rotation rate. These account for the majority of the pulsar population. Their spin periods range from 0.1 s to a few

²<http://www.physics.mcgill.ca/~pulsar/magnetar/main.html>

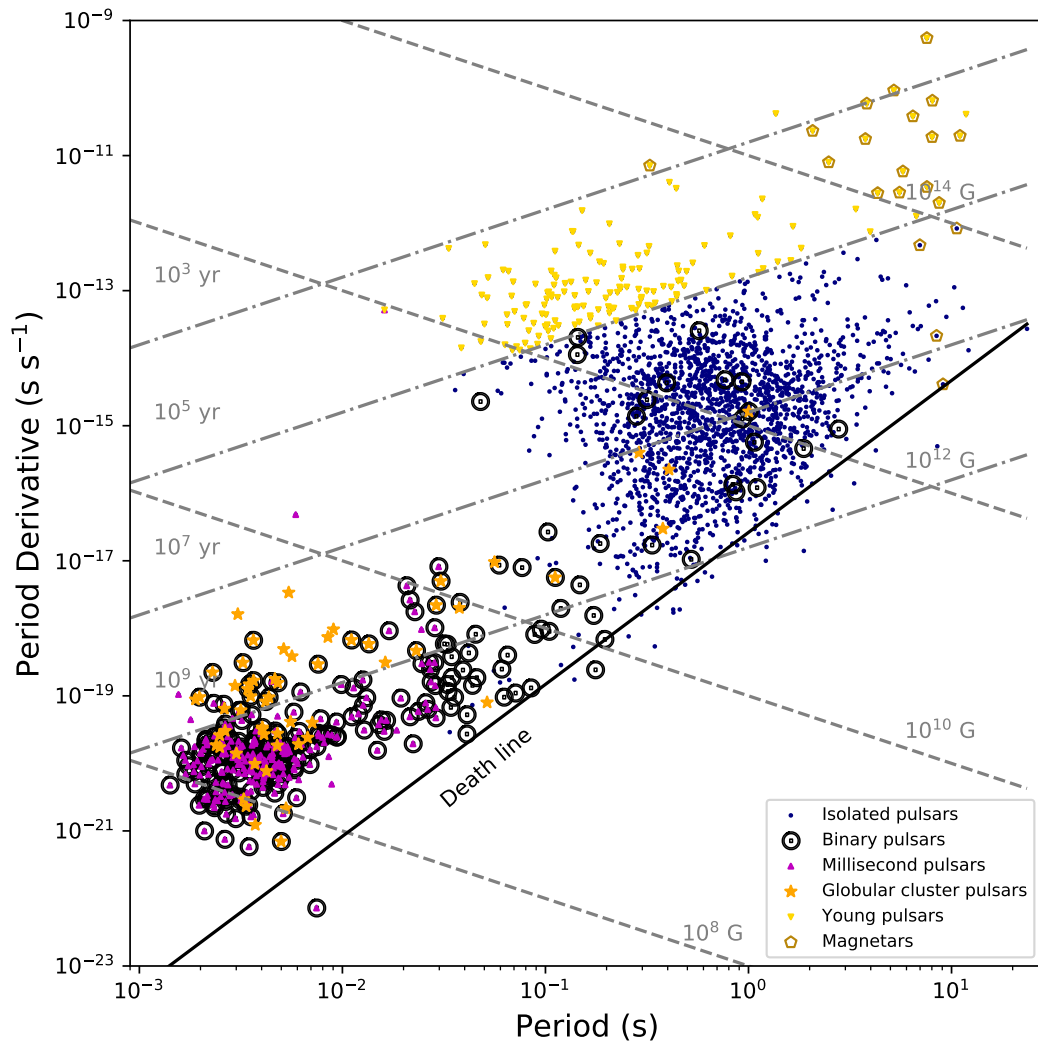


Figure 1.3: A $P - \dot{P}$ diagram of the pulsar population. Different classes of pulsar population are shown in different colors and shapes. The dashed-dot and dashed lines represent characteristic age and surface magnetic fields respectively. Black line shows the *death line* assuming multipolar magnetic field configuration from Zhang et al. 2000.

seconds with surface magnetic fields of around 10^{10} - 10^{13} G. Pulsars in this category evolve over long timescales; their characteristic ages range from 300 Kyr to 1 Gyr. Over time if these pulsars do not interact with any stellar objects, they will eventually slow down such that the induced electric fields will not be sufficient to accelerate particles and emit strong coherent radio emission (Chen & Ruderman, 1993). Thus the NS pulsations eventually become invisible in our observable sky, and they cross the so-called “death-line”. The exact location of this death line is unknown as various theories differ in their prediction and there are some pulsars found even beyond this line.

1.5.2 Binary Pulsars

The black circles in the $P - \dot{P}$ plane represent the binary pulsar population. Binary pulsars are members of binary systems; their companions can be either a planet (the first such system found was PSR B1257+12 by Wolszczan & Frail 1992), a brown-dwarf, a main-sequence star, a white-dwarf, a NS, another pulsar or even a black hole (BH) (yet to be found). A schematic representation showing possible formation scenarios for various types of pulsar binaries formed from different progenitor masses is shown in Figure 1.4 (also see e.g. Stairs 2004). Each of these types of systems have different characteristics that provide insights into both the pulsar and its companion’s nature and into the evolutionary history of the binary and its local environment. This information is crucial in understanding the formation links from X-ray binaries to pulsars. Another important aspect of studying pulsar binaries is that they can be used for measuring NS masses and testing theories of gravity (as discussed in Section 1.8).

1.5.3 Recycled pulsars

A pulsar’s life cycle starts at the top left corner, and it continues to move towards the lower right of the $P - \dot{P}$ plane until its radiation is too weak to be visible or stops abruptly, which is when it crosses the death line (Ruderman & Sutherland, 1975; Zhang et al., 2000; Zhang, 2003). After this stage, if it interacts with another star, it can revive as a recycled pulsar and appear in the bottom left region. Owing to its extremely small spin-down rate, it then continues to exist in this region for a long time. If on the other hand, the binary gets disrupted in the recycling process or the pulsar has a massive companion, its recycling can halt and it can become a mildly recycled pulsar (which can then either become isolated or remain in a binary). Below we discuss different categories of recycled pulsars.

Millisecond pulsars

The second-largest island on the bottom left represent the recycled pulsar population, most of which are “millisecond pulsars” (MSPs). They are characterised by their small spin periods, $P < 20$ ms. The fastest pulsar known PSR J1748-2446ad (commonly known as Terzan 5ad, Hessels et al. 2006) has a spin period of 1.39

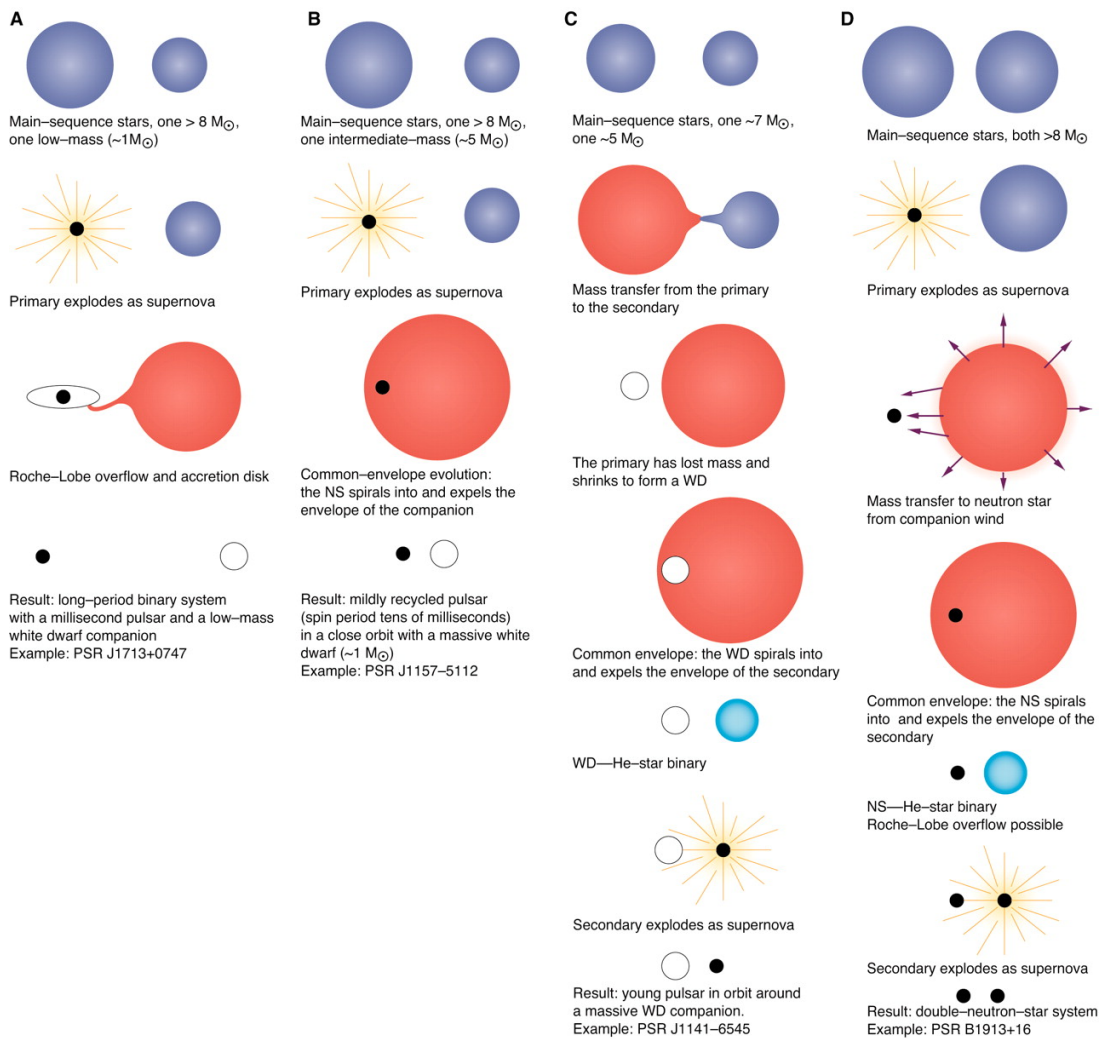


Figure 1.4: Schematic representation of binary pulsar formation scenarios taken from [Stairs \(2004\)](#). Case A shows binaries with low-mass companions, cases B and C show binaries with intermediate-mass companions while case D shows the MSP evolution with high-mass companions.

ms. MSPs are also characterised by their low spin-down rates, $\dot{P} < 10^{-17} \text{ s s}^{-1}$, and relatively weak magnetic fields of around $10^8 - 10^{10}$ G compared to normal pulsars. Even though they have such short spin periods, we cannot characterise them as young pulsars as their low spin period derivatives lead to large characteristic ages (see equation 1.7). Thus, it is evident that the formation process of MSPs is distinct from the normal pulsar population and requires a mechanism of spinning up the pulsars to millisecond periods.

In 1982, after the discovery of the first MSP, PSR B1937+21 (Backer et al., 1982), Alpar et al. (1982) proposed the formation mechanism of MSPs from binary systems. The evolution process begins with two main sequence (MS) stars in a binary. The massive (primary) star initially undergoes a SN (due to a shorter life cycle) and forms a pulsar. If the binary survives the supernova, the secondary MS star will evolve and become a red giant. During this phase, it will fill its Roche lobe – a teardrop-shaped region bounded by a critical gravitational equipotential of the star. The matter will start to leak through the inner Lagrangian point (L1) of the system as the outer layers of the plasma will no longer be gravitationally bound to the star. The gravitational pull of the companion pulsar will thus start accreting matter towards itself and gain angular momentum from its companion star (Bhattacharya & van den Heuvel, 1991). This process, called recycling, can continue for $10^7 - 10^9$ years if the progenitor MS companion mass is low enough ($\sim 0.1 - 1 M_{\odot}$). Such binaries are commonly known as a Low Mass X-ray Binaries (LMXB). The continued long-term exchange of angular momentum results in a highly spun-up “recycled” pulsar rotating every few milliseconds – an MSP. The accretion process also results in the quenching of the pulsar magnetosphere and reduces the magnetic field. MSPs are extremely stable rotators with their timing precision reaching that of atomic clocks over a timescale of a few years (Davis et al., 1985). This clock-like stability makes them useful probes for various applications that we will discuss in Section 1.8. As can be seen from Figure 1.3, about 80% of the MSP population exist as binary pulsars, this confirms the evolution scenario of MSPs via accreting X-ray binaries. The majority of MSPs have helium WD companions resulting from low-mass progenitor stars, while some also have massive WDs (CO or ONeMg) and semi-degenerate companions (*spider pulsars*), as discussed below.

Mildly recycled pulsars

Another class of pulsars with binary evolutionary history are “mildly recycled pulsars”. On the $P - \dot{P}$ diagram, they lie between MSPs and normal pulsars having a slightly higher P and \dot{P} compared to MSPs. The formation of a fully recycled MSP with small rotational periods is possible because the low-mass donor star of the LMXB system evolves slowly resulting in a long-lived accretion process. On the contrary, if the donor star’s mass is higher such as in an intermediate-mass X-ray binary (IMXB) system where $M_{\text{donor}} \sim 1 - 10 M_{\odot}$ or in a high-mass X-ray binary (HMXB) system with $M_{\text{donor}} \geq 10 M_{\odot}$, the accretion phase is unstable and

is continued only for short-timescales (Tauris & van den Heuvel, 2006). Thus, the NS does not have much time to spin up, and its period remains in the range ~ 10 -200 ms. The short-lived accretion phase is still thought to reduce the magnetic field ($10^9 - 10^{11}$ G) of the NS but only to a lesser extent than a fully recycled MSP. Another effect due to the short timescale of this phase is that the binary has a relatively higher eccentricity (upto 10^{-2}) compared to the fully recycled MSPs which undergo a more complete circularization. This is confirmed from the observations of mildly recycled pulsars with massive companions such as either a Carbon-Oxygen (CO) WD or an Oxygen-Neon-Magnesium (ONeMg) WD (Tauris et al., 2000, 2011, 2012). Chapter 5 discusses the timing analysis of one such mildly recycled pulsar system with a heavy WD companion, PSR J1952+2630. The companion of mildly recycled pulsars can also be another NS: it can form if the donor star is $> 10 M_{\odot}$ and the binary survive a SN (Tauris & van den Heuvel, 2006). Such binaries have higher eccentricities (e) compared to mildly recycled PSR-WD binaries, for instance, the Hulse-Taylor pulsar (PSR B1913+16) has $e=0.62$ (Hulse & Taylor, 1975), and the double pulsar (PSR J0737-3039A/B) has $e=0.09$ (Burgay et al., 2003).

Eclipsing binaries

There exist a distinct sub-class of MSPs commonly known as “spider pulsars” (see Freire 2005 and Roberts 2013 for reviews). These systems are usually in tight binaries with orbital periods < 24 h and have very low-mass companions. The pulsar in these systems is in the process of ablating mass from its companion, so the pulses appear eclipsed as the pulsar moves across its orbit through dense plasma regions. These binaries are commonly categorised into two classes based on the companion’s mass: “Black widow pulsars” (BWPs) with $M_c \lesssim 0.05 M_{\odot}$ and “Redback pulsars” (RBPs) with $M_c \sim 0.1 - 0.5 M_{\odot}$. Companion stars of BWPs are known to ablate through the strong pulsar winds, while companions of RBPs might also occasionally undergo mass loss via Roche Lobe Overflow, with resulting accretion of the NS triggering a temporary LMXB; those systems are known as “transitional MSPs” (Archibald et al., 2009; Papitto et al., 2013). The companion star of RBPs is non-degenerate, thus they are known to show eclipses for a much longer duration (up to 60 % of the orbit) and with stronger orbital variability compared to BWPs.

1.6 Pulsars in Globular Clusters

Globular clusters (GCs) are a gravitationally bound group of $10^4 - 10^6$ stars concentrated in a region of about a few pc. They orbit their host galaxy’s halo and bulge, and are condensed and nearly spherical structures. The densities in their cores can reach up to $10^2 - 10^6$ stars per cubic parsec, which is several orders of magnitude more than that of the galactic field.

They are amongst the oldest objects in the universe with ages ~ 10 -12 Gyr (VandenBerg et al., 2013). Their old age is inferred from their Main Sequence Turn Off

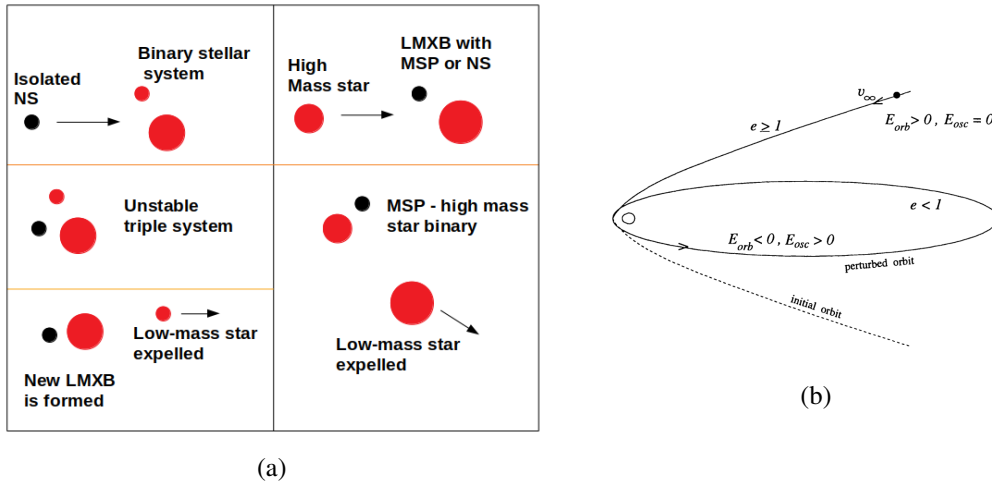


Figure 1.5: Left: Schematic representation of two types of exchange encounters. Right: Schematic representation of a tidal capture event (Figure taken from [Mardling \(1996\)](#)).

(MSTO) point in the Hertzsprung-Russell (H-R) diagram (where stars formed around the same time burn all their fuel and start to move away from the main-sequence branch). Observations have found 157 GCs till now (as per Harris Catalogue³) in the Milky Way.

The high central densities of GCs promote increased dynamical interactions among stars. Interestingly, GCs are the one of the few places in the universe where close stellar encounters occur at a timescale shorter than the life cycle of the stars. Thus, stellar systems are subject to exchange interactions, tidal captures, and collisions. As a result, a large population of “exotic” objects are created, including MSP binaries with unconventional properties, blue straggler stars, and cataclysmic variables.

When old NSs interact with stellar binary systems, they form an unstable triple system from which the less massive companion is kicked out (due to a tendency for energy equipartition ([Hut, 1983](#))), the surviving binary then goes through an LMXB phase and the NS recycles to form an MSP (see Figure 1.5a). A large number of such interactions lead to about 3 orders of magnitude more LMXBs per unit stellar mass in GCs compared to the galactic field ([Clark, 1975](#)). In total, 258 pulsars in 36 GCs are known TO DATE⁴. Figure 1.6 shows the comparison of the pulsar population⁵ in GCs and in the Galactic field. We can see that there is a clear abundance of binary pulsar population and recycled pulsars (both MSPs and mildly recycled pulsars) in GCs compared to Galactic field, implying an abundance in NS binaries. Below we discuss various types of stellar interactions, in addition to the LMXB scenario discussed above, that could result in the population of NS binaries in GCs:

³<http://physwww.physics.mcmaster.ca/~harris/mwgc.dat>

⁴<https://www3.mpifr-bonn.mpg.de/staff/pfreire/GCpsr.html>

⁵Numbers taken from ATNF catalogue v1.67

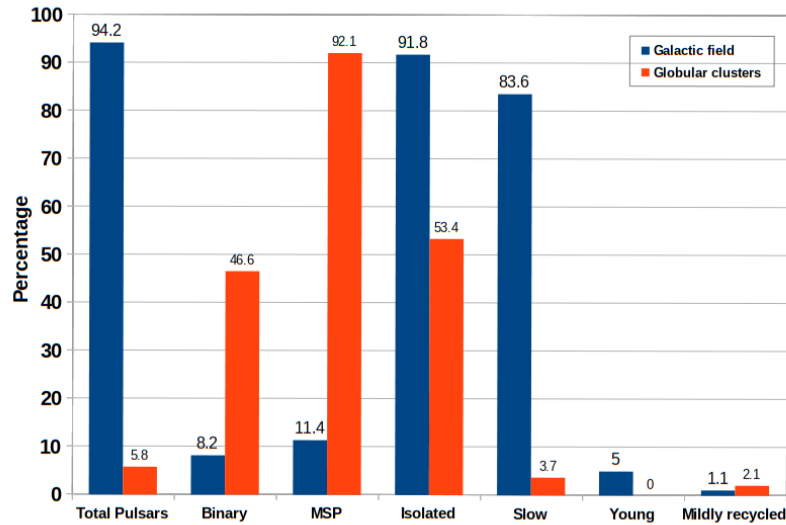


Figure 1.6: Histogram of fraction of different kinds of pulsar population in GCs and galactic field respectively. The difference in the abundances of MSP and binary pulsar population in GCs can be clearly seen.

- *Exchange interaction*: These occur when a single star interacts with a binary system consisting of NS and a low-mass companion star (commonly a He WD). In case the new perturbing star is more massive than the existing companion, former will throw out the lighter companion to form a new binary containing a NS and a high mass star (see Figure 1.5a). Since a binary is involved in this type of interaction, there is a large cross-section for an encounter. Thus this is the most dominant type of interaction found in GCs.
- *Tidal capture*: This occurs when an isolated neutron star flying by close to a main-sequence star gets gravitationally bound by the star to form a binary, (Clark, 1975) (see Figure 1.5b). Ivanova et al. (2008) suggest that only 2% of NSs create binaries this way.
- *Direct collision*: This occurs when there is a head-on collision of a neutron star with a binary. Only about 5% of NSs are expected to form binary through this process (Ivanova et al., 2008).

These processes become theoretically more common in GCs with a stellar encounter rate Γ (Verbunt & Hut, 1987). Confirming this, many studies have shown that the number of LMXBs and their products, MSPs, generally increase with the Γ of their host GCs.

Figure 1.7 shows a histogram of pulsar population found in GCs. As expected from the considerations above, this is dominated by MSPs, however, the presence of

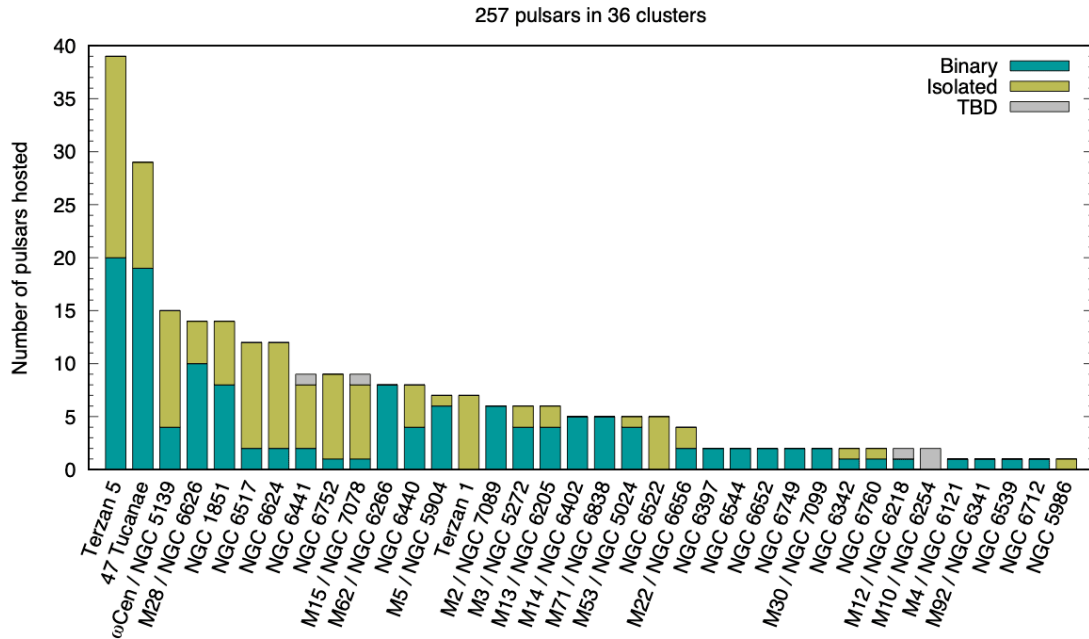


Figure 1.7: Histogram of pulsar population in Globular clusters. Two pulsars (M3C and NGC 6749B) are likely real but need confirmation. Credit: Alessandro Ridolfi

slow and relatively young pulsars is intriguing as there exist no massive stars in GCs that can undergo SN.

These pulsars appear almost exclusively in GCs with dense cores. These have a high stellar interaction rate per binary, γ (Verbunt & Freire, 2014) resulting in increased number of binary encounters any particular system can expect over its lifetime. This leads to the following:

- widespread disruption of binaries, resulting in a large predominance of isolated MSPs in such clusters (e.g. out of 9 MSPs in M15, only one is a confirmed binary)
- disruption of LMXBs, halting the accretion phase, and creating either partially recycled pulsars, slow pulsars, or young MSPs such as M28A and NGC6624A with ages of only 25Myr,
- secondary exchange encounters, where previously recycled pulsars (either fully recycled in a MSP - WD system, or partially recycled in a LMXB) exchange their light donor with more massive degenerate companions, producing systems where the recycled pulsar is in eccentric orbit with a massive companion (such as NGC 1851A or M15C),
- more number of compact orbit binaries due to the release of binary potential energy with every encounter,

- many more perturbations in binaries due to passing by stellar object, creating many of eccentric binaries even if no secondary exchange encounters occur.

This distinction among pulsar population in GCs is corroborated from the observations of core-collapse clusters with high values of γ , such as NGC 6624, NGC 6517, M15, Terzan 1, NGC 6342, or NGC 6752, as seen in Figure 1.7. The type of MSP population seen in GCs with low-density cores (such as 47 Tucanae, M13, or M5) is very similar to the MSP population seen in the galactic field (e.g. [Ridolfi et al. 2016](#)). Once formed, X-ray binaries in such clusters have a small probability of having a second stellar encounter in their lifetime, thus they evolve conventionally like other pulsars in the galactic field with periods in the range of 2-8 ms.

1.7 Interstellar Effects

Before reaching the telescope on Earth, a pulsar signal passes through the cold and ionized interstellar medium (ISM) on its way. The inhomogeneous and turbulent gas in the ISM affects the radio pulsar signal in four different ways: dispersion, scattering, scintillation, and Faraday rotation.

1.7.1 Dispersion

If ISM were a perfect vacuum, a broadband (multi-frequency) radio pulsar signal would reach the observer on Earth with all frequencies arriving simultaneously. However, since the ISM consist of cold ionised gas, the phase velocity of the signal is instead reduced based on a frequency-dependent factor known as refractive index, μ .

[Hewish et al. \(1968\)](#) first noted this effect in the radio pulsations from the first pulsar, B1919+21, where lower frequency signals arrived later compared to higher frequency ones. Such delay in the arrival time of the pulsar signal is known as a dispersive delay and is quantified by the *Dispersion Measure* (DM) of the pulsar. It is proportional to the integrated column density of electrons passed by the pulsar signal in the ISM, represented as (see [Lorimer & Kramer 2012](#) for derivation):

$$DM = \int_0^d n_e dl \text{pc cm}^{-3} \quad (1.9)$$

where n_e is the electron number density for ISM and d is the distance to the pulsar. Typically, a constant value of $n_e \simeq 0.03 \text{ cm}^{-3}$ can be assumed. The delay between two different radio frequencies of a signal is represented as follows:

$$\Delta t \simeq 4.15 \text{ ms} \times (v_1^{-2} - v_2^{-2}) \times DM \quad (1.10)$$

where v_1 and v_2 are frequencies in GHz. We can measure the DM of the pulsar by measuring Δt in the radio signal. Additionally, by assuming an electron density model of the Galaxy (two most commonly used models derived from independent distance

measurements are NE2001, Cordes & Lazio 2002 and YMW2016, Yao et al. 2017), we can derive the distance to the pulsar from Equation 1.9. Conversely, with the knowledge of DM and the distance to the pulsar (such as via parallax measurements or through its association to a globular cluster), we can also estimate the electron density content along the line of sight. Such methods are useful to refine the Galactic models mentioned above.

1.7.2 Faraday Rotation

Faraday rotation is another effect on the pulsar signal due to the magnetised ionised plasma of ISM. As the electromagnetic pulsar signal travels through the ISM, the free electrons present in the medium are forced to move circularly along the direction of the polarised electric field of the signal, and perpendicular to the direction of the magnetic field (due to Lorentz force). This lead to a difference in the index of refraction experienced by the two circular polarizations (left-hand and right-hand) of the signal, which in turn changes their phase velocities. Since a linearly polarised wave can be thought of as a superposition of the two circularly polarised waves, the change of speed results in a change in the effective angle of the linear polarisation. Such rotation in the plane of linear polarisation is known as *Faraday rotation*. The phase lag of an EM wave of frequency, ν , propagating a distance, d in the ionized ISM is given by:

$$\Delta\psi(\nu) = -k(\nu)d, \quad (1.11)$$

where k is the wavenumber i.e. $2\pi n(\nu)/c$ and $n(\nu)$ is the refractive index. The new local refractive index in the presence of the circular polarisation of the signal is then represented as (Lorimer & Kramer, 2012):

$$n(\nu) = \sqrt{1 - \frac{\nu_p^2}{\nu^2} \mp \frac{\nu_p^2 \nu_B}{\nu^3}}, \quad (1.12)$$

where ν_p is the plasma frequency and ν_B is the called the cyclotron frequency which is dependent on the line of sight magnetic field, B_{\parallel} such that:

$$\nu_B = \frac{eB_{\parallel}}{2\pi m_e c}. \quad (1.13)$$

Assuming ν is significantly larger than both ν_p and ν_B , we can derive the differential phase rotation between the two circular polarisations as follows:

$$\Delta\psi_F(\nu) = \frac{e^3}{\pi m_e^2 c^2 \nu^2} \int_0^d n_e B_{\parallel} dl. \quad (1.14)$$

The change in linear polarisation position angle, ψ will be half of the change in circular polarisation (Lorimer & Kramer, 2012), thus:

$$\Delta\psi = \frac{1}{2} \frac{e^3 \lambda^2}{\pi m_e^2 c^4} \int_0^d n_e B_{\parallel} dl = \lambda^2 \times \text{RM}, \quad (1.15)$$

where λ is the wavelength and RM is a quantity known as *rotation measure* and is given by:

$$\text{RM} = \frac{e^3}{2\pi m_e^2 c^4} \int_0^d n_e B_{\parallel} dl. \quad (1.16)$$

By measuring the RM and DM for a pulsar, we can combine Equations 1.9 and 1.16 to determine the average magnetic field along the line of sight as follows:

$$\langle B_{\parallel} \rangle = 1.23 \mu\text{G} \left(\frac{\text{RM}}{\text{rad m}^{-2}} \right) \left(\frac{\text{DM}}{\text{pc cm}^{-3}} \right)^{-1}. \quad (1.17)$$

Studies based on estimates of RMs and DMs of pulsars help us determine the magnetic field strengths of large-scale structures (e.g. Han et al. 2006, 2018) in both the galactic disk as well as galactic halo (e.g. (Abbate et al., 2020)).

1.7.3 Scattering

The turbulent/inhomogeneous nature of the ISM impacts the pulsar signal with another noticeable effect, known as *scattering*. The irregularities in the electron density, for instance due to the supernova shock wavefronts or HII regions, can continuously change the local refractive index of the ISM that is experienced by the pulsar signal while it travels towards Earth. Thus, parts of the signal deviate and propagate through multiple different paths (see Figure 1.8a). Hence the signal that reaches Earth does not arrive simultaneously and some part of it comes later, creating a “tail” like feature in the pulse profile.

Assuming a simple thin-screen model given by Scheuer (1968), scattering timescale due to the turbulent plasma located mid-way in pulsar’s path varies as a function of frequency and is given by:

$$\tau_s = d^2 \nu^{-4}, \quad (1.18)$$

where d is the distance to the pulsar and ν is the frequency of the signal. A signal at a lower frequency is more heavily scattered compared to the one at a higher frequency.

Considering the in-homogeneities follow a *Kolmogorov* like spectrum, the intensity of the pulsar signal observed as a function of time is represented as an exponential of the delay (Lorimer & Kramer, 2012):

$$I(t) \propto e^{-\Delta t / \tau_s}, \quad (1.19)$$

where Δt is the geometric time delay due to a longer optical path. Due to this effect, an originally narrow pulsar signal is visible as a one-sided exponential function to the

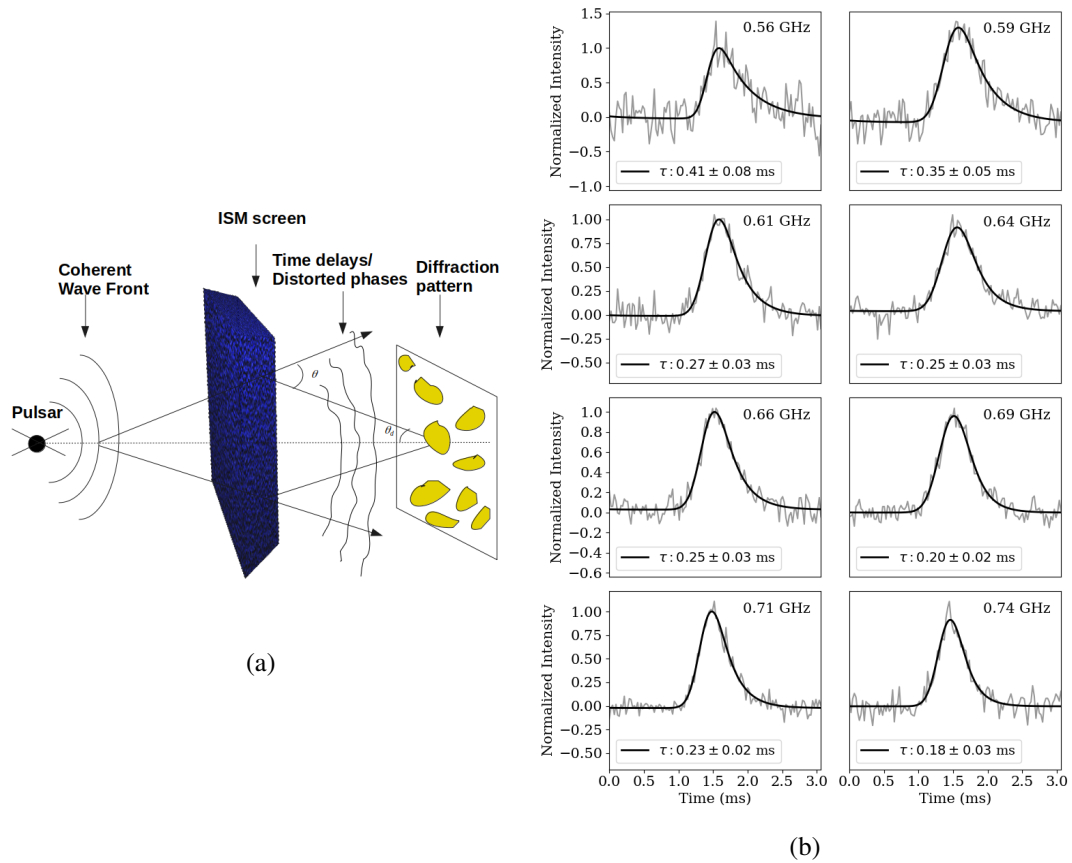


Figure 1.8: Left: Schematic representation of the thin-screen model showing multi-path propagation of light due to turbulent ISM. The initially coherent pulsar signal is distorted due to ISM irregularities. Right: Measured scattering in PSR J1807-2459A profile observed in the GMRT dataset at different frequencies. The scattering timescale, τ increases with decreasing frequency (see legend). Black line is the smooth fitted profile and gray line is the observed profile. Figure credit: Lucy Oswald

observer. An example of this effect for different frequencies is shown in Figure 1.8b for PSR J1807-2459A (as seen in the GMRT data).

1.7.4 Scintillation

The inhomogeneities in the ISM also cause fluctuations in the observed intensity of the pulsar signal, such effect is called *scintillation*. An example of one of the most commonly seen scintillation is the twinkling of stars due to Earth's atmosphere. Such variation in pulsar signal is both spatial and temporal, due to the relative transverse motion of the pulsar or the medium. These intensity fluctuations occur due to constructive and destructive interference of the signal that travels through slightly different paths across the ISM. The condition for interference is that the phase of waves must differ by less than one radian (Lorimer & Kramer, 2012):

$$2\pi\Delta\nu\tau_s < 1, \quad (1.20)$$

where $\Delta\nu$ is the observed bandwidth of the signal. Thus, $\Delta\nu \propto 1/\tau_s \propto v^4$ would give us a limiting bandwidth, also known as *scintillation bandwidth*, below which the scintillation pattern will be visible. The dynamic spectrum of this pattern represent the variation of the pulse intensity as a function of time and frequency. The size of regions in this spectra with enhanced intensities (commonly known as *scintles*) can give us the scintillation time and frequency scales for a pulsar.

1.8 Science with Pulsars

1.8.1 Direct detection of GWs

The extremely stable pulses from MSPs allow us to do high precision timing of pulsars. Thus by using an ensemble of MSPs collectively as a timing array, it is possible to directly detect nano-Hertz GW signals (~ 1 -100 nHz) (Hellings & Downs, 1983; Foster & Backer, 1990). One of the main contributors to such low-frequency GW background are mergers of supermassive black hole binaries (SMBH) in the early universe (Chen et al., 2019; Chen et al., 2020). To exploit a large sample of MSPs through different telescopes, several Pulsar Timing Array (PTA) projects have been initiated, such as Parkes Pulsar Timing Array (PPTA) in Australia (Manchester et al., 2013), European Pulsar Timing Array (EPTA) (van Haasteren et al., 2011), and North American Nanohertz Observatory for Gravitational Waves (NANOGrav) (McLaughlin, 2013). In addition to these, above collaborations collectively form International Pulsar Timing Array (IPTA) (Hobbs et al., 2010) that aim to detect GWs using a global interferometer.

1.8.2 Tests of gravity theories

Ever since the theory of general relativity (GR) has been proposed as a theory of gravity, it has been crucial to verify its validity over varying gravitational field strengths. Different theories of gravity present different observational predictions in various regimes of gravity. Albert Einstein first proposed three classical tests of gravity: a) precession of perihelion - GR predicts a perihelion shift of 42.98" per century for Mercury that aligns well with the observations, b) deflection of light by gravity - first tested during the solar eclipse in 1919 by comparing the apparent position of stars against the sun, and c) gravitational redshift of light - GR predicts that light is red-shifted when it moves away from the gravitational field, this was first tested by Daniel M. Popper in 1954 using the light emitted from a white-dwarf. Later, gravitational time dilation (commonly known as Shapiro delay) was also added to this list of classical tests. Precision experiments through lunar laser ranging (Müller et al., 2019) have also been used to test GR. A detailed review discussing various tests that GR has passed is presented in Wex (2014) (also see references within). All the above effects have been tested in the quasi-stationary weak-field regime of our solar system Turyshev (2008); Asmodelle (2017).

However, a quasi-stationary strong field that creates a significant curvature in the spacetime is only present around strongly self-gravitating bodies, thus only compact objects such as NSs and BHs can be used to test GR in this regime. Through high precision radio pulsar timing of stable pulsars, especially in binary systems, we can detect several of the relativistic effects on their orbits and the propagation of radiation in their vicinity as a consequence of the strong-field gravity. In pulsar timing, these relativistic effects are quantified with the so-called “post-Keplerian (PK) parameters” in a theory independent way (see Section 2.5.2). These parameters include the rate of change of longitude of periastron ($\dot{\omega}$), the orbital decay (\dot{P}_b), the Shapiro delay parameters: range (r) and shape (s), and the Einstein delay (γ). Each of these PK parameters depend on the known Keplerian parameters with the pulsar and companion mass as the two unknown free parameters, assuming a theory of gravity. Thus the measurement of a PK parameter yields a line on a plot with component masses, commonly known as *mass-mass* diagram (see Figure 1.9). Measurement of two PK parameters in a binary can constrain both the pulsar and the companion’s mass, while measuring three or more PK parameters will over-determine the system of equations, thus providing one or more tests of the theory of gravity that is used to draw the lines in the diagram.

Incidentally, the first test of gravity was possible with the first pulsar binary discovered, PSR B1913+16, commonly known as Hulse-Taylor pulsar. It is a double NS system (Hulse & Taylor, 1975) in a short orbit of 7.75 hr. The measured advance of periastron for this system is $4.22^\circ \text{ yr}^{-1}$. This relativistic effect is so strong that one day shift in precession in this system is comparable to a century’s precession shift in Mercury. In general relativity, this gives us the total mass of the system. A second effect, the Einstein delay, was also measured, yielding a determination of both component masses. In this system, a third PK parameter was also measured, the orbital

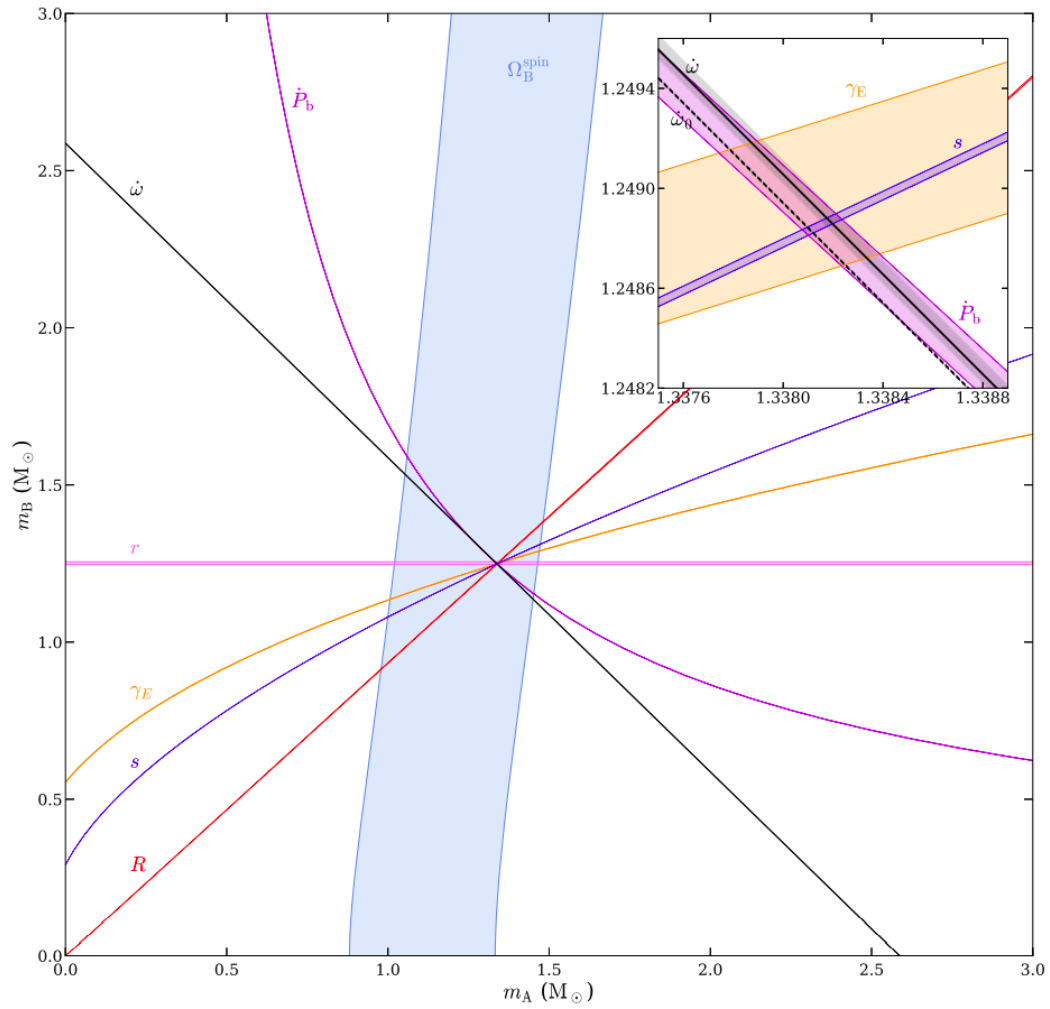


Figure 1.9: Mass-mass diagram for the double pulsar showing measurement of six PK parameters and the mass ratio, R . Figure taken from [Kramer et al. \(2021\)](#)

decay; which aligns remarkably well with the GR prediction of the quadrupolar GW emission for the masses determined from $\dot{\omega}$ and γ , this provided the first evidence for the existence of GWs (Taylor & Weisberg, 1982, 1989). Owing to many possibilities this system provide for understanding gravitational physics, its discoverers Russell Hulse and Joseph Taylor were awarded the 1993 Nobel prize in Physics .

A binary that has played a crucial role in providing multiple tests of GR is the double pulsar system, PSR J0737-3039 (Burgay et al., 2003) - the only known system with two pulsars orbiting each other (Lyne et al., 2004). Recent work by Kramer et al. (2021) presented measurement of seven PK parameters in the long-term timing of the pulsars in this system, yielding seven independent tests that GR passes (as shown in Figure 1.9). In addition to the PK parameters, they also measured the mass ratio of two pulsars ($R = m_A/m_B$) and several other next-to-leading order effects in this system. With a highly precise measurement of the orbital decay due to GWs, they showed a remarkable agreement with GR at a relative precision of 1.3×10^{-4} (with 95% confidence), this system presents the most precise test of GR through pulsar timing as of yet.

A highly precise test of the strong equivalence principle has also been possible with the triple system, PSR J0337+1715 (composed of a NS-WD binary in orbit with another WD) (Ransom et al., 2014; Tauris & van den Heuvel, 2014). In addition to testing GR, the triple system and binaries with significant differences in their gravitational self-energy can help search for the dipolar GW emission (predicted by alternative theories of gravity) and the violation for universality of free fall. Some of the best constraints on scalar-tensor theories (STTs) have been put by PSR J1738+0333 (Freire et al., 2012), PSR J0348+0432 (Antoniadis et al., 2013), and PSR J0337+1715 (Archibald et al., 2018; Voisin et al., 2020).

1.8.3 Mass measurements and NS EOS

The supra-nuclear densities prevalent at the center of NS present a unique regime to probe the strong nuclear forces. One can add some constraints to this crucial problem of understanding the nature of such matter (exclusively found in NSs) through pulsar astronomy. As discussed in Section 1.3, the largest NS mass measured with pulsar timing can rule out many EOSs (as shown in Figure 1.1) (Antoniadis et al., 2013; Fonseca et al., 2021). A crucial requirement to measure the NS mass is the measurement of at least two PK parameters (as discussed in Section 1.8.2).

Through pulsar timing, we have been able to measure precise masses of 49 pulsars⁶ ranging from 1.17 to 2.08 M_{\odot} (see Figure 1.10). The observations from optical spectroscopy of white-dwarf counterparts have also proven valuable for this purpose (Antoniadis et al., 2012, 2013). Recently, with the help of X-ray timing and spectroscopy of the NS surface using Neutron Star Interior Composition Explorer (NICER; Gendreau & Arzoumanian 2017), it has been possible to constrain the radius of the most

⁶https://www3.mpifr-bonn.mpg.de/staff/pfreire/NS_masses.html

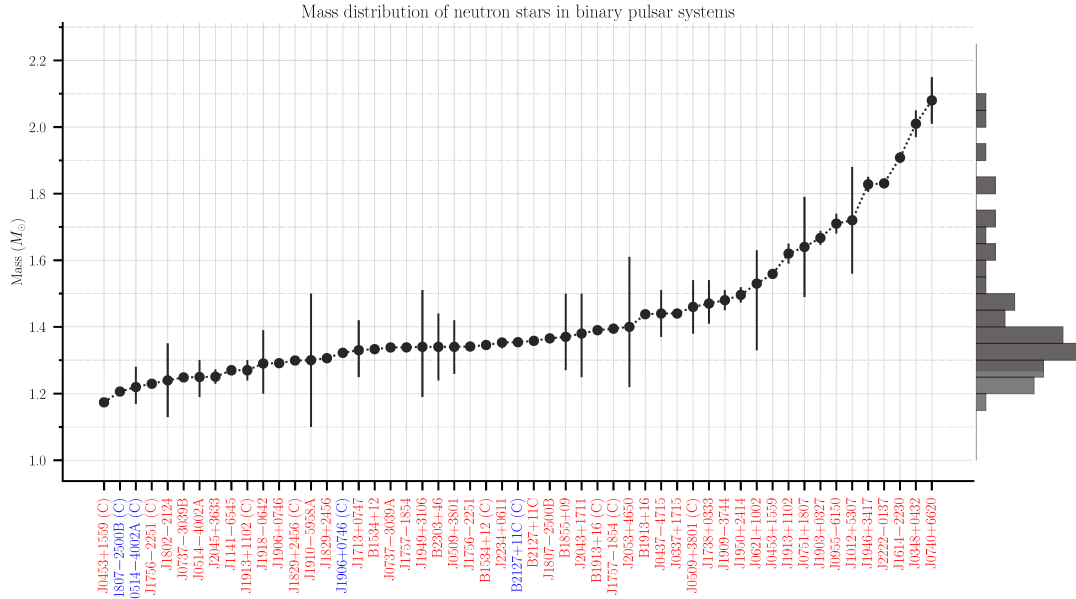


Figure 1.10: NS mass measurements from radio pulsar timing. The letter C in parentheses to pulsar name indicate a NS companion to a pulsar that is itself not a pulsar. The blue names are the companion sources which could either be a NS or a massive WD. Right side of the plot shows the histogram of the masses. Credit: Vivek V. Krishnan.

massive NS known to date, PSR J0740+6620 ($\sim 2.07M_{\odot}$) to $12.39^{+1.30}_{-0.98}$ km (Riley et al., 2021). Furthermore, radio pulsar timing can also allow us to directly measure MOI from relativistic effects, its measurement can play a crucial role to identify the EOS (e.g. see Hu et al. 2020, Kramer et al. 2021 for its measurement in the Double Pulsar system). These recent advancements in the observational studies of NSs have brought us closer than ever to narrowing down their actual EOS.

1.8.4 Science with GC pulsars

The scientific advantage of observing pulsars in GCs is multi-faceted. The long-continued dynamical evolution in GCs lead to a phenomenon called *mass-segregation*. In this process, because of the equipartition of energy (1st law of Thermodynamics), the total kinetic energy is distributed among all the stars, the lighter objects thus attain high velocities and fly towards the outskirts, while heavier objects attain low velocities and accumulate towards the core of the clusters. Thus, most of the pulsars in GCs are located in a small area within the core radii of these clusters, covering only around a few arcminutes of the sky. Since the primary beam of most telescopes can easily cover such areas, multiple pulsars can be observed and timed within a single telescope pointing (Freire, 2013). Thus longer observing times can be allocated for GC observations, which improve our sensitivity to facilitate new pulsar discoveries and also enable high precision radio timing of pulsars in GC.

Another important advantage comes from the fact that GCs harbour a large population of LMXBs and MSP binaries (Clark, 1975). Studying these systems can provide insights into the evolutionary link from LMXBs to MSPs formation. Additionally, the population of accreting binaries and transitional MSPs (systems that alternate between accretion powered X-ray emission state and rotation powered radio emission state, Papitto et al. 2013) in GCs can help understand the accretion physics of dense matter in NSs and even BHs.

In GCs, there exist a large population of MSPs with unconventional properties (commonly referred to as “exotic” systems), for instance, binaries with high eccentricities, or MSPs with high mass companions (Freire et al., 2004a; Lynch et al., 2012; DeCesar et al., 2015). The measurement of PK parameters such as the relativistic advance of periastron in the former and Shapiro delay in the latter example is easier in such exotic binaries (discussed in detail in Chapter 2). As discussed in Section 1.8.3, these measurements allow an estimate of the component masses, thus helping us constrain the EOS of NS matter.

Pulsars in GCs also help understand the cluster dynamics itself. The gravitational potential of the cluster exerts an additional acceleration on pulsars that can be observed in the spin period and orbital period derivatives of these systems. By estimating these contributions on multiple pulsars located at various distances from the cluster core, one can predict the cluster potential model (Phinney, 1993; Freire et al., 2017a; Prager et al., 2017). Additionally, by estimating the DM and position of the pulsars, we can get an insight into the distribution of the ionised intra-cluster medium (Freire et al., 2001). Furthermore, a comprehensive study of RMs of pulsars in a cluster can provide a better understanding of the cluster’s magnetic field distribution (Abbate et al., 2018).

1.9 Thesis Outline

This thesis focuses on the search and timing analysis of MSP binaries. The first half of this thesis presents two pulsar search surveys to discover exotic MSP binaries. These surveys are targeted on GCs which are known to host some of the most exotic pulsar binaries (owing to their large stellar densities). The second half of this thesis explores the timing analysis and the scientific potential of two MSP binaries in the galactic field: PSR J1952+2630 and PSR J1012–4235. Here follows a brief outline of the thesis:

- In Chapter 2, I first provide an overview of the data acquisition process with radio telescopes. I then present the methods used to search for pulsars in time-domain searches with emphasis on the techniques used in the searches performed as part of this thesis. Next, I discuss an overview of the procedure used to create radio images of GCs. These images were made as part of the pulsar search survey carried out with GMRT. In the end, I cover the basic techniques used in the timing analysis of both newly discovered and previously known pulsars.

- In Chapter 3, I describe the pulsar search survey conducted with the upgraded GMRT. I discuss the detection and timing analysis of the new discovery, PSR J1835-3259B. Then, I present the characteristics of the pulsars re-detected in this survey. I also discuss the detection and properties of four newly identified steep spectrum radio sources found in the images of the observed GCs.
- In Chapter 4, I present the first GC pulsar search survey carried out with the MeerKAT radio telescope. I discuss the detection and timing analysis of eight new MSPs discovered as part of this survey.
- In Chapter 5, I present the results from the timing analysis of PSR J1952+2630 carried out with the Arecibo radio telescope. I discuss the detection of three relativistic effects in this system and provide the constraints on the pulsar and its companion's mass. I also discuss the future potential of this system as a gravitational laboratory.
- In Chapter 6, I discuss the results from the timing analysis of PSR J1012–4235 carried out with the MeerKAT radio telescope. I present the detection of Shapiro delay in this system and the measurements of the component masses and inclination. I also discuss the constraint this system can put in future on the variation of gravitational constant.

How to search, time and image a Pulsar?

Contents

2.1	Data acquisition with radio telescopes	32
2.1.1	Reflectors	32
2.1.2	Front-end	33
2.1.3	Back-end	34
2.2	Time domain searches	36
2.2.1	Interference mitigation	37
2.2.2	De-dispersion	37
2.2.3	Periodicity search	38
2.2.4	Acceleration and jerk searches	39
2.2.5	Candidate selection and confirmation	40
2.3	Image domain searches in globular clusters	41
2.3.1	Interferometric data acquisition	42
2.3.2	Flagging and calibration	43
2.3.3	Imaging	45
2.4	Orbital parameter estimation	48
2.5	Timing a pulsar	49
2.5.1	TOA creation	49
2.5.2	Timing Model	50
2.5.3	Residual fit and parameter estimation	53

In this chapter, I present the methods and techniques used for most of the data analysis in this thesis work. These include the steps involved in the time-domain search pipeline used for the pulsar searches conducted with uGMRT and MeerKAT as part of this thesis (in section 2.2). In section 2.3, I discuss another approach to search for pulsars in the synthesis radio images of GCs and outline the process used to create such images as part of this thesis. Next, I discuss the procedures used for estimating the orbital parameters of a newly discovered pulsar, and the methods used to carry out the timing analysis of both the newly discovered pulsars (discussed in Chapter 3 and 4) and the well-timed pulsars (PSR J1952+2630 and PSR J1012-4235 discussed in Chapter 5 and 6).

2.1 Data acquisition with radio telescopes

The procedure of acquiring pulsar data from radio telescopes involves three main instrumental set-ups: a) the reflecting surface that can either be a single dish or an array of antennas (in the case of interferometers), b) the front-end that collects and amplifies the radio signal, and c) the back-end that converts the amplified signal into a format that can be readily processed. In the following sections we discuss each of these components in detail.

2.1.1 Reflectors

Reflectors are the reflecting surface (or antenna) of a radio telescope that collect the electromagnetic waves (in radio frequency) and reflect them towards the primary or secondary focus of the antenna. These can have different geometrical shapes such as parabolic, spherical, or cylindrical, and varying focal plane configurations such as axial, offset, Cassegrain, or Gregorian. At the focus point, a number of interchangeable receivers that are sensitive to different wavelengths are placed. Since pulsars inherently emit weak radio waves with flux densities ranging from a few μJy to a few mJy , a large collecting area is needed to improve their detection sensitivity. This is achieved by either using single-dish telescopes with large diameters, such as 64-m Parkes radio telescope in Australia (Edwards, 2012; Hobbs et al., 2020), the 100-m Green Bank telescope (GBT) in the US (Lockman, 1998; Minter et al., 2021), the 100-m Effelsberg radio telescope in Germany (Wielebinski, 2004) (Effelsberg and the GBT are the largest fully steerable single-dish telescopes), the 305-m Arecibo spherical reflector dish, built in the natural skin-hole in Puerto Rico (which has unfortunately collapsed on 2020 Dec. 1), and the Five-hundred-meter Aperture Spherical Telescope (FAST) in China, the largest single dish telescope (Nan et al., 2011; Qian et al., 2020), etc., or by using interferometers with antennas spread across a large area to ensure large total collecting area, such as Giant Meterwave Radio Telescope (GMRT) (Swarup et al., 1991) in India and MeerKAT radio telescope (Booth & Jonas, 2012) in South Africa.

I have used radio data from three different telescopes: GMRT, MeerKAT and Arecibo. Below, I describe the interferometers in detail. The GMRT is an array of 30 fully steerable parabolic radio telescopes each with a diameter of 45-m. The dish design is based on the so-called ‘SMART’ concept (Stretch Mesh Attached to Rope Trusses): a light-weighted mesh-shaped structure that can easily support the load of a large diameter dish. Of the 30 dishes, 14 occupy a compact central array region of about 1 square km, while the remaining are spread in a ‘Y’-shaped configuration, with the longest baseline covering about 25-km. It is one of the most sensitive telescopes at frequencies below 1 GHz. In 2017, it underwent a major upgrade that included an increase in the frequency bandwidth coverage and a real-time coherent de-dispersion facility (discussed in Section 2.1.3). The MeerKAT radio telescope, inaugurated in 2018, is a precursor to the Square Kilometer Array (SKA). It is an interferometer with 64 working antennas that cover a maximum baseline of 8-km. Each dish has an

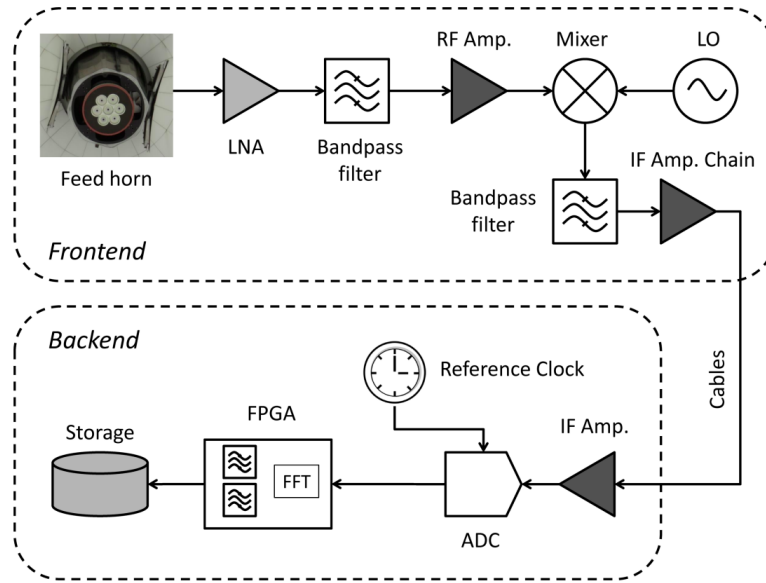


Figure 2.1: Schematic of components of a typical radio telescope’s front-end and back-end. Figure taken from [Cameron \(2018\)](#).

effective diameter of 13.5-m with an offset Gregorian configuration.

2.1.2 Front-end

Figure 2.1 shows different stages through which a signal passes after its collection at the feed horn and before it is digitised and used for scientific analysis.

In the Front-end component of a radio telescope (also called receiver), the radio signal is first collected by the feed horn that converts it into electrical signals of two orthogonal polarization modes. From then on, the processing of both the polarization channels is carried out separately. The signal is then amplified using low noise amplifiers (LNA) that are cryogenically cooled (to a few degrees Kelvin) to minimize the effect of thermal noise. Since this process will equally amplify all the collected frequencies, a band-pass filter is then used to remove the unwanted frequency ranges, such as from the terrestrial signals. The typical shape of the resultant band-pass (centered around desired frequency) is made similar to a boxcar function, although realistically, some parts of the band could be more sensitive to the receiver response than others leading to a more complex band-pass pattern. There are several complexities involved in the processing of a high-frequency signal, such as significant power losses in its transmission process or difficulties maintaining the required hardware. Thus the incoming signal is down-converted to a lower frequency while retaining all the information content. This is done by using a *mixer* that combine the incoming radio frequency signal (f_{RF}) with a monochromatic signal from a Local Oscillator (LO) (f_{LO}), and create a signal with an intermediate frequency (IF), defined by $f_{IF} = f_{RF} \pm f_{LO}$.

This IF signal is passed through another band-pass filter to save only its lower frequency component (i.e. $f_{RF} - f_{LO}$). The signal is then passed through a series of amplifiers in order to achieve a stable amplification before sending it to the back-end.

2.1.3 Back-end

A back-end of a telescope is a combination of hardware and software components responsible for the digitization of the signal and its conversion in a format that can be readily used for the scientific applications. The digitization is done using Analogue-to-Digital Converters (ADCs). To retain all the information, the data is sampled at a frequency at least larger than twice the maximum frequency of the analogue signal (which is essentially the bandwidth after down-conversion) (following the Nyquist-Shannon Theorem, [Shannon 1949](#)). The digitized data are then channelised in frequency using *Polyphase Filterbank (PFB)* which performs Fast Fourier Transform (FFT) on the data such that N samples are translated into $N/2$ frequency channels (in the form of complex voltages). This technique also takes care of any leakage of the data from adjacent frequency bins (spectral leakage), which is common in the older FFT back-ends. This is done by multiplying a sinc function with the time-series to create a desired top-hat like response for each channel that is flatter. For pulsar data, the signal needs to be channelised into narrow frequency channels to allow for the correction of ISM dispersion smearing (see Section 1.7.1). Based on the user's need, these channelized data (henceforth spectra) are processed and stored in different formats. Below I discuss three common formats used in pulsar astronomy for different purposes.

Baseband Mode

In this mode, raw complex voltages that are output from the PFB are directly recorded at their native time and frequency resolution. These data are recorded in DADA¹ format. There is more flexibility in the analysis with such data, as the frequency and time resolution can be easily exchanged in the analysis stage. It is useful where high time or frequency resolution is required, such as for single pulse analysis, scintillation studies (where highly resolved scintles are needed), or high precision timing of pulsars. However, such high resolution comes at a cost of a very voluminous data that is difficult to store and take longer to process, thus this mode is only used for specific purposes.

Incoherent search mode

If the Baseband data is not required, the complex spectral data are multiplied by their complex conjugates (thus obtaining measurements of total intensity) and then, for each channel, this power is integrated across few tens of samples (for a length we call the “integration time”, t_{samp}) in order to save storage space, which is then stored for

¹<http://psrdada.sourceforge.net/>

further processing. These data are used to search for new pulsars, thus it should have enough time and frequency resolution to fit the desired searching purposes:

a) The frequency resolution should be sufficient to avoid losing MSP signals to intra-channel dispersive smearing, t_{ds} , at least for a wide range of DMs. From Equation 1.10, we find that

$$t_{\text{ds}} = 8.3 \times \text{DM} \left(\frac{\nu}{\text{GHz}} \right)^{-3} \left(\frac{\Delta\nu}{\text{MHz}} \right) \mu\text{s}, \quad (2.1)$$

where ν is the central frequency and $\Delta\nu$ is the bandwidth of each channel.

b) The integration time t_{samp} should not be very different from t_{ds} . In the absence of scattering, the total time resolution of the system, t_{res} will be:

$$t_{\text{res}} = \sqrt{t_{\text{samp}}^2 + t_{\text{ds}}^2}. \quad (2.2)$$

For the desired range of DMs, t_{res} should be small enough to cover period ranges of all the known pulsars such that there are sufficient number of time bins in each pulse phase (32-64 bins at-least), which results in integration times of tens of μs .

However, the data should not be over-sampled (with $t_{\text{samp}} \ll t_{\text{ds}}$) as the purpose of such data is to discover pulsars rather than analyse their properties; over-sampling unnecessarily increases the data rate. This is especially important as the computational processes performed by the search pipelines (which search over a large range of DMs, periods, and period derivatives) can take significantly long for large data-sets. After recording, at the search stage, the pipelines apply relative time shifts for many trial DMs, thus removing the dispersive effect of the ISM. However, the intra-channel dispersive smearing cannot be removed at that stage, representing thus a fundamental limit of this type of data.

Coherent Search Mode

On the other hand, if the nominal DM of the target is known, for instance in the case of targeted surveys on GCs with at-least one known pulsar, the phases of the complex voltages (resulting from the FT of the sampled signal) are rotated based on the known DM. The inverse FT of this spectrum then yields the DM corrected real valued time signal. This technique, known as *coherent dedispersion* (Hankins, 1971; Hankins & Rickett, 1975), removes the dispersive smearing present within each channel and thus provide a signal with much better time resolution compared to the incoherent case. Since it is a computationally expensive process that needs to be carried out before the final data are stored, it is often performed in real-time as part of the telescope back-end (e.g. De & Gupta 2016). Because of the improved time resolution, these data have generally shorter integrations, but broader channels, since intra-channel dispersive smearing is not an issue (some channelization is still needed because of RFI and DM differences between pulsars in a GC, or variations of the DM for individual pulsars).

Generally, no polarisation information is required in both types of search-mode data, thus the two polarizations can be integrated and only the total intensity needs to be stored. These data are commonly stored in *filterbank* or *PSRFITS* formats (a standard FITS-based format) in the form of a 2-D array, with time-samples as one axis and frequency channels (corresponding to each time bin) as another. An advantage of using search-mode data for analysis is that it can be easily folded over time and frequency when the pulsar parameters become known, making it also useful for timing purposes, especially for newly discovered pulsars. Using search data from GCs, we can not only search for new pulsars, but also time any previously known pulsars in that GC.

Timing/Fold Mode

This type of data format is widely used for pulsar timing analysis and is recorded for pulsars with a known *timing solution*. In this mode, since DM of the pulsar is known, coherent de-dispersion is carried out in real-time. Subsequently, by making use of the known pulsar parameters (timing solution or “ephemeris”), the DM corrected channelised data are recorded in a folded format such that the pulses from each rotation lie on top of each other. Since the integrated pulse profile is highly stable compared to the individual pulses, high precision timing analysis to monitor changes in the pulse arrival times can be performed with such data. The folded nature of the data allows us to save storage, thus we can make this data higher resolution compared to the search mode data by recording a large number of phase bins for each integrated profile. Since several pulse phases are added to create sub-integrations, this format also subsides any temporal RFI that may arise while observing. A disadvantage of such pulsar specific data, especially in the case of GCs, is that we lose sensitivity to any other pulsars present in the same data-set. For timing purpose, in order to coherently integrate observations from different epochs and different telescopes, it is important that these observations have accurately recorded time stamps. The data files recorded in this format are called *folded archive files*.

2.2 Time domain searches

The time domain search techniques used by pulsar astronomers to find new and interesting pulsar systems have advanced significantly over the past decade. Two of the most commonly used softwares that provide a number of useful routines to carry out pulsar searches are PRESTO (Ransom, 2011) and SIGPROC (Lorimer, 2011). One of the main difference between these is the way they search for binary pulsars: the former corrects the Doppler smearing of pulse in the Fourier domain while the latter does this in the time domain. The pipeline used in the pulsar search surveys presented in this thesis (chapters 3 and 4) is based on PRESTO. Below we discuss in detail the steps carried out either manually or by the pipeline for these searches.

2.2.1 Interference mitigation

Radio Frequency Interference (RFI) is the unwanted terrestrial signal that appears in the data. Various sources of RFI include satellites, mobile networks, Wi-Fi, television, and radars among others. Since the pulsar signal is a weak radio source, any amount of moderately strong RFI can greatly affect the search sensitivity. Thus the first step in any pulsar search pipeline includes RFI mitigation. RFI with different signatures/trends can appear into the data, these can be broadly categorised as: a) time-domain RFI which appears for a small fraction of time, b) frequency-domain RFI which appears either in a narrow range of frequencies or across some portion of the band, and c) periodic RFI that appears in the data as regular bursts. Both time-domain and frequency-domain RFI can be removed from the data by identifying regions with abnormal median and mean power. In the PRESTO based search pipeline this is done using the `rfifind` routine. The terrestrial signals, even if periodic, do not mimic the typical dispersion sweep ($\propto \frac{1}{\nu^2}$) caused by the ISM, which is present in all pulsar signals. Thus the periodic RFI is identified by noting frequencies of strong periodic signals in the time-series (see Section 2.2.2) (that is frequency integrated data) with no de-dispersion i.e. at $DM = 0 \text{ pc cm}^{-3}$. These frequencies are then removed from the rest of the data processing.

The detection sensitivity for a pulsar can also decrease due to another type of noise that appears in the radio data, referred as *red noise*. It occurs as long-term variations in the power levels produced by the observing set-up and thus become important for observations with longer integration times. Since this noise appears in the low-frequency end of the power spectra (hence the name ‘red’ noise) it can reduce the detection sensitivity for long-period pulsars in the Fourier domain (see Section 2.2.3). To correct for this effect, we normalise the power-spectrum by using PRESTO’s `rednoise` routine (described in Lazarus et al. 2015). Fast Folding Algorithm (FFA, Staelin 1969) is another search algorithm that is often used to reduce the effect of red noise and improve sensitivity for slow pulsars (e.g. Cameron et al. 2017; Parent et al. 2018).

2.2.2 De-dispersion

Following RFI excision, the next step is to correct the dispersion sweep of pulses present across the frequency bandwidth due to ISM (as explained in Section 1.7.1). Since the DM (or distance) of the pulsar to be discovered is not known a priori, the data are de-dispersed, i.e. corrected for the time delay, for a range of DM values (using Equation 1.10). The decision for the range of DMs to search is broadly based upon: a) the type of survey and the characteristics of its data, and b) the computational power available. In the case of a targeted survey, such as on GCs with at-least one known pulsar, a nominal DM estimate of the cluster is known beforehand, so the data are de-dispersed only for a small range of DMs around the cluster’s typical DM value. On the other hand, if we search for pulsars in a blind survey, we can search as deep as we like i.e. we are not limited by the distance to the target source. Thus a typical DM

range is then only limited by the computational power that we have: commonly these searches range from 1-5000 pc cm⁻³.

Furthermore, it is also crucial to fix an optimum DM step size at which the time-series are created. Choosing a large step size can lead to decreased sensitivity to pulsars with DMs further away from the central DM of each step. This is because the pulses can get smeared in the frequency integrated time-series which are eventually searched for periodicity if the actual DM is largely offset from the trial DM. While a very small step size can lead to longer computational times without any gain in sensitivity. In the pipeline used in this thesis, the optimum step size is chosen using a routine called `DDplan`². This routine also outputs the optimum downsampling of the time-series needed to avoid any over-sampling in the data (either due to unavoidable intra-channel smearing, t_{ds} or originally highly sampled data) to minimise the computational time or power needed for the searches. To summarise, using the scheme from `DDplan`, the data are first de-dispersed over a range of DMs, then scrunched or integrated in frequency, and finally downsampled in time, to create a number of time-series. This is done collectively for a range of DMs using a routine known as `prepsubband/mpiprepsubband`³.

2.2.3 Periodicity search

In the next step, each time-series is searched for periodicities in the Fourier domain using FT, using which the frequency of periodic pulses clearly stand out from the thermal noise in the power spectrum. Because the time-series are uniformly sampled and finite, a Discrete Fourier Transform (DFT) ([Arfken & Weber, 2005](#)) is an appropriate choice. For kth sample, a DFT \mathcal{F}_k is defined as:

$$\mathcal{F}_k = \sum x_n e^{-2\pi ink/N}, \quad (2.3)$$

where N are the total number of elements and x_n is the data point on the sampled time-series. From the complex DFT output, the power spectrum is calculated as:

$$P_k = Re(\mathcal{F}_k)^2 + Im(\mathcal{F}_k)^2. \quad (2.4)$$

In pulsar analysis, we use a more computationally efficient implementation of DFT known as Fast Fourier Transform (FFT) ([Brigham & Yuen, 1978](#)). This algorithm reduces the number of operations performed on a single time-series from $O(N^2)$ to $O(N \log(N))$. For this purpose, in the searches in this thesis we used routine `realfft` based on the Fastest Fourier Transform in the West (FFTW) library⁴.

Pulsar signal from most pulsars is non-sinusoidal and concentrated in a narrow region of the rotational phase. Thus in the power spectrum, the signal's power is unevenly distributed among the fundamental frequency and its higher order harmonics.

²<https://github.com/scottransom/presto/blob/master/bin/DDplan.py>

³<https://github.com/scottransom/presto/blob/master/src/prepsubband.c>

⁴<http://www.fftw.org>

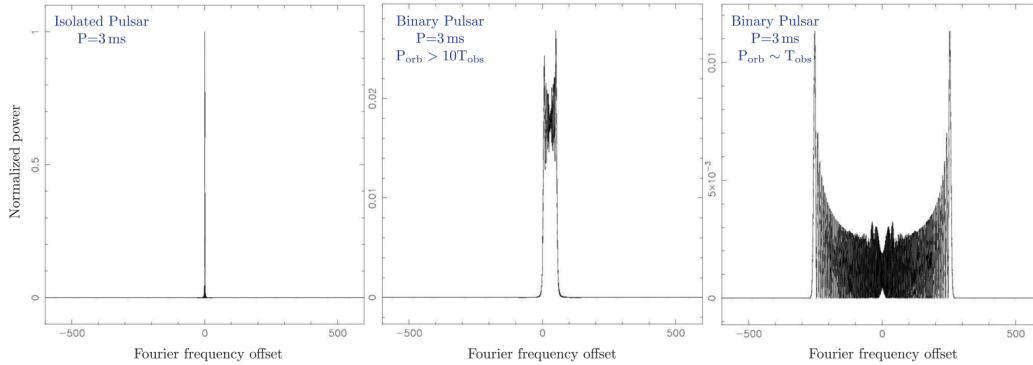


Figure 2.2: Power spectrum for a 3ms pulsar, for three different cases: isolated pulsar showing one single peak (left), binary pulsar with large orbital period such that $P_{\text{orb}} > 10t_{\text{obs}}$ (center), and binary pulsar with compact orbit such that $P_{\text{orb}} \sim t_{\text{obs}}$ (right). Credit: Scott Ransom.

In order to retain the full strength of the signal, it is thus crucial to combine as much power as possible from the harmonics, this process is known as *harmonic summing*. A common technique used for this purpose is given by [Taylor & Huguenin \(1969\)](#). It involves stretching the power spectrum by an integer factor and then summing it to original un-stretched spectrum. This creates a spectrum with the summed power of the bins in fundamental and harmonic frequencies, resulting in an enhanced SNR of the pulse while leaving behind the noise. Typically, search pipelines create and search the summed spectra with up to 16 harmonics.

2.2.4 Acceleration and jerk searches

Above procedure is enough to identify isolated pulsars or those that are not accelerated from their local environment. However, in the case of binary pulsars where the pulsar orbits the binary system's center of mass, the signal is Doppler shifted as it moves across the orbit. This lead to a time-varying observed period (P_{obs}) and period derivative (\dot{P}_{obs}) ([Lorimer & Kramer, 2012](#)):

$$P_{\text{obs}}(t) = P_i \left[1 + \frac{v_l(t)}{c} \right], \quad (2.5)$$

$$\dot{P}_{\text{obs}}(t) = P_i \frac{a_l(t)}{c}, \quad (2.6)$$

where P_i is the intrinsic period and v_l and a_l are the line-of-sight velocity and acceleration of the pulsar. In the Fourier domain, the effect of this time-varying signal is that the power from each harmonic is spread to many Fourier bins, decreasing the pulsar's detection significance in the power spectrum, as shown in [Figure 2.2](#). To correct this effect, techniques such as *acceleration and jerk searches* are carried out to regain the full strength of the signal.

In the acceleration search, it is assumed that a_l is constant over the course of observation length. PRESTO translates this acceleration to the number of Fourier bins over which the power gets smeared, this number is given by the parameter, z and is represented as:

$$z = \Delta t_{\text{obs}}^2 \frac{a_l}{cP}, \quad (2.7)$$

where Δt_{obs} is the integration length of the observation. Considering a Fourier bin size of Δf_{bin} , the range of frequency bins up to which the smeared power will be recovered around a given frequency f_0 is given by $[f_0 - z_{\text{max}}\Delta f_{\text{bin}}, f_0 + z_{\text{max}}\Delta f_{\text{bin}}]$, where z_{max} corresponds to the largest z values searched in a particular survey.

The constant acceleration assumption is approximately valid only if the observing time is less than about 10% of the orbital period (Johnston & Kulkarni, 1991), which means for shorter observation lengths much smaller orbital periods (thus larger acceleration values) can be searched. Thus to avoid breaking this assumption, an observation can be divided into multiple smaller segments to decrease the observing time. This technique, known as *segmented acceleration*, can be useful in detecting bright binaries that do not lose significant sensitivity with smaller integration times.

A better, but more computationally expensive approach that is more sensitive to relatively faint pulsars or tight binaries consisting of highly accelerating pulsars or those with high rate of change of acceleration is known as *jerk search* (Andersen & Ransom, 2018). It accounts for the smeared power due to a linearly varying acceleration, and it is implemented by PRESTO through the w parameter, that is a function of acceleration derivative (\dot{a}_l) as follows:

$$w = \Delta t_{\text{obs}}^3 \frac{\dot{a}_l}{cP}; \quad (2.8)$$

the maximum value of w searched in survey is given by w_{max} .

In the search analysis presented in this thesis, I have carried out both acceleration and jerk searches in Fourier domain using routine `accelsearch` included in PRESTO.

2.2.5 Candidate selection and confirmation

The number of resulting candidates from the above mentioned periodicity searches can reach several thousands. The majority of these candidates are either RFI, harmonically related candidates, or candidates found multiple times at slightly different parameters. In order to isolate these from real pulsars, the pipeline uses PRESTO routine `accel_sift.py` to first filter out the least significant candidates and then remove the harmonically related candidates. It also removes the candidates which do not have a peak in the SNR vs DM curve (representing a characteristic dispersion sweep from ISM) and thus are most likely RFI. This process results into few hundreds of candidates that are then examined visually. The number of final candidates are several thousands in the case of blind surveys, thus many different approaches such as machine learning algorithms have been developed recently (Eatough et al., 2010; Lee et al., 2013; Morello et al., 2014; Zhu et al., 2014) to reduce their number.

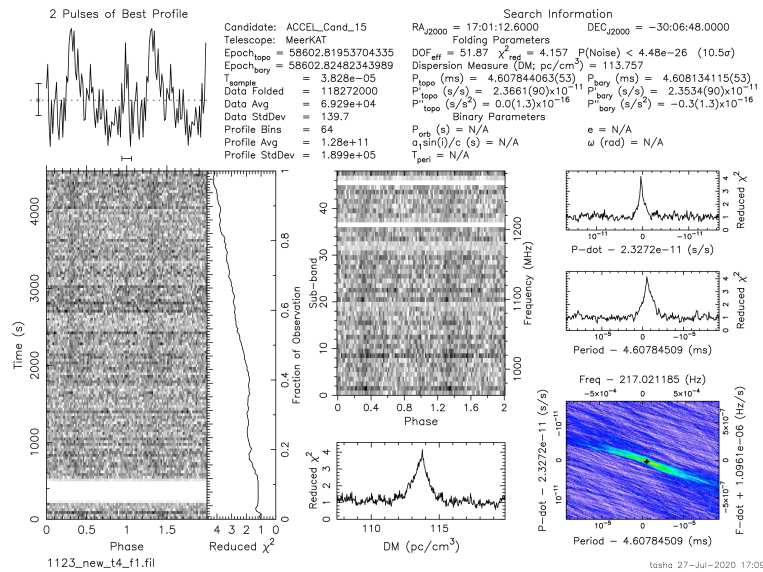


Figure 2.3: Diagnostic plot created by `prepfold` for PSR J1701–3006G (or M62 G) discovered in the GC survey performed with the MeerKAT radio telescope (discussed in Chapter 4.)

The final list of candidates are then folded in the raw data i.e. the raw data are first de-dispersed at each candidate’s DM and then folded based on the period and period derivative of the candidate such that each rotational phase is integrated. All above steps are done using PRESTO’s routine `prepfold` that outputs a final diagnostic plot. It also searches for optimum period, period derivative, and DM of the candidate over a small range to enhance its resulting SNR. Figure 2.3 shows the diagnostic plot that led to the discovery of PSR J1701–3006G (or M62G). If a candidate appears consistent in time (except black-widow or redback binaries which could be eclipsed due to intra-binary plasma) and frequency, and show a statistically distinct period, period derivative (if any), and DM, it is identified as a likely pulsar. A pulsar candidate (especially a faint one) is generally said to be confirmed if it is found in more than one observation.

2.3 Image domain searches in globular clusters

The large distances of several kpc to GCs make it difficult to detect even bright MSPs, thus deep surveys with longer observation times are needed to improve their detection sensitivity. However, as the distance (or DM) of many of the clusters is not known a priori, the time-domain pulsar search pipelines have to extensively search for a large range of DMs (and accelerations and jerks) which makes it computationally challenging to search long observations.

We can overcome these difficulties with radio interferometric imaging of GCs.

With radio continuum imaging, we can discover and localise pulsars in these GCs. They can be distinguished from other radio sources found in GCs (such as Active Galactic Nuclei or stellar mass black holes) by identifying steep-spectrum point-like sources (due to their compact and steep spectrum nature, with spectral index $\alpha < -1.0$). Indeed, the first millisecond pulsar and the first pulsar discovered in a GC (M28A) was found from radio imaging with the Westerbork Synthesis Radio Telescope (WSRT) and the Very Large Array (VLA) respectively (Backer et al., 1982; Hamilton et al., 1985; Lyne et al., 1987).

Once a pulsar candidate is identified in an image, we can follow it up with time-domain observations by pointing the telescope's beam directly at the source location to improve its detection sensitivity (in the examples above, the radio pulsations were found using the Jodrell Bank 75-m and the Arecibo 305-m telescopes). If pulsations are found in these time domain searches, then the pulsar's DM will be known, this will give us an estimate of the nominal DM of the cluster (and also its distance). The search pipelines can then be more efficient as: a) they will have shorter DM ranges to search thus making them computationally efficient, and b) longer observation times will be possible, both providing improved detection sensitivity to new pulsars. Additionally, time-domain observations with *coherent de-dispersion* mode can then be carried out to improve the sensitivity of both previously known and unknown pulsars. Imaging clusters can also help identify pulsars which are either present at the outskirts of the cluster core and are missed by the limited beam size of the telescopes (most of which only cover the core of the clusters), or part of short orbit binaries thus missed by the limitations of our search techniques.

2.3.1 Interferometric data acquisition

Below we briefly discuss the format of the data acquired by Interferometers (or synthesis arrays) used to create radio images (see Thompson 1989 for detailed discussion).

The total interferometric response from two antennas is represented in the form of a complex *visibility function* (or spatial coherence function) as follows:

$$V = R_c - iR_s, \quad (2.9)$$

where R_s and R_c are the response functions from the sine and cosine correlators (used to cross-correlate and integrate the signals from two antennas to create a time-average product of voltages) which are functions of the observing frequency (ν) and the time delay between antennas (τ_g). The visibility function in the form of source brightness distribution, $I_\nu(\mathbf{s})$, is represented as follows:

$$V_\nu(\mathbf{b}) = \iint I_\nu(\mathbf{s}) e^{-2\pi i \nu \mathbf{b} \cdot \mathbf{s} / c} d\Omega, \quad (2.10)$$

where Ω is the solid angle over sky, \mathbf{b} is the baseline vector that connect the antennas, and \mathbf{s} is the unit vector pointing towards the source location in the sky. In other

words, the interferometric pattern observed by the interferometer in the form of visibility function is directly related to the source brightness, the brightness distribution can thus be extracted from the coordinate transformations from the “visibility domain” to the “image domain”. If we consider an interferometer with antennas spread across both East-West and North-South direction having u and v as the coordinate axes, respectively, the baseline vector \mathbf{b} can then be represented as the distance between antennas in units of the number of wavelengths (λ), such that $\mathbf{b} = (\lambda u, \lambda v, 0)$. In the image domain, the unit direction vector \mathbf{s} in the sky can be represented as projections (l, m) on the (u, v) plane, respectively. Thus in the above equation, $\mathbf{b} \cdot \mathbf{s} / \lambda = ul + vm$, for which the visibility function becomes:

$$V_v(u, v) = \iint I(l, m) e^{-2\pi i(ul + vm)} dl dm, \quad (2.11)$$

which is clearly a 2-D FT of the intensities (or brightness distribution) in the sky. Hence by measuring the response function of the antennas over time and thus measuring visibilities over the (u, v) plane, we can get the sky brightness distribution with the inverse FT. An adequate sampling of the (u, v) plane will help model the emission better and result in an accurate image.

The phase of the visibility function is proportional to the baseline response projected on the sky (in the form of interference fringes), and thus gives us the location information of the source, while its amplitude is proportional to the sky brightness distribution and provides us with the flux density of the source.

All the processing of visibility data in this thesis is done with the widely used “Common Astronomy Software Applications” (CASA)⁵ package (McMullin et al., 2007a), so we will limit our discussion to the procedure performed using this software. Below we discuss the practical steps used in this thesis work to produce radio images of GCs from the visibility data acquired from GMRT.

2.3.2 Flagging and calibration

Before beginning to process the visibilities, it is important to discard any data that is corrupted, this process is referred as *flagging*. Corrupted data can arise from various sources such as terrestrial signals, antenna tracking inaccuracies, malfunctioning antennas or receivers, or other data recording errors. For smaller datasets (such as GMRT GC data used in this thesis), this data can be removed interactively using the CASA task `plotms` routine. The RFI present in the spectra and time chunks of the data are removed by identifying anomalous power levels. Any non-working antennas are identified from the observation’s log and the baselines connecting those antennas are also manually flagged from the data.

The observed visibilities differ from the true visibilities due to several factors that lead to the errors in measurements, these can be broadly categorised as: a) propagation errors, for instance due to time-varying changes in atmospheric (ionospheric

⁵<https://casa.nrao.edu/>

and topographic) and weather conditions, b) geometric errors such as inaccuracies in antenna locations and pointings, or errors from wide bandwidth of the signal as different frequencies may have different delays, and c) instrumental errors such as from array reconfiguration, instabilities in the electronics (that lead to change in signal path length), instrumental noise, or varying frequency response from antennas. The process of correcting for these errors (with both long and short-term variations) in the visibility data and determining the true visibilities that combine to form an accurate image, is known as *calibration*. The basic procedure involves correcting for these errors by observing a primary calibrator source (also known as bandpass or flux calibrator) during the observation session. It is usually a compact, bright, and flat spectrum source such as a quasar with previously known good estimates of its shape, flux, and spectrum. By using the instrument response to this primary calibrator, the correction models for both the phases and amplitudes are derived in the form of Jones matrices, J_{ij} (also composed of complex numbers, discussed in detail in Hamaker et al. 1996; Hamaker 2000). These are then applied to the target source's visibilities, such that:

$$V_{ij} = J_{ij} V_{ij}^{\text{true}}, \quad (2.12)$$

where V_{ij}^{true} are the true visibilities for ij^{th} baseline. Below we discuss three main steps carried out in CASA for the calibration purpose.

A majority of the corrections to the phases of the visibilities are performed with a method known as *multi-band fringe-fitting* which corrects for the slopes of phases at small frequency and time intervals. One antenna is set as a phase reference and the solutions for all the other antennas are derived relative to that antenna. This procedure mainly corrects for the time-independent geometric and propagation errors. The solutions are first derived using the primary calibrator, and are then applied to the target's data. This is commonly referred as *delay calibration*.

Next, in order to correct for the amplitudes as a function of frequency, we correct for the bandpass of antennas, and since these effects are stable over long period of time they can be assumed time-independent, thus correction models created from the flux calibrator can be directly transferred to the target data. This is commonly known as *bandpass calibration*.

Finally, to correct for all the antenna-based time-dependent offsets in amplitude and any residual offsets in phase, present due to changing instrument response, weather conditions, etc., *complex gain calibration* is performed. In this case, the correction models derived from the primary calibrator are first transferred to a secondary calibrator (also known as a phase calibrator or gain calibrator) which is observed close to the target location. Its proximity to the target help determine all the time-varying corrections accurately. The solutions derived from this calibrator are then interpolated and applied to the target source's data.

In the GMRT GC survey presented in this thesis, each observation session included a 3-5 minute scan both before and after the target observation on a phase calibrator (such as 1830-360) and ~ 10 -minute scan before the target observation on a bandpass

calibrator (such as test pulsar B1839+09).

Once close to true visibilities are derived for the target source, the imaging steps to map sky brightness distribution can be performed on this data.

2.3.3 Imaging

The first step in creating an image after calibration is to create a sampling function (with M points) that can be represented in terms of a 2-D Dirac delta function such that:

$$S(u, v) = \sum_{k=1}^M \delta(u - u_k, v - v_k). \quad (2.13)$$

In the image domain, the inverse FT of this sampling function is known as a *point spread function* or *dirty beam*, given by $s(l, m) = \mathcal{F}^{-1}\{S(u, v)\}$. To account for the unequal densities in the (u, v) plane, a weighting function $W(u, v)$ chosen appropriate for our application is used. For instance, long baselines improve the angular resolution to point sources and shorter baselines are sensitive to extended structures. This function modifies the dirty beam, such that $s(l, m) = \mathcal{F}^{-1}\{W(u, v) \times S(u, v)\}$.

The inverse FT of the sampled visibilities, i.e. $V(u, v) \times S(u, v)$ is known as a *dirty image*:

$$\begin{aligned} I^D(l, m) &= \iint S(u, v) V(u, v) e^{i2\pi(ul+vm)} dl dm, \\ &= \mathcal{F}^{-1}\{S(u, v) \times V(u, v)\}, \\ &= s(l, m) \otimes I(l, m). \end{aligned} \quad (2.14)$$

Last relation comes from the convolution theorem, using which we can express the dirty image as a convolution of the point spread function and the true image (or sky brightness distribution) $I(l, m)$ (as discussed before it is an inverse FT of $V(u, v)$). Thus, we can get the true image by de-convolving the point spread function from the dirty image. In practice, the widely used procedure to do this is CLEAN de-convolution algorithm (Högbom, 1974) which is implemented in the CASA task `tclean` function as follows:

First, a dirty image formed from the inverse FT of observed visibilities is initialised as a residual map. The position and strength of the brightest pixels (essentially point-like sources in GC data) in this map are then identified. The dirty beam (i.e., the response function to a point source) is scaled to the peak, multiplied by the gain factor (typically 0.1), then subtracted from the map at the position of the bright source. After each iteration, we can identify fainter sources in the residual map. The above procedure is repeated until all the chosen sources have peaks below a user-defined threshold (usually chosen as 3 times the rms noise) in the residual map. The accumulated point-source model, also known as clean component list, include all the bright sources selected. This is then convolved with a CLEAN beam which is a Gaussian model fitted to the central lobe of the dirty beam. Finally, to get useful diagnostics of

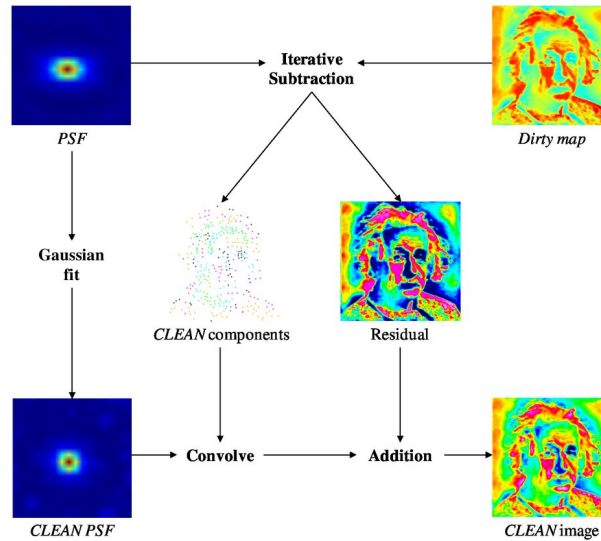


Figure 2.4: Representation of CLEAN algorithm implemented in CASA's `tclean`. Figure taken from Taylor et al. (2014).

the noise, the residual map is added to this CLEAN image. Figure 2.4 explains the Högbom CLEAN algorithm with a block diagram.

To remove any residual calibration errors, another type of calibration, known as *self calibration* can be performed on the model created after the first few iterations of `tclean`. In this method, the bright sources taken as clean components are used to improve the complex gain solutions (both amplitude and phases). To derive a short enough solution interval such that short-term atmospheric phase changes are taken into account, the calibration process is repeated a couple of times (generally targeting several minutes of solution interval) with improved `tclean` model. This process can be repeated until no further improvement is evident from a given self-calibration step. To create GC images in this thesis, a few rounds of phase-only self calibration were carried out. Figure 2.5 shows a radio image of GC NGC 6652 created as part of the GMRT GC survey presented in this thesis (see Chapter 3). The sources labelled 2, 3, and 4 are unknown bright point-like sources within the tidal radii of the cluster. Of these sources 2 and 3 are relatively steep spectrum with index, $\alpha < -1$, and are likely undiscovered pulsars.

Once a likely pulsar is confirmed from the time-domain searches (either via first imaging GCs or directly detecting it in time-domain data), it should then be followed up to determine its properties and potential for science. In the next two sections, we discuss the procedure involved in creating a timing solution for a pulsar.

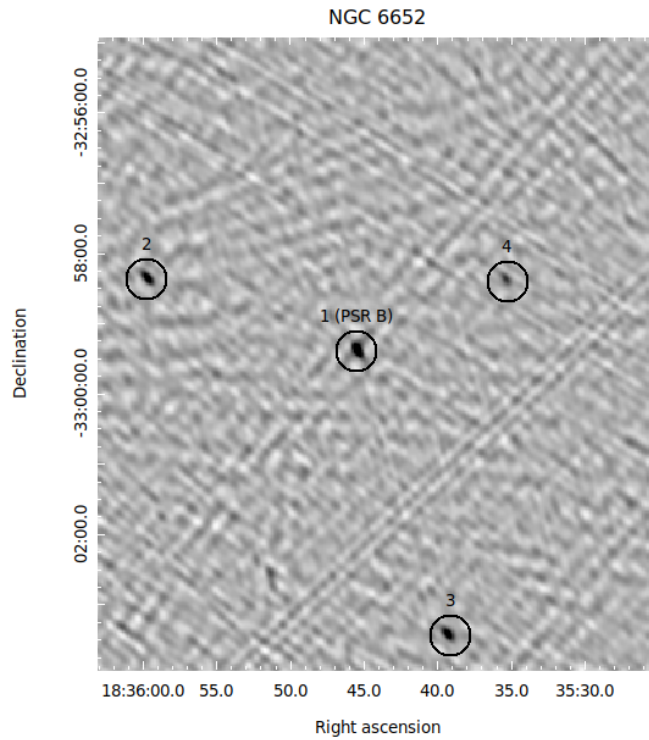


Figure 2.5: Radio image of NGC 6652 created from the GMRT visibility data recorded simultaneously with the time-domain data. Source 1 coincides with the timing position of NGC 6652B while sources 2, 3, and 4 are bright point-like sources within the tidal radii of the cluster.

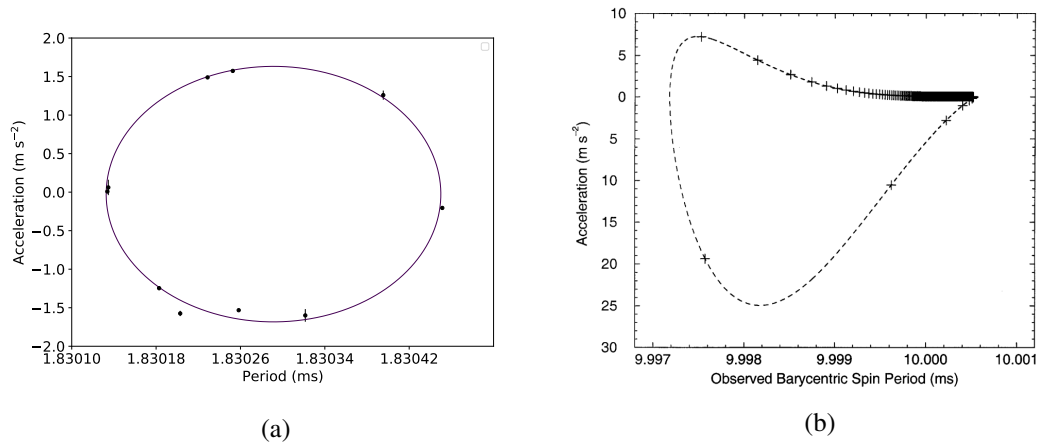


Figure 2.6: Period-Acceleration plot for a near-circular orbit of PSR J1835–3259B discovered in GC survey carried out with GMRT presented in Chapter 3 (left) and for a simulated eccentric binary with $e = 0.9$ (right) (taken from Freire et al. 2001)

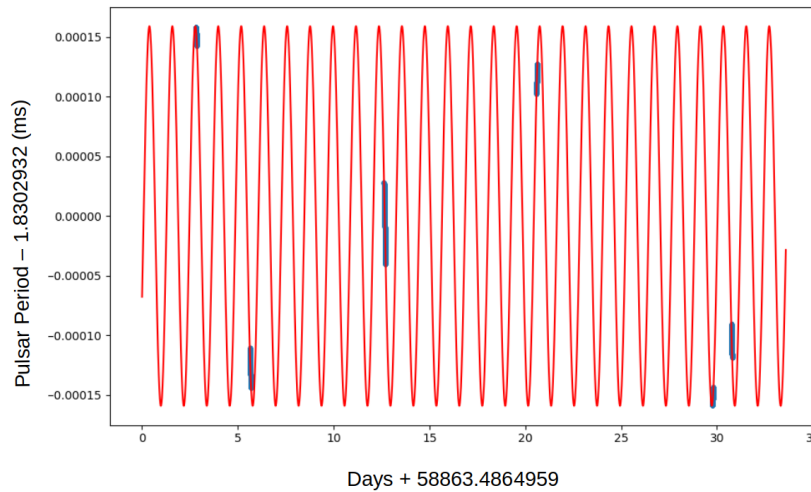


Figure 2.7: `fit_circular_orbit.py`'s period vs time plot for PSR J1835–3259B.

2.4 Orbital parameter estimation

If the newly discovered pulsar is observed to change period (either in a single observation or across different observations), it is likely in a binary system (unless its local environment affects it or it is a magnetar). In order to determine a rough estimate of orbital parameters of the binary, so the pulsar can be easily re-detected in future observations without having to perform the searches again, one simple approach that is used in this thesis is the period-acceleration diagram method (Freire et al., 2001). The plot of the observed period and line-of-sight acceleration (determined from the observed period derivative using Equation 2.6) of each detection have a characteristic shape, for instance, near-circular binaries form an ellipse-like pattern in the plot while eccentric binaries create more complex shapes, see Figures 2.6a, 2.6b. Using this method, through the position and semi-major axis of the ellipse in the plot, one can determine the approximations for semi-major axis, eccentricity, orbital period, and epoch of periastron of the orbit. The advantage of this method is that it has no dependence on time, thus it is especially useful for sparse detections of pulsars, as long as a good part of the orbital phase is covered, which is usually the case for newly discovered systems.

With the rough estimates of binary parameters we can then use a more precise approach that directly fits for the intrinsic non-varying spin period and a Keplerian orbit to the observed time-varying spin period. This method is only useful if a large number of detections already exist for a pulsar or a very good guess of initial parameters determined from the Period-Acceleration method is used for the fit. Codes such as FITORBIT⁶ or PRESTO's `fitorb.py/fit_circular_orbit.py` (see Figure 2.7) can

⁶<https://github.com/gdesvignes/fitorbit/>

be used for this purpose.

2.5 Timing a pulsar

If the pulsar to be timed is newly discovered, the timing model is not precise enough to do a real-time folding of the observations, so the observation is carried out in *search mode*. Once sufficient observations are taken and a robust timing model (referred as ephemeris) with an estimate of orbital parameters is derived from the methods above, the data from search mode can be easily re-folded. The follow-up observations can then be performed in timing-mode (or fold-mode) with real-time coherent de-dispersion. These observations must have a good orbital coverage such that there is data across all parts of the orbit to precisely constrain the orbital parameters. To perform timing analysis, data from each epoch must be correctly time-stamped with the start time of the observation monitored using local observatory's time that is usually recorded with a hydrogen maser clock. This is then compared to atomic clocks on the GPS satellites and the differences are recorded in clock correction files, these files are then used to correct the time-stamps later in the analysis.

With pulsar timing, the pulse Times-of-Arrival (TOA) are compared to the prediction of the timing model/solution. From this comparison, if there exist any trend(s) in the residuals, that means there is some physical effect leading to additional time-delays in the pulse arrival times that is not accounted by the current timing model. Thus, a new parameter based on the residual trend must be added to the existing solution and fit with the data (see Section 2.5.3). Since pulsars (especially MSPs) are extremely stable rotators, it is possible to create a timing model that can predict every single rotation of the pulsar (in the data-set) to a good precision, such a model is referred as *phase-connected timing solution*. This model commonly contains rotational, astrometric, and ISM related effects, and in the case of binary pulsars, orbital parameters along with the relativistic effects (discussed in detail in Section 2.5.2).

The most commonly used software package for data reduction and TOA derivation is PSRCHIVE (Hotan et al., 2004a; van Straten et al., 2012a). The software packages used in this thesis to analyse the TOAs and derive the timing solutions are TEMPO⁷ and TEMPO2 (Edwards et al., 2006; Hobbs et al., 2006). Below we discuss in detail the practical steps, including the binary models, generally used in pulsar timing to create and refine a timing solution.

2.5.1 TOA creation

TOAs are the time stamps (measured in *Modified Julian Date*, MJD) assigned to each integrated pulse profile that has a sufficiently high SNR. They are measured from the cross-correlation between the integrated profiles of the data and a standard template that serve as a reference profile. Standard template can either be: a) a high SNR

⁷<http://tempo.sourceforge.net>

profile from a single observation, b) an integrated profile created by adding all the observations, or c) a noise-less profile formed from fitting an analytical function to the integrated profile, for instance, routine `paas` fits von Mises distribution to the pulse profile while `psrsmooth` smooths the profile with a wavelet transform (Kramer et al., 1994; Demorest et al., 2013). PSRCHIVE's routine `pat` is used to do the cross-correlation and determine the offsets of a fixed reference point between the template's profile and the integrated profiles of real data. Individual profile's TOA is determined from the addition of this offset to the epoch of a fiducial point of the profile closest to the mid-point of the corresponding sub-integration (determined from the start time of each observation).

2.5.2 Timing Model

A timing model of a pulsar mainly includes the following set of parameters:

- rotational parameters that include spin period and its higher order derivatives,
- astrometric parameters that include position (RA and DEC), proper motion, and parallax of the pulsar,
- ISM-related parameters such as dispersion measure and its higher order time derivatives, and
- in the case of binary pulsars, Keplerian parameters and post-Keplerian parameters that are measured as higher order post-Newtonian approximations. These describe the observed orbital motion.

The TOAs measured at the telescope on Earth are topocentric, thus we must apply following three transformations to convert them to pulsar's proper time, T : a) from topocentric time (τ_{sat}) to solar system barycentric (SSB) time, b) from SSB time to binary system's barycenter (BB) time, and c) from BB time to pulsar's reference time.

The proper time in pulsar's reference frame can be represented as a collection of the following terms:

$$T = \tau_{\text{sat}} + \Delta_{\text{clock}} - D/f^2 - (\Delta_{\text{R}}^{\odot} + \Delta_{\text{E}}^{\odot} + \Delta_{\text{S}}^{\odot}) + (\Delta_{\text{R}} + \Delta_{\text{E}} + \Delta_{\text{S}}), \quad (2.15)$$

where Δ_{clock} includes the clock corrections of the observatory time standard (as mentioned in Section 2.5) and the transformations to convert from τ_{sat} to SSB time, D/f^2 is the contribution from dispersion delay from ISM experienced by the pulsar signal at frequency f , and all the Δ^{\odot} terms represent the time-delays introduced by the solar system, which include contributions from:

- Römer delay, $\Delta_{\text{R}}^{\odot}$ - a classical geometric delay due to motion of the Radio telescope relative to the SSB,
- Einstein delay, $\Delta_{\text{E}}^{\odot}$ - a delay due to relativistic time dilation arising from the space-time coordinate frame transformation from the telescope to SSB, and

- Shapiro delay, Δ_S^\odot (Shapiro, 1964) - time delay due to longer optical path of light when passing through curved space-time of solar system objects.

If the pulsar is in a binary system, similar set of corrections are required when transforming from the BB time to pulsar's proper time, these are represented with Δ_R , Δ_E , and Δ_S in Equation 2.15. Each of these binary contributions are measured in terms of binary parameters which are used to describe the orbital motion. We discuss these parameters in detail below.

Binary terms:

The line-of-sight component of the orbit of a binary pulsar (the only part we can measure via timing) can be described by the following five Keplerian parameters:

- orbital period (P_b),
- eccentricity (e),
- longitude of periastron (ω),
- epoch of periastron (T_0), and
- projected semi-major axis, $x = a_p \sin i$, where a_p is the semi-major axis and i is the inclination of the orbit.

With x and P_b , we can estimate the mass function of the binary as follows (Lorimer & Kramer, 2004):

$$f(m_p, m_c) = \frac{4\pi}{T_\odot} \frac{x^3}{P_b^2} = \frac{(M_c \sin i)^3}{(M_p + M_c)^2}, \quad (2.16)$$

where M_p and M_c are pulsar and companion mass, and $T_\odot = GM_\odot/c^3 = 4.92549094764\mu\text{s}$ is the Solar mass parameter in time units. The individual masses or i cannot be determined, but we can assume a M_p (say $1.4 M_\odot$) to obtain estimates of M_c for a range of inclinations: for instance, assuming $i = 90^\circ$, we can constrain the minimum M_c , that can give us insight into the nature of the companion.

Better understanding of the pulsar binary comes from more precise measurement of both M_c and M_p , so in addition to Equation 2.16, we need more equations relating the component masses. These come from the measurement of Post-Keplerian (PK) parameters, which quantify relativistic effects in the orbital motion of the pulsar and the propagation of its signal (the aforementioned Shapiro delay, Δ_S) in a theory-independent way (Damour & Taylor, 1992a). These measurements result from the comparison of the observed orbital motion with a theoretical model of the orbital motion.

There are several theory-independent binary models, implemented in the timing softwares, that can be used to estimate the Keplerian and PK parameters. One of the most commonly used model is DD model (Damour & Deruelle, 1985; Damour & Deruelle, 1986). In this model Shapiro delay is measured with two parameters, range,

r and shape, s . A variation of DD model is ELL1 model (Lange et al., 2001) that is commonly used for pulsar binaries with small eccentricity, in which case there is a high correlation between ω and T_0 measurements. This model resolves this issue by fitting for the Laplace-Lagrange parameters, $\varepsilon_1 = e \sin \omega$ and $\varepsilon_2 = e \cos \omega$ instead of eccentricity, and replacing ω with the epoch of ascending node, T_{asc} .

Other two theory-independent models derived from these are the DDH (Weisberg & Huang, 2016) and ELL1H models; they differ from the DD and ELL1 models because they use the orthometric parameterisation of the Shapiro delay (Freire & Wex, 2010). This is done to avoid the high correlation between the r and s parameters, especially for low inclinations. These models introduce orthometric amplitude, h_3 and orthometric ratio, ζ , such that:

$$\zeta = \sqrt{\frac{1 - \bar{c}}{1 + \bar{c}}}, \quad (2.17)$$

where

$$\bar{c} = \sqrt{1 - s^2} = \cos i, \quad (2.18)$$

$$h_3 = r\zeta^3. \quad (2.19)$$

Apart from the above mentioned theory-independent models, there is a commonly used theory-dependent model, referred as DDGR model (Taylor, 1987; Taylor & Weisberg, 1989), that assumes GR as the theory of gravity, and fits directly for the masses in the TOAs (thus deriving consistent PK parameters).

If a theory of gravity is assumed, the PK parameters can be represented as functions of both the Keplerian parameters and the component masses. We now list the commonly measured parameters in pulsar binaries and their dependence on the masses and Keplerian parameters as predicted by GR (Lorimer & Kramer, 2004):

- The advance of periastron, $\dot{\omega}$ which measures the precession of the pulsar binary's orbit over time:

$$\dot{\omega} = 3T_{\odot}^{2/3} \left(\frac{P_b}{2\pi} \right)^{-5/3} \frac{1}{1 - e^2} (M_p + M_c)^{2/3}, \quad (2.20)$$

- The Einstein delay, γ that measure the delay due to gravitational redshift in the presence of companion's gravity and time dilation due to pulsar's varying speed as it moves in the elliptical orbit:

$$\gamma = T_{\odot}^{2/3} \left(\frac{P_b}{2\pi} \right)^{1/3} e \frac{M_c(M_p + 2M_c)}{(M_p + M_c)^{4/3}}, \quad (2.21)$$

- The orbital period decay, \dot{P}_b that measure the rate at which the orbital period decrease due to the emission of quadrupolar GWs (as predicted by GR):

$$\dot{P}_b = -\frac{192\pi}{5} T_{\odot}^{5/3} \left(\frac{P_b}{2\pi} \right)^{-5/3} \left[\frac{1 + (73/24)e^2 + (37/96)e^4}{(1 - e^2)^{7/2}} \right] \frac{M_p M_c}{(M_p + M_c)^{1/3}}, \quad (2.22)$$

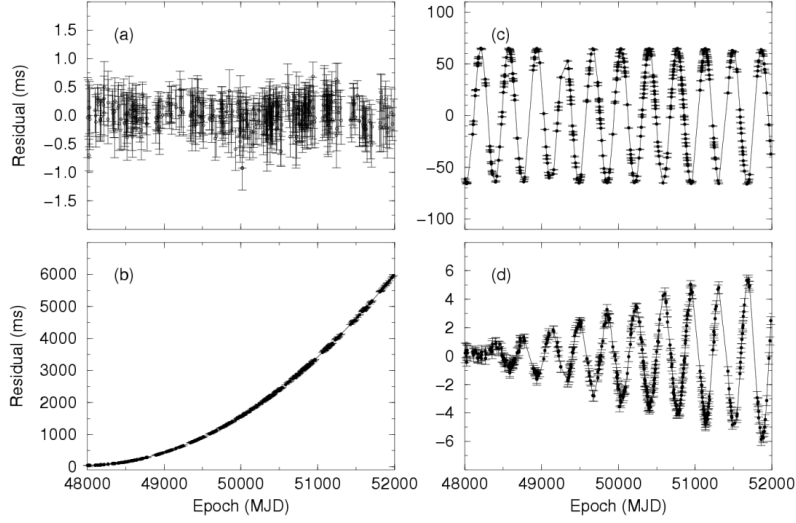


Figure 2.8: Representation of residuals as a function of time. Panel *a* shows post-fit residuals when timing solution accounts for all the trends in the data, while rest of the panels show residuals with characteristic patterns for unaccounted parameters that need to be fit in the data, such as frequency derivatives (panel *b*), position (panel *c*), and proper motion (panel *d*). Figure taken from [Lorimer & Kramer \(2012\)](#)

- The Shapiro delay is the delay in travel time of pulse as it passes through the curved space-time near companion's potential. In the DD model, the two PK parameters that quantify it are:

$$r = T_{\odot} M_c, s \equiv \sin i = T_{\odot}^{-1/3} \left(\frac{P_b}{2\pi} \right)^{-2/3} x \frac{(M_p + M_c)^{2/3}}{M_c}. \quad (2.23)$$

Since the Keplerian parameters are generally precisely known for binary pulsars, the masses are the only free parameters left in these equations, thus a measurement of two PK parameters will uniquely constrain the masses for a given theory. With the measurement of three or more PK parameters, one can test the consistency of the assumed theory of gravity. A graphical representation of this is shown in Figure 1.9 where each measurement of these PK parameters predict $M_p - M_c$ and $\cos i - M_c$ relations (referred as a mass-mass and mass-inclination diagram).

In the next section, we discuss how the TOAs from timing observations are used to fit the parameters of these binary models.

2.5.3 Residual fit and parameter estimation

Once TOAs are transformed to the proper time of the pulsar (as discussed in Section 2.5.2), they are converted in terms of the rotational phase of the pulsar, $\phi(T)$ which can be expressed as a Taylor expansion:

$$\phi(T) = \nu T + \frac{1}{2} \dot{\nu} T^2 + \frac{1}{6} \ddot{\nu} T^3 + \dots, \quad (2.24)$$

where ν , $\dot{\nu}$, and $\ddot{\nu}$ are the spin frequency and its time derivatives. Since there are integer number of pulsar rotations between two TOA measurements, the difference in the phases of the TOAs must always be an integer number. The rotational phase of each TOA is compared to the rotational phase predicted by the timing model. The residuals from this comparison are then inspected visually as a function of time and orbital period of the binary. Reduced chi-square, χ_{red}^2 resulting from the timing software is then used to estimate the quality of the timing model's fit:

$$\chi_{\text{red}}^2 = \frac{1}{N_{\text{dof}}} \sum_i \left(\frac{\phi_i(T) - \phi_i^{\text{theo}}}{\sigma_i} \right)^2, \quad (2.25)$$

where N_{dof} is the total number of degrees of freedom, ϕ_i^{theo} is the theoretical prediction of the rotational phase for i^{th} TOA, $\phi_i(T)$ is its observed phase, and σ_i is its measurement uncertainty. If $\chi_{\text{red}}^2 \sim 1$, the timing solution used is good enough to predict the TOAs within the uncertainties, the residuals will be distributed around zero in a Gaussian form in such case. If instead the $\chi_{\text{red}}^2 \gg 1$, there will be some trends in the residuals, that means the initial timing model is missing some parameter that should be fitted in the data (see Figure 2.8). Based on the pattern and timing baseline of the trend in the residuals, the user can indicate which parameters should be fit in the model. With time, as more observations get added to the timing analysis, additional trends corresponding to unaccounted time delays appear in the residual plot, the corresponding parameter then must be added to the timing model. For instance, with increased timing baseline of the fit we can include additional long-term effects visible in the pulse arrival times. Such as in order to fit for the position of the pulsar (RA and DEC), timing observations must be performed for at-least one year, similar is the case if we want to fit for proper motion of the pulsar. Timing softwares such as TEMPO or TEMPO2 are used to iteratively fit for the parameters to minimise the χ_{red}^2 and get a timing model with the least parameter uncertainties. If possible, all the data should be re-folded with this improved timing solution to further reduce the TOA uncertainties and get the best timing solution.

Upgraded GMRT survey for pulsars in globular clusters. I: Discovery of a millisecond binary pulsar in NGC 6652 (Summary)

In this chapter, I provide a brief summary of the work presented in the article titled “Upgraded GMRT survey for pulsars in globular clusters. I: Discovery of a millisecond binary pulsar in NGC 6652”, which is published in *Astronomy & Astrophysics*, Volume 664, August 2022, Article Number A54 (Gautam et al., 2022). The article is attached in its original form in Appendix A. The work is granted for non-exclusive right of re-publication.

As the lead author of this publication, I have performed the GMRT data reduction, searched all the GCs, carried out follow-up observations with GMRT, performed the timing analysis of the new discovery, determined flux and spectral index estimates of the re-detections, created radio images of the clusters (with help from R. S. Wharton), and written the manuscript.

The full author list is **T. Gautam**, A. Ridolfi, P. C. C. Freire, R. S. Wharton, Y. Gupta, S. M. Ransom, L. S. Oswald, M. Kramer, and M. E. DeCesar.

3.1 Context

Due to their dense stellar environments, Globular Clusters (GCs) host some of the most exotic MSP binaries. Such binaries with unconventional properties are valuable in providing neutron-star mass measurements and testing GR. However, due to large distances to GCs (of several kpc), we can only detect the brightest pulsar population in our search surveys (e.g. Bagchi et al. 2011; Hessels et al. 2015). Thus a large pulsar population remains undetected due to lack of telescope sensitivity. Hence whenever new observing systems with better sensitivity become available, there is a steep increase in the number of pulsar discoveries in GCs.

At low radio frequencies, the Giant Metrewave Radio Telescope (GMRT) has been one of the most sensitive telescope that plays a crucial role in discovering steep-spectrum radio pulsars (e.g. Freire et al. 2004b; Bhattacharyya et al. 2016; Joshi et al. 2009; Bhattacharyya et al. 2021). In 2017, the legacy GMRT underwent a major up-

grade (Gupta et al., 2017) and a new facility known as the upgraded GMRT (uGMRT) was inaugurated. The upgrade included more sensitive receivers that operate at lower system temperatures and cover a wider bandwidth (~ 200 MHz) that is 10 times larger than that of the legacy GMRT. Additionally, the real-time coherent de-dispersion facility was also installed as part of the upgrade. This facility is especially important for GCs at larger distances, in which case the DMs of the pulsars are high. Such clusters have not been included in previous pulsar search surveys with GMRT because the pulsations from high-DM pulsars were smeared out due to large intra-channel dispersion at low frequencies. These improvements represent a significant increase in the pulsar's detection sensitivity, which will lead to an increase in the number of discoveries.

The uGMRT, being an interferometer, also simultaneously record visibility data collected from the entire array. These data are helpful to create continuum radio images of the entire GCs to discover and localise steep spectrum radio sources that can likely be pulsars but might have been missed in the previous surveys due to a limited phase array beam size of the time-domain pulsar searches.

3.2 Aims

The instrumental improvements of the uGMRT and the sensitive low-frequency bands, which complement those of the other high frequency GC pulsar surveys, provide a leap in the search sensitivity. This motivated us to start a new GC pulsar survey with the uGMRT at low radio frequencies (< 1 GHz). In this work, we searched for radio pulsars in a group of eight southern GCs. We targeted clusters with high interaction rates per binary (γ), as discussed in Chapter 1 such clusters have environments that create exotic pulsar binaries. Additionally, we prioritised clusters with high DM to obtain an increase in the sensitivity compared to previous surveys. We also imaged these clusters to have independent measurements of the radio fluxes of known pulsars in them and to identify new steep spectrum radio sources that could be pulsars.

3.3 Methods

We observed eight target GCs with the uGMRT from April 2017 to September 2018. The observations were conducted at 650 MHz (Band 4 receivers) on Terzan 5, NGC 6441, NGC 6440, and NGC 6544, and at 400 MHz (Band 3 receivers) on NGC 6652, NGC 6539, NGC 1851, and M 30. The data was recorded with a bandwidth of 200 MHz and used the digital GWB system of the uGMRT. We performed segmented acceleration and jerk searches (discussed in Chapter 2) on the dataset and the search procedure was based upon the pulsar searching package PRESTO¹ (Ransom et al., 2002).

¹<https://www.cv.nrao.edu/~sransom/presto/>

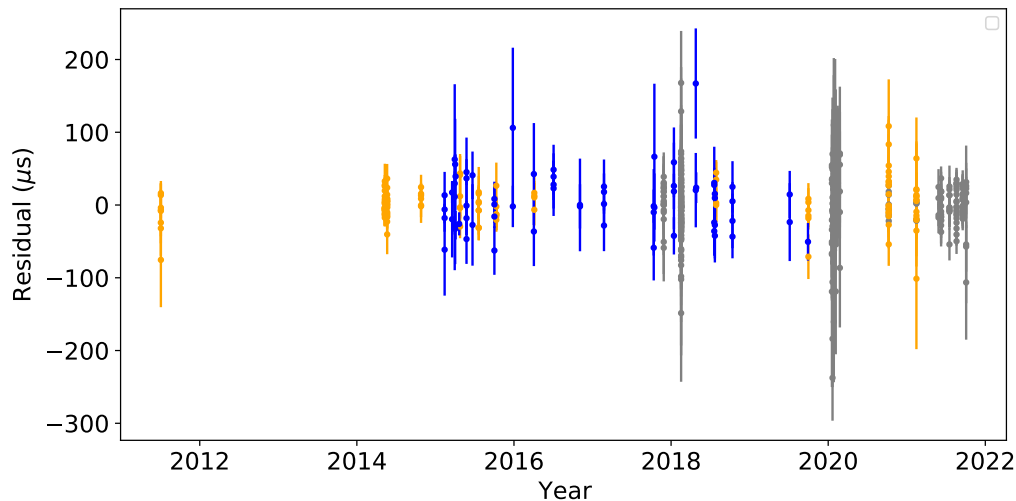


Figure 3.1: Residuals obtained with phase-connected solution of NGC 6652B. Grey points are ToAs derived from the data taken with uGMRT at frequencies below 1000 MHz, while orange points represent GBT ToAs derived from L-band data within 1000-1700 MHz, and blue points show GBT S-band data above 1700 MHz.

Using the interferometric data on these clusters continuum radio images were created. The procedure used standard tasks incorporated in CASA (McMullin et al., 2007b) to carry out flagging, calibration, and imaging on the dataset. To produce radio maps of the clusters, we used the CASA task `tclean` in the multi-term multi-frequency synthesis (MT-MFS) mode (Rau & Cornwell, 2011), which calculated the in-band spectral indices for all sources detected.

3.4 Results and conclusions

As a result of the searches, we discovered PSR J1835–3259B (or NGC 6652B), a 1.83-ms pulsar in the GC NGC 6652 at a DM of 63.48 pc cm^{-3} . This is the second pulsar in this cluster. Using the initial set of orbital parameters derived from the follow-up uGMRT observations, we could re-detect the pulsar in archival GBT L- and S-band data recorded from the year 2011 to 2020 using the Green Bank Ultimate Pulsar Processing Instrument (GUPPI) (Ransom et al., 2009) back-end. With the help of these detections we derived a phase-connected timing solution for this system (see Figure 3.1 for the post-fit residuals of all the data). This solution used a total time baseline of 10 years, including 4 years of uGMRT data (collected from follow-up timing observations of the system) and 9 years of GBT archival data. The binary has a wide orbit of 28.56 hrs and a low eccentricity of 3.5×10^{-5} . The low eccentricity indicate that the system has not interacted with other systems since recycling process.

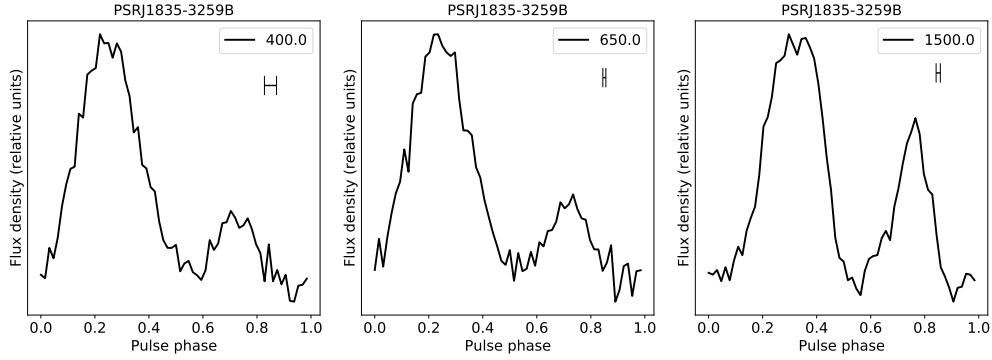


Figure 3.2: Intensity profiles as function of rotational phase of NGC 6652B obtained with Band-3 receiver of uGMRT at 400 MHz, Band-4 receiver of uGMRT at 650 MHz, and L-band receiver of GBT at 1500 MHz. Flux number on y-axis is relative. The horizontal bars show the time resolution of the system for the DM of the pulsar. For the GBT profile, this is merely the adopted bin size of the profile. The profiles were visually aligned.

Assuming a pulsar mass of $1.4M_{\odot}$ we derived a median companion mass of $0.21 M_{\odot}$, which is consistent with the P_b-M_{WD} relation given by [Tauris & Savonije \(1999a\)](#) for MSPs with helium WD companions. Figure 3.2 shows the integrated pulse profile of the pulsar i.e. the intensity vs spin phase at three different frequencies obtained from detections with the uGMRT and GBT data. The pulsar shows a clear interpulse that becomes more pronounced at higher radio frequencies.

In the case of GC pulsars, the observed orbital period derivative includes additional contributions from galactic field acceleration (a_{gal}), GC acceleration (a_{gc}), and the pulsar's composite proper motion (μ) as follows:

$$\left(\frac{\dot{P}_b}{P_b}\right)_{obs} = \left(\frac{\dot{P}_b}{P_b}\right)_{int} + \frac{a_{gc}}{c} + \frac{a_{gal}}{c} + \frac{\mu^2 d}{c}. \quad (3.1)$$

Since the new pulsar binary has a negligible gravitational wave damping due to a large orbit, we can neglect the contribution from the intrinsic orbital decay. Using the observe orbital period derivative, we obtain a GC acceleration of $3.3 \pm 6.3 \times 10^{-9} \text{ms}^{-2}$ which does not constrain the mass model of the cluster. Since similar acceleration contributions affect the observed spin period derivative, we can use the total acceleration calculated from the above expression to derive the intrinsic spin period derivative (\dot{P}_{int}) using the following expression:

$$\left(\frac{\dot{P}}{P}\right)_{int} = \left(\frac{\dot{P}}{P}\right)_{obs} - \left(\frac{\dot{P}_b}{P_b}\right)_{obs}. \quad (3.2)$$

We estimate a 1σ upper limit on $\dot{P}_{int} \leq 6.7 \times 10^{-20} \text{ss}^{-1}$. With this estimate we put a lower limit on the characteristic age of 0.43 Gyr and an upper limit on the surface magnetic field of $3.5 \times 10^8 \text{G}$. These estimates are consistent with the MSP systems that have helium WD companions ([Freire et al., 2017b](#)). Following the publication

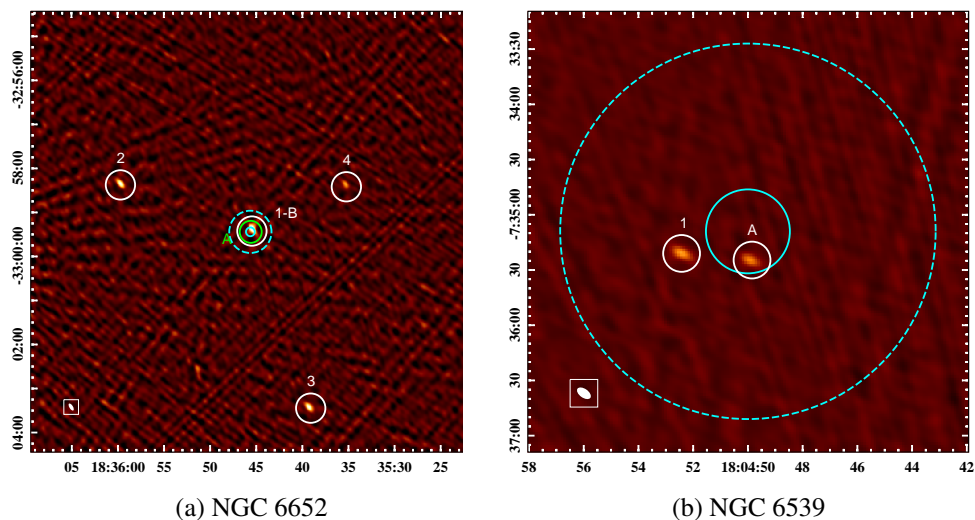


Figure 3.3: Radio images of NGC 6652 and NGC 6539 GCs observed with the uGMRT. X and Y axis represent RA (hh:mm:ss) and DEC ($^{\circ}$: $'$: $''$), respectively. The cyan-coloured circle shows the core radius, and the dashed cyan circle shows the half-mass radius.

of this work, γ -ray pulsations have also been detected from this pulsar (Zhang et al., 2022).

For the pulsars re-detected in the GCs observed in this survey, we estimated their flux densities, spectral indices, scattering timescales, and scattering indices from the pulsations detected in the time-domain data. Some of these pulsars have steeper (< -2) than expected spectral indices, despite the fact that they were discovered in the surveys with higher frequencies. By comparing the scattering timescales of several of the re-detected pulsars with the theoretical predictions given by Bhat et al. 2004, we find that the measured values are considerably smaller than predictions in most cases. This means that it was easier than expected to detect (or discover) these pulsars in the low-frequency surveys.

From the radio images of all the clusters (e.g. see Figure 3.3 for images of NGC 6652 and NGC 6539), we determined the continuum flux densities and spectral indices of all the pulsars visible in these images. Figure 3.4 shows a comparison between the flux density estimates from the radiometer equation and from the images. We highlight the pulsars in binaries or eclipsing binaries, and with large duty cycles. For some pulsars, we observe an anomalous imaging flux in the comparison. We notice that the excess flux is not caused by the interaction with the companion (which can enhance the pulsar flux for eclipsing binaries), but is instead caused by the emission at all spin phases. Thus the only reliable predictor for the excess imaging flux is a large duty cycle. A good example for this is the new discovery NGC 6652B. We identified a steep spectrum radio source (labelled 1 in Figure 3.3) that is associated with the timing position of this pulsar. This pulsar is the brightest of all the sources in the images and has radio pulsation all throughout the spin phase (as seen in Figure 3.2).

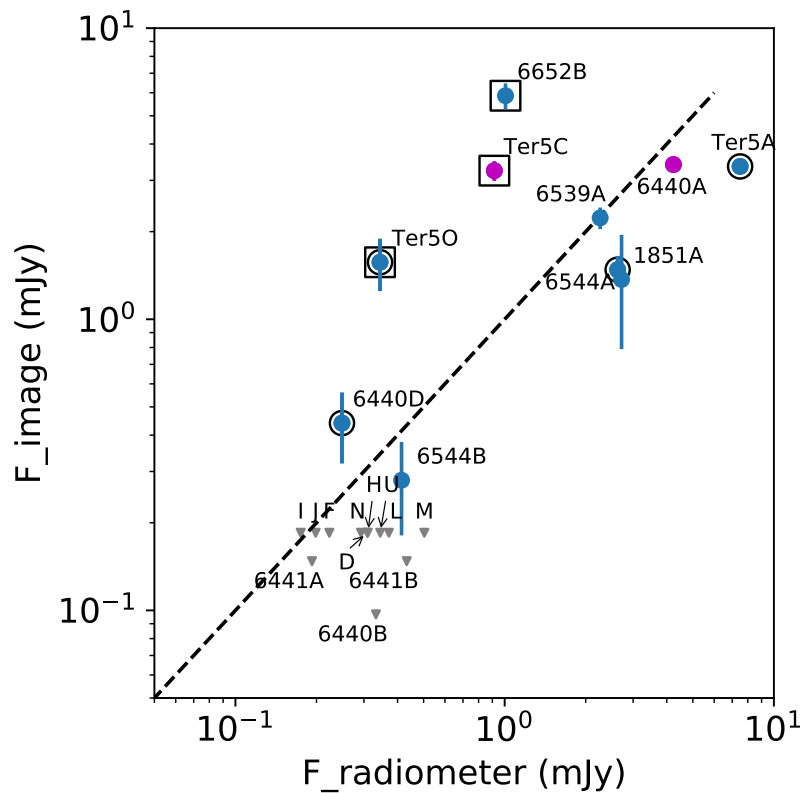


Figure 3.4: Comparison of flux density estimates from radio images and folded profiles at 400 MHz for pulsars NGC 1851A, NGC 6544A, NGC 6544B, NGC 6652B, and NGC 6539A, and at 650 MHz for the rest. Blue points represent binary systems, while magenta points represent isolated systems. Pulsars in eclipsing binary systems are marked with black circles, and pulsars with large duty cycles are marked with squares. Points in grey represent the upper limits for pulsars with no measured flux in imaging. The dashed line represents the linear expected trend. The only factor correlating with an imaging flux excess is the large duty cycle.

In the image of cluster NGC 6652, we identified three other radio sources in this cluster that are not associated with the position of the other known pulsar in this cluster. We also find one radio source each in NGC 6539, Terzan 5, NGC 6440, and NGC 6544. Cross-checking with previous surveys, we find that the three sources in NGC 6652 and one source in NGC 6539 have not been detected before (shown in Figure 3.3). These sources are candidate pulsars that we plan to follow up on in the future time-domain pulsation searches. These detections advocate the need to search for pulsars in the radio images of GCs. Since the outer parts of GCs are not generally covered in the pulsation searches, detecting steep spectrum radio sources in the images of clusters allow for identification of new pulsars. Additionally, imaging clusters can also help identify pulsars that might be too accelerated for detection through pulsar surveys. We can thus aim to get a complete characterisation of the pulsar population in GCs with the help of Interferometers such as uGMRT.

Eight new millisecond pulsars from the first MeerKAT globular cluster census (Summary)

This chapter is based on the article titled “Eight new millisecond pulsars from the first MeerKAT globular cluster census”, which is published in *Monthly Notices of the Royal Astronomical Society* (Ridolfi, A., Gautam, T. et al., 2021), Volume 504, Issue 1, June 2021, Pages 1407–1426. The article is attached in its original form in Appendix B.

I am one of the two corresponding authors of this publication. I have performed the search analysis on the GCs M62, Terzan 5, NGC6752, and NGC6624, and discovered pulsars M62G and NGC6752F. I also independently re-detected pulsars Terzan 5an and NGC6624G in my search analysis. I was involved in the timing analysis for pulsars NGC6752F, M62G, and Terzan5 an, and contributed to parts of the manuscript corresponding to these pulsars. Below, I provide a brief summary of the paper, highlighting my contribution.

The full author list is A. Ridolfi, **T. Gautam**, P. C. C. Freire, S. M. Ransom, S. J. Buchner, A. Possenti, V. Venkatraman Krishnan, M. Bailes, M. Kramer, B. W. Stappers, F. Abbate, E. D. Barr, M. Burgay, F. Camilo, A. Corongiu, A. Jameson, P. V. Padmanabh, L. Vleeschower, D. J. Champion, W. Chen, M. Geyer, A. Karastergiou, R. Karuppusamy, A. Parthasarathy, D. J. Reardon, M. Serylak, R. M. Shannon and R. Spiewak.

4.1 Context

In 2018, the South African 64-dish MeerKAT radio telescope array which is a precursor of the Square Kilometer Array - SKA1-mid (Dewdney et al., 2009) was inaugurated. Since the telescope is situated at a latitude of -30° , it is the only radio telescope, other than Parkes, to have high sensitivity to southern GC pulsars. The MeerKAT telescope has a gain of 2.8 KJy^{-1} , which is 4 times higher than that of Parkes and 1.4 times higher than that of GBT. Such significant increase in the raw sensitivity, especially for pulsars in southern GCs, motivates the need to search for new pulsars with MeerKAT.

Since similar search mode dataset can be used to search for new discoveries and perform the timing analysis for existing pulsars in the clusters, this work is a result of

the joint collaboration between two MeerKAT Large Survey Projects (LSPs), namely MeerTIME¹ (Bailes et al., 2020) under which high precision timing of pulsars is carried out, and TRAPUM² (TRANSients and PULsars with MeerKAT, Stappers & Kramer 2016) that aims to discover new pulsars and transient events.

4.2 Aims

In this work, we conduct the first census of pulsars with the MeerKAT radio telescope. For this purpose, we targeted nine southern GCs. The target selection is based on three main criteria. First, majority of the chosen clusters are either rich clusters with a large number of pulsars (to increase the number of discoveries) or core-collapse clusters such that the chance of discovering exotic pulsar binaries is enhanced (as discussed in Chapter 1). Second, each cluster hosts at-least one pulsar, so the DM of the cluster is known. This makes it easier to perform searches and data acquired for such clusters can be used to perform the timing analysis of previously known pulsars. Lastly, most of the clusters we chose are at lower declinations where previously only the Parkes telescope could be used for pulsar surveys, thus MeerKAT's four times greater sensitivity is bound to provide a significant improvement in the number of discoveries in such clusters.

4.3 Methods

The searches were carried out using PULSAR_MINER³ v1.1, which is an automated pipeline built upon the PRESTO⁴ v2.1 pulsar searching package (Ransom et al., 2002). Acceleration searches were performed on full length observations (typically 2.5 hr) and segmented acceleration searches were carried out on 60, 30, 15, and 5 min segments. As discussed in Chapter 2, such technique is useful in discovering bright pulsar binaries in compact orbits.

Following the pulsar discoveries, dedicated orbital campaigns were carried out with the MeerKAT telescope to measure and refine the binary parameters for some of the discoveries. Using the initial ephemeris, several of the new pulsars were re-detected in Parkes and GBT archival data, this allowed us to carry out a long-term timing analysis for a few of the discoveries. We used PSRCHIVE⁵ package (Hotan et al., 2004b; van Straten et al., 2012b) to do most of the data reduction of the timing observations and TEMPO⁶ was used to derive the timing solutions of pulsars.

¹<http://www.meertime.org>

²<http://www.trapum.org>

³https://github.com/alex88ridolfi/PULSAR_MINER

⁴<https://www.cv.nrao.edu/~sransom/presto/>

⁵<http://psrchive.sourceforge.net>

⁶<http://tempo.sourceforge.net>

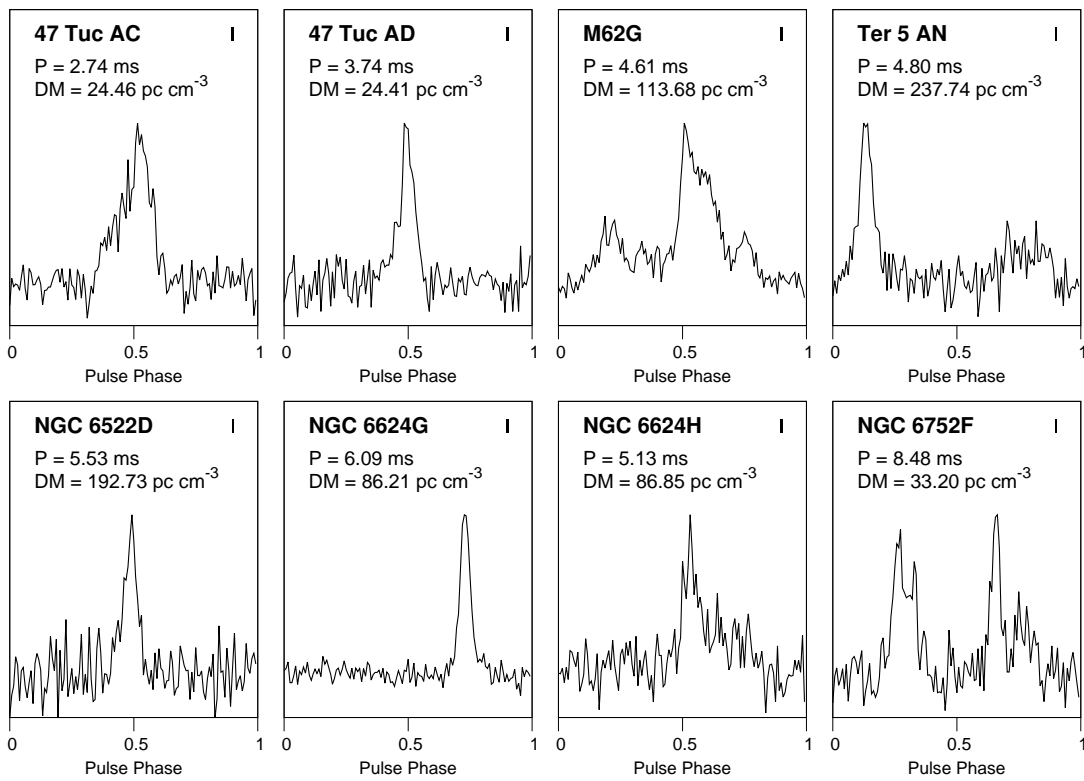


Figure 4.1: Integrated pulse profiles of the eight MSPs discovered, with their spin period and DM indicated. The horizontal section of the tiny bars on the top-right of each panel shows the sampling time of the native-resolution (sampling time of $9.57 \mu\text{s}$) MeerTime search-mode data.

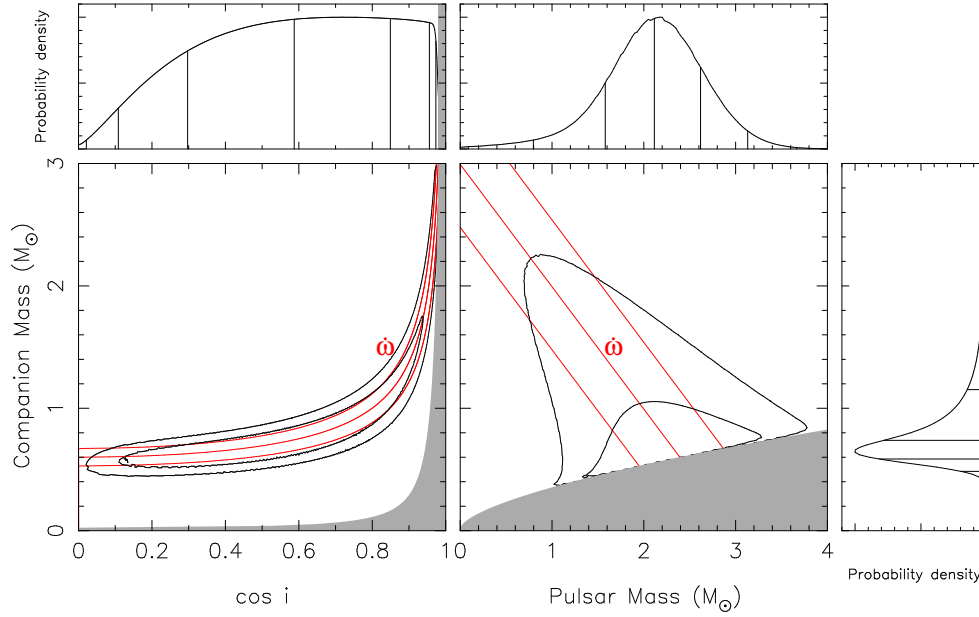


Figure 4.2: Mass-inclination and mass-mass diagram for Ter 5 an. The main square panels depict the $\cos i$ - M_c and M_c - M_p planes. The red lines depict the masses consistent with the measurement of $\dot{\omega}$ and its $\pm 1\text{-}\sigma$ uncertainties, under the assumption that this effect is dominated by the GR contribution and that GR is the correct theory of gravity. The contours include 68.3 and 95.4% of a 2-D PDF derived from the χ^2 of TEMPO fits that assumed all GR effects to be according to the masses and orbital inclination at each point. The side panels show the PDF of $\cos i$ (top left), M_p (top right) and M_c (right) derived by marginalizing the aforementioned 2-D PDFs. The estimated median pulsar mass is $2.13 M_\odot$ and median companion mass is $0.75 M_\odot$.

4.4 Results and conclusions

In this survey, we discovered eight new MSPs in six clusters, five of which are in binary systems (NGC 6624G, M62G, Terzan 5an, 47 Tucanae ac, and 47 Tucanae ad), and three are isolated pulsars (NGC 6752F, NGC 6522D, NGC 6624H). The spin periods of these pulsars are in a narrow range of 2.74–8.48ms. We carried out early follow-up of these MSPs and determined their timing solutions. Below I highlight some of the important characteristics of the systems on which I contributed to developing a timing solution:

- *Terzan 5an*: It is a 4.8-ms binary pulsar. With the help of dense orbital campaign on the system with the MeerKAT telescope, we obtain refined orbital parameters that led to re-detection of this pulsar in a large number of archival GBT observations. These detections provided a total time baseline of 16 years for this pulsar, from 2004–2020. With this long baseline, we derived a phase-connected solution for this system. The pulsar is located just outside the cluster’s core radii, as shown in Figure 4.3. It has an eccentricity of 6.5×10^{-3}

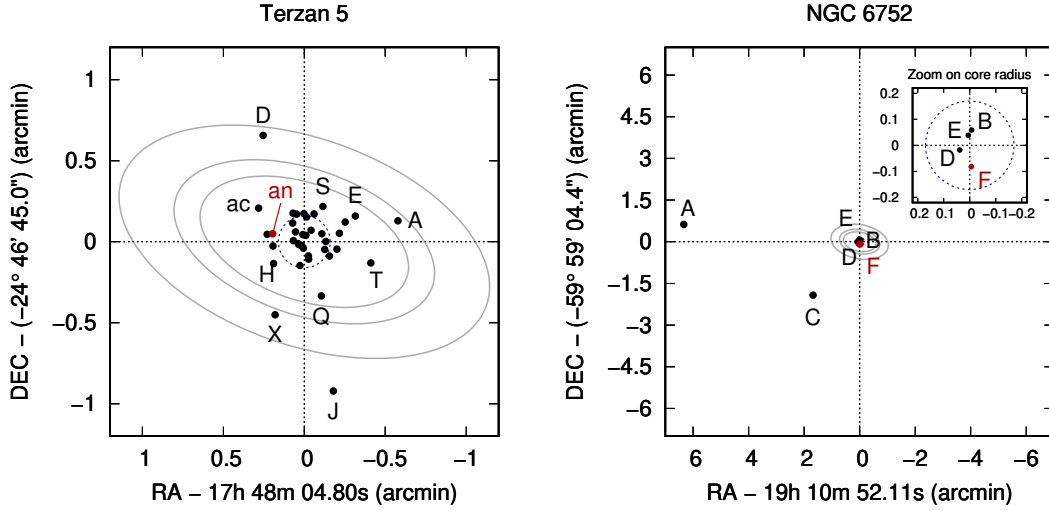


Figure 4.3: MeerTime L-band tied array beams, shown through their contours as solid grey lines at their 50 percent level of power, for one sample observation of GC Terzan 5 and NGC 6752F. We show the size of the beam for the top edge frequency (inner ellipse), center frequency (middle ellipse) and bottom edge frequency (outer ellipse). For both the clusters, we show the core radius (dashed blue line) as well as all the pulsars with a precisely determined position (black dots for the previously known pulsars, red dots for the discoveries presented here).

and an orbital period of 9.6 days. We could measure an advance of periastron $\dot{\omega} = 0.009 \pm 0.001 \text{ deg yr}^{-1}$, which constrained the total mass of the system to $2.97 \pm 0.52 M_{\odot}$. We could also put a constraint on the pulsar mass, $M_p = 2.13_{-1.32}^{+1.01} M_{\odot}$ and the companion mass, $M_c = 0.75_{-0.25}^{+1.38} M_{\odot}$ at the 2σ confidence level. Figure 4.2 shows the mass-mass plot for this pulsar. The measurement of the orbital period derivative in this system allowed us to determine the acceleration of the system in the field of GC, using this we could constrain the intrinsic spin period of the pulsar to $8.49 \pm 0.02 \times 10^{-22}$. From this we constrained the surface magnetic field, $B_s \leq 3.1 \times 10^8 \text{ G}$, and a characteristic age of the pulsar, $\tau_c \geq 3.75 \text{ Gyr}$.

- *M62G*: It is a 4.61-ms binary pulsar. The pulsar has a steep-spectrum as it was first detected in the lower half of the MeerKAT band. The orbital period of the binary is 18.48 hrs and it has a small eccentricity of 9.1×10^{-4} . We could only derive a partially phase-connected solution for this system due to its non-detection in any archival data and a small timing baseline formed from the MeerKAT observations.
- *NGC 6752F*: It is an 8.48-ms MSP. Since the pulsar was not found to change period among several observations, it is a confirmed isolated pulsar. With the same spin period, we could re-detect this pulsar in 40 earlier observations of this cluster taken with the Parkes radio telescope from 1999–2016. Even

though the pulsar appears faint in most of these detections, strong scintillation provides a few of the bright detections with Parkes. With these detections, we get a ~ 20 year (1999-2020) of total time baseline, using which we derived a phase-connected timing solution for this pulsar. The pulsar is located about 0.1 arcmin south of the nominal cluster center but within the cluster core radii (as shown in Figure 4.3). We have measured the proper motion of the pulsar $\mu_{\text{tot}} = 6.8 \pm 2.2 \text{ mas yr}^{-1}$, and considering a distance to the cluster of 4.0 kpc (Harris, 2010), we calculated the transverse velocity of the pulsar of $\sim 129 \text{ km s}^{-1}$. Considering GC proper motion estimate (by Gaia Collaboration et al. 2018), the relative transverse velocity of the pulsar lies in the range of 19-87 km s^{-1} . Although the uncertainty is large, this value is consistent with the escape velocity of the cluster of $\sim 30 \text{ km s}^{-1}$ (Colpi et al., 2003).

Of the three remaining binaries discovered in this survey, NGC 6624G is one of the rare MSP binary found in this survey. It is a 6.09-ms pulsar binary with a high eccentricity of 0.38 and an orbital period of 1.54 days. Due to its high eccentricity, we could measure an advance of periastron in the system of $0.217 \pm 0.004 \text{ deg yr}^{-1}$ using only several timing observations with MeerKAT. This lead to constraint on the total mass of the system of $2.65 \pm 0.07 M_{\odot}$, and the pulsar and companion mass of $2.10_{-1.23}^{+0.19} M_{\odot}$ and $0.53_{-0.09}^{+1.30} M_{\odot}$, respectively (at 2σ confidence). The high companion mass means that it could either be a massive white-dwarf or a neutron star. This indicates that the system is a product of a ‘‘secondary’’ exchange encounter (discussed in Chapter 1), i.e. the original companion that spun up the pulsar was ejected and replaced by the current companion. The remaining two binaries are part of the GC 47 Tucanae: 47 Tuc ac and 47 Tuc ad, these have compact orbits of 4.3 hrs and 7.6 hrs, respectively. They belong to a class of eclipsing pulsars, known as ‘spiders’.

The discoveries in this work increases the observed differences between the MSP population seen in core-collapse GCs and non core-collapse GCs. In the clusters that are not core-collapsed (47 Tucanae, M62, Terzan 5), we only discovered pulsar binaries and no isolated MSPs. This is expected as these clusters have low interaction rates per binary (as discussed in Chapter 1). Thus a pulsar binary in such clusters can evolve undisturbed post accretion phase and form an MSP binary with similar characteristics as of those found in the galactic disc. In the clusters that are core-collapsed (NGC 6522, NGC 6624, NGC 6752), three out of four new discoveries are isolated MSPs, indicating that the pulsar was separated from its original companion after accretion. This conclusion is further supported by the fact that the only binary discovered in such clusters in our survey (NGC 6624G) exhibits properties of an exchange encounter.

Relativistic effects in a mildly recycled pulsar binary: PSR J1952+2630

This chapter is based on the article titled “Relativistic effects in a mildly recycled pulsar binary: PSR J1952+2630”, which is submitted to *Astronomy & Astrophysics* on 08 August, 2022. The content of the submitted manuscript remains unchanged, but it is formatted to fit the template of the thesis.

As the lead author of this publication, I have carried out the timing observations with the Arecibo radio telescope and performed all the data analysis presented in this work except the RVM fit discussed in Section 5.4.1 (performed by M. Kramer) and the part on constraints on Damour-Esposito-Farèse (DEF) gravity discussed in Section 5.6.2 (carried out by A. Batrakov).

The full author list is **T. Gautam**, P. C. C. Freire, A. Batrakov, M. Kramer, C. C. Miao, E. Parent, and W. W. Zhu.

Contents

5.1	Abstract	70
5.2	Introduction	70
5.3	Observations and data reduction	73
5.3.1	Observations	73
5.3.2	Data Reduction	74
5.3.3	Timing analysis and binary models	75
5.4	Results	77
5.4.1	Polarisation Calibration	77
5.4.2	Timing Solution	79
5.4.3	Astrometry	80
5.4.4	Kinematic Effects on the spin and orbital periods	80
5.4.5	Advance of periastron	82
5.4.6	Shapiro delay	82
5.4.7	Orbital Period Derivative	84
5.5	Mass measurements	84
5.6	PSR J1952+2630 as a gravitational laboratory	87
5.6.1	Simulations	88
5.6.2	Constraints on DEF gravity	91
5.6.3	Additional orbital parameters	95

5.1 Abstract

We report the results of timing observations of PSR J1952+2630, a 20.7 ms pulsar in orbit with a massive white-dwarf companion. We perform six months of timing observations with the Arecibo radio telescope in 2020, and used data from FAST from 2021. Together with previously published data, this represents a total timing baseline of 11 years since its discovery in 2010. We present, for the first time, a polarimetric profile of the pulsar and determined its rotation measure (RM), $-145.79 \pm 0.15 \text{ rad m}^{-2}$. With the increased timing baseline, we get improved estimates for astrometric, spin, and binary parameters for this system. In particular, we obtain an order of magnitude improvement on the proper motion, and, for the first time, the detection of three post-Keplerian parameters in this system: the advance of periastron $\dot{\omega}$, orbital decay \dot{P}_b , and the Shapiro delay (measured in the form of h_3 parameter). With the detection of these relativistic effects, we constrain the pulsar mass to $1.20^{+0.28}_{-0.29} M_{\odot}$ and its companion mass to $0.97^{+0.16}_{-0.13} M_{\odot}$. The current value of \dot{P}_b is consistent with the GR expectation for the masses obtained using $\dot{\omega}$ and h_3 , the excess ($4.2^{+70.2}_{-73.1} \text{ fs s}^{-1}$) represents a limit on the emission of dipolar gravitational waves (GWs) from this system. This results in a limit on the difference in effective scalar couplings for the pulsar and companion (predicted by scalar-tensor theories of gravity, STTs) of $|\alpha_p - \alpha_c| < 4.8 \times 10^{-3}$ (68% C.L.), which does not yield a competitive test for STTs. However, our simulations of future timing campaigns of this system, based on the timing precision we have achieved with FAST, show that by the year 2032 the precision of \dot{P}_b and $\dot{\omega}$ will allow for much more precise masses and much tighter constraints on the orbital decay contribution from dipolar GWs, resulting in $|\alpha_p - \alpha_c| < 1.3 \times 10^{-3}$ (68% C.L.). For comparison, from PSR J1738+0333 and PSR J2222-0137 we obtain $|\alpha_p - \alpha_c| < 1.9 \times 10^{-3}$ and $< 3.3 \times 10^{-3}$, respectively. We also present the constraints this system will put by 2032 on $\{\alpha_0, \beta_0\}$ parameters of DEF gravity and found them to be comparable to those by PSR J1738+0333. Unlike PSR J1738+0333, PSR J1952+2630 will not be limited in its mass measurement and has the potential to place even more restrictive limits on DEF gravity in future. Further improvements to this test will likely be limited by uncertainties in the kinematic contributions to \dot{P}_b , due to lack of precise distance measurements.

5.2 Introduction

Millisecond pulsars (MSPs), especially those located in binary systems, provide us with a unique opportunity to gain insights in fundamental physics, not only for tests

of gravity theories (Berti et al., 2015), but also for the study of the unknown state of matter (and its equation of state, or EOS) in the centres of neutron stars (NSs), a fundamental problem in the study of the strong nuclear force (Özel & Freire, 2016). These studies are done using a technique known as “pulsar timing” - a method of modelling the physical effects affecting the times of arrival of their radio pulsations (ToAs, Taylor 1992), these are the spin and its variations, astrometry, and interstellar effects. This technique is especially powerful for MSPs because of their stable rotation and the high ToA precision. Furthermore, because of their evolution, most MSPs are members of binary systems. In these cases, their timing provides, in addition, exquisite measurements of their orbital motion. The detection of relativistic effects in the orbital motion provided the first confirmation of the existence of gravitational waves (Taylor & Weisberg, 1989) and nowadays allows a wide range of studies of gravity theories (e.g., Freire et al. 2012; Antoniadis et al. 2013; Anderson et al. 2019; Voisin et al. 2020; Kramer et al. 2021; Guo et al. 2021; Zhao et al. 2022) and constraints on the EOS (e.g., Özel & Freire 2016; Fonseca et al. 2021).

Thus, it is of high scientific importance to discover and time pulsar systems where orbital relativistic effects can be precisely measured. This was one of the main goals of the Pulsar Arecibo L-band Feed Array (PALFA) survey (Cordes et al., 2006; Lazarus et al., 2015) that was carried out from 2004 to 2020 using the 7-beam receiver of the 305-m Arecibo radio telescope located near Arecibo, Puerto Rico, USA. This scanned the Galactic longitudes accessible to that telescope (especially $25^\circ < \ell < 77^\circ$) for low Galactic latitudes ($|b| < 5^\circ$). The large telescope sensitivity made it possible for the survey to achieve high sensitivity with relatively short pointings. This made it sensitive to compact systems with very high accelerations, as shown by the discovery of three compact double neutron star systems (DNSs): PSR J1906+0746, the youngest DNS (Lorimer et al., 2006; van Leeuwen et al., 2015), PSR J1913+1102, the first merging, strongly asymmetric DNS (Lazarus et al., 2016; Ferdman et al., 2020), and PSR J1946+2052, the most compact DNS known in our Galaxy, with an orbital period of only 1h 53m (Stovall et al., 2018). Overall, the survey discovered a total of 207 pulsars¹, with 38 of them being MSPs, defined here somewhat arbitrarily as having $P < 25$ ms.

In this survey, a computationally intensive analysis was carried out with the help of distributed computing project, Einstein@Home (Knispel et al., 2010; Allen et al., 2013) to search for isolated or binary pulsars with orbits longer than 11 minutes. PSR J1952+2630 was the first binary pulsar system discovered with this pipeline (Knispel et al., 2011). With a spin period of 20.7 ms, it is one of the aforementioned MSPs. It has a relatively short 9.4-hr orbit with a massive white dwarf (WD) companion, the orbital eccentricity was already known to be small ($e \leq 1.7 \times 10^{-3}$). Assuming a pulsar mass (M_p) of $1.4M_\odot$, they obtained a minimum M_c of $0.95 M_\odot$. The system’s low eccentricity excludes the possibility of the companion being another NS, it is very likely a massive white dwarf (WD) star. The relatively large spin period

¹<http://www.naic.edu/~palfa/newpulsars/>

(compared to most MSPs) is commonly found among other similar intermediate-mass binary pulsar systems (IMBPs; Camilo et al. 2001); the difference is that the orbit is unusually short for such systems.

Unlike the commonly accepted formation scenario of low-mass binary pulsars (LMBPs) from low mass X-ray binaries (LMXB), where a NS spins up or is “recycled” during the accretion of matter from its evolved low-mass companion star (Alpar et al., 1982; Radhakrishnan & Srinivasan, 1982; Bhattacharya & van den Heuvel, 1991; Verbunt, 1993), intermediate-mass X-ray binaries (IMXBs) are thought to undergo a completely different mechanism of recycling. Their hydrogen-rich massive donor stars (2-10 M_{\odot}) do not provide sufficient time for recycling the NS through accretion. A possible formation mechanism of IMBPs in short orbits with a Carbon-Oxygen (CO) WD companion is discussed by Tauris et al. (2011, 2012). It involves a common envelope phase (CE) that circularises the binary and reduces its orbital period, followed by Case BB Roche Lobe Overflow (RLO) phase, which continues long enough to recycle the NS to its small rotational periods.

To develop a phase connected timing solution and thus derive precise spin, astrometric and orbital parameters, Lazarus et al. (2014) carried out further timing observations of PSR J1952+2630 with the Arecibo telescope. With their added baseline, they confirmed the high mass of the companion $> 0.93M_{\odot}$ and measured a small but significant orbital eccentricity, $e \sim 4.1 \times 10^{-5}$. The measured spin-down implies that the characteristic age of the system is 77 Myr, younger than most recycled pulsars, and especially when compared with other IMBPs. To investigate the nature of the WD’s progenitor, they simulated evolutionary models using Langer stellar evolution code (Tauris et al., 2011, 2012) and predicted two solutions for the companion’s progenitor’s nature: a) a 1.17 M_{\odot} ONeMg WD created from a 2.2 M_{\odot} He star, and b) a 1.02 M_{\odot} CO WD formed from a 1.9 M_{\odot} He star. Since the orbital solution at that time did not allow a measurement of the PK parameters, there was no measurement of the component masses. Hence, neither of these scenarios could be confirmed. However, they suggested that continued timing would eventually lead to a measurement of three PK parameters, $\dot{\omega}$, \dot{P}_b and possibly the orthometric amplitude of the Shapiro delay h_3 (Freire & Wex, 2010), indicating that additional timing could result in precise mass measurements, and a clarification of the real nature of this system.

This work presents the results from the radio timing of this pulsar, which make use of an additional six months of timing observations performed with the Arecibo radio telescope in 2020 and two additional observations carried out with the Five hundred meter aperture spherical radio telescope (FAST) (Nan et al., 2011; Qian et al., 2020) in 2021. With an 11 year long timing baseline, we can now measure, as predicted, the proper motion of the system, and $\dot{\omega}$, \dot{P}_b , and h_3 .

The structure of the paper is as follows. Section 5.3 gives details on all observations and how the resulting data were analysed. In Section 5.4, we present the main results of our polarimetry and timing analysis, with a discussion of the main new parameters. In Section 5.5, we discuss the masses for the components, and on

the constraints from the orbital decay measurement of this system. In Section 5.6, we discuss the potential of PSR J1952+2630 as a gravitational laboratory. Here we simulate future timing in order to determine the level of precision we might achieve in our mass measurements and tests of gravity theories with this system, in particular limits on dipolar GW emission, a prediction of alternative theories of gravity. Using our improved proper motion measurement, we can now calculate the uncertainty on the kinematic contributions to \dot{P}_b , which provides the ultimate limit on the precision of intrinsic \dot{P}_b . In this section, we also discuss the constraints this system will put on DEF gravity. We list our conclusions in Section 5.7.

5.3 Observations and data reduction

5.3.1 Observations

After the discovery of PSR J1952+2630 in 2010, the binary was regularly observed from July 2010-September 2011 as part of the PALFA survey with the 7-beam ALFA receiver of the Arecibo telescope. These observations were taken with the Mock Spectrometers² (see details in Table 5.1). Afterwards, Lazarus et al. (2014) carried out dedicated timing observations of this system using the ‘L-wide’ receiver of the Arecibo telescope, which has a larger bandwidth, see details in Table 5.2. In the beginning, three 3 h observations were performed and subsequently, 1 h observations were carried out every month for the next 11 months. These observations were taken in Stokes I, i.e., only total intensity was recorded with integrated polarisation information. These data were later dedispersed and folded at the spin period of the pulsar (according to the best available ephemeris), producing an archive of pulse profiles (henceforth "archive") with 512 profile bins, as described by Lazarus et al. (2014).

From February 2020 to July 2020, we performed another timing campaign on this system with Arecibo using again the ‘L-wide’ receiver. This campaign made use of the new more sensitive wide-bandwidth back-end system, the Puerto Rico Ultimate Pulsar Processing Instrument, (PUPPI³). Importantly, and unlike the Mock spectrometer, this back-end can use coherent dedispersion to completely remove any signal smearing caused by the dispersion; this is especially important for PSR J1952+2630 given its high DM of $\sim 315.3 \text{ cm}^{-3} \text{ pc}$; furthermore the back-end allows for the recording of Full Stokes data. We observed this system for a total of 24 h: 12 observations of 2 h each. These data were folded by PUPPI using the best available ephemeris for the pulsar in 2048-bin profiles, producing pulse profile archives immediately. This greatly reduces the amount of data to be recorded, thus allowing for the full-Stokes data to be recorded as well.

Additionally, to follow up on this system with better sensitivity, regular timing ob-

²<https://www.naic.edu/~astro/mock.shtml>

³<http://outreach.naic.edu/ao/scientist-user-portal/astronomy/puppi-observing-and-support-guide>

Table 5.1: Observation Details

Observatory	Receiver	Backend	Epoch (MJD)	Date	Coherently de-dispersed
Arecibo	L-wide	Mock spectrometers	55407-55816	July 2010 - Sept 2011	no
Arecibo	L-wide	Mock spectrometers	55889-56218	Nov 2011 - Oct 2012	no
Arecibo	L-wide	PUPPI	58881-59053	Feb - July 2020	yes
FAST	19-beam	ROACH	59507, 59554	Oct - Dec 2021	no

Table 5.2: Data parameters.

Epoch (MJD)	Central frequency (MHz)	Bandwidth (MHz)	Number of channels	Sampling time (μ s)	Number of profile bins	Typical length (min)
55407-55816	1300.168	172.032	512	65.47	512	5-10
	1450.168	172.032	512	65.47	512	5-10
55889-56218	1185.958	172.032	2048	83.33	512	60
	1358.042	172.032	2048	83.33	512	60
	1530.042	172.032	2048	83.33	512	60
	1702.042	172.032	2048	83.33	512	60
58881-59053	1380.781	800	512	0.64	2048	120
59507, 59554	1250.0	500	256	49.152	256	15

servations are being performed with the FAST radio telescope. In this work, we have included the data from the latest two FAST observations in 2021. This data was taken with the ROACH backend in full stokes. High resolution search-mode data with 4096 channels is recorded originally but for our purpose of determining achievable timing precision with FAST for simulations, we have only used its downsampled version (see details in Table 5.2).

5.3.2 Data Reduction

To remove the temporal and spectral radio interference (RFI) created by terrestrial signals in the PUPPI archives, we used CoastGuard’s (Lazarus et al., 2016) RFI-removal script, `clean.py`. We made use of two of its algorithms: `rcvrstd` and `surgical`, the former zero-weights the bad frequency channels which have no receiver response, and the latter removes the folded profiles affected by RFI. This is done by first fitting individual sub-integration profiles with the integrated pulse profile, and then removing the sub-integrations that were outliers in the resulting residual profiles (see Lazarus et al. 2016 for more details on the algorithms).

To achieve consistent results and improve post-fit residuals, we re-analyzed the archives obtained from the Mock spectrometers by Lazarus et al. (2014) in a way consistent with our analysis of the PUPPI archives. In this analysis we used the standard routines in the PSRCHIVE pulsar package (Hotan et al., 2004a; van Straten et al.,

2012a). Each of the initial PSRFITS format files were first cleaned of RFI using PSRCHIVE’s interactive cleaning library `pazi`.

For each Mock spectrometer archive, the pulse profiles were added in time and frequency (i.e., “scrunched”) using PSRCHIVE’s routine `pam`. This resulted in much smaller archives with two sub-banded profiles per epoch (of typically 5-10 min) at frequencies of 1300 MHz and 1400 MHz for earlier data (2010-2011), and four sub-banded profiles (of typically 15 minutes) at frequencies mentioned in Table 5.1 for the data taken in 2011-2012. For the latest PUPPI data, we scrunched the 11 min archive files into eight sub-bands and a single 11-min sub-integration using `pam`; and for the FAST data, we created 30 sub-integrations for every 2 minute file.

For the Mock archives, we then phase aligned the profiles at their corresponding central frequencies using an improved ephemeris and added them together using `psradd`. We created two standard profiles at frequencies 1300 MHz and 1530 MHz. Both the standard profiles were then fully scrunched in time and frequency and fitted with several von Mises functions using `paas` to create two analytic templates. Of these, the 1300 MHz template was cross-correlated to create ToAs using `pat` for 1300 MHz, 1185 MHz, and 1358 MHz, while the 1530 MHz template was used for 1450 MHz, 1530 MHz and 1702 MHz archive files. Since all the above-mentioned data is broadband, pulse profile variations across the observed frequencies can increase the post-fit uncertainties, thus we used standard templates with multiple frequencies.

For PUPPI data, to determine the best scrunching scheme, we created ToAs using both the frequency integrated and multi-frequency (sub-banded) templates (created using the FDM algorithm of `pat`). Additionally, if there exist sharp features in the polarization profile, the timing precision can improve significantly, thus both the templates were created with and without integrated polarization (using matrix template matching, `pat`’s MTM algorithm). We then compared the resulting fit of the timing model using four templates mentioned above. The sub-banded template with integrated polarisation had the least post-fit root-mean-square (RMS) and parameter uncertainties, thus this was used to create the final ToAs. All the PUPPI observations were added together to create a single multi-frequency template with eight sub-bands, which was then cross-correlated with the similarly sub-banded data using `pat`. We get a typical ToA residual uncertainty of $20 \mu\text{s}$.

To create ToAs from two FAST observations, we integrated the observations to create a single archive with integrated frequency channels, and used `paas` to create a noise-less standard template.

5.3.3 Timing analysis and binary models

The timing analysis was done using the TEMPO⁴ pulsar timing software. In this analysis, the ToAs are first converted to a terrestrial time standard, UTC(NIST) which is a version of Coordinated Universal Time maintained by the US National Institute

⁴<http://tempo.sourceforge.net>

of Standards and Technology. The converted time is then translated to the solar system barycentric (SSB) time using the solar system ephemeris, DE436 (maintained by NASA’s Jet Propulsion Laboratory, JPL, [Folkner & Park 2016](#)). The program then minimizes the difference between the ToAs and the arrival times predicted by the model ephemeris, known as the timing residuals, by varying the timing parameters. These timing parameters are presented in Barycentric Dynamical Time (TDB) units. As a starting point, we used the ephemeris from [Lazarus et al. \(2014\)](#).

The descriptions of the orbit we used are based on the “DD” model of [Damour & Deruelle \(1986\)](#). This provides a quasi-Keplerian description of the orbit, with small perturbations, which in this case are assumed to be relativistic, that are detectable in the timing. These are quantified in a theory-independent way by a set of “Post-Keplerian” (PK) parameters. Such a description was found to work for many alternative theories of gravity ([Damour & Taylor, 1992b](#)). One of these PK parameters, measurable in binary systems with eccentric orbits (where we can measure the longitude of periastron, ω), is the rate of advance of periastron, $\dot{\omega}$. A second PK parameter, the orbital decay caused by the emission of gravitational waves (GW), \dot{P}_b , can be measured in binaries with short orbits due to their higher rates of GW damping. Additionally, in binaries with a favourable combination of high orbital inclination (i), large companion mass (M_c) and good timing precision, we can measure an additional relativistic effect known as Shapiro delay ([Shapiro, 1964](#)), which is a retardation of the arrival times of the radio pulses caused by the spacetime curvature near its companion; this is quantified by two PK parameters that yield direct estimates of M_c and $\sin i$ in a wide range of gravity theories. This effect is especially pronounced near superior conjunction, when the companion is closest to our line of sight to the pulsar. A final PK parameter, the Einstein delay, is not measurable for systems with small orbital eccentricities like PSR J1952+2630, so we won’t discuss it here.

The measurement of PK parameters is important: with two such parameters in the same system can generally constrain the pulsar mass (M_p) and M_c . To do this, we must be confident that the observed orbital effects are purely relativistic, and then assume a particular gravity theory, like general relativity (GR), to calculate the masses from the PK parameters. Since each EOS for dense matter predicts a maximum NS mass, the measurement of a large NS mass can rule out many acceptable EOSs ([Antoniadis et al., 2013](#); [Fonseca et al., 2021](#)). Measurement of three or more PK parameters in the same system provides a test of the self-consistency for any gravity theories than can link the two masses and Keplerian orbital parameters to the PK parameters (see [Kramer et al. 2021](#) for the ultimate example of this).

In this work, the system’s orbital parameters are measured using two different binary models based on the DD description: the DDGR and the ELL1H+ models. Apart from the five Keplerian parameters (projection of semi-major axis x , eccentricity e , orbital period P_b , and both the epoch (T_0) and longitude of periastron (ω) at T_0), the DDGR model fits directly for M_c and total mass (M_T) by assuming that all relativistic effects detectable in the TOAs are as predicted by GR for that pair of masses.

The ELL1H+ model is, like the DD model, theory-independent. We use it to investigate which relativistic parameters are detectable in the timing, and also to provide a more accurate description of some of the orbital parameters. For binaries with low eccentricity, there is a strong correlation in the Keplerian parameters T_0 and ω used in the DD model, this leads to high uncertainties in their measurements. To avoid this strong correlation, the ELL1 model (Lange et al., 2001) take as reference the epoch of ascending node, T_{asc} rather than T_0 ; this quantity is well-defined even for circular orbits. Additionally, it fits for the Laplace-Lagrange parameters $\varepsilon_1 = e \sin \omega$ and $\varepsilon_2 = e \cos \omega$ instead of e and ω . Furthermore, by using T_{asc} as the reference for measuring P_{B} , we also avoid its strong correlation with the measurement of $\dot{\omega}$. Due to this lack of correlation we could measure T_{asc} with a precision of ~ 20100 times better than T_0 , and get an improvement on P_{b} measurement by a factor of 3200.

Another strong correlation - especially a low orbital inclinations - is seen in the Shapiro delay implementation in the DD and ELL1 models, where it is quantified by two PK parameters, range ($r \equiv T_{\odot} M_{\text{c}}$, where $T_{\odot} \equiv \mathcal{G} \mathcal{M}_{\odot}^{\text{N}} / c^3 = 4.9254909476412669 \dots \mu\text{s}$ is an exact quantity, see Prša et al. 2016) and shape ($s \equiv \sin i$). The ELL1H model, an extension of the ELL1 model, prevents this correlation by re-parameterizing the Shapiro delay with two different PK parameters, the orthometric amplitude (h_3) and orthometric ratio (ζ) (Freire & Wex, 2010). In our analysis, we used ELL1H+ model (implemented in TEMPO by N. Wex for the analysis of the PSR J2222–0137 data, see Guo et al. 2021) which makes use of the exact expression of Eq. (31) of Freire & Wex (2010), and includes an extra term of the order of $x e^2$ in the Römer delay expansion (as shown in Eq. 1 of Zhu et al. 2019).

5.4 Results

5.4.1 Polarisation Calibration

Being one of the most polarized radio sources, analysis of polarization in pulsars help understand their radio beam's geometry and its emission mechanism (Radhakrishnan & Cooke, 1969). We performed the polarisation calibration on the PUPPI data-set of this pulsar using noise-diode scans that were carried out for ~ 92 seconds at the beginning of each observation. Each calibration scan and its corresponding target observation was manually cleaned with `pazi`, and then calibration was applied on each epoch using `pac` routine of PSRCHIVE. To determine the best fit rotation measure (RM), we first created an integrated profile by adding all the observations in time using `psradd` and `pam`, and then fit for RM in this high SNR profile (that had 512 channels and 2048 sample bins) using `rmfit` routine. This routine runs trials with various RM values to find the best fit by optimising the fraction of linear polarisation in the profile. We deduced an RM of $-145.79 \pm 0.15 \text{ rad m}^{-2}$ using this method. Figure 5.1 shows the calibrated polarisation profile of the pulsar with both linear and circularly polarised components. To correct for the Faraday rotation, all the observations were

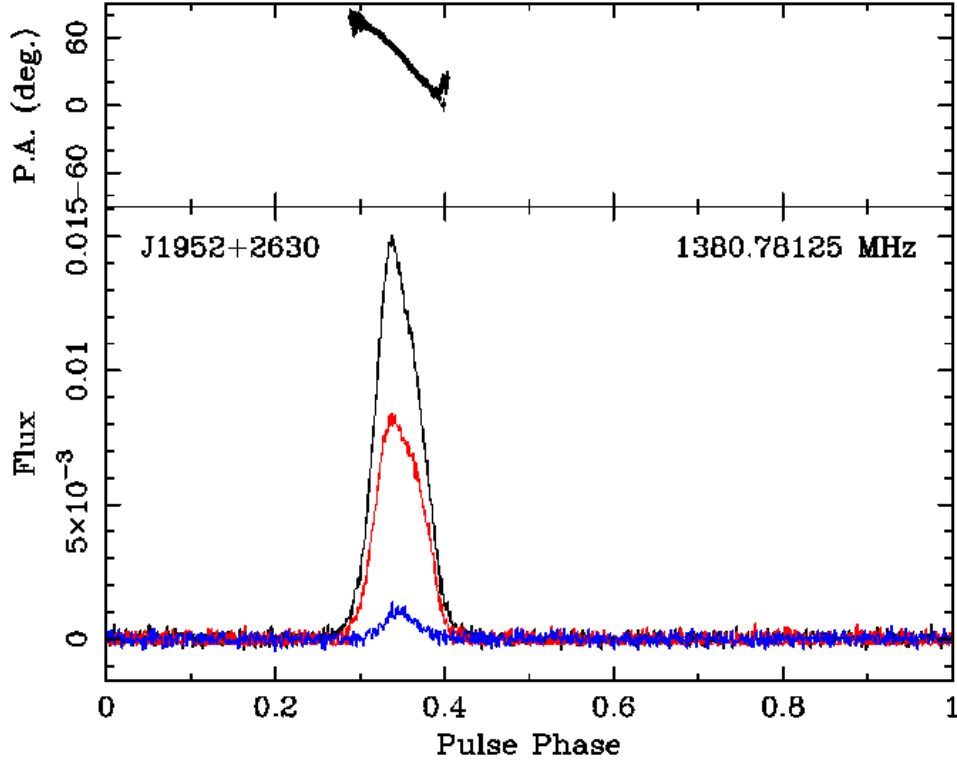


Figure 5.1: The total intensity is shown in black, while linear and circular polarisation is shown in red and blue, respectively, as a function of longitude. Top panel shows the polarisation angle (PA) swing across the rotational phase.

then de-rotated using the above-mentioned RM value to create archive files with better profile resolution. These archives were then used to create a polarised template which was used to decide the best ToA scheme.

The polarisation position angle (PA) sweep across the rotational phase of the pulse can allow us to predict the geometry of the pulsar's beam. According to [Radhakrishnan & Cooke \(1969\)](#), the PA sweep creates an S-shaped curve along with the pulse phase, that can be modelled using the Rotating Vector Model (RVM), given by:

$$\tan(\psi - \psi_0) = \frac{\sin(\alpha) \sin(\phi - \phi_0)}{\sin(\alpha + \beta) \cos(\alpha) - \cos(\alpha + \beta) \sin(\alpha) \cos(\phi - \phi_0)}, \quad (5.1)$$

where ψ is the observed PA of the pulsar beam as it sweeps across our line of sight, α is the projection of magnetic inclination angle, and β is the impact parameter or closest approach of the magnetic axis to the line of sight. ψ_0 and α_0 represent their respective values at a fiducial reference plane. We did an MCMC fit of this model on the PA swing of its profile, which provided constraint on α of $19.5^{+8.4}_{-8.5}$ deg and viewing angle, ζ (defined as $\alpha + \beta$) of $27.5^{+11.6}_{-11.8}$ deg. ζ represents the value for

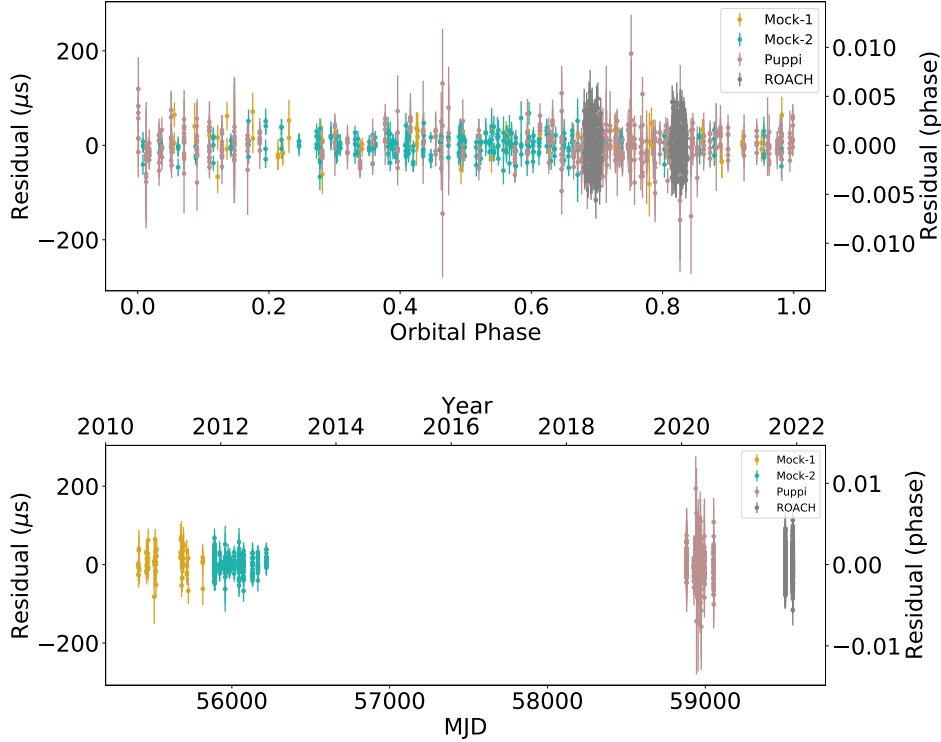


Figure 5.2: Post-fit residuals of ToAs from Arecibo data (with Mock and PUPPI backends) and FAST data (with ROACH backend) as a function of year (below) and orbital phase of pulsar (top). Different colors show residuals for different backends. Points labelled Mock-1 and Mock-2 show different set of timing observations with Mock spectrometers (see Table 5.1).

inclination angle (i), if the spin vector of the pulsar is aligned with the orbital angular momentum vector. However, since the duty cycle of the pulsar is small ($\sim 7\%$) in this case, there exist a large covariance between α and ζ , because of which we can not constrain the i and β well. The minimum inclination of the binary calculated from its mass function and the allowed maximum M_c of $1.48 M_\odot$ is 28 deg, while the inclination derived from timing analysis is 71.72 deg. Thus, the system's inclination was not well constrained from the above-mentioned RVM fit.

5.4.2 Timing Solution

The timing solution of PSR J1952+2630 resulting from the fit using both ELL1H+ and DDGR binary models is shown in Table 5.3. Compared to the previous work on this pulsar, we have extended the timing baseline by more than 9 years and increased the number of ToAs by a factor of 3.5. Fitting a total 1475 ToAs, we get a weighted RMS of $\sim 24.2 \mu\text{s}$ with a reduced χ^2 of 1.01 using the DDGR model. The uncertainties of ToAs from different backends were individually scaled such that reduced- χ^2 of each data-set is 1. Figure 5.2 shows the post-fit residuals of ToAs as a function of the epoch

of observation and the orbital phase of the binary.

5.4.3 Astrometry

Relative to the values published by [Lazarus et al. \(2014\)](#), we achieved an order of magnitude improvement in the Right Ascension (RA) and a factor of 2 improvement in the Declination (DEC). We could also refine the proper motion of the system in RA by an order of magnitude and measure the proper motion in DEC for the first time. The total proper motion of the system is $5.89(23)$ mas yr⁻¹. The distance prediction from the DM of this pulsar is 9.56 kpc from the NE2001 electron density model ([Cordes & Lazio, 2002](#)) and 10.03 kpc from the YMW16 model ([Yao et al., 2017](#)). Considering the NE2001 value with a 20% error, we constrain the transverse velocity of the system to $267(53)$ km s⁻¹.

5.4.4 Kinematic Effects on the spin and orbital periods

The observed arrival times of the pulses are affected by the relative accelerations between the pulsar binary and the Solar System. These include: a) the Shklovskii effect ([Shklovskii, 1970](#)), an apparent centrifugal acceleration and b) the line-of-sight acceleration acting on pulsar due to the difference in the Galactic acceleration on the pulsar and the Solar System.

The Shklovskii effect, a_{shk} is simply $\mu^2 d$, where μ is the total proper motion, and d is the distance to the pulsar.

The galactic acceleration includes contributions from both the Galactic rotation and vertical accelerations to the disk of the galaxy ($a_{\text{gal}} = a_{\text{gal,disc}} + a_{\text{gal,rot}}$), these are given by [Damour & Taylor \(1991\)](#), [Nice & Taylor \(1995\)](#), [Lazaridis et al. \(2009\)](#) as follows:

$$a_{\text{gal,rot}} = -\frac{\Theta_0^2}{R_0 c} \left(\cos l + \frac{\beta}{\beta^2 + \sin^2 l} \right) \cos b, \quad (5.2)$$

$$a_{\text{gal,disc}} = -\left(2.27 z_{\text{kpc}} + 3.68(1 - e^{-4.3 z_{\text{kpc}}})\right) |\sin b|, \quad (5.3)$$

where $\beta \equiv (d/R_0) \cos b - \cos l$ and $z_{\text{kpc}} \equiv |d \sin b|$ in kpc. R_0 is the distance to the galactic center, taken as $8.275(34)$ kpc and Θ_0 is the galactic rotation velocity that is taken to be $240.5(41)$ km s⁻¹ ([Gravity Collaboration et al., 2021](#); [Guo et al., 2021](#)). PSR J1952+2630 is close to the Galactic disk ($b = -0.376$ deg); this means that $a_{\text{gal,rot}}$ will be by far the dominant component, with the vertical acceleration $a_{\text{gal,disc}}$ being almost perpendicular to the line of sight.

The observed spin period derivative of the pulsar (\dot{P}_{obs}) include these acceleration contributions as additional Doppler shift effect:

$$\frac{\dot{P}_{\text{obs}}}{P} = \frac{\dot{P}_{\text{int}}}{P} + \frac{a_{\text{shk}} + a_{\text{gal}}}{c}, \quad (5.4)$$

Table 5.3: Timing solution of PSR J1952+2630 with DDGR and ELL1H+ models. Values in brackets are 1σ uncertainties, and values without uncertainties are derived from the corresponding binary model. Values in square brackets are not fit but derived assuming GR. ^a Assumed value derived from *sini* parameter in the DDGR solution. ^b Assuming NE2001 distance and uncertainty

PSR J1952+2630		
Binary Model	DDGR	ELL1H+
Observation and data reduction parameters		
Reference epoch (MJD)	55407.0	55407.0
Span of timing data (MJD)	55407.146 - 59554.385	55407.146 - 59554.385
Solar system ephemeris	DE436	DE436
Terrestrial time standard	UTC(NIST)	UTC(NIST)
Time units	TDB	TDB
Number of ToAs	1475	1475
Weighted residual RMS (μ s)	24.201	24.198
χ^2	1466.43	1466.10
Reduced χ^2	1.0065	1.0069
Astrometric and spin parameters		
Right Ascension, α (J2000)	19:52:36.840244(57)	19:52:36.8402341(58)
Declination, δ (J2000)	26:30:28.0840(11)	26:30:28.0843(11)
Proper motion in α , μ_α (mas yr ⁻¹)	-2.58(17)	-2.57(17)
Proper motion in δ , μ_δ (mas yr ⁻¹)	-5.29(24)	-5.38(25)
Spin frequency, ν (Hz)	48.2337753923167(47)	48.2337753923193(49)
Spin frequency derivative, $\dot{\nu}$ (10 ⁻¹⁵ Hz s ⁻¹)	-9.93790(9)	-9.93791(9)
Dispersion Measure, DM (pc cm ⁻³)	315.3168(17)	315.3166(17)
Binary parameters		
Orbital period, P_b (days)	0.39188050(21)	0.391878632876(93)
Projected semi-major axis, x_p (lt-s)	2.7981770(18)	2.7981793(49)
Orbital eccentricity, e	4.226(99) $\times 10^{-5}$...
Longitude of periastron, ω (deg)	289.56(1.64)	...
Epoch of periastron, T_0 (MJD)	55407.6178(18)	...
Epoch of ascending node, T_{asc} (MJD)	...	55407.3025831(1)
ϵ_1	...	-0.000039(2)
ϵ_2	...	0.000013(1)
Advance of periastron, $\dot{\omega}$ (deg/yr)	[1.5998941]	1.80(26)
Shapiro shape, $s = \sin i$	[0.9495500]	...
Orbital period derivative, \dot{P}_b (10 ⁻¹² s s ⁻¹)	[-0.0943648]	-0.096(46)
Orthometric ratio, ζ	...	0.722852 ^a
Orthometric amplitude, h_3 , (μ s)	...	1.49(61)
Total binary mass, M_T (M_\odot)	2.19(38)	[2.61 ^{+0.58} _{-0.54}]
Companion mass, M_c (M_\odot)	0.95(12)	...
Derived parameters		
Galactic longitude, l (deg)	63.254	63.254
Galactic latitude, b (deg)	-0.376	-0.376
DM derived distance from NE2001 model (kpc)	9.5647	9.5647
DM derived distance from YMW16 model (kpc)	10.03	10.03
Galactic height, z (kpc)	-0.063(12)	-0.063(12)
Magnitude of total proper motion, μ (mas yr ⁻¹)	5.89(23)	5.96(24)
Transverse velocity ^b , v_T (km s ⁻¹)	267(53)	270(54)
Spin period, P (s)	0.020732360091375(2)	0.020732360091373(2)
1st Spin period derivative, \dot{P} (10 ⁻¹⁸ s s ⁻¹)	4.27162(4)	4.27162(4)
Intrinsic spin period derivative, \dot{P} (10 ⁻¹⁸)	4.270(3)	4.270(3)
Characteristic age, τ_c (Myr)	76.91	76.92
Surface magnetic field, B_s (10 ⁹ G)	9.49	9.49
Spin-down energy, \dot{E} (10 ³³ erg s ⁻¹)	18.92	18.92
Kinematic contribution to \dot{P}_b (10 ⁻¹⁵ s s ⁻¹)	1.8 ^{+5.1} _{-3.4}	2.5 ^{+5.2} _{-3.5}
Mass function, $f(M_p)$ (M_\odot)	0.15317962(43)	0.15318146(81)
Pulsar mass, M_p (M_\odot)	1.24(26)	...
Einstein delay, γ (s)	2×10^{-7}	...
Relativistic orbital deformation, δ_θ (10 ⁻⁶)	4.674351	...
Relativistic orbital deformation, δ_r (10 ⁻⁶)	4.4226831	...

where \dot{P}_{int} is the intrinsic spin period derivative of the pulsar. Considering the astrometric parameters from the fit with DDGR model, we estimated the cumulative kinematic contribution in the spin period derivative, $P \left(\frac{a_{\text{shk}} + a_{\text{gal}}}{c} \right)$ as $1.14 \times 10^{-21} \text{ s s}^{-1}$. This is much smaller than \dot{P}_{obs} , so when we subtract it from the latter value we get \dot{P}_{int} of the system of $4.2704(32) \times 10^{-18} \text{ s s}^{-1}$, which is very similar to the uncorrected value. With this value, we estimated the surface magnetic field, B_s of $9.49 \times 10^9 \text{ G}$, characteristic age, τ_c of 76.91 Myr, and the rate of loss of rotational energy \dot{E} of $18.92 \times 10^{33} \text{ erg s}^{-1}$ for this pulsar (all estimated using the relations in Lorimer & Kramer 2012). The detailed study of the spin evolution of this system presented by Lazarus et al. (2014) therefore remains valid.

Similar accelerations from proper motion (Shklovskii effect), galactic disc, and galactic rotation also contribute in the observed orbital period derivative measurement:

$$\dot{P}_{\text{b,obs}} = \dot{P}_{\text{b,int}} + \dot{P}_{\text{b,shk}} + \dot{P}_{\text{b,gal}}. \quad (5.5)$$

Figure 5.3 shows these contributions as a function of the distance to the pulsar. If we assume a 20% error in the NE2001 model's distance prediction, we get a maximum uncertainty of 1.91 kpc in its measurement. This uncertainty in distance implies an uncertainty in the estimation these kinematic contributions in \dot{P}_b , $1.8_{-3.4}^{+5.1} \text{ fs s}^{-1}$ (see dashed lines in figure 5.3). Since the curves are relatively flat, any improvement in the distance measurement in future will not significantly change this constraint. As we will discuss in detail in Section 5.6, this contribution will also present the final constraint in the $\dot{P}_{\text{b,obs}}$ precision in future.

5.4.5 Advance of periastron

Using the ELL1H+ binary model, we obtain a rate of change of the longitude of periastron of the binary ($\dot{\omega}$) of $1.80(26) \text{ deg yr}^{-1}$. Assuming GR as a theory of gravity, this PK parameter depends on the Keplerian parameters and the total mass of the system (M_T) as follows:

$$\dot{\omega} = 3T_{\odot}^{2/3} \left(\frac{P_b}{2\pi} \right)^{-5/3} \frac{1}{1-e^2} M_T^{2/3}, \quad (5.6)$$

where masses are expressed in solar units. From this relation, we obtain $M_T = 2.61_{-0.54}^{+0.58} M_{\odot}$. This value is consistent with DDGR model's fit for M_T of 2.19 (38) M_{\odot} .

5.4.6 Shapiro delay

In our ELL1H+ timing solution, we could also fit for the Shapiro delay. Assuming GR, the orthometric parameters relate to M_c and i as follows:

$$\zeta = \frac{\sin i}{1 + \sqrt{1 - \sin^2 i}}, \quad (5.7)$$

$$h_3 = T_{\odot} M_c \zeta^3. \quad (5.8)$$

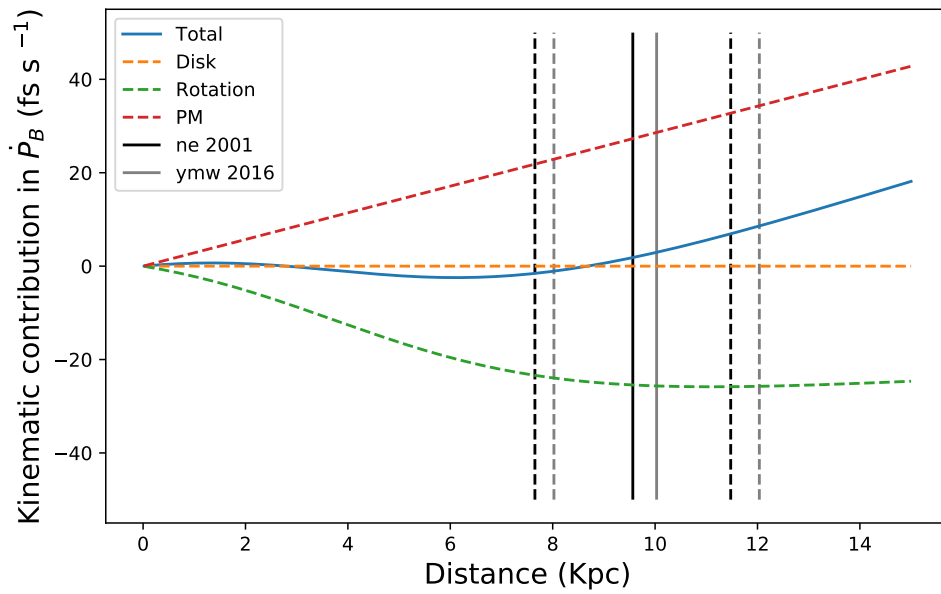


Figure 5.3: Total kinematic contribution to the observed orbital decay, $\dot{P}_{b,\text{gal}}$ is shown as a function of distance to the pulsar in the blue curve. Red, orange, and green curves represent individual contributions due to galactic disc acceleration, galactic rotation (or differential) acceleration, and proper motion of the pulsar, respectively, with errors in R_0 and θ_0 providing negligible contributions. The vertical black line marks the DM distance from the NE2001 model with 20% uncertainty in the model shown as dashed black lines. Grey lines show an estimate of the DM distance from the YMW16 model. The maximum uncertainty in total kinematic contribution is 5.1 fs s^{-1} .

Due to a weak Shapiro delay signature in the data, we fixed the ζ parameter to a constant value, 0.722, that corresponds to the best inclination from the DDGR model ($i = 71.72$ deg), and only fit for h_3 parameter. From this, we get a 2σ detection of h_3 parameter, $1.49(61) \mu\text{s}$.

5.4.7 Orbital Period Derivative

The third PK parameter measured in this system is the orbital period derivative, \dot{P}_b . The ELL1H+ binary model's fit give a $\dot{P}_{b,\text{obs}}$ of $-96(46) \text{ fs s}^{-1}$. Removing the Kinematic contributions (discussed in Section 5.4.4) from $\dot{P}_{b,\text{obs}}$, we get $\dot{P}_{b,\text{int}} = -97_{-51}^{+49} \text{ fs s}^{-1}$.

The DDGR model does not directly fit for the orbital decay and instead fits for M_c and M_T using all relativistic effects in a consistent way. From the best-fit masses, it assumes that the orbital decay is due to quadrupolar GW emission predicted by GR, $\dot{P}_{b,\text{GR}}$ as follows:

$$\dot{P}_{b,\text{GR}} = -\frac{192\pi}{5} T_\odot^{5/3} \left(\frac{P_b}{2\pi}\right)^{-5/3} f(e) \frac{M_p M_c}{(M_p + M_c)^{1/3}}, \quad (5.9)$$

where

$$f(e) = \frac{1 + \frac{73}{24}e^2 + \frac{37}{96}e^4}{(1 - e^2)^{7/2}}. \quad (5.10)$$

Using this model, the derived $\dot{P}_{b,\text{GR}}$ is $-94(27) \text{ fs s}^{-1}$.

5.5 Mass measurements

With the DDGR binary model, we obtain directly M_T of $2.19(38) M_\odot$ and M_c of $0.95(12) M_\odot$, this gives M_p of $1.24(26) M_\odot$. Using these values along with the mass function of this system, we get an orbital inclination of 71.72 deg.

We now check whether the three PK measurements from ELL1H+ solution are, according to GR, consistent with these two masses and with each other. The mass constraints that result from $\dot{\omega}$, \dot{P}_b , and h_3 and their $1-\sigma$ uncertainties can be represented on the pulsar and companion mass plane ($M_p - M_c$) and on the companion mass and inclination planes ($\cos i - M_c$), see Figure 5.4. Since the curve of h_3 parameter cross $\dot{\omega}$ and \dot{P}_b curves relatively steeply in these plots, it is this measurement of Shapiro delay that gives us the stronger constraints on the individual masses and inclination. All PK parameters agree in a particular region of the maps, which coincides with the masses derived from the DDGR solution (given by the black crosses). This means that GR provides a satisfactory and self-consistent description of all the relativistic effects in this system. However, given the low precision of the measurement of all PK parameters, this test of GR is not particularly constraining.

In order to better constrain the masses and avoid any correlations that might be present between the parameters, we created a self-consistent χ^2 map on a 2-D grid of

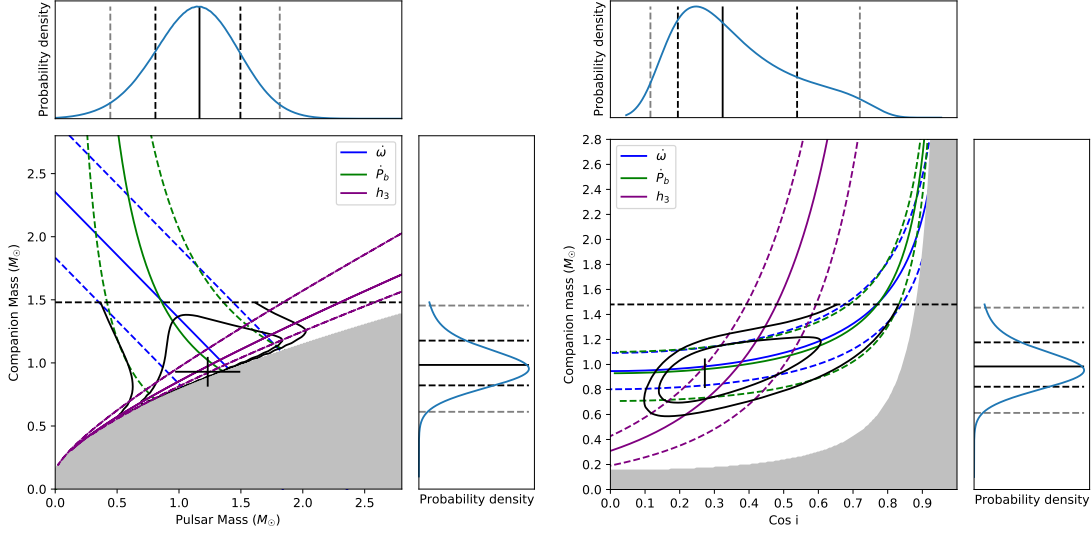


Figure 5.4: Constraints on the M_c , M_p , and $\cos i$ derived from the measurement of three relativistic PK parameters are shown. Black dashed line shows the maximum M_c constraint of $1.48 M_\odot$. Colored dashed lines depict the 1σ uncertainty on the measurements. Black contours show the likelihood or 2-D PDFs at 68 % (inner) and 95 % (outer) confidence from the χ^2 maps on $\cos i - M_c$ and $M_p - M_c$ grids, derived from the DDGR fit. The corner plots represent the marginalised 1-D PDFs of each of these measurements and vertical lines on these mark the median, 1σ , and 2σ estimates. The black crosses indicate the best masses from the DDGR solution and the best inclination derived from the mass function using those masses.

$\cos i$ and M_c . For each point in the grid, we estimated M_T using the mass function, and keep it and M_c fixed in a DDGR solution, using TEMPO to fit for all other parameters. The resulting χ^2 values for each point on the $\cos i - M_c$ grid are then recorded and converted to 2-D probability distribution function (PDF), following Splaver et al. (2002):

$$p(\cos i, M_c) \propto e^{\frac{\chi_{\min}^2 - \chi^2}{2}}, \quad (5.11)$$

where χ_{\min}^2 is the minimum χ^2 value in the whole grid. A corresponding 2-D PDF grid for the $M_p - M_c$ plane is also derived using the mass function. Importantly, we do not sample values of M_c above $1.5M_\odot$, because that is the upper mass limit for a rigidly rotating WD.

The solid black lines in Figure 5.4 show contours that include 68% and 95% of the total probability in these 2-D PDFs. To determine the resulting constraints for M_p , M_c , and $\cos i$, these 2-D PDFs are marginalised and converted to 1-D PDFs. Following this, we get the median value and 1σ uncertainty on M_p of $1.20^{+0.28}_{-0.29} M_\odot$, M_c of $0.97^{+0.16}_{-0.13} M_\odot$, and inclination of $70.55^{+6.15}_{-11.02}$ deg; these are, again, consistent with the solution from DDGR model.

Using the DDGR model, we can fit for contributions to the variation of the orbital

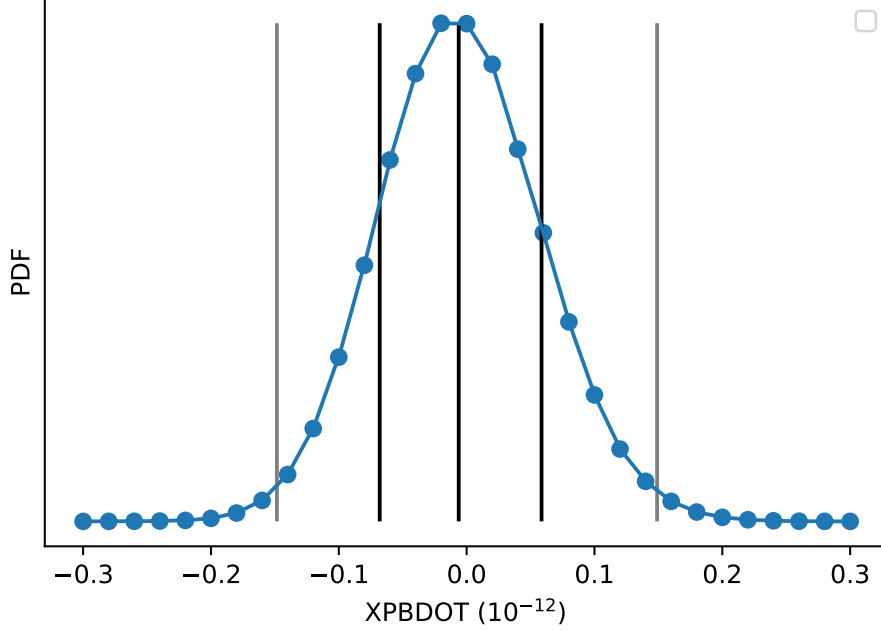


Figure 5.5: 1D Probability density function of $\dot{P}_{b,x}$ derived from the best fit χ^2 of DDGR solution. Blue dots represent the grid points over which the TEMPOfit was done and blue curve shows the interpolated function. Black vertical lines represent the median and 1σ values and gray lines show the 2σ constraint. We get 1σ estimate of $\dot{P}_{b,x}$ as $-6_{-68}^{+58} \times \text{fs s}^{-1}$.

period other than the GR orbital decay, using the XPBDOT parameter, which quantifies $\dot{P}_{b,x} = \dot{P}_{b,\text{obs}} - \dot{P}_{b,\text{GR}}$. For this parameter, we obtain a null result, implying that the kinematic contributions are certainly smaller than our current measurement uncertainties: Indeed, the predicted kinematic contribution in \dot{P}_b of $1.8_{-3.4}^{+5.1} \text{fs s}^{-1}$ is an order of magnitude smaller than the measured uncertainty in \dot{P}_b of 46fs s^{-1} (from the ELL1H+ model).

In order to estimate $\dot{P}_{b,x}$ precisely, we mapped a 3-D grid of M_c , $\cos i$, and $\dot{P}_{b,x}$. We determined the best-fit χ^2 over each point in this grid using the DDGR binary model and then estimated the marginalised probability distribution for $\dot{P}_{b,x}$ (as shown in Figure 5.5). We get a median value with 1σ uncertainty of $-6_{-68}^{+58} \text{fs s}^{-1}$ on $\dot{P}_{b,x}$, implying a negligible value symmetric around zero. In future, when more precise mass measurements are available, this method will be useful for robust estimates of $\dot{P}_{b,x}$ and its uncertainty. As we will see now, this will be important for constraining alternative gravity theories.

5.6 PSR J1952+2630 as a gravitational laboratory

Apart from quadrupole GW emission implied by GR, other alternative theories of gravity can also have observable implications. One common signature predicted by several of these theories but not by GR is the emission of dipolar GWs (Eardley, 1975; Damour & Esposito-Farèse, 1996). Such emission, if present, will be observable as an additional contribution to the orbital decay.

Thus for any measurement of orbital decay, we can subtract the contributions from kinematic effects and the quadrupole GW emission to estimate the remaining contribution (also known as the ‘excess’ orbital decay, $\dot{P}_{b,xs}$), which is an upper limit on the dipolar GW contribution.

From the current timing of PSR J1952+2630, we estimated this quantity by subtracting the predicted kinematic contributions from the $\dot{P}_{b,x}$ estimate (calculated from the 3-D χ^2 map discussed in Section 5.5), which does not include the quadrupolar GW contribution, as follows:

$$\dot{P}_{b,xs} = \dot{P}_{b,x} - \dot{P}_{b,gal} - \dot{P}_{b,shk}. \quad (5.12)$$

We get $\dot{P}_{b,xs}$ of $4.2^{+70.2}_{-73.1} \text{fs s}^{-1}$, this value being negligible means that no dipolar GW emission is detectable and that GR passes the test posed by the measured PK parameters for PSR J1952+2630.

Scalar-tensor theories (STT) of gravity predict the emission of scalar waves in asymmetric systems that have significantly different gravitational self-energies, such as NS-WD binaries. Because of this, the scalar field in the theory will couple differently with both objects in the binary, which acquire a scalar “charge” (or effective coupling strength) given by α_p and α_c . This is important because the dipolar GW emission depends on the difference between α_p and α_c .

We can use the above prediction of $\dot{P}_{b,xs}$ to put a constraint on the difference in effective scalar couplings of the pulsar and its companion as predicted by STTs. Following equation 4 of Cognard et al. (2017), assuming a negligible eccentricity in this system, it can be calculated as follows:

$$|\alpha_p - \alpha_c|^2 < \delta \dot{P}_b^D \left(\frac{P_b}{4\pi^2} \right) \left(\frac{1}{T_\odot M_c} \right) \frac{(q+1)}{q}, \quad (5.13)$$

where $q(=M_p/M_c)$ is the mass ratio and $\delta \dot{P}_b^D$ is the orbital decay from dipolar GW emission. Considering the 1σ uncertainty in $\dot{P}_{b,xs}$ as $\delta \dot{P}_b^D$, we obtain a limit on $|\alpha_p - \alpha_c| < 4.8 \times 10^{-3}$. This is not competitive with current tight constraints for other systems, estimated similarly from 1σ error in $\dot{P}_{b,xs}$: for PSR J1738+0333 $|\alpha_p - \alpha_c| < 1.90 \times 10^{-3}$ (Freire et al., 2012) and for PSR J2222–0137 $|\alpha_p - \alpha_c| < 3.3 \times 10^{-3}$ (Guo et al., 2021). However, as we will see now, the situation will improve significantly with continued timing.

5.6.1 Simulations

To determine the potential of this system in measuring precise component masses and testing GR, we simulated continued timing up to the year 2039. We first assumed a conservative scheme of orbital campaigns, once every two years till 2027 and then once every three years till 2039 with the FAST radio telescope. Our simulations are based on the timing precision of our current FAST data, which are about twice as precise as our Arecibo data, thus we considered an RMS of $11 \mu\text{s}$ for our simulations. At 48 ToAs every hour, every 9-hour orbit results in 432 simulated ToAs. Each of these orbital campaigns covers the short orbit fully, thus including always the important orbital phases near superior conjunction, where the Shapiro delay is more pronounced. The masses and orbital parameters assumed in the simulation correspond to the best current DDGR fit.

We created fake ToAs with TEMP02 software for this purpose. Adding these fake ToAs to our data yields about a factor of 6 improvement in the measurement of $\dot{\omega}$, and a factor of 4 improvement in the h_3 parameter. This implies that we will get highly precise mass estimates and a compelling test of GR with this system in future. Figure 5.6 plots the estimates of PK parameters from this simulation on the measurements of component masses and inclination in the $M_p - M_c$ and $\cos i - M_c$ diagrams.

Even though the detection significance of all the PK parameters will improve by at least a factor of 4σ , the improvement in the orbital decay measurement will be much faster (since its uncertainty proportional to $T^{-5/2}$, where T is the timing baseline). However, that improvement will soon halt because of the limited precision of the kinematic contributions to the observed \dot{P}_b (due to the lack of precise distance estimates) of 5.1 fs s^{-1} . Assuming an orbital campaign is performed with FAST every year, the simulated precision will reach this limit in the year 2025, as shown in Figure 5.7, requiring only 3 more orbital campaigns with FAST. This precise \dot{P}_b will, together with the improved measurement of h_3 , yield a very significant improvement in the component masses, under the assumption of GR.

From then onwards, the quality of the GR test with this system will continue improving because of the improvements from $\dot{\omega}$ and h_3 . This will take longer because for these parameters the uncertainties decrease at a slower rate, $T^{-3/2}$ and $T^{-1/2}$ respectively. The GR test stops improving when the uncertainty on $\dot{\omega}$ yields a value of M_T that is more precise than that derived from \dot{P}_b (which is limited by the uncertainty in the estimate of the kinematic contribution to \dot{P}_b). This will only happen after 2032 if four campaigns every year are carried out, and after the year 2036 if an yearly campaign is carried out (see Figure 5.7). If more sparse observations are assumed, with observations once every two years till 2027 and once every three years, we will reach this limit only by 2039.

Since the measurement of orbital decay will be limited in future, we can use this limit to put constrain on the difference of effective scalar coupling strengths. The dipolar GW emission contribution to \dot{P}_b must be smaller than this precision. Thus assuming $\delta\dot{P}_b^D$ of 5.1×10^{-15} , we get $|\alpha_p - \alpha_c| < 1.30 \times 10^{-3}$ (68% C.L.), marginally better than

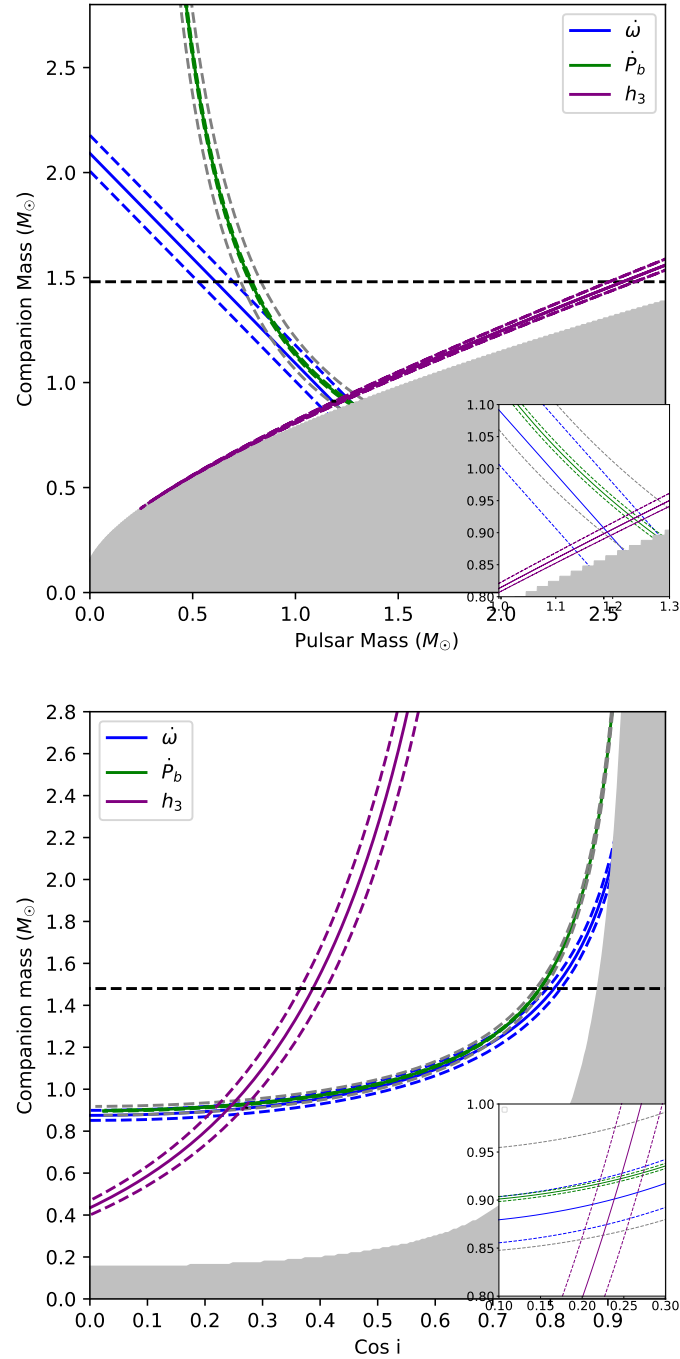


Figure 5.6: Representation of measurements of three PK parameters in future assuming timing campaigns with FAST until year 2039, which is when the mass uncertainties reach kinematic precision. Dashed lines show 1σ uncertainties, gray dashed lines represent the kinematic limit on \dot{P}_b measurement coming from distance uncertainty.

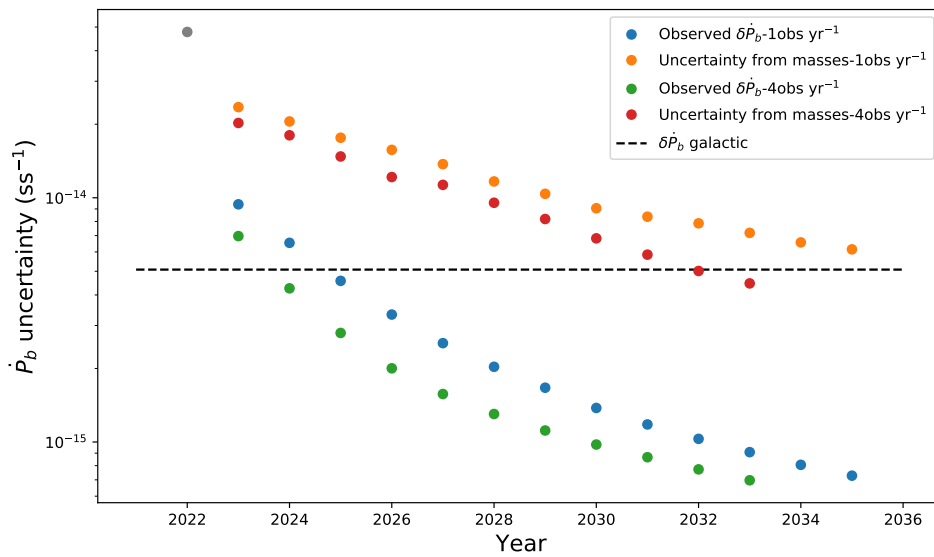


Figure 5.7: \dot{P}_b uncertainty variation with simulated orbital campaigns are shown for campaigns once (blue) and four (green) times every year. The precision of \dot{P}_b predicted by GR as $\dot{\omega}$ uncertainty decreases over the years is shown with orange and red points. The grey point shows the present value, and the dashed line represents the limit due to kinematic uncertainty.

the current limit from PSR J1738+0333, but independent of WD atmosphere models. Therefore, PSR J1952+2630 has the potential to provide very stringent radiative tests of certain alternative gravity theories in the near future.

The analysis based on the measured excess rate of the orbital decay $\dot{P}_{b,x}$ is straightforward but has some disadvantages. In a particularly selected SST the effective coupling strength of a compact object can strongly depend on the mass, especially for a neutron star (α_p) due to the scalarization effect (Damour & Esposito-Farese, 1993). Thus, the importance of the derived limit on the difference of effective scalar coupling strengths $|\alpha_p - \alpha_c|$ significantly depends on the masses of a binary system. The large uncertainty in the mass measurements for PSR J1952+2630 forces us to investigate the variation in α_p value with a mass. We now discuss the fully consistent analysis in more detail.

5.6.2 Constraints on DEF gravity

In this section we would like to concentrate on the particular class of STT – Damour-Esposito-Farèse (DEF) gravity (Damour & Esposito-Farese, 1993; Damour & Esposito-Farèse, 1996). DEF gravity is a mass-less scalar-tensor gravity theory with one long-ranged scalar field φ non-minimally coupled to the curvature scalar. The theory is described by two arbitrary parameters $\{\alpha_0, \beta_0\}$ which enter the coupling function that determines how the scalar field φ couples to matter. DEF gravity fully recovers GR when both the parameters approach zero: $\alpha_0 = 0, \beta_0 = 0$. The theory predicts the well investigated phenomenon – spontaneous scalarization of neutron stars. It is a fully nonperturbative effect (Damour & Esposito-Farese, 1993) resulting in the strong growth of the scalar field in the interiors of the compact object while the scalar field in the exterior space-time stays negligible. Compact objects in DEF gravity obtain special gravitational form-factors (i.e. effective coupling strengths α_p, α_c , their derivatives with respect to the scalar field, etc.) which enter the observable variables (PK parameters) and can be directly calculated from the structure equations. A very important prediction of DEF gravity which can be tested with binary pulsars is the dipolar contribution to the rate of the orbital period change \dot{P}_b^D . For the present paper we use DEF gravity as a powerful framework with two arbitrary parameters $\{\alpha_0, \beta_0\}$ to perform radiative tests of gravity.

In this work we apply the DDSTG timing model to place limits on DEF gravity (Batra et al. in prep). It is a novel approach superior to the traditional method based on the measured PK parameters (PK method). The DDSTG model is based on the aforementioned DD model, and is developed specifically to constrain scalar-tensor gravity theories. It is implemented in the TEMPO software and utilizes internally the theoretical predictions for PK parameters in DEF gravity. PK parameters in DEF gravity depend on two masses of the pulsar and the companion, their gravitational form-factors and the choice of the equation of state (EOS). The model is supplied with pre-calculated grids of NSs gravitational form-factors for a set of different EOS. For a WD companion we assume a weak field approximation $\alpha_c = \alpha_0$ which is sufficient

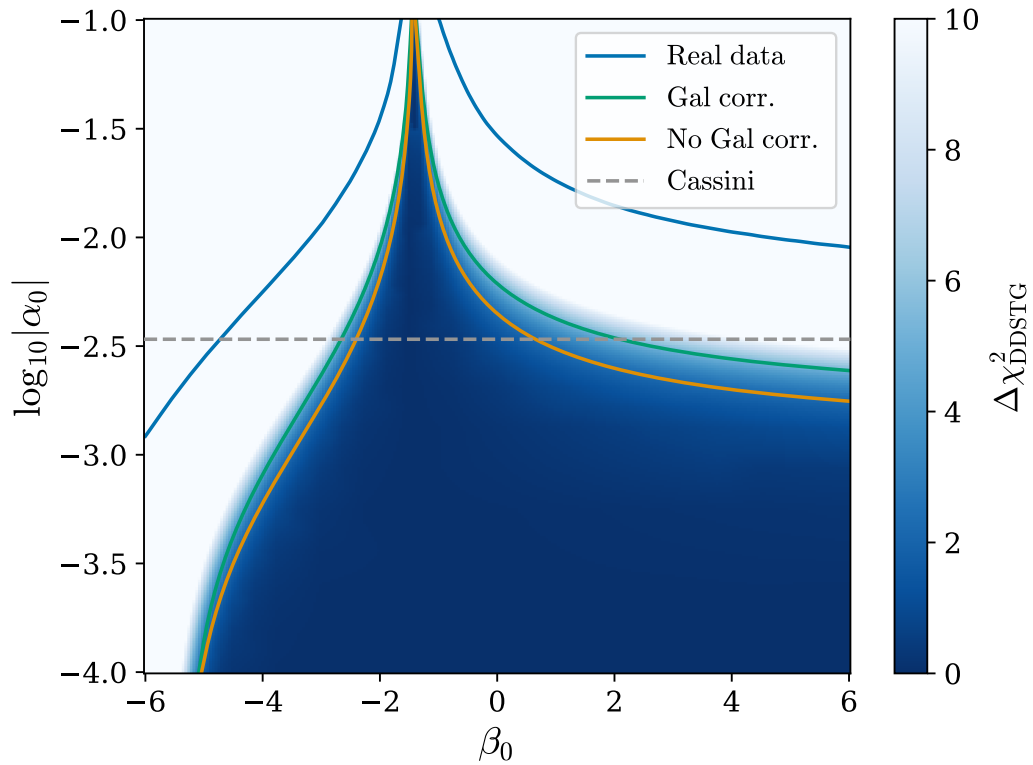


Figure 5.8: $\Delta\chi^2$ map in Damour-Esposito-Farèse (DEF) gravity space $\{\alpha_0, \beta_0\}$ for the simulated dataset (2023-2032) with four campaigns every year. The tests are performed using the DDSTG timing model and assuming stiff MPA1 EOS. The solid lines correspond to the 68% CL limits ($\Delta\chi^2 \simeq 2.28$). Limit with the blue line is based on the existing TOAs. The blue shade and the orange line are the results for the simulated TOAs not accounting for the Galactic uncertainty in $\dot{P}_{b,xS}$. The green line shows the corrected limit, with $\dot{P}_{b,xS}$ taken at its 1σ limit. The grey dashed line is the limit from the Solar System Cassini experiment ($\alpha_0^2 \lesssim 1.15 \times 10^{-5}$).

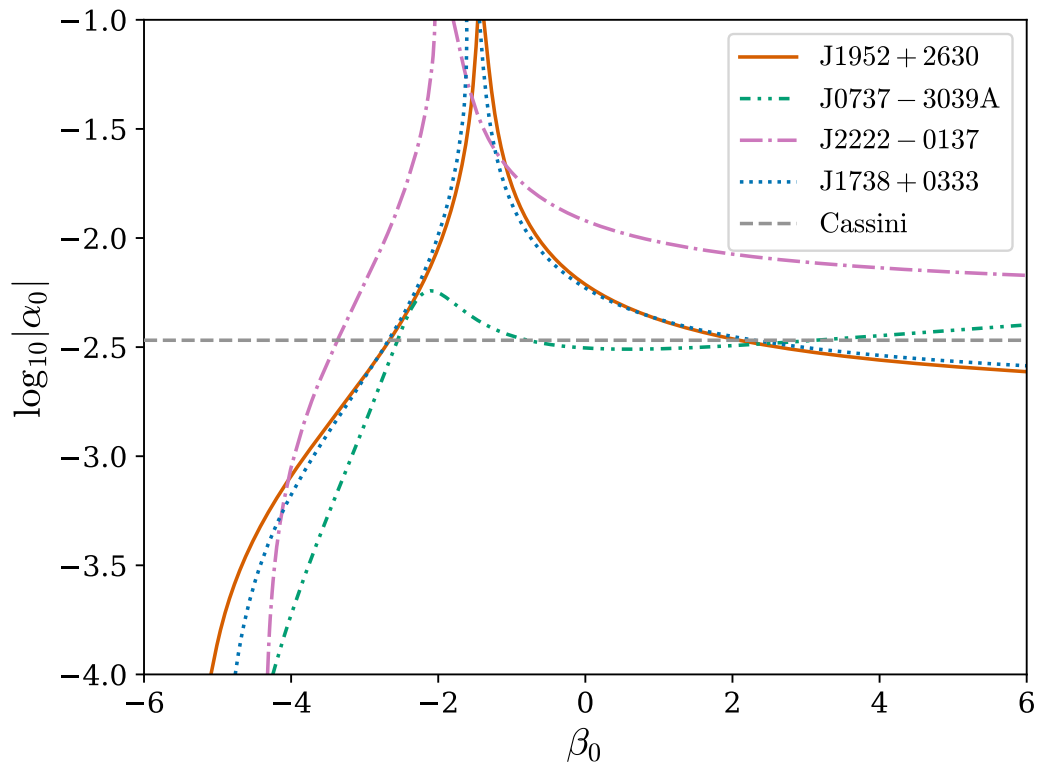


Figure 5.9: Comparison of existing limits placed on DEF gravity space $\{\alpha_0, \beta_0\}$ by radiative tests from different pulsars to the predictions for J1952+2630. All limits are taken for 68% CL and assume MPA1 EOS. The limit for J1952+2630 is predicted by the DDSTG timing model based on the simulated data set for observations from 2023 till 2032 with four campaigns every year. The limits for other pulsars are calculated by the traditional PK method based on the current measured PK parameters published in the literature (see Table 5.4). We do not include the limit from the Triple System PSR J0337+1715 because of its non-radiative origin despite being more restrictive in the large range of β_0 .

due to the small compactness of a WD.

The DDSTG model fits two masses of the objects along with Keplerian, spin, and astrometric parameters directly to the timing data without any intermediate steps. The timing data can show strong correlations which are hard to account for using the traditional PK method (Anderson et al., 2019). On the contrary, the direct fit of the theory to the data naturally accounts for all possible correlations between PK and other parameters and exploits weakly measured relativistic effects.

In Figure 5.8 we present limits on DEF gravity obtained by the DDSTG model for the PSR J1952+2630. We compare the limits calculated for the existing data set (1475 TOAs) and the simulated one (18752 TOAs from 2023 – 2032 with 4 campaigns per year). For the present investigation we assume the stiff EOS MPA1 (Müther et al., 1987) in the piecewise polytropic approximation (Read et al., 2009) and use the corresponding grid of gravitational form-factors. MPA1 has a relatively high maximum mass of the neutron star $M_{\max} = 2.461M_{\odot}$. Stiff equations of state generally produce more conservative limits on DEF gravity for most of $\{\alpha_0, \beta_0\}$ plane compared to soft equations of state. For a selected pair of $\{\alpha_0, \beta_0\}$ parameters TEMPO fits the best χ^2 value. The minimum χ_{\min}^2 in $\{\alpha_0, \beta_0\}$ domain corresponds to the statistically preferred theory parameters. The obtained χ_{\min}^2 value is statistically in agreement with the GR value χ_{GR}^2 for $\alpha_0 = 0, \beta_0 = 0$. The shifted quantity $\Delta\chi^2 = \chi^2 - \chi_{\min}^2$ has the χ^2 statistics with 2 degrees of freedom and used to perform statistical tests. We derive contours of $\Delta\chi^2$ to place limits on $\{\alpha_0, \beta_0\}$ within the desired confidence level limit (we used 68% CL that corresponds to $\Delta\chi^2 \simeq 2.28$).

TEMPO does not allow us to internally account for the uncertainty in $\dot{P}_{b,x}$ due to the Galactic and Shklovskii contributions, thus the value $\dot{P}_{b,x}$ is set fixed for each run of TEMPO. Ideally, one has to calculate a dense grid of χ^2 over $\alpha_0 - \beta_0 - \dot{P}_{b,x}$ parameters and then marginalize over $\dot{P}_{b,x}$ with the prior corresponding to the uncertainty of the $\dot{P}_{b,x}$ term. But such an approach is very computational intensive. In Figure 5.8 we present the contours for two fixed $\dot{P}_{b,x}$ values – one is the calculated prediction 1.8 fs s^{-1} and the second is shifted by the uncertainty $1.8 + 5.1 = 6.9 \text{ fs s}^{-1}$. The $\Delta\chi^2$ contour with the $\dot{P}_{b,x}$ value shifted by 1σ uncertainty gives a slightly conservative but still reasonable limit on DEF gravity parameters. The more accurate account for $\dot{P}_{b,x}$ uncertainty would give slightly better results in between the shifted and not shifted contours.

To put limits on DEF gravity parameters $\{\alpha_0, \beta_0\}$ the pulsar must have at least three measured PK parameters (or other parameters depending on masses such as the mass ratio q). All radiative tests strongly depend on the precision in the \dot{P}_b measurement. PSR J1952+2630 shows $\dot{P}_b, \dot{\omega}$, and h_3 measurements at present (see Table 5.4), and ζ prediction in the future. Two important limiting factors that affect the test of the DEF gravity in this system are: a) the precision of $\dot{\omega}$, and b) the mass of the pulsar M_p . The spontaneous scalarization of the NS, which predicts the strong dipolar contribution $\delta\dot{P}_b^D$ term, happens in the nonlinear area with $\beta_0 \lesssim -4.4$ and only for relatively massive NS, $M_p \gtrsim 1.5M_{\odot}$, for instance, PSR J2222–0137 (Guo et al., 2021). Current

Table 5.4: Binary pulsar systems used for comparing constraints on the DEF theory in Figure 5.9. The measured PK parameters published in the literature along with other information are used for calculating limits. M_c and the mass ratio q for J1738+0333 are measured from the optical observations of the companion. Value in bracket is expected to be measured in the future.

Name	Observed parameters	reference
J1952+2630	$\dot{\omega}, \dot{P}_b, h_3, (\zeta)$	this work
J0737–3039A	$\dot{\omega}, \gamma, \dot{P}_b, r, s, q$	Kramer et al. (2021)
J2222–0137	$\dot{\omega}, \dot{P}_b, h_3, \zeta$	Guo et al. (2021)
J1738+0333	\dot{P}_b, M_c, q	Freire et al. (2012)

measurement of $M_p \sim 1.2M_\odot$ for PSR J1952+2630 is relatively small and thus does not place restrictive limit in this region. However, the error bars on the masses are large, so the constraints from this pulsar can become restrictive in future if M_p turns out to be larger.

Figure 5.9 shows a comparison between the limits that PSR J1952+2630 will present in the future (assuming four orbital campaigns per year from 2023-2032) and the current best constraints put by other systems on $\{\alpha_0, \beta_0\}$ plane. We include systems which are powerful in terms of radiative tests (see Table 5.4). PSR J1952+2630 can place restrictive limits comparable to the current limits from PSR J1738+0333 ($M_p \sim 1.46M_\odot$ and $M_c \sim 0.18M_\odot$) for the positive $\beta_0 > 2$ region. The latter system has been dominant this region so far (Freire et al., 2012) but since the precision on its component masses is limited (Antoniadis et al., 2012), there is little scope for further improvements. This will not be the case for PSR J1952+2630 as the constraints on mass measurements will continue to improve with precise $\dot{\omega}$ values in future. As discussed above, the limiting constraints for this pulsar will eventually come from poor estimate of the kinematic contributions due to large uncertainties in its distance measurement. On the contrary, pulsar binaries such as PSR J2222–0137 and the Double Pulsar J0737–3039A have the potential to provide further restrictive constraints on the radiative tests in future. The discussion above shows that radiative tests in terms of DEF gravity framework are characterized not only by the constraint on the $|\alpha_p - \alpha_c|$ parameter but also the properties of a binary system such as the masses of the companions.

5.6.3 Additional orbital parameters

We have measured no additional PK parameters nor any other constraints on the orbital geometry of the PSR J1952+2630 system from our current timing data. The simulations we have just made can be used to find out whether such measurements might be possible.

The most likely detection is that of the second Shapiro delay parameter (ζ in our chosen parameterisation). This is less secure than the detection of h_3 , as it depends more strongly on the largely unknown orbital inclination of the system (see Figure 5.4). In our simulations, which assumed an inclination of 74° (close to the peak of probability in that Figure), we can obtain a significant detection of this parameter, about $14\text{-}\sigma$. However, for lower inclinations, which are still possible, the significance of this detection will be much lower.

In Table 5.3, we can see that the value of the relativistic γ (which quantifies the slowdown of the pulsar at periastron relative to apastron caused by a combination of special relativistic time dilation and general relativistic gravitational redshift) expected for the most likely mass combination is very small, about $0.2\ \mu\text{s}$. The reason is clearly the very small orbital eccentricity of this system. Measuring this effect in our simulations, we obtain an uncertainty of $5\ \mu\text{s}$, which is certainly not enough for the detection of such a small γ .

Additionally, for a timing baseline that is shorter than the full precession timescale ($360^\circ/\dot{\omega} \sim 200\ \text{yr}$ in this case), the effect of γ cannot be distinguished from that of the secular variation of the projected semi-major axis, \dot{x} (Ridolfi et al., 2019). For this system, the \dot{x} is likely dominated by the change of the viewing angle on the binary caused by the proper motion (Kopeikin, 1996). We calculated this effect for an inclination of 74° , which yields $|\dot{x}| < 7 \times 10^{-16}\ \text{lt-s s}^{-1}$. When we try to measure this effect from our simulated data, we obtain an uncertainty of $3.7 \times 10^{-15}\ \text{lt-s s}^{-1}$, which is certainly not sufficient for the detection of this effect either.

5.7 Summary and conclusions

In this paper, we presented the results from the continued timing of PSR J1952+2630 with the Arecibo telescope. We showed the polarimetric profile of this pulsar and measured RM of $-145 \pm 0.15\ \text{rad m}^{-2}$. However, a fit for PA swing could not yield a good measure of its inclination. We showed improved precision on astrometric, orbital, and kinematic parameters, with an order of magnitude improvement in the proper motion of $5.89(23)\ \text{mas yr}^{-1}$.

We presented, for the first time, the measurement of three PK parameters: $\dot{\omega}$, \dot{P}_b , and the orthometric amplitude of the Shapiro delay, h_3 . Assuming GR, these yield M_p to $1.24(26)\ M_\odot$ and M_c to $0.95(12)\ M_\odot$, indicating the companion is likely a CO WD formed from a He star. Given the uncertainty of M_c , the possibility of an ONeMg WD is less likely but still possible.

This system has some promise as a gravitational laboratory. First, with our improved proper motion estimates, we calculated the kinematic contributions to observed orbital decay due to Galactic accelerations and Shklovskii effect. The uncertainty of these contributions (due to limited distance measurement) represents the ultimate limit on the improvement in the measurement of the orbital decay of this system.

Despite this limitation, the system has the potential to place stringent constraints on

the DEF gravity parameters $\{\alpha_0, \beta_0\}$ similar to PSR J1738+0333, which is currently the best radiative test in the $\beta_0 > 2$ region, but with the advantage of the masses being determined from timing measurements, thus being independent of WD spectroscopy and its interpretation with WD atmosphere models. Our simulations show that such a test is feasible within the near future: much improved masses will be known by 2025, and a test comparable to that of PSR J1738+0333 by 2032 if four short orbital campaigns are performed every year with FAST.

The early knowledge of the component masses will be important, not only for elucidating the nature of the WD companion, but also for a better understanding of the possibilities of this system for tests of gravity theories. In particular, if $M_p > 1.5 M_\odot$ (something that is still allowed by the current uncertainties), then measurements with this system might provide not only excellent constraints on α_0 , but also introduce constraints on the phenomenon of spontaneous scalarization that are even tighter than current limits on this phenomenon (see Figure 2 of [Zhao et al. 2022](#)).

One final remark about the timing of this system. At first sight, its low eccentricity (only 4.2×10^{-5}) and unremarkable Shapiro delay (barely detectable) do not suggest it is a promising gravity laboratory. All relativistic effects measured in this system to date are small and difficult to measure, resulting in PK parameters with large uncertainties. However, a dedicated study has revealed that an apparently unremarkable system might still have a lot to teach us. This shows that detailed studies of apparently unpromising systems can occasionally reveal real jewels.

Acknowledgements

We thank Norbert Wex for useful discussions and suggestions. TG thanks Alessandro Ridolfi for help with data analysis of polarisation data. The Arecibo Observatory is a facility of the National Science Foundation operated under cooperative agreement by the University of Central Florida and in alliance with Universidad Ana G. Mendez, and Yang Enterprises, Inc. . This work made use of the data from FAST (Five-hundred-meter Aperture Spherical radio Telescope). FAST is a Chinese national mega-science facility, operated by National Astronomical Observatories, Chinese Academy of Sciences. EP supported by the H2020 ERC Consolidator Grant "MAGNESIA" under grant agreement No. 817661 and National Spanish grant PGC2018-095512-BI00.

Detection of Shapiro delay in the highly inclined millisecond pulsar binary PSR J1012-4235

The work presented in this chapter is a manuscript in preparation.

A preliminary list of authors is **T. Gautam**, P. C. C. Freire, J. Wu, V. Venkatraman Krishnan, M. Kramer, F. Camilo, MeerTime relbin et al.

Contents

6.1	Introduction	99
6.2	MeerKAT observations	101
6.3	Data reduction	102
6.4	Polarisation calibration	103
6.5	Timing analysis	104
6.5.1	Binary models	104
6.5.2	Results from radio timing	105
6.5.3	Mass constraint from the Shapiro delay detection	105
6.5.4	Kinematic effects on the spin and orbital period	110
6.6	Gamma and radio profiles	112
6.7	Conclusion	112

6.1 Introduction

Due to their rotational stability, millisecond pulsars (MSPs) provide remarkable timing precision and thus have proven to be excellent probes of the physics of dense matter in Neutron stars and gravity. With the help of pulsar timing, we can model the physical effects acting on the radio pulses and correct for their corresponding delays produced in the pulse arrival times (TOAs).

In the case of binary pulsars, this modelling leads to the detection of several relativistic effects acting on the pulses. These have been parameterised in a theory-independent form with the so called “post-Keplerian (PK) parameters” (Damour & Taylor, 1992b). Assuming a theory of gravity, PK parameters are expressed as functions of the Keplerian parameters, and the pulsar and its companion mass. Thus, a

measurement of two PK parameters can directly constrain the component masses of the system, and a detection of three or more PK parameters will over-determine the system and provide tests of the gravity theory assumed.

In this paper, we present the detection of one such relativistic effect in PSR J1012–4235: the Shapiro delay (Shapiro, 1964). This effect is observed when the radio pulses are delayed as they pass through the deeper parts of the gravitational potential of the pulsar companion, thus it is more easily observed in the edge-on binaries.

The MeerKAT telescope (Jonas & MeerKAT Team, 2016), with its 64-dish array, has provided excellent timing sensitivity for pulsars in the southern hemisphere (Bailes et al., 2020). With the aim of performing high precision timing for a number of pulsar systems, a Large Science Project (LSP) called MeerTIME (Bailes et al., 2016, 2020) is being carried out. One program under this project is the relativistic binary program (referred as “RelBin”). It specifically targets relativistic binary pulsars for the purpose of measuring relativistic effects, constraining NS masses, and testing GR, along with constraining alternative theories of gravity (Kramer et al., 2021). Another MeerTIME program is the “pulsar timing array (PTA)” that aims to use MSPs for the detection of gravitational waves (Parthasarathy et al., 2021; Spiewak et al., 2022).

PSR J1012–4235 was discovered using the Parkes radio telescope in a survey (Camilo et al., 2015) that targeted unidentified γ -ray sources found with the Large Area Telescope (LAT) (Atwood et al., 2009) on the Fermi γ -ray space telescope. It is a 3.1 ms pulsar in a binary system, orbiting its companion every 37.9 days. In the discovery paper, by fitting for the changes in the barycentric period due to Doppler shift, the orbital parameters of the binary were determined. The binary was identified with having low eccentricity < 0.001 and a light pulsar companion $< 0.2 M_{\odot}$ likely a Helium-core white dwarf (WD).

From 2013 to 2015, additional timing campaigns were performed on this system with the 64-m Parkes radio telescope and the Green Bank Telescope (GBT), and a phase-connected timing solution, with improved constraints on the position and orbital parameters, was derived. Recently, to exploit the enhanced timing sensitivity with MeerKAT, this system was added to the MeerTIME LSP program. It has been regularly observed from 2019-2022 with the aim of measuring relativistic effects and constraining the component masses.

In this paper we present, for the first time, the phase-connected timing solution for PSR J1012–4235 derived by making use of the data obtained from the timing campaigns with the Parkes, GBT, and MeerKAT radio telescopes. We obtain precise measurements of proper motion, position, and orbital parameters. Additionally, with the help of dedicated orbital campaigns with MeerKAT, especially around superior conjunction, we measure a strong Shapiro delay signature in this system. With the help of this detection we have constrained the inclination of the binary and both the pulsar and its companion’s mass.

This paper is organised as follows: in section 6.2 we describe the data-set used

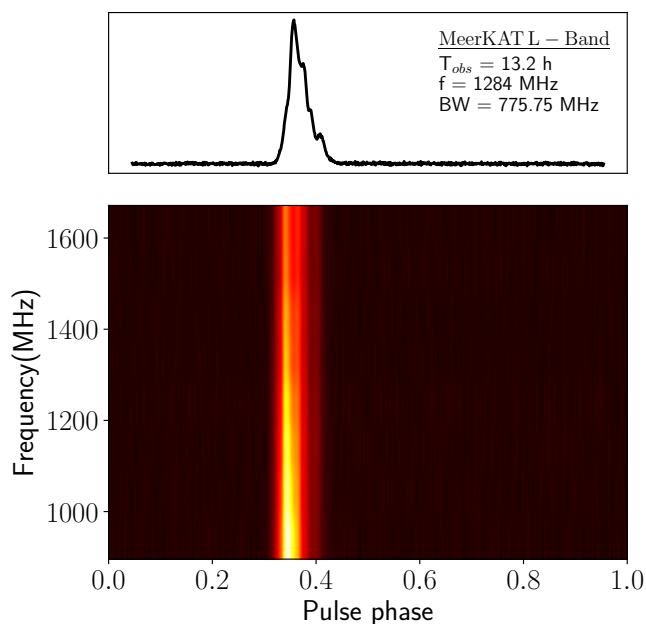


Figure 6.1: MeerKAT L-Band profile integrating total 13.2 hr of data. Top: Intensity vs rotation phase, bottom: Frequency vs rotation phase. Number of phase bins are 1024 and SNR is 977.

for the analysis in this work, in section 6.3 we discuss the data reduction procedure, in section 6.4 the polarisation profile of this pulsar is discussed. In section 6.5 we discuss the timing analysis and its results, in section 6.6 we discuss the gamma-ray pulse profile of this pulsar and compare its features with the radio profile, and finally in section 6.7 we summarise the results of this paper.

6.2 MeerKAT observations

The instrumentation and set-up for pulsar observations with MeerKAT are explained in detail in Bailes et al. (2020). The timing observations for this pulsar were performed as part of both PTA and RelBin programs. All the observations were carried out with L-band receiver and used the PTUSE backend. Typical observation times of PTA observations were ~ 5 min, and of Relbin observations, that focused on getting a better orbital coverage, were ~ 34 min. In addition, we carried out one long observation of ~ 5 hrs covering superior conjunction under RelBin program. All the observations covered an effective bandwidth of 775.75 MHz divided across 928 frequency channels. The MeerKAT data used in this work were taken between April 2019-January 2022, and amount to a total of 72 observations covering 13.2 hours. The integrated pulse profile from MeerKAT observations is shown in Figure 6.1. The details of all the observations used in this work are listed in Table 6.1.

Table 6.1: Observation Details

Observatory	Epoch (MJD)	Receiver	Central frequency (MHz)	Bandwidth (MHz)	#TOAs	EFAC
Parkes	56469-57039	20-cm multibeam	1382	400	169	1.64
GBT	56522-56732	820 MHz receiver	820	200	93	1.26
MeerKAT	58595-59604	L-band	1283	775	3446	1.04

6.3 Data reduction

All the MeerKAT data reduction was performed using the standard pulsar analysis software PSRCHIVE (Hotan et al., 2004a; van Straten et al., 2012a). All the MeerKAT L-Band data were passed through a data reduction pipeline, MEERPIPE (Parthasarathy et al., 2021), which first performs the RFI excision using a modified version of COASTGUARD (Lazarus et al., 2016), and then carry out the polarisation and flux calibration. In this process, to remove the low power levels at the edges of the bandpaas, all observations were chopped from their original bandwidth of 856 MHz to 775.75 MHz. The pipeline outputs a consistent data set, with similar bandwidth and central frequency, that can be readily used for timing analysis.

To calculate the time-of-arrivals (TOAs) of each high SNR integration in the data, we cross-correlate it with a standard template of the pulse profile. Since the intrinsic profile shape of a pulse can vary with frequency, using a single template created by integrating in frequency can smear some of the profile features and lead to increased TOA uncertainty. Thus a template with multiple frequency sub-bands can provide a smaller TOA uncertainty. Additionally, sharp features in the profiles with different polarisation can help improve the timing precision further, thus a template with non-integrated polarisation can be useful in some cases. In order to identify the best suited standard template for our case that would give the smallest residual RMS from the fit, we created four different types of templates and produced TOAs with each of them:

1. 1F1P: integrated in both frequency and polarisation, created with paas routine,
2. 8F1P: sub-banded to eight frequency channels and integrated completely in polarisation, we used Fourier domain with Markov chain Monte Carlo (FDM) algorithm of pat routine,
3. 1F4P: integrated in frequency but with full Stokes parameter profiles, created using matrix template matching (MTM) algorithm of pat routine, and
4. 8F4P: sub-banded to eight frequency channels and non-integrated polarisation profiles with full Stokes parameters.

In addition to these, templates with four rather than eight channels in schemes (2) and (4) were also created for comparison. We find that the best template providing minimum parameter uncertainties for our data-set is the one labelled (2) i.e. integrated

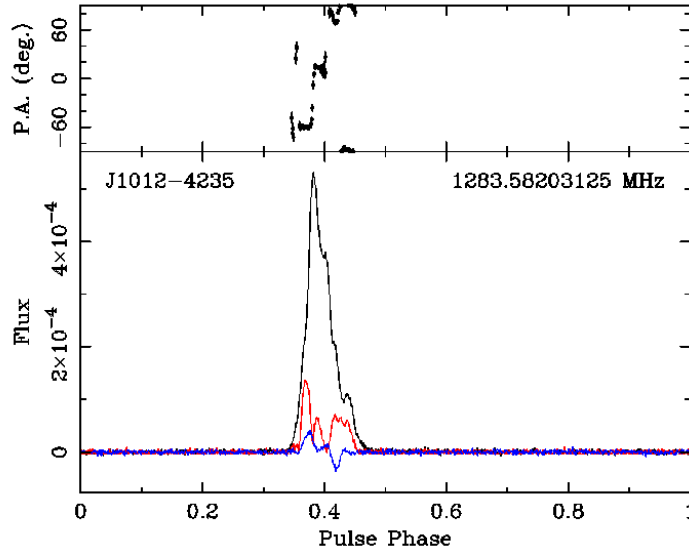


Figure 6.2: Polarisation calibrated profile of PSR J1012–4235 formed from MeerKAT L-band data. The red color shows linear polarisation and the blue color shows circular polarisation across the rotational phase. Upper panel shows the polarisation angle swing across the rotational phase.

in polarisation but sub-banded to eight frequency channels. Typically, we generated TOAs for 1-minute sub-integrations, leading to eight TOAs per minute. The total number of TOAs extracted from each data-set is given in Table 6.1.

6.4 Polarisation calibration

A description of the polarisation calibration of the MeerKAT data of this pulsar is provided by Spiewak et al. (2022). The system have a rotation measure (RM) of 61.80 rad m^{-2} . Figure 6.2 shows the polarization calibrated profile of this pulsar created by integrating all the 73 observations covering a total of 13.2 hrs of MeerKAT’s L-band data. All the polarised flux is concentrated in the on-pulse region with no additional polarised components visible anywhere in the off-pulse region. After thoroughly analysing the intensity in the pulse profile and reducing the detection threshold for the polarised components, we can confirm that we do not detect any signature of the inter-pulse in the radio pulse profile as might be expected from the high inclination of the orbit (shown in Section 6.5.2) and the fact that the pulsar is likely an orthogonal rotator.

Only 11% of the total flux is polarised of which the majority is linearly polarized,

with fractional linear polarisation, $L/I = 23\%$ and fractional circular polarisation, $V/I = 1.7\%$ ($|V|/I = 6.3\%$). The circular polarisation reverses its sign exactly at the center of the on-pulse region. The position angle (PA) swing (see top panel of Figure 6.2) shows a steep curve in the first half of the pulse while there appears to be an orthogonal mode jump in the second half.

6.5 Timing analysis

For the timing analysis, we used pulsar timing software TEMPO¹. The software first transfers all the TOAs from UTC to terrestrial time standard “TT(BIPM)” that is defined by International Astronomical Union (IAU). To account for the Earth’s motion, we used the solar system barycentric times (SSB) using NASA’s JPL solar system ephemeris, DE436 (Folkner & Park, 2016). TEMPO then calculates the phase residuals of each of the TOAs by comparing them to TOAs predicted by an initial timing model. We used the ephemeris presented in Camilo et al. (2015) as our initial model. It then adjusts the timing parameters to minimise the residual χ^2 . To compensate for the under-estimated TOA uncertainties, possibly from any left-over systematic effects, we used separate weighting factors for each back-end, these are multiplied to their respective TOA uncertainties before the fit (see Table 6.1).

6.5.1 Binary models

To fit for the binary parameters, we used the ELL1H+ binary model. This is a theory independent model (Lange et al., 2001; Freire & Wex, 2010) that is derived from the DD model (Damour & Deruelle, 1985, 1986). For low eccentricity binaries, this model avoids the correlation between the epoch of periastron, T_0 and the longitude of periastron, ω . This is done by re-parameterising the orbit and measuring the epoch of ascending node, T_{asc} instead of T_0 . By changing the reference of time for the measurement of P_b to a well defined measure of T_{asc} for near-circular orbits, the model also avoids the strong correlation between P_b and $\dot{\omega}$. Thus we obtain a significant reduction in the measurement uncertainties of the orbital parameters. Additionally, rather than directly fitting for the eccentricity, this model fits for the Laplace-Lagrange parameters: $\varepsilon_1 = e \cos \omega$ and $\varepsilon_2 = e \sin \omega$.

The DD model measures the Shapiro delay in the form of two PK parameters: range (r) and shape (s), such that $r = T_{\odot} M_c$, and $s = \sin i$, assuming GR as a theory of gravity. This effect is quantified through the fit of the companion mass M_c , and the inclination i . The ELL1H+ model uses the orthometric parameterization of Shapiro delay to remove the high correlation present between the r and s parameters, leading to a robust measurement of this effect. It fits for the orthometric amplitude, h_3 and the

¹<http://tempo.sourceforge.net>

orthometric ratio parameter, ζ ($=h_3/h_4$) which are represented as:

$$\zeta = \frac{\sin i}{1 + \sqrt{1 - \sin^2 i}}, h_3 = T_{\odot} M_c \zeta^3. \quad (6.1)$$

The ELL1H+ model includes an extra term of the order of xe^2 in the expansion of the Römer delay (Zhu et al., 2019). Since the next order term, $O(xe^3)$ (0.9ns) is much smaller than our timing precision of Shapiro delay $\delta h_3 \sim 55$ ns, ignoring the xe^3 term has no effect on our Shapiro delay measurement, thus we can safely use this model. This model is implemented in the latest versions of TEMPO (> 13.102).

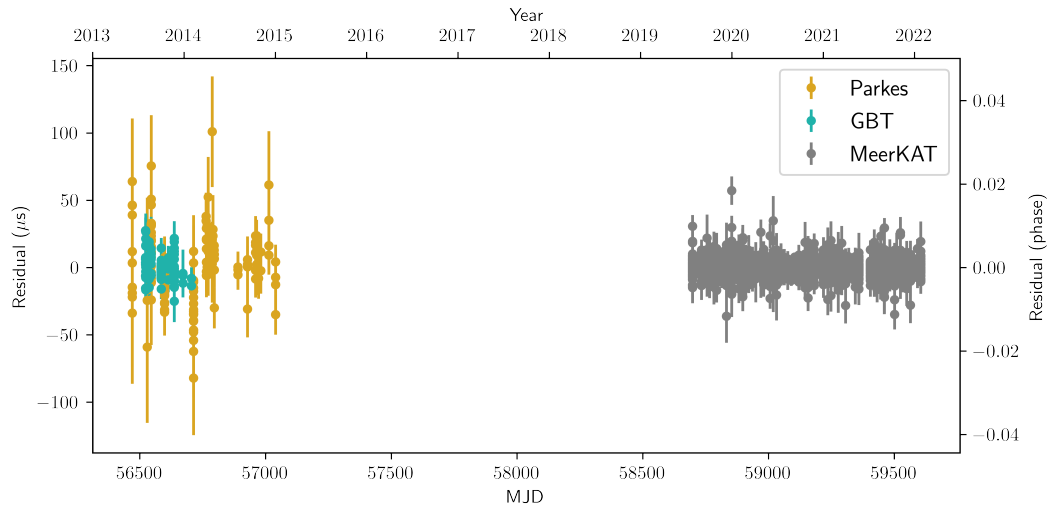
6.5.2 Results from radio timing

From the fit of ELL1H+ binary model, we derived a phase-connected timing solution for this system (see Table 6.2). This is a unique solution of the binary that correctly predicts the pulse arrival times for every rotation of the pulsar in the data-set. The solution is coherent among the early (Parkes and GBT) data and the MeerKAT data as the rotational phase error for the ~ 5 year gap in the timing baseline is only $\sim 0.2\%$. Figure 6.3a shows the TOA residuals after fitting for the model parameters in the data as a function of time. In this resulting best-fit solution, apart from well constraining the astrometric and orbital parameters, we measure variations in DM and spin frequency, leading to three significant DM derivatives ($\sim 10\text{-}\sigma$) and one frequency derivative. Additionally, we could also constrain a parallax of 0.96(52) mas, and proper motion in RA and DEC direction resulting in a total proper motion, μ_{tot} of 6.313(67) mas yr^{-1} . Using the ELL1H+ binary model, we find a strong detection of Shapiro delay with an h_3 of 1.232(55) μs and ζ of 0.9667(48). The effect of Shapiro delay leading to measurable delays in the pulses around superior conjunction can be clearly seen in Figure 6.3b. This detection implies a companion mass $M_c = 0.276(16) M_{\odot}$, and a $\sin i = 0.99945(16)$ i.e. an inclination i of 88.1° . The pulsar mass (M_p) derived from these measurements using the mass function is $1.43(13) M_{\odot}$. Our prediction of the companion mass of $\sim 0.27 M_{\odot}$ aligns well with the $P_{\text{orb}} - M_{\text{WD}}$ relationship presented by Tauris & Savonije (1999b) for He WDs. The eccentricity of 3.4×10^{-4} and the orbital period of 37.9 days of this system also agree well within the theoretical prediction by Phinney & Kulkarni (1994) for MSP-WD binaries.

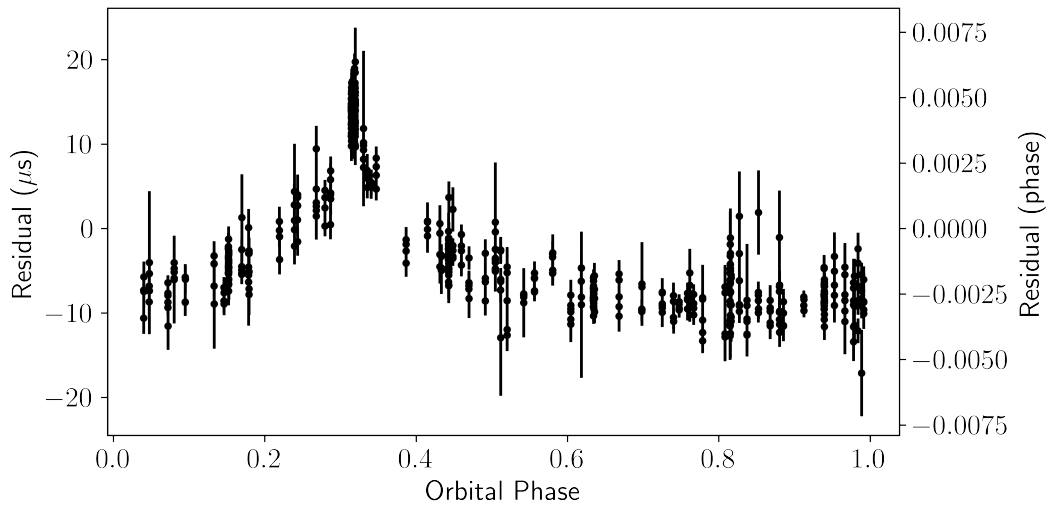
Regarding the measurement of advance of periastron ($\dot{\omega}$) in this binary, its prediction from GR gives a value of $6.5 \times 10^{-4} \text{ }^{\circ}\text{yr}^{-1}$, while our fit for this parameter has an uncertainty of $1.9 \times 10^{-3} \text{ }^{\circ}\text{yr}^{-1}$ i.e. an order of magnitude larger than the predicted value, thus we can not constrain this parameter yet. However, measuring this parameter should be feasible in the near future with continued MeerKAT timing.

6.5.3 Mass constraint from the Shapiro delay detection

In order to derive the best estimates for the masses and to better understand their correlations, we created a uniform grid of points on the $(\cos i - M_c)$ plane and derived the



(a)



(b)

Figure 6.3: (a) Post fit residuals for PSR J1012–4235 showing TOAs from Parkes, GBT, and MeerKAT data, with error bars representing $1\text{-}\sigma$ uncertainty in TOAs. (b) Residuals of MeerKAT TOAs excluding the fit for Shapiro delay effect but fixing all the other system and orbital parameters obtained from full fit. The orbital phase is measured from periastron and the peak in the Shapiro delay signature occurs around the phase of superior conjunction of the pulsar.

Table 6.2: Phase-connected timing solution for PSR J1012–4235 using the ELL1H+ binary model.

Pulsar J1012–4235	
Right Ascension, α (J2000)	10:12:12.9388460(49)
Declination, δ (J2000)	–42:35:53.403104(59)
Proper Motion in α , μ_α (mas yr ^{–1})	–3.689(62)
Proper Motion in δ , μ_δ (mas yr ^{–1})	5.123(70)
Parallax (mas)	0.96(52)
Spin Frequency, f (s ^{–1})	322.4619326648763(32)
1st Spin Frequency derivative, \dot{f} (Hz s ^{–1})	–6.790(1)×10 ^{–16}
Reference Epoch (MJD)	59111.238529
Start of Timing Data (MJD)	56469.292
End of Timing Data (MJD)	59604.959
Dispersion Measure, DM (pc cm ^{–3})	71.650567(83)
1st derivative of DM, DM1 (pc cm ^{–3} yr ^{–1})	0.000682(97)
2nd derivative of DM, DM2 (pc cm ^{–3} yr ^{–2})	0.00165(15)
3rd derivative of DM, DM3 (pc cm ^{–3} yr ^{–3})	0.000429(53)
Solar System Ephemeris	DE436
Terrestrial Time Standard	TT(BIPM2019)
Time Units	TDB
Number of TOAs	3708
Residual RMS (μ s)	3.49
Binary Parameters	
Binary Model	ELL1H+
Projected Semi-major Axis, x_p (lt-s)	21.26306886(30)
ϵ_1	–0.000140982(17)
ϵ_2	0.0003156843(91)
Epoch of ascending node, T_{asc} (MJD)	58862.548525714(40)
Epoch of Periastron, T_0 (MJD)	[58897.98262(27)]
Orbital Eccentricity, e	[3.4573(1)×10 ^{–4}]
Longitude of Periastron, ω (deg)	[335.9349(26)]
Orbital Period, P_b (days)	37.9724631876(32)
h_3 (μ s)	1.232(55)
ζ	0.9667(48)
Sini	0.99942 ^{+0.00015} _{–0.00018}
Mass Function, $f(M_p)$ (M_\odot)	0.0071585168(3)

Table 6.3: Derived parameters for PSR J1012–4235.

Derived Parameters	
Galactic longitude, l (deg)	274.2176
Galactic latitude, b (deg)	11.2246
DM-derived distance from NE2001 model (kpc)	2.51
DM-derived distance from YMW16 model (kpc)	0.37
Distance from timing parallax (kpc)	$1.04^{+1.23}_{-0.36}$
Composite proper motion μ (mas yr ⁻¹)	6.313(67)
Transverse velocity (using distance from timing parallax), v_T (km s ⁻¹) ..	$31.1^{+36.8}_{-10.8}$
Spin Period, P (s)	0.00310114124707943(3)
Observed spin period derivative, \dot{P}_{obs} (10 ⁻²¹ s s ⁻¹)	6.5300(14)
Total kinematic contribution to spin period derivative, \dot{P}_{kin} (10 ⁻²¹ s s ⁻¹) .	$-0.024^{+0.0024}_{-0.0006}$
Intrinsic Spin-down, \dot{P}_{int} (10 ⁻²¹ s s ⁻¹)	$6.5539^{+0.0006}_{-0.0024}$
Surface Magnetic Field, B_s (10 ⁸ G)	1.44
Characteristic Age, τ_c (Gyr)	7.50
Spin-down power, \dot{E} (10 ³³ erg s ⁻¹)	8.68
Rotation Measure (rad m ⁻²)	61.80
Companion Mass, M_c (M _⊙)	0.276(16)
Pulsar Mass, M_p (M _⊙)	1.43(13)
Total Mass, M_{tot} (M _⊙)	1.710(149)
Total kinematic contribution to orbital period derivative, $\dot{P}_{\text{b,kin}}$ (10 ⁻¹⁴ s s ⁻¹)	$-2.06^{+1.43}_{-0.47}$
GR contribution to orbital period derivative, $\dot{P}_{\text{b,GR}}$ (10 ⁻¹⁷ s s ⁻¹)	$-1.68^{+0.20}_{-0.21}$

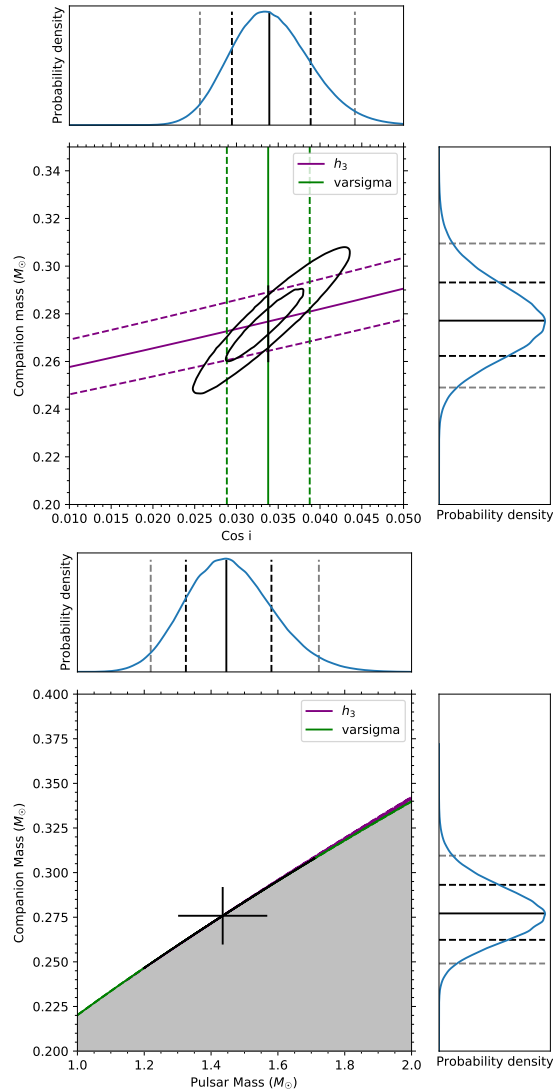


Figure 6.4: Constraints on the M_c , M_p , $\cos i$ derived from the measurement of Shapiro delay. Colored dashed lines depict the 1σ uncertainty on the measurement. Black contours show the likelihood or 2-D PDFs at 39 % (inner) and 85 % (outer) confidence ellipse from the χ_{red} maps on $\cos i - M_c$ and $M_p - M_c$ grids, derived from the ELL1 binary model fit. The corner plots represent the marginalised 1-D PDFs of each of these measurements and vertical lines on these mark the median, 1σ , and 2σ estimates. The black crosses indicate the best masses fit by the DDGR solution and the best inclination derived from the mass function using those masses.

best-fit χ^2 values from the TEMPO fit of this model on each of the points in this grid. These χ^2 values are then converted to the likelihood of the points in this grid using the relation by Splaver et al. (2002): $p(\cos i, M_c) \propto e^{\frac{\chi_{\min}^2 - \chi^2}{2}}$, where χ_{\min}^2 is the minimum χ^2 value. The likelihoods are also translated to the $(M_p - M_c)$ grid afterwards. In Figure 6.4, we plot the Shapiro delay parameters derived from the ELL1H+ model on the $(\cos i - M_c)$ and $(M_p - M_c)$ planes, the black contours represent the 39% (inner) and 85% (outer) confidence ellipses on the 2-D grids, which essentially represent the 1- σ and 2- σ error bars in 1-D PDFs. The corner plots show these 1-D PDFs for M_c , M_p , and $\cos i$. The vertical lines in these plots represent the median, 1- σ , and 2- σ limits for each of these parameters. Using this method, we get $\cos i = 0.0339_{-0.0044}^{+0.0049}$ implying an inclination of $88.06_{-0.25}^{+0.28}$ deg, $M_c = 0.270_{-0.015}^{+0.016} M_{\odot}$, and $M_p = 1.44_{-0.12}^{+0.13} M_{\odot}$, with errors representing 1- σ uncertainties.

6.5.4 Kinematic effects on the spin and orbital period

The distance estimates from the Galactic electron density models are highly discrepant. The YMW16 model (Yao et al., 2017) predicts a distance of 0.37 Kpc while the NE2001 model (Cordes & Lazio, 2002) predicts 2.51 Kpc. In the timing solution however, we could fit for a parallax of 0.95(52) mas, indicating a distance, d ($=1/\text{parallax}$) of $1.04_{-0.36}^{+1.23}$ kpc, a value in between the predictions from both the models. This distance yields a low transverse velocity (v_T) of $31.1_{-10.8}^{+36.8}$ km s $^{-1}$, which is common for recycled pulsars (Hobbs et al., 2005).

The observed spin period derivative includes contribution not only from the intrinsic spin period derivative but also from the accelerations acting on the pulsar (due to kinematic effects). Two major effects leading to these accelerations are a) due to proper motion of the pulsar and b) due to the galactic acceleration (Lorimer & Kramer, 2012):

$$\frac{\dot{P}_{\text{obs}}}{P} = \frac{\dot{P}_{\text{int}}}{P} + \frac{\mu^2 d}{c} + \frac{a_{\text{gal,disc}}}{c} + \frac{a_{\text{gal,rot}}}{c}, \quad (6.2)$$

where \dot{P}_{int} is the intrinsic spin period derivative, $a_{\text{gal,disc}}$ is the vertical acceleration contribution from the galactic disc, and $a_{\text{gal,rot}}$ is the acceleration due to the differential rotation of the galaxy. These galactic accelerations are calculated from the following expressions (Damour & Taylor, 1991; Nice & Taylor, 1995; Lazaridis et al., 2009):

$$a_{\text{gal,rot}} = -\frac{\Theta_0^2}{R_0 c} \left(\cos l + \frac{\beta}{\beta^2 + \sin^2 l} \right) \cos b, \quad (6.3)$$

$$a_{\text{gal,disc}} = -\left(2.27 z_{\text{kpc}} + 3.68(1 - e^{-4.3 z_{\text{kpc}}}) \right) |\sin b|, \quad (6.4)$$

where $\beta \equiv (d/R_0) \cos b - \cos l$ and $z_{\text{kpc}} \equiv |d \sin b|$ in kpc. R_0 is the distance to the galactic center, 8.275(34) kpc, and Θ_0 is the galactic rotation velocity, 240.5(41) km s $^{-1}$ (values taken from Gravity Collaboration et al. 2021). The contribution from the

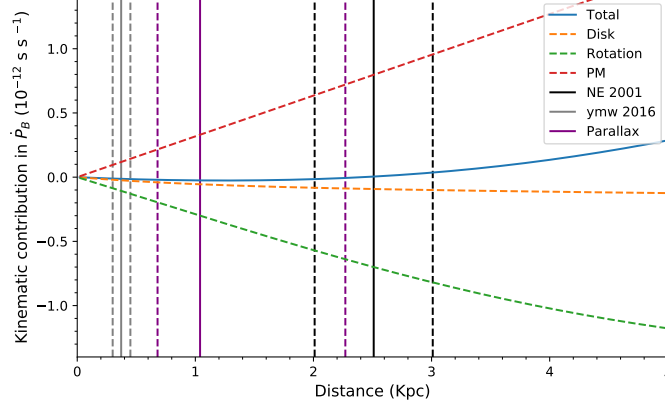


Figure 6.5: Acceleration contributions to orbital period derivative due to kinematic effects as a function of distance. Orange and green curves show the vertical and differential accelerations from galactic disc while red curve shows the contribution from proper motion of the pulsar. Blue curve represents the total acceleration contribution. Distance uncertainty of 20% is assumed on the DM distance predictions from NE2001 (black vertical lines) and YMW16 model (cyan vertical lines) while 1- σ uncertainty is shown for the parallax measurement from timing (purple vertical lines).

composite proper motion of the system, also known as Shklovskii effect, is given by $\frac{\mu^2 d}{c}$, where d is the pulsar's distance from Earth. Assuming the distance predicted by our parallax measurement, the total acceleration acting on the system is calculated to be $-6.3_{-1.4}^{+4.4} \times 10^{-21} \text{ s}^{-1}$. Using this estimate, we get $\dot{P}_{\text{int}} = 6.55 \times 10^{-21} \text{ s s}^{-1}$, which is very close to the observed \dot{P}_{obs} because the kinematic term is comparatively small. With this estimate of \dot{P}_{int} , we estimate the surface magnetic field, B_s , the characteristic age, τ_c , and the spin-down luminosity of the system, \dot{E} of the pulsar using the equations in Lorimer & Kramer (2012). Table 6.3 presents these estimates along with their 1- σ uncertainties.

Similar kinematic effects as discussed above affect the measurement of the observed orbital period derivative, $\dot{P}_{b,\text{obs}}$ as well. Assuming the distance from the parallax, we estimate the total kinematic contribution $\dot{P}_{b,\text{kin}} = -2.06_{-0.47}^{+1.43} \times 10^{-14} \text{ s s}^{-1}$. The expected orbital decay due to the quadrupolar GW emission from this system is $-1.68_{-0.21}^{+0.20} \times 10^{-17} \text{ s s}^{-1}$ (assuming GR). The observed \dot{P}_b has an uncertainty of $5 \times 10^{-12} \text{ s s}^{-1}$, which is two orders of magnitude higher than the contributions from kinematic effects and nearly five orders of magnitude higher than the intrinsic orbital decay. Therefore, we can not put a limit on the intrinsic orbital period derivative or on the contribution from kinematic effects from timing yet.

Figure 6.5 shows each of the contributions on $\dot{P}_{b,\text{obs}}$ from the kinematic effects as a function of distance. As we can see there, the contribution to \dot{P}_b from the kinematic effects (blue curve) is extremely flat. This turns out to be one of the most

interesting features of this system. Even with the relatively large distance uncertainty, this contribution is not only small but it has a small associated uncertainty, $\delta\dot{P}_{b,\text{kin}} = 2 \times 10^{-14} \text{ s s}^{-1}$. This has an important consequence: we will be able to obtain an unusually tight constraint on the variation of the gravitational constant \dot{G}/G (Will, 1993; Uzan, 2011). The reason is that, with additional MeerKAT observations, the precision of $\dot{P}_{b,\text{obs}}$ will keep improving relatively fast, with $T^{-5/2}$, where T is the timing baseline. This will result in improving estimates of the intrinsic \dot{P}_b , which will only be limited by the $\delta\dot{P}_{b,\text{kin}}$. The constraint on \dot{G}/G will then be proportional to $\delta\dot{P}_{b,\text{kin}}/P_b = 1.9 \times 10^{-13} \text{ yr}^{-1}$. For PSR J1713+0747, which currently provides the best limit on this parameter, this parameter is $8.07 \times 10^{-13} \text{ yr}^{-1}$. Therefore, improving the \dot{P}_b measurement of PSR J1012–4235 has the potential for an order of magnitude improvement of \dot{G}/G relative to the limit provided by PSR J1713+0747. This improvement will likely be better because the continued timing will also improve the parallax, which will further restrict the allowed range of distances and the values of $\delta\dot{P}_{b,\text{kin}}$.

6.6 Gamma and radio profiles

The Parkes survey by Camilo et al. (2015) was aimed at unidentified γ –ray sources. PSR J1012–4235 was found in the γ –ray source 3FGL J1012–4235. With our new timing solution obtained from radio data, we re-folded the gamma ray data to create a gamma-ray pulse profile. We use a single phase-connected solution on both the radio and gamma-ray data such that the profiles are phase-aligned i.e. the start of rotational phase indicate the same reference epoch. Figure 6.6 shows the comparison of both the profiles. Although the inter-pulse is missing from the radio observations, it is clearly seen in the gamma-rays. The peak of the main pulse (the pulse visible in both radio and gamma rays) in gamma rays lags the pulse-peak in radio profile and appear at the location of the shoulder-like feature in the radio profile.

Further analysis in an attempt to constrain the pulsar magnetosphere and possibly get improvements in the timing solution by adding gamma-ray data will be carried out in the future.

6.7 Conclusion

In this paper, we presented the results of the timing analysis of PSR J1012–4235 performed with the data taken with the Parkes (1.5 years), GBT (7 months), and MeerKAT (2.7 years) radio telescopes, covering a total time baseline of 9 years. We presented the phase-connected timing solution of this pulsar which include refined estimates for astrometric, kinematic, and orbital parameters. We have measured the proper motion of the pulsar of 6.3 mas yr^{-1} . With the help of dense MeerKAT observation that cover the superior conjunction of the pulsar, we detected a significant Shapiro delay signature in the binary i.e. the first relativistic effect in this system.

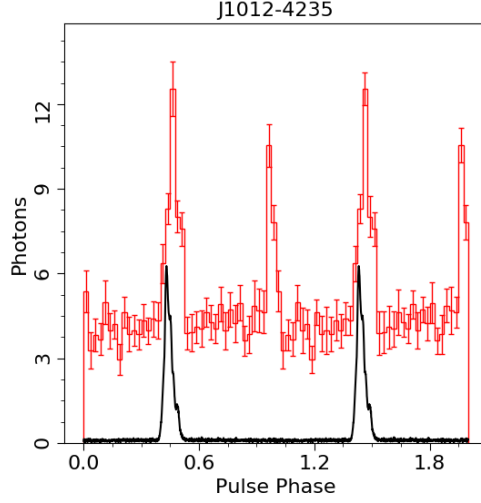


Figure 6.6: Comparison of the gamma-ray pulse profile (red) with the radio profile (black) of PSR J1012–4235. The profile is formed using a phase connected solution (ephemerides) such that both the folds take the same reference epoch as the start of the profile.

We obtain a $22\text{-}\sigma$ detection of h_3 parameter of $1.232(55)\ \mu\text{s}$ and a $200\text{-}\sigma$ detection of $\zeta = 0.9667(48)$. This yields a measurement of the component masses and orbital inclination: $M_p = 1.44^{+0.13}_{-0.12}\ M_\odot$, $M_c = 0.270^{+0.016}_{-0.015}\ M_\odot$ and $i = 88.06^{+0.28}_{-0.25}\ \text{deg}$ or $91.94^{+0.25}_{-0.28}\ \text{deg}$ (due to $\sin i$ ambiguity from Shapiro delay measurement).

Using the phase-connected solution, we also phase-aligned the radio- and gamma-ray profiles of the pulse. This alignment shows that the pulse peak of the radio profile precedes the gamma profile’s peak, which in turn aligns with one of the features of the radio profile.

Lastly, with the proper motion and parallax measurements from timing, we constrained the kinematic contributions to the observed spin period and orbital period derivatives. We note that the curve for the contribution of the kinematic effects to the $\dot{P}_{\text{b,obs}}$ is nearly flat within the range of distances allowed by our measurement of the parallax. Thus, despite the large uncertainty in the distance measurement, we obtain a very small uncertainty in the kinematic contributions to \dot{P}_{b} . This represents the limiting factor for estimating the intrinsic \dot{P}_{b} of the system from future timing measurements. Thus, continued timing of this system will eventually result in a limit on \dot{G}/G that is one order of magnitude better than the current best limit on this parameter obtained from PSR J1713+0747.

Conclusion and future work

Contents

7.1 Summary and conclusion	115
7.2 Future work	119
7.2.1 TRAPUM GC pulsar survey	119
7.2.2 Imaging GCs to search for pulsars	119
7.2.3 Single pulse study of eclipsing binaries	120
7.2.4 Timing pulsar binaries for gravity tests	121

7.1 Summary and conclusion

In this thesis we have investigated two equally important aspects of radio pulsar science: a) discovering pulsar binaries, and b) exploiting them for various science applications with the help of radio timing.

Discovering MSPs in binaries is crucial to unfold many fundamental mysteries associated with pulsars, ISM, GCs, or even the nature of the gravitational field, these include, the nature of matter and radio pulse emission mechanism in NSs, formation and evolution of various types of pulsar binaries, understanding magnetic fields in the ISM and GCs, constraining gravitational potential models in GCs, testing GR and constraining alternative theories of gravity, and many more. As discussed in Chapter 1, GCs due to their immense stellar densities promote tidal interactions with two and three body stellar encounters, making them factories of MSP binaries, some of them with unconventional properties. Since they serve as invaluable targets to discover exotic pulsar binaries, the pulsar search surveys carried out as part of this thesis (presented in Chapters 3 and 4) are targeted on GCs.

The known population of pulsars in GCs are only the tip of the iceberg. Given their large distances, all surveys for pulsars in GCs are sensitivity limited. Thus, whenever new telescope facilities are installed or existing telescopes undergo major upgrades in their receivers and(or) backends, we witness a steep increase in the number of MSP discoveries (Dai et al., 2020; Pan et al., 2021; Ridolfi, A., Gautam, T. et al., 2021; Bhattacharyya et al., 2021; Ridolfi et al., 2022a; Gautam et al., 2022). Additionally, since the high frequency surveys can miss relatively steep spectrum pulsars, surveys

at low frequencies are crucial to discover this pulsar population. Below we summarise two pulsar search surveys presented in this thesis:

- In Chapter 3, we presented one such survey carried out with the upgraded GMRT at frequencies of 400 MHz and 650 MHz. This low frequency survey made use of the fact that the new wide-bandwidth receivers allow for an improved detection sensitivity for steep spectrum pulsars. Along with this the installation of online coherent de-dispersion facility at the telescope (that removes the intra-channel dispersive smearing from the pulses based on the nominal DM of the cluster) allows for an enhanced search sensitivity for pulsars especially in distant clusters where the dispersion is more pronounced. In this survey, we targeted eight GCs, five of which have high DM ($> 100 \text{ pc cm}^{-3}$), to search for isolated and binary pulsar systems using advanced Fourier domain acceleration and jerk search techniques discussed in Chapter 2.

The searches resulted in the discovery of an MSP in a binary system, NGC 6652B, rotating every 1.83 ms. With continued timing observations, we constrained the Keplerian parameters of the binary using timing methods described in Chapter 2. We find that the pulsar is in a near-circular orbit with an orbital period of 28.7 hrs. We constrained the minimum companion mass to $0.21 M_{\odot}$ indicating a Helium WD companion. Using the archival GBT data, we obtain a *phase-connected* solution for the binary that spans over 10 years.

As discussed in Chapter 2, an interesting advantage for targeted searches in GCs is the ability to simultaneously detect all the known pulsars in the host clusters by folding the search mode observations with their respective ephemerides. We were able to re-detect 22 known pulsars in this same survey and estimate the flux densities for 18 of these, of these 15 did not have any previously reported flux estimates at such low frequencies. With these flux measurements, we could better constrain the spectral indices for these pulsars. In addition, using the fact that the observations were recorded with wide-bandwidth (200 MHz), we could also determine scattering timescales and scattering indices for 7 of these pulsars. Such estimates are also helpful to determine the best timing band to follow-up pulsars for precision pulsar timing.

Moreover, with the help of simultaneously recorded visibility data from the phased array, we created radio images of these clusters to identify steep spectrum compact sources in them. We identified three new radio sources in NGC 6652, and one new radio source in NGC 6539. As discussed in detail in Section 2.3, identifying such sources in the radio images of GCs help us detect previously undiscovered pulsars that might have been missed by either the small receiver beam size or limited search techniques of previous surveys on these clusters.

- In Chapter 4, we presented another pulsar search survey targeted on GCs, also carried out with an interferometer, this time making use of the recently inaugurated MeerKAT radio telescope. For southern sky GCs (with declination $< -45^{\circ}$),

our survey sensitivity is more than five times better than previously performed GC survey with the Parkes radio telescope (Possenti et al., 2003). In this survey we targeted nine GCs at L-band (1.4 GHz) in the southern hemisphere, and prioritised core-collapse clusters that are likely to form exotic pulsar binaries.

As expected from the exceptional sensitivity of MeerKAT, we discovered eight new MSPs in six GCs in this survey. The discoveries include two eclipsing pulsar binaries (or spider pulsars): 47 Tuc ac and 47 Tuc ad in compact orbits (< 0.32 days) with low-mass companions, three wide orbit (> 0.7 days) pulsar binaries: NGC 6624G, M62G, and Terzan 5an, and three isolated MSPs: NGC 6652D, NGC 6624H, and NGC 6752F. These discoveries assert the known differences in the GC pulsar population i.e. a dominant population of isolated pulsars and exotic pulsar binaries in the core-collapse clusters. This is due to a higher number of dynamical interactions and larger interaction rates per binary in such clusters (see Chapter 1). In our survey, all the three isolated MSPs are found in core-collapse clusters, while four out of five binaries are found in non core-collapse clusters. The properties of the only binary discovered in a core-collapse cluster in our survey (NGC 6624G) are, as expected, unconventional. The binary has a high eccentricity of 0.38, and the pulsar companion is likely either a heavy WD or a NS. As discussed in Chapter 1, such systems are likely a result of secondary exchange encounter where the original companion that recycled the pulsar is replaced by a high mass star, this interaction gives the system its high eccentricity. Of the new discoveries, we presented a *phase-connected* solution for Terzan 5an, NGC 6624G, and NGC 6752F, and a partially connected solution for M62G.

With the use of the tiling capabilities of the TRAPUM acquisition system, we identified the position of pulsars in NGC 6624. Localising pulsars is useful in deriving a good timing solution for both the previously known pulsars and new discoveries. This survey served as a test-bed for the more sensitive ongoing TRAPUM GC pulsar survey (discussed in Section 7.2.1).

The pulsar search surveys (such as the ones presented in this thesis) have unveiled, and will unveil new interesting pulsar systems, either isolated or in binaries. In order to understand their nature and reveal their scientific potential, it is crucial to perform long-term radio pulsar timing. As mentioned in the Introduction, radio timing, specially on relativistic binaries, has many exciting applications: for instance, observation of relativistic effects (quantified by the PK parameters, see Section 2.5) allows measurements of the mass of the pulsar and its companion, shedding light on the formation and evolution of the binary. Additionally, the self-consistency of the masses predicted by several PK parameters yield precise tests of GR and restrictive limits on the alternative theories of gravity.

In the following chapters of this thesis (5 and 6), we provide two prime examples of this type of applications:

- In Chapter 5 we discuss the timing analysis of PSR J1952+2630 - a 20.7 ms pulsar in a short orbit (9.4 hrs) with a heavy WD companion. We performed six months of timing observations with the 305-m Arecibo radio telescope in 2020 and combined them with the discovery and early timing observations carried out from 2010-2012 and more recent observations with the FAST radio telescope. Using this 11-year timing baseline, we improved the spin, astrometric, and orbital parameters for this system and detected three relativistic effects: the advance of periastron, the orbital period decay, and the Shapiro delay.

With the detection of these effects, we constrained the mass of the pulsar ($M_p = 1.20^{+0.28}_{-0.29} M_\odot$) and the WD ($M_c = 0.97^{+0.16}_{-0.13} M_\odot$). We used the TOA uncertainty achieved with the FAST telescope to simulate the data to determine the system's potential as a gravitational laboratory. We found that by year 2032, with four orbital campaigns every year, this system has the potential to provide some of the most restrictive limits on the nature of gravitational waves, providing in particular strict limits on dipolar gravitational wave emission, and to constrain the alternative gravity theories that predict such emission. We quantify these constraints within the Damour-Esposito-Farèse (DEF) gravity by obtaining limits on its $\{\alpha_0, \beta_0\}$ parameters. These limits are comparable to PSR J1738+0333 which is currently the best radiative test in $\beta_0 > 2$ region. Interestingly, unlike the latter system, PSR J1952+2630 can keep improving on its mass measurements with time, and thus has the potential to provide improvements in these parameters, especially if the pulsar mass turns out to be larger, $M_p > 1.5 M_\odot$. The restrictive factor for this system will be the uncertainty of the kinematic contributions that appear in the measurement of the orbital decay, this limit comes from the poor estimate of its distance.

- In Chapter 6, we present another pulsar binary that we studied as part of this thesis: PSR J1012–4235. It is a 3.1 ms pulsar in a 37.9 day binary orbit with a WD companion. This pulsar was first identified in gamma rays with the Fermi telescope and later the pulsations were discovered in radio from a pulsar search survey carried out with Parkes radio telescope. To improve the orbital parameters and identify the nature of the companion and the NS, we performed three years of timing observations on this system with the MeerKAT radio telescope. Apart from refining orbital and astrometric parameters, we detected a significant relativistic Shapiro delay signature in the system. This yielded a precise orbital inclination and masses for the pulsar and the companion: $i = 88.06^{+0.28}_{-0.25}$ deg, $M_p = 1.44^{+0.13}_{-0.12} M_\odot$, and $M_c = 0.270^{+0.016}_{-0.015} M_\odot$. The companion mass agrees well with the prediction of [Tauris & Savonije \(1999b\)](#) for the formation of MSP-He WDs, thus it is likely a Helium WD.

An important result of our measurement of the parallax and proper motion of the system is the conclusion that additional timing with MeerKAT will allow a limit on the variation of gravitational constant, \dot{G}/G , that is one order of magnitude

better than any current measurements with binary pulsars.

7.2 Future work

7.2.1 TRAPUM GC pulsar survey

One of the MeerKAT array's large science project is to search and discover exotic pulsar binaries in GCs. The TRAPUM GC survey is being carried out for this purpose. This survey makes use of the whole MeerKAT array (with 56 to 64 antennas), thus significantly improving the search sensitivity compared to the census presented in Chapter 4 which exploited only the core of the array (38-42 antennas). The TRAPUM acquisition system creates 200-400 synthesized beams that cover 1-4 arcminutes of sky, this makes the survey especially sensitive to pulsars present at the outskirts of the clusters. An interesting advantage of this survey is that each synthesized beam is around 12 arcseconds in size, thus a pulsar discovered in one of the beams can be instantly localised by comparing its detection SNR in the nearby beams. This localisation, as performed for NGC 6624G (discussed in Chapter 4), is extremely important for: a) improving detection sensitivity in follow-up timing observations, and b) deriving a correct timing solution by fixing a more accurate pulsar position in the timing model. The enhanced sensitivity of this survey is bound to create a new wave of pulsar discoveries that will soon be followed by exciting science applications. We can already see an example of this: 13 new pulsars have been recently discovered in a single GC, NGC 1851 as part of this survey (Ridolfi et al., 2022b). At the time of writing this, there have been 54 new pulsars discovered in GCs¹, including eight in the census presented in this thesis.

One shortcoming of such survey is that a large number of synthesized beams must be processed and searched to cover the entire extent of GCs, this requires a significant amount of storage and processing power. The processing can get especially challenging if advanced searches are carried out (such as jerk search) or if the cluster host no previously known pulsar, in which case a large range of DMs must be searched (based on the non precise distance to the cluster). We can overcome this issue by mapping the entire clusters with radio imaging and identifying possible new pulsars even in the outskirts of the clusters.

7.2.2 Imaging GCs to search for pulsars

With radio imaging of GCs, unlike in time-domain searches, we can map the entire clusters for radio sources, thus discovering the rarely explored pulsar population located outside the cluster's core radii. We can identify bright radio sources as likely pulsars by checking three main aspects: a) their shape - pulsars are compact point-like sources, b) their spectra - pulsars have steep spectrum, c) their polarisation - pulsars

¹<http://trapum.org/discoveries/>

are highly polarised sources, and d) their scintillation - pulsars in some clusters scintillate. After localising likely pulsar sources in the synthesized images, we can point the telescope array on their position, and significantly improve their detection sensitivity in the follow-up time-domain observations that will assist to confirm if the source is a pulsar.

This approach (as was used to detect the first GC pulsar: M28A [Lyne et al. 1987](#)) will be highly efficient in discovering the first pulsar in clusters, where no pulsar have been found to date. This is because for the clusters with unknown nominal DMs (i.e. uncertain distances), the computational times for time-domain searches can become increasingly large with a large range of DMs to search. Through radio mapping we can quickly localise and discover the brightest, steep spectrum sources in the cluster without having to perform any deep time-domain observations, making it a more economic approach compared to the MeerKAT surveys. This procedure will allow us to: a) detect the brightest sources in the cluster with no dependence on their vicinity to the cluster core, and b) narrow down the DM ranges to search in the time-domain surveys that will follow after the first discovery. Looking at multiple advantages of this method, interferometric surveys will evidently play a crucial role for GC pulsar surveys in future, especially to explore a large number of clusters for new pulsars.

7.2.3 Single pulse study of eclipsing binaries

An advantage of high resolution search mode data acquired for pulsar search surveys, especially the one that is coherently de-dispersed, is its applicability for single pulse analysis of eclipsing pulsars (“spiders”, see Chapter 1). Single pulses are pulses coming from individual rotations of pulsars that are brighter by a factor more than 5-10 times the time-averaged flux of the normal pulses. This substantial change in the flux of the pulses is thought to arise from the lensing effect of the intra-binary plasma that is ablated from the pulsar’s companion ([Main et al., 2018](#); [Bilous et al., 2019](#)). Thus this effect is more pronounced in the region near the ingress and egress of the eclipse and such pulses are correlated over time. By studying these pulses, we can derive a lens model for the plasma and resolve the pulsar’s magnetosphere up to several kms, this will help us get insight into the pulse emission locations ([Main et al., 2018](#)). Additionally, by analysing the polarisation of these pulses, we can constrain the magnetic field strengths of the intra-binary plasma ([Li et al., 2019](#)).

Interestingly, in the search mode data recorded for our GMRT GC survey (discussed in Chapter 3), we detected both the ingress and egress of an eclipse in Terzan 5A. Analysing individual pulses in this data revealed several single pulses with intensities more than 10 times the average pulse intensity (as also seen by [Bilous et al. 2019](#)). In future, we plan to exploit this data to constrain the intra-binary plasma properties. Similar analysis can also be carried out for another eclipsing binary pulsar that is re-detected in our ongoing TRAPUM GC survey: NGC6342A. The origin of the eclipsing material in this binary is unclear as its slow rotation (~ 1 s) is not

sufficient to drive the plasma winds from its companion (van Kerkwijk et al., 2000). Several of the measured properties of this system do not align with any known pulsar binary formation scenario. For instance, it is a young pulsar in a GC, but considering its near-circular orbit, there is a rare possibility that it underwent an AIC or exchanged its companion, additionally it is further away from the cluster core, making it further difficult to explain its formation. In our two four-hr long observations of this cluster, we covered a large range of orbital phases of this binary, and detected several eclipses. From the initial analysis of this data, we identified many single pulses in this pulsar with magnifications (= single pulse intensity/average intensity) up to 13, we plan to delve deeper into this analysis to attempt to solve some of the mysteries associated with this binary's formation mechanism. Similar study can be performed on other eclipsing pulsars that are re-detected in the existing GC search mode data. This type of analysis can save a large amount of telescope time and storage space in future, and can be used as a preliminary study for these systems.

7.2.4 Timing pulsar binaries for gravity tests

Even though the low eccentricity and low-precision measurements of relativistic effects in PSR J1952+2630 might at first suggest that the system may not yield good constraints on gravity theories, dedicated timing analysis (as discussed in Chapter 5) and simulations have revealed its exciting potential as a gravitational laboratory by constraining DEF gravity parameters. A similar result is seen in the timing analysis of PSR J1012–4235 (presented in Chapter 6), which show that, in the near future, the system can place a restrictive limits (an order of magnitude better than current constraints) on the variation of gravitational constant.

These results are inspiring, for they show that persistent timing and detailed analysis of particular systems can reveal great scientific potential. By digging diligently, we can occasionally find some real jewels.

**Paper titled “Upgraded GMRT survey
for pulsars in globular clusters. I:
Discovery of a millisecond binary
pulsar in NGC 6652”**

The paper *Gautam et al. A&A (2022), Volume 664, August 2022, Article Number A54* is reproduced below in its original form with permission by ESO.

Upgraded GMRT survey for pulsars in globular clusters

I. Discovery of a millisecond binary pulsar in NGC 6652

T. Gautam^{1,*}, A. Ridolfi^{1,2}, P. C. C. Freire¹, R. S. Wharton³, Y. Gupta⁴, S. M. Ransom⁵, L. S. Oswald^{6,7},
 M. Kramer¹, and M. E. DeCesar⁸

¹ Max-Planck-Institut für Radioastronomie, Auf dem Hügel 69, 53121 Bonn, Germany
 e-mail: tgautam@mpi-fr-bonn.mpg.de

² INAF – Osservatorio Astronomico di Cagliari, Via della Scienza 5, 09047 Selargius (CA), Italy

³ NASA Postdoctoral Program Fellow, Jet Propulsion Laboratory, California Institute of Technology, Pasadena, CA 91109, USA

⁴ National Centre for Radio Astrophysics, Tata Institute of Fundamental Research, Pune 411007, Maharashtra, India

⁵ National Radio Astronomy Observatory, 520 Edgemont Rd., Charlottesville, VA 22903, USA

⁶ Department of Astrophysics, University of Oxford, Denys Wilkinson building, Keble road, Oxford OX1 3RH, UK

⁷ Magdalen College, University of Oxford, Oxford OX1 4AU, UK

⁸ George Mason University, Fairfax, VA 22030, resident at US Naval Research Laboratory, Washington, DC 20375, USA

Received 7 January 2022 / Accepted 27 May 2022

ABSTRACT

Context. Globular clusters (GCs) contain a unique pulsar population, with many exotic systems that can form only in their dense stellar environments. Such systems are potentially very interesting for new tests of gravity theories and neutron-star mass measurements.

Aims. The leap in sensitivity of the upgraded Giant Metrewave Radio Telescope (uGMRT) in India, especially at low radio frequencies (<1 GHz), motivated a new search for radio pulsars in a group of eight southern GCs. We aim to image these clusters in order to have independent measurements of the radio fluxes of known pulsars and the identification of bright radio sources that could be pulsars missed by pulsation search pipelines due to their inherent limitations.

Methods. The observations were conducted at 650 MHz (Band 4 receivers) on Terzan 5, NGC 6441, NGC 6440, and NGC 6544, and at 400 MHz (Band 3 receivers) on NGC 6652, NGC 6539, NGC 1851, and M 30. Segmented acceleration and jerk searches were performed on the data. Simultaneously, we obtained interferometric data on these clusters, which were later converted into radio images.

Results. We discovered PSR J1835–3259B, a 1.83-ms pulsar in NGC 6652; this is in a near-circular wide orbit of 28.7-h with an unidentified low-mass ($\sim 0.2 M_{\odot}$) companion, likely a helium white dwarf. We derived a ten-year timing solution for this system. We also present measurements of scattering, flux densities, and spectral indices for some of the previously known pulsars in these GCs.

Conclusions. A significant fraction of the pulsars in these clusters have steep spectral indices. Additionally, we detected eight radio point sources not associated with any known pulsar positions in the radio images. There are four newly identified sources, three in NGC 6652 and one in NGC 6539, as well as one previously identified source in NGC 1851, NGC 6440, NGC 6544, and Terzan 5. Surprisingly, our images show that our newly discovered pulsar, PSR J1835–3259B, is the brightest pulsar in all GCs we have imaged; like other pulsars with broad profiles (Terzan 5 C and O), its flux density in the radio images is much larger than in its pulsations. This indicates that their pulsed emission is only a fraction of their total emission. The detection of radio sources outside the core radii but well within the tidal radii of these clusters show that future GC surveys should complement the search analysis by using the imaging capability of interferometers, and preferentially synthesise large number of search beams in order to obtain a larger field of view.

Key words. pulsars: individual: J1835–3259B – pulsars: general – globular clusters: general – scattering – stars: neutron

1. Introduction

With immense stellar densities of up to 10^6 stars per cubic parsec, the cores of globular clusters (GCs) are unique environments for tidal captures and the exchange encounters of stellar systems (Sigurdsson & Phinney 1995; Pooley et al. 2003). Interactions of old neutron stars (NSs) with low-mass stars form a large population of low-mass X-ray binaries (LMXBs) in GCs, about three orders of magnitude more numerous per unit stellar mass than in the Galactic field (Clark 1975).

If the LMXB is not disturbed by close stellar encounters (which are exceedingly rare in the Galactic disc), then the NS in the binary will continue accreting mass from its evolving

companion (Alpar et al. 1982; Radhakrishnan & Srinivasan 1982; Bhattacharya & van den Heuvel 1991). When accretion stops, we have a binary system with a low-eccentricity orbit consisting of a pulsar with a spin period of a few milliseconds and generally very small spin-down rates; these are known as ‘millisecond pulsars’ (MSPs). Their companions are either light white dwarf (WD) stars or a low-mass non-degenerate star (in which case, we likely have an eclipsing system). In some cases, the MSP has no companion at all, possibly because it was completely ablated by winds from the pulsar. Almost all pulsars in the Galactic disc with spin periods smaller than 8-ms fit into these groups.

The large number of LMXBs per unit stellar mass in GCs should result in a similarly enhanced MSP population. Since the discovery of the first GC pulsar, PSR B1821–24 (Lyne et al. 1987), a total of 246 pulsars in 36 GCs have been discovered to

* Member of the International Max Planck Research School (IMPRS) for Astronomy and Astrophysics at the University of Bonn.

date¹; this population includes about a third of all known MSPs. As expected, most of these are found in GCs with a large stellar encounter rate, Γ (Verbunt et al. 1987).

The pulsar populations in the different GCs are strikingly different. In 47 Tucanae, the spin periods of the 29 known pulsars range between 2 and 8-ms (Ridolfi et al. 2016, 2021; Freire et al. 2017). The same is true for other GCs, particularly those with low-density cores. The cluster 47 Tucanae is important because, although it has a large Γ (hence the large number of MSPs), it has a low interaction rate ‘per binary’, γ (Verbunt & Freire 2014). This means that once an LMXB forms, there is little chance of it being disturbed again; this results in a set of MSPs similar to the Galactic MSP population described above.

However, in GCs with very high core densities, such as core-collapse clusters, γ is much higher. This means that once an LMXB forms, there is a much higher probability that it will be disturbed, either as an LMXB or later as an MSP–WD system. This results in a large number of binary disruptions, with many isolated and partially recycled pulsars present (instead of the fully recycled pulsars seen in low-density GCs).

Such perturbations can create ‘exotic’ binary systems, which have unconventional properties. In all clusters, relatively close interactions increase the orbital eccentricities of many MSP–WD binaries by orders of magnitude compared to those observed in the Galactic disc (Phinney 1992). In high- γ clusters, secondary exchange encounters – where a previously recycled pulsar acquires a new companion – can create eccentric pulsar binaries with high-mass degenerate companions such as another NS or a heavy WD (NGC 1851A, Freire et al. 2004; Ridolfi et al. 2019; NGC 6544B, Lynch et al. 2012; NGC 6652A, DeCesar et al. 2015 and NGC 6624G, Ridolfi et al. 2021), which are unlike any observed in the Galactic disc. This mechanism could potentially create an MSP–black hole (BH) system, which would offer a unique laboratory for tests of the fundamental properties of gravitational physics (Wex & Kopeikin 1999; Liu et al. 2014). For this reason, searching for pulsars in high- γ GCs is a high priority.

One important feature of the MSP population in GCs is that we only detect its brightest members. The reason for this is the large distances to GCs, typically of the order of 10 kpc. This means that a large pulsar population remains undetected, yet there are likely several thousands in the Galactic GC systems (e.g., Bagchi et al. 2011; Hessels et al. 2015). The main barrier to detecting this large population is primarily a lack of sensitivity. Therefore, whenever new observing systems with higher sensitivities become available, there is a large increase in the number of known pulsars in GCs.

The previous wave of discoveries happened in the mid-2000s. This was brought about by the use of sensitive, broadband L (1–2 GHz) and S -band (2–4 GHz) receivers, leading to quite a few new discoveries at Parkes (Camilo et al. 2000; Possenti et al. 2005), Arecibo (Hessels et al. 2007), the Green Bank Telescope (GBT; Ransom et al. 2005; Freire et al. 2008), and the Giant Metrewave Radio telescope (GMRT; Freire et al. 2004). The inauguration of a new generation of extremely sensitive radio telescopes such as FAST (Nan & Li 2013) and MeerKAT (Booth & Jonas 2012; Jonas & MeerKAT Team 2016; Camilo et al. 2018) and major upgrades to existing facilities, such as the installation of technologically advanced digital back-ends and new broad-band receivers with lower system temperatures, is now resulting in another wave of discoveries,

with close to 100 new pulsars found as of April 2022 (e.g., Ridolfi et al. 2021; Pan et al. 2021).

One of the facilities that have recently become available is the upgraded GMRT (Gupta et al. 2017), henceforth uGMRT. The GMRT has long been one of the most sensitive telescopes at low radio frequencies, and for that reason, it has played an important role in discovering steep-spectrum pulsars (e.g., Freire et al. 2004; Bhattacharyya et al. 2016, 2021; Joshi et al. 2009). With the recently installed sensitive receivers operating at lower system temperatures covering a wide bandwidth of ~ 200 MHz (more than ten times that of the GMRT), along with the installation of a real-time coherent de-dispersion facility, the uGMRT represents a significant improvement in sensitivity compared to the GMRT. For that reason, it will have a critical role in discovering steep-spectrum pulsars. As described in detail below, the new coherent de-dispersion facility is especially helpful for clusters with higher dispersion measures (DMs); in earlier GMRT surveys, radio pulsations from high-DM pulsars were smeared out at low frequencies due to intra-channel dispersion. In addition, the interferometric nature of the GMRT allows the simultaneous recording of visibility data from the full array; this results in radio images of entire clusters and the detection of radio sources that may be missed by the limited size of phase array beams – some of which could be undiscovered pulsars.

These instrumental improvements and the low-frequency bands, which complement those of the other ongoing GC pulsar surveys, motivated us to start a GC pulsar survey with this instrument. Indeed, all recent sensitive surveys for pulsars in GCs were made in the L or S band. Such high-frequency surveys can be biased towards detecting relatively flat-spectrum sources compared to the low-frequency surveys with similar observational setups. Thus, low-frequency surveys are crucial in the detection of previously undetected steep-spectrum pulsars if they exist, and they help characterise the known pulsars at these frequencies.

In this paper, we report the first results from this survey, from observations of eight GCs at 400 MHz (Band 3) and 650 MHz (Band 4) with the new GMRT Wideband Backend (GWB; Reddy et al. 2017) system of the uGMRT. In Sect. 2, we discuss the survey, including the GC selection criteria, the observations performed to date, estimates of the survey sensitivity, and the data analysis. In the following sections, we describe some of the survey results, which illustrate the variety of topics that can be addressed with the type of data we obtained. The discovery and timing analysis of PSR J1835–3259B, the first pulsar found in this survey, are discussed in Sect. 3. In Sect. 4, we discuss some of the characteristics of the previously known pulsars in these clusters that were detected in our observations, namely their flux densities, spectral indices and scattering timescales. Section 5 presents the imaging analysis and discusses the point radio sources found in the radio images of these clusters. Finally, Sect. 6 provides the summary and conclusions of this paper.

2. Survey details

2.1. Target selection

The considerations made above regarding the interaction rate per binary were the primary guides of our target selection. We chose GCs known to contain eccentric and, in most cases, binary pulsars with high mass ($>0.5 M_{\odot}$) companions (NGC 1851, Terzan 5, NGC 6441, NGC 6440, NGC 6539, NGC 6544), or suspected of having them, such as M 30 (see Ransom et al. 2004;

¹ As of 2022 April 6, see <https://www3.mpi-fr-bonn.mpg.de/staff/pfreire/GCpsr.html>

Table 1. Properties of clusters observed, from [Harris 1996](#) (2010 revision).

Cluster	Coordinates of cluster center (RA, Dec)	Core radius (R_c) (arcmin)	Tidal radius (R_t) (arcmin)	Distance (kpc)	Previously Known Pulsars	Binaries	Core-collapsed
NGC 1851	05:14:06.69, -40:02:48.89	0.06	6.52	12.1	1	1	No
Terzan 5	17:48:04.80, -24:46:45.00	0.18	6.66	10.3	38	19	No
NGC 6440	17:48:52.68, -20:21:39.70	0.13	5.83	8.4	6	3	No
NGC 6441	17:50:13.06, -37:03:05.20	0.11	7.14	11.7	4	2	No
NGC 6539	18:04:49.89, -07:35:24.69	0.54	20.88	8.4	1	1	No
NGC 6544	18:07:20.58, -24:59:50.40	0.05	2.13	2.7	2	2	Yes
NGC 6652	18:35:44.86, -32:59:25.10	0.10	6.31	10.0	1	1	Yes
M30	21:40:22.40, -23:10:48.79	0.06	18.97	8.0	2	2	Yes

see Table 1). Searching such clusters for more exotic binaries is especially valuable for scientific follow-up as it is in such binaries that we have been able to precisely measure the NS masses ([Lynch et al. 2012](#); [Ridolfi et al. 2019](#)) – and in one case (M15C) even perform a test of GR ([Jacoby et al. 2006](#)). Furthermore, as mentioned before, the secondary exchange encounters that formed these binaries could in principle form MSP–MSP or MSP–BH systems.

Another advantage of this group of GCs is that the known DMs make the search process easier. Furthermore, the timing of some pulsars known in these clusters has already benefited from our additional GMRT observations ([Ridolfi et al. 2019](#)). Finally, they are located south of the Arecibo and FAST survey areas, where the sensitivity of the uGMRT is competitive, particularly at lower radio frequencies.

Previous low-frequency GMRT GC surveys ([Freire et al. 2004](#)) were restricted to low-DM clusters because of intra-channel dispersive smearing. If we use a filterbank as a back-end, this is given by

$$\tau_{\text{DM}} = 8.3 \times \Delta\nu \times \text{DM} \nu^{-3} \mu\text{s}, \quad (1)$$

where $\Delta\nu$ represents bandwidth of an individual channel in MHz and ν represents the centre frequency of the band (GHz), with $\nu \gg \Delta\nu$. Clusters with large DM values exhibit larger pulse smearing within a frequency channel, which increases further for the lower frequencies used in previous GMRT surveys (~ 320 MHz, [Freire et al. 2004](#)). For instance, a cluster with a $\text{DM} > 100 \text{ pc cm}^{-3}$ would lead to a smearing timescale of more than 1.27-ms at 400 MHz (considering a channel bandwidth of 97.6 KHz). Because of this, some of the high-DM clusters have not been searched effectively for pulsars at these lower frequencies: instead, all pulsars in the high-DM GCs Terzan 5, NGC 6440 and NGC 6441 have been found with the S-band system of the GBT or, more recently, in MeerKAT L-band surveys ([Ridolfi et al. 2021](#)).

The use of the uGMRT real-time coherent de-dispersion pipeline coherently removes most of this intra-channel dispersive smearing for clusters with a known DM. This is done by de-convolving the voltages detected by the receiver with the inverse of the transfer function of the interstellar medium. As shown by [Ridolfi et al. \(2019\)](#), this greatly increases the effective time resolution of the data and the signal-to-noise ratio (S/N) of the folded pulse profiles. This means that we can substantially increase the DMs of the clusters we survey at lower frequencies, despite the much larger bandwidths of the uGMRT receivers. Five of the eight GC targets mentioned above have high DMs ($> 100 \text{ pc cm}^{-3}$); the three high-DM clusters we mentioned above have a $\text{DM} > 200 \text{ pc cm}^{-3}$.

For observations at low frequencies, the pulse profile is also smeared by interstellar scattering, which we discuss in Sect. 2.3.

The coherent de-dispersion technique does not allow the removal of this effect; the pulsars will only remain detectable if scattering time, τ_{sc} , is generally shorter (preferably much shorter) than the pulse period. In order to determine the effect of scattering on the pulse profiles, we observed four of these clusters at 650 MHz. Pulsars whose profiles are negligibly scattered at this frequency will be observed at even lower frequencies in future observations. This process is also important in determining the best timing band for individual pulsars.

2.2. Observations

We observed the eight target GCs with the GMRT from April 2017 to September 2018. The low-DM clusters NGC 6652 and M30 were observed at 400 MHz, and the others at 650 MHz (see Table 2). The observations were performed with a bandwidth of 200 MHz and utilised the digital GWB system. We recorded a ‘phased-array’ (PA) voltage stream in which the voltages from the antennae used in each observation are added coherently with time delays appropriate for the region of the sky targeted. From these voltages, a first processing pipeline at GMRT calculates the total intensities for each 0.097 MHz channel and integrates them for 81.92 μs ; this is known as the PA data. To maintain the correct phasing of the array, we observed a phase calibrator (chosen closest to the target) for three mins after every 1-h in Band-4 (650 MHz) observations and after every 30 min in Band-3 (400 MHz) observations. This is shorter than our intended integration times (see Table 2); for this reason, when we do the calibration we keep taking data continuously, in order to maintain time coherence for the whole observation. The samples taken during the time the telescope is not pointed at the target were later replaced with the median bandpass values using PRESTO’s `rfifind` routine. Since all target GCs have known associated DMs, we could also use a second processing pipeline (available at GMRT since September 2017) that divided the band into 0.195 MHz channels and coherently de-dispersed each channel’s voltage stream in real-time at the DM of the cluster ([De & Gupta 2016](#)). After de-dispersion, the total power for each channel was integrated for 20.48 μs , resulting in the ‘coherently de-dispersed’ (CD) data.

We used 12 of the central square antennas (closely distributed set of antennas at the central region of the GMRT configuration) to create the PA beam, which gave us a maximum baseline of 1.1 km. This resulted in PA and CD beams of sizes \AA ; 2.3; and \AA ; 1.5; at 400 MHz and 650 MHz, respectively, and allowed us to cover the cores (where most of the compact objects are expected to be found) of all GCs (the core radius of the largest GC, NGC 6539, is $\sim \text{\AA}$; 0.5;).

In parallel, u - v visibilities are also calculated from the voltages of all functioning antennae in the array (up to 30 of them),

Table 2. Observation details.

Cluster	Observation (Epoch)	Frequency (MHz)	Integration Time (s)	Target position	Coherent DM (pc cm ⁻³)
NGC 1851 (*)	58051	400	2400	J0514–4002A	52.15
Terzan 5	58332	650	6660	Cluster center	238.73
NGC 6440	58363	650	7498	J1748–2021A	223.00
NGC 6441	58332	650	6660	J1750–3703C	232.00
NGC 6539 (*)	57829	400	9744	B1802–07	186.32
NGC 6544	58363	650	7500	J1807–2459A	135.50
NGC 6652	58084, 58165	400	2400	J1835–3259A	63.35
M30	58102	400	1938	J2140–2310B	25.09

Notes. (*) Only the longest epoch was searched in this survey; we plan to search the whole dataset thoroughly in the future.

this gave us baselines with lengths up to ~ 25 km. These were recorded every 16-s and allowed the imaging of a good fraction of the primary beam of the antennae, with a spatial resolution that is significantly better than that of the central square. To enable high sensitivity for faint pulsars, each cluster was observed for more than 30 mins.

2.3. Survey sensitivity

The minimum detectable flux density in this survey for a pulsar can be calculated with the radiometer equation (Dewey et al. 1985):

$$S = \frac{S/N \beta T_{\text{sys}}}{G \sqrt{n_{\text{pol}} \text{BW}_{\text{eff}} \Delta t_{\text{obs}}}} \sqrt{\frac{\zeta}{1-\zeta}}, \quad (2)$$

where the total system temperature, T_{sys} is 130 K for 400 MHz and 102.5 K for 650 MHz. The total gain of the 12 antennae of the central array, G , is 4.2 K Jy⁻¹; the number of polarisations summed n_{pol} is 2; the minimum S/N is chosen to be 10; the length of a typical observation, Δt_{obs} , is 2 h; the usable bandwidth BW_{eff} is taken as 180 MHz (considering ~ 20 MHz loss due to MUOS satellites); and the signal loss due to digitisation, β , is close to (and assumed to be) 1, because our samples had 16 bits. ζ is the observed duty cycle of the pulse defined as the ratio of observed width and pulse period.

The observed pulse width can be affected by the interstellar medium in the form of scattering, dispersion smearing across individual frequency channels, dispersion smearing due to the finite DM step size of the time series, and finite time sampling. Since the CD data is coherently de-dispersed at the nominal DM of the cluster, there was very little contribution to pulse broadening from dispersive smearing across each channel. Assuming a negligible contribution from scattering, only contributions from finite sampling time and DM step size are added in the estimation of ζ ; this means that these sensitivity curves represent a best-case scenario. The intrinsic pulse width is assumed to be 8% of the pulse period, which is a sensible number between the typical values of MSPs and slow pulsars (a similar value is also used for the sensitivity estimate of a GC survey with MeerKAT, Ridolfi et al. 2021).

Figure 1 shows the minimum sensitivity of 400 and 650 MHz surveys. For slow pulsars ($P > 50$ ms), sensitivity is up to 50 μ Jy for Band-4 and 60 μ Jy for Band-3 observations, while for fast pulsars ($P \sim 5$ ms) it is up to a minimum flux density of ~ 100 μ Jy. Bold sensitivity curves represent the case where the pulsar candidate's actual DM is considered the farthest from the trial DM

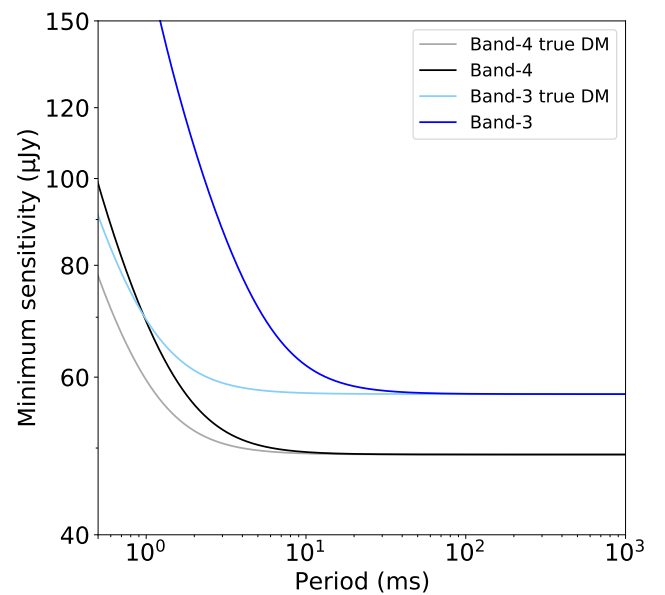


Fig. 1. Minimum detectable flux density as a function of spin periods. Black and blue lines indicate sensitivity curves for 650 MHz and 400 MHz receivers. Lighter shades represent respective sensitivity curves if the DM trial value is the same as the true DM of a pulsar candidate.

value at which the time series are created, that is, the true DM value is assumed at the edge of the DM step size. Lighter shaded curves represent the sensitivity if a pulsar candidate's actual DM happens to be the same as the trial DM value; in which case, there is a lower sensitivity threshold.

2.4. Data Reduction

For the 650 MHz observations, the receivers' response had large variations, leading to significant power changes within the bandpass. Therefore, the initial data reduction involved flattening the band shape. This was done using the data reduction software GPTool² by re-normalising the data of each frequency channel to the bandpass average of that channel.

The next step involved down-sampling the dataset from its native digitisation of 16-bit to the more commonly used 8-bit format to make it compatible with the commonly used pulsar software. The bitshift for this conversion was chosen such that

² <https://github.com/chowdhuryaditya/gptool>

the test pulsar in each epoch had the highest S/N. We used `ugmrt2fil`³ to down-sample and then convert the data into SIGPROC's (Lorimer 2011) filterbank format, this allowed us to use the latest version of PRESTO and perform more advanced acceleration and jerk searches.

2.5. Search technique

The search procedure used in this survey is based upon the pulsar searching package PRESTO⁴ (Ransom et al. 2002); the routines mentioned below are from this package. We used a modified version of an automated pipeline PULSAR_MINER⁵ v1.1. This pipeline consists of the following steps.

The first step consist of removing the effect of radio interference due to terrestrial signals. This was done by using the routine `rfifind`⁶, which creates a mask by identifying abnormalities of mean and variances in user-defined, averaged, time, sub-integration, and frequency channel ranges in the data. This step is crucial to identifying narrow-band RFI signals. The masks generated from this routine were used throughout the search analysis to zap bad channels and time integrations from the de-dispersed time series and the original data. In our case, typically around 10–15% of the data were removed at this step. In order to zap the broadband RFI signals, which may be periodic but do not have a dispersion peak at a finite DM due to their terrestrial nature, we created a 0-DM time series using the routine `prepdata` and searched for strong periodic signals (and their harmonics) in the data. The frequencies were then noted in a ‘`zaplist`’ file, which was used later in the analysis to remove these signals from the finite DM time series. In addition, the frequencies and harmonics of already known pulsars in these clusters were also added to this list to reduce the resulting number of candidates from these searches.

The second step involves creating a de-dispersed time series of the masked data for a range of DM values. Since the DMs of all the clusters searched were known beforehand, we searched these clusters with a DM range from $DM_{\min} - 5 \text{ pc cm}^{-3}$ to $DM_{\max} + 5 \text{ pc cm}^{-3}$, where DM_{\min} and DM_{\max} are the minimum and maximum DMs of known pulsars in each cluster. We used PRESTO's `DDP1an.py` routine to calculate the optimum DM step size and down-sampling factor (to reduce the effective time resolution). This step accounted for the dispersion smearing across each channel and helped reduce the total computational time. This scheme was then used to create the time series with the `prepsubband` routine.

The third step performs a Fourier transform on each time series to extract the periodic signals. This was done with the `realfft` routine. The pipeline then removed the red noise in the Fourier power from each of these power spectra to flatten fluctuations due to receiver or acquisition systems.

In the next step, these power spectra were searched for periodic components using PRESTO's `accelsearch` routine. It search for frequencies and their harmonics (with power summed up to the 8th harmonic in this search) and shortlist strong periodic signals. In binary pulsars, the orbital acceleration along the line of sight (a) cause a change in the Doppler shift that smears the pulsed signal in the Fourier domain by a number of Fourier bins: $z = \frac{T^2 a}{Pc}$, where P and T are the observed spin period and

the observation time. In our survey, the maximum values of z , z_{\max} used are ± 30 , 300, and 600. To efficiently use the computing power, we first prioritised the searches with lower values of z_{\max} , (± 30 , 300), and then as computing power became available with higher values (± 600). This resulted in sets of searches with maximum accelerations of ~ 3.5 , 34.7, and 70 ms^{-2} for a 5-ms pulsar in a 1-h-long observation. To be sensitive to highly relativistic binaries where the effect of orbital variations can smear the signal in an epoch, each observation was segmented into three to four chunks of ~ 15 – 20 min; this extended the acceleration range up to 560 ms^{-2} and 1100 ms^{-2} , respectively. The routine `accelsearch` can only search for constant acceleration across the integration length, which is an assumption valid only for about one-tenth of the orbit (Johnston & Kulkarni 1991). Thus, to search for compact binaries with improved detection sensitivity in longer time segments, we used the ‘Jerk search’ method (Andersen & Ransom 2018). This algorithm search for a linear change of the acceleration with time (\dot{a}) within the observation span and thus help regain the S/N of the folded profile. For this search, we used the parameter $w_{\max} (\frac{\dot{a}T^3}{Pc})$ of 600, this made our search sensitive for a maximum acceleration change of 1.23 ms^{-2} across a 15-min integration time. Jerk searches were also performed on both 15–20 min segments and the full data span. The candidates from these searches were limited to a period range of 1-ms to 15-s.

The resulting candidates were then shortlisted using `ACCEL_sift.py`. It removes duplicates and harmonics from the candidate list and sorts the candidates based on their Fourier significance. We used the default 3σ threshold that is sufficient to find real pulsar candidates given the large number of trials) and DM peak.

Finally, these candidates were folded both in their corresponding time series and the original filterbank files using the `prepfold` routine. The respective detection parameters for each of the candidates were taken from the files produced by `accelsearch`. Nearly 500–1000 candidates were shortlisted, depending upon the observation length and RFI severity in each observation. Based on the typical total number of trials in our Fourier domain searches (following Eq. (6) of Andersen & Ransom 2018), we obtain a false-alarm threshold S/N (Lorimer & Kramer 2012) of 8.5. The candidate viewing was then performed by visually inspecting folded pulse profiles of each pulsar candidate. This was followed by several checks for harmonics to confirm their nature.

Since the data were coherently de-dispersed, there was negligible intra-channel dispersion smearing; thus, the time resolution was not limited by these smearing timescales. Because of the high time resolution, we needed a smaller DM step size in order not to degrade that resolution via DM smearing when adding the channels. This step is especially crucial at low frequencies as the dispersion smearing become more pronounced. Hence, a large number of time series had to be searched. Thus, to efficiently search the clusters, we used the `Hercules`⁷ computing cluster located at the MPG's computer centre in Garching. The modified version of PULSAR_MINER⁸ was able to perform parallel processing with 184 available nodes, each with 24 CPU cores, where each time series was allotted an individual node (using SLURM⁹) to perform acceleration and jerk searches.

³ <https://github.com/alex88ridolfi/ugmrt2fil.git>

⁴ <https://www.cv.nrao.edu/~sransom/presto/>

⁵ https://github.com/alex88ridolfi/PULSAR_MINER

⁶ https://www.cv.nrao.edu/~sransom/PRESTO_search_tutorial.pdf

⁷ <https://docs.mpcdf.mpg.de/doc/computing/clusters/systems/Radioastronomy.html>

⁸ <https://github.com/tgautam16/jerksearch.git>

⁹ <https://slurm.schedmd.com>

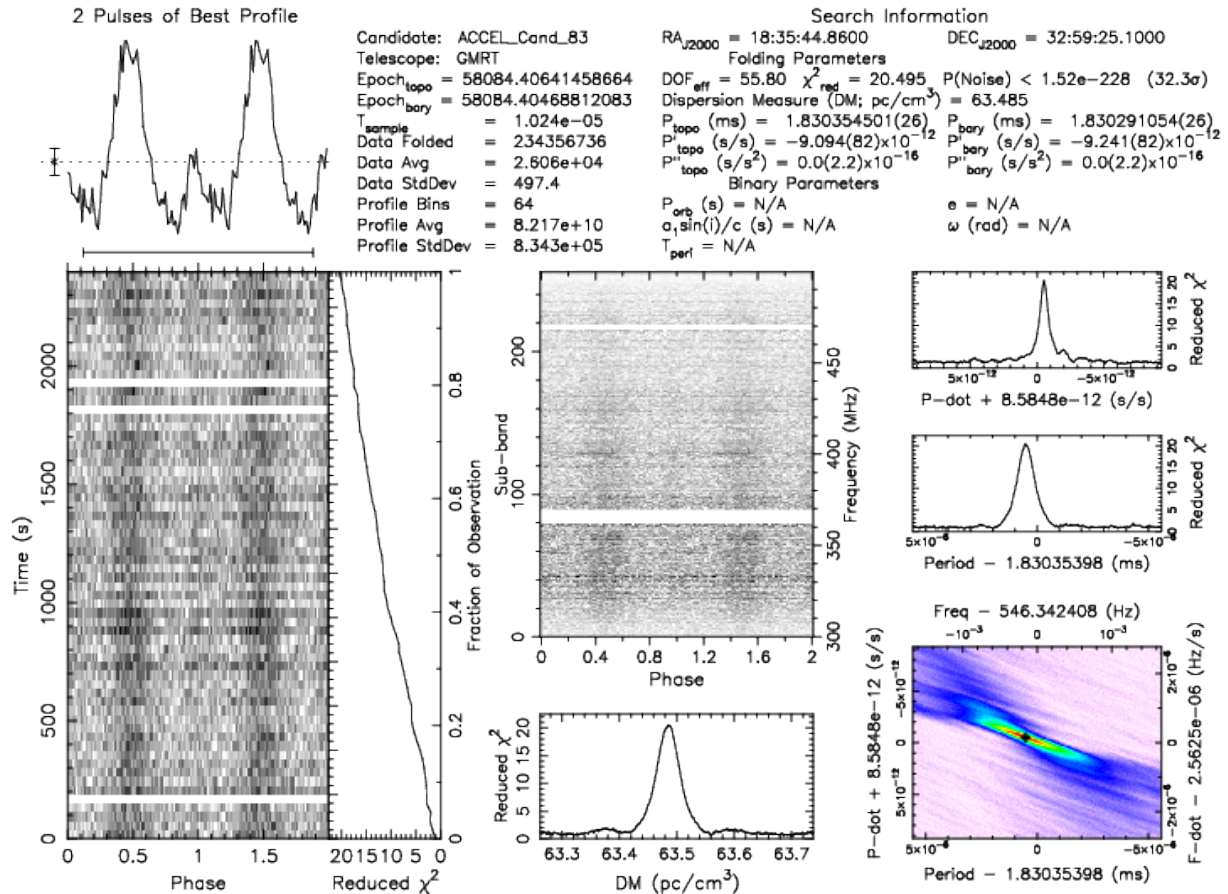


Fig. 2. Discovery plot of NGC 6652B folded with prepfold showing time vs. phase and frequency vs. phase intensity in greyscale.

Likewise, the folding process took place on a single node, making use of 48 threads that folded 24 candidates concurrently.

3. A new pulsar: PSR J1835-3259B in NGC 6652

3.1. Discovery, follow-up, and timing

The search analysis of these clusters resulted in one confirmed discovery, PSR J1835-3259B in NGC 6652. The letter ‘B’ indicates that this is the second pulsar discovered in this cluster, the first being PSR J1835-3259A (DeCesar et al. 2015); we henceforth refer to both as NGC 6652A and NGC 6652B. Interestingly, did not detect NGC 6652A, neither in imaging (see Sect. 5) nor in our PA and CD datasets, even though its position is well within the positions of those beams. This means that it likely has a flat radio spectrum.

NGC 6652B is a 1.83-ms pulsar found in a 40-min GMRT observation of its parent cluster taken on 27 November, 2017 with the 400 MHz (Band 3) receivers, at a DM of 63.48 pc cm⁻³. It was found by the acceleration search with a zmax of 30; the initial detection (see prepfold plot in Fig. 2) had an acceleration of 1.5 ms⁻², clearly indicating that it is a member of a binary system. The pulsar was visible in another 400 MHz observation taken in February 2018, which confirmed its discovery and was also subsequently detected in GMRT 650 MHz observations. Later, it was detected in archival GBT L- and S-band observations taken from 2011 to 2020 with the Green Bank Ultimate Pulsar Processing Instrument (GUPPI) (Ransom et al. 2009) back-end that were originally made to time NGC 6652A. Figure 3 shows the variation of radio intensity with spin phase

of the pulsar (its integrated ‘pulse profile’) at three different frequencies. In all of them, it shows a clear interpulse, which becomes more pronounced at higher radio frequencies.

For new binary pulsars, it is important to determine the nature of the binary companion, along with the orbital, spin, and kinematic properties of the system to find the potential of the pulsar for future scientific studies. We followed up this system with regular uGMRT observations using Band 3 (400 MHz) from January-March 2020.

Each 1-h-long observation was made with exactly the same settings as the discovery observation, also recording CD data from the central array. This allowed us to maintain consistency among these and discovery observations. The pulsar was detected in 12 out of 13 observations. The flux of this pulsar in PA data was nearly 3–5 times smaller than the discovery observation, and hence we had to use the jerk search method to re-detect it. To identify the cause of these variations, we compared the flux density of this source in the radio images to that in the timing observations. Within measurement uncertainties, the imaging flux densities were consistent with a constant value, confirming that the flux density of this pulsar did not vary between these observations. We have not been able to determine the origin of this discrepancy, and, in particular, whether it was a problem in the recording of the PA data.

For initial estimates of the orbital parameters, we used the velocity-acceleration method discussed by Freire et al. (2001): we plotted the barycentric period and acceleration values from each epoch where the pulsar was visibly bright (Fig. 4). We fit an ellipse to these detections and find the best fit that is consistent with a nearly circular orbit. This fit yields approximate

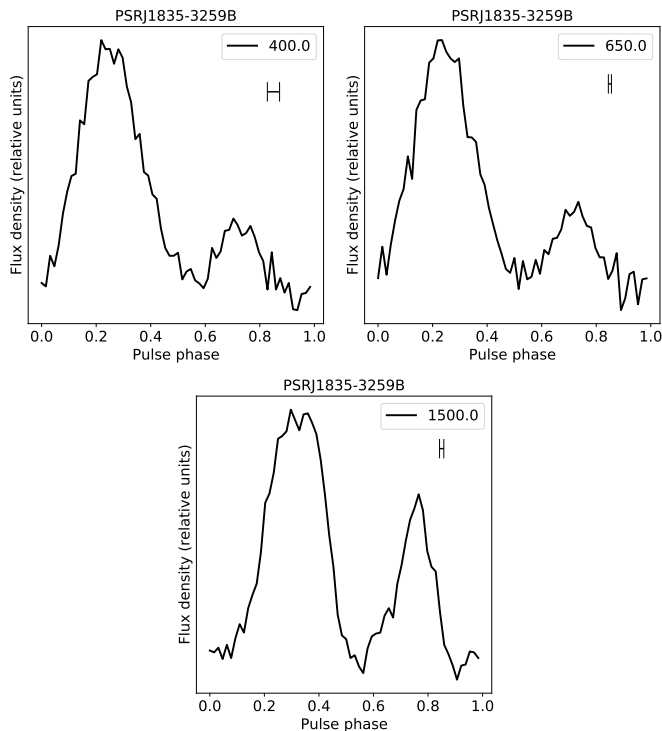


Fig. 3. Intensity profiles as function of rotational phase of NGC 6652B obtained with Band-3 receiver of GMRT at 400 MHz, Band-4 receiver of GMRT at 650 MHz, and L-band receiver of GBT at 1500 MHz. Flux number on y-axis is relative. The horizontal bars show the time resolution of the system for the DM of the pulsar. For the GBT profile, this is merely the adopted bin size of the profile. The profiles were visually aligned.

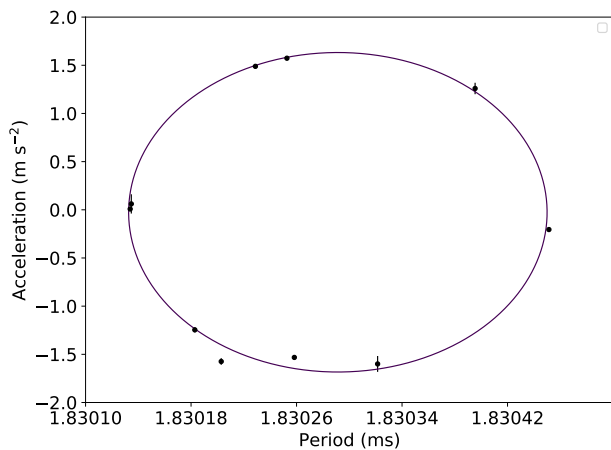


Fig. 4. Period vs. acceleration for timing observations taken on 27 November 2017; 18, 21, and 28 January, 2020; and 5, 14, and 15 February 2020. Line-of-sight acceleration is calculated using observed period derivatives, $a_l = \frac{\dot{P}}{P}$ where P and \dot{P} are the observed spin period and spin period derivative in each detection. The pulsar turns out to be in an orbit with $P_b \sim 1.197$ d and $x \sim 1.43$ lt-s.

estimates of the intrinsic spin period of the pulsar, P_0 (1.83029 ms), orbital period P_b (1.1605 days), projected semi-major axis, x (1.3984 lt-s), and the time of passage at the ascending node, T_{asc} (58084.5910). We then refined the estimates of T_{asc} for all detections using SPIDER_TWISTER¹⁰ (see

Sect. 2 of [Ridolfi et al. 2016](#)). With these more precise values of T_{asc} for each epoch, we refined the orbital period P_b based on the periodogram method discussed in [Freire et al. \(2001\)](#) and also used by [Ridolfi et al. \(2016\)](#), which looks for common sub-multiples of the differences of all T_{asc} that are consistent with our initial estimate of P_b . With these first-order parameters in place, we were then able to look at the precise variation of spin period as a function of time; this was done with PRESTO's routine `fit_circular_orbit.py`. This resulted in much improved estimates for P_b , x , and T_{asc} , with which we created a starting ephemeris to fold all pulsar observations.

We used the PSRCHIVE¹¹ package ([Hotan et al. 2004](#); [van Straten et al. 2012](#)) tools for the timing analysis after this point. The folded profiles were converted to ‘archive’ files using `psrconv`, and these archives were then cleaned of narrow-band RFI using `pazi`. Standard templates of the pulse profile were then made separately for the GMRT 400 and 650 MHz observations, and together for the GBT L -band and S -band observations. This was done by adding the folded archive files from bright observations together using `psradd` to develop integrated profiles; these are shown in Fig. 3. These profiles were then interactively fitted with multiple von Mises functions to create analytic noiseless profiles using `paas`. These standard templates hence created were used to calculate the topocentric times of arrival (ToAs) using `pat`. We made ToAs for four different sub-bands at Band 3 of the GMRT, two sub-bands for Band 4 of the GMRT, and two sub-bands for the L - and S -bands of the GBT; this allowed precise tracking of DM variations. We made ToAs every few mins; the time scale varied due to S/N considerations.

These ToAs were then analysed with the TEMPO¹² software, where we first used the orbital and spin parameters determined above. The program calculates the differences between the ToAs and the arrival time predicted by the timing model (the timing residuals) and then minimises the residuals by adjusting the parameters in the timing model. Binary pulsars with low eccentricities have high correlations between the longitude of periastron, ω and epoch of periastron T_0 ; for this reason, we used the ELL1 model ([Lange et al. 2001](#)) to describe the time delays of the pulses caused by the orbital motion as a function of time. In this model, the Keplerian parameters ω , T_0 , and e are replaced by the time of ascending node, T_{asc} , which can be measured precisely even for circular orbits, and the two Laplace-Lagrange parameters, $\epsilon_1 = e \sin \omega$ and $\epsilon_2 = e \cos \omega$.

In the first stage of timing a newly discovered pulsar, the estimated spin, orbital, and astrometric parameters are not precise enough to calculate the exact number of rotations between the ToAs of different observations, but they can still fit the orbital parameters to obtain residuals that are flat within each observation, that is, we can determine the number of rotations between ToAs within each observation. This was done using TEMPO by including time offsets between observations. With the resulting ephemeris, we could confidently re-fold all our observations and proceed to phase-connect all of them; that is, we could determine the rotation counts between observations (for a detailed description of the process, see [Freire & Ridolfi 2018](#)). We then move onto connecting timing observations spaced further and further apart until we were able to connect all the GMRT observations for this pulsar, plus all GBT observations. The resulting timing solution, which spans a total of ten years, is presented in Table 3. The residuals obtained with this solution are shown in Fig. 5.

¹¹ <http://psrchive.sourceforge.net>

¹² <http://tempo.sourceforge.net>

¹⁰ https://github.com/alex88ridolfi/SPIDER_TWISTER

Table 3. Timing solution of NGC 6652B.

Right Ascension, α (J2000)	18:35:45.4704(1)
Declination, δ (J2000)	-32:59:25.48(1)
Proper Motion in α , μ_α (mas yr ⁻¹)	-7.7(5)
Proper Motion in δ , μ_δ (mas yr ⁻¹)	-4(4)
Spin Frequency, f (s ⁻¹)	546.36058616286(10)
1st Spin Frequency derivative, \dot{f} (Hz s ⁻²)	-1.2962(1) $\times 10^{-14}$
Reference Epoch (MJD)	58736.720
Start of Timing Data (MJD)	55750
End of Timing Data (MJD)	59490
Dispersion Measure, DM (pc cm ⁻³)	63.5083(6)
1st derivative of DM, DM1 (pc cm ⁻³ yr ⁻¹)	0.0237(6)
2nd derivative of DM, DM2 (pc cm ⁻³ yr ⁻²)	0.0055(9)
3rd derivative of DM, DM3 (pc cm ⁻³ yr ⁻³)	-0.0126(9)
4th derivative of DM, DM4 (pc cm ⁻³ yr ⁻⁴)	-0.015(2)
5th derivative of DM, DM5 (pc cm ⁻³ yr ⁻⁵)	-0.0050(6)
Solar System Ephemeris	DE436
Terrestrial Time Standard	TT(BIPM)
Time Units	TDB
Number of ToAs	526
Residuals RMS (μ s)	22.40
Binary Parameters	
Binary Model	ELL1
Projected Semi-major Axis, x (lt-s)	1.430841(2)
First Laplace-Lagrange parameter, η	-2.7(4) $\times 10^{-5}$
First Laplace-Lagrange parameter, κ	-2.2(3) $\times 10^{-5}$
Epoch of passage at Ascending Node, T_{asc} (MJD)	58866.2655109(6)
Orbital Period, P_b (days)	1.19786320(1)
Orbital Period derivative, \dot{P}_b (10^{-12} s s ⁻¹)	0.86(1.08)
Derived Parameters	
Spin Period, P (s)	0.0018302930799293(3)
Maximum Spin Period derivative, \dot{P} (s s ⁻¹)	6.65 $\times 10^{-20}$
Mass function, $f(M_b)$ (M_\odot)	0.0021920077(95)
Minimum companion mass, $M_{c,\text{min}}$ (M_\odot)	0.18
Median companion mass, $M_{c,\text{med}}$ (M_\odot)	0.21
Eccentricity, e	3.49(35) $\times 10^{-5}$
Longitude of periastron, ω ($^\circ$)	230(5)
Time of periastron, T_0 (MJD)	58867.03(1)
Offset from GC center in α , θ_α	0.033
Offset from GC center in δ , θ_δ	0.019
Total offset from GC center, θ_\perp (arcmin)	0.038
Proj. distance from GC center, r_\perp (pc)	0.111
Proj. distance from GC center, r_\perp (core radii)	0.383

The timing solution includes a refined DM estimate of 63.5083 pc cm⁻³ plus a variation modelled by five significant DM derivatives. The fit for proper motion of the system is consistent with the proper motion estimate of GC NGC 6652 mentioned in [Vasiliev & Baumgardt \(2021\)](#).

3.2. Characteristics of the new binary pulsar

As we can see in Fig. 3, the profile of NGC 6652B has two broad components approximately 180 degrees from each other, with emission occurring during most of the spin phase. The secondary component becomes more prominent at higher radio frequencies. A comparison with the time resolution of the system (horizontal bars in the plots in that figure) shows that these pulse components, being much wider than the time resolution, are intrinsically broad. The role of scattering in this is limited since the profile has basically the same characteristics at 1.5 GHz.

The pulsar and its companion complete an orbit every 1.197 days. The projected semi-major axis of its orbit is 1.43 lt-s. Assuming a pulsar mass of 1.4 M_\odot , the companion has

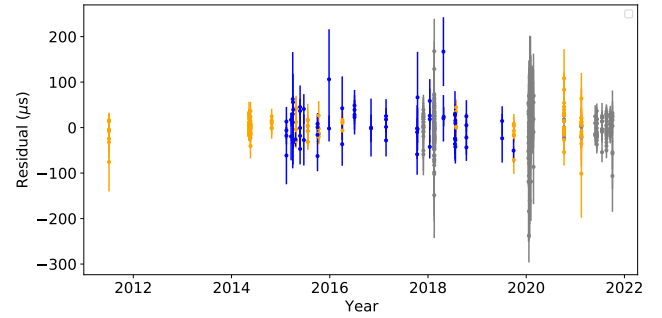


Fig. 5. Residuals obtained with phase-connected solution of NGC 6652B in Table 3. Grey points are ToAs derived from data taken at frequencies below 1000 MHz, while orange points represent GBT ToAs derived from L -band data within 1000–1700 MHz, and blue points show S -band data above 1700 MHz.

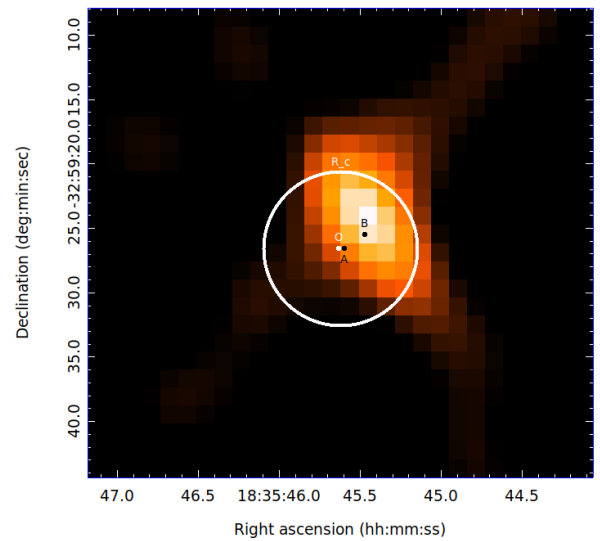


Fig. 6. Pulsar positions in NGC 6652. Derived timing position of NGC 6652B is shown with black label B. The cluster centre is marked with the letter O; it is assumed to be at RA = 18h35m45.63s, and Dec = -32°59′26.6″. The pulsar is offset from centre of the cluster by 0.033′ in RA and 0.018′ in Dec. The position of NGC 6652A is also shown for comparison. The white circle represents the core radius (0.1′) of the cluster. The pixels show radio intensity in our 400 MHz (Band 3) interferometric image of the cluster, a radio source is clearly coincident with the position of NGC 6652B. NGC 6652A is not detected in the image, nor are its pulsations detectable in our PA and CD data.

a minimum mass of 0.176 M_\odot , consistent with the P_b - M_{WD} relation given by [Tauris & Savonije \(1999\)](#) for MSPs with helium WD companions. The orbital eccentricity is small but significant, $(3.49 \pm 0.35) \times 10^{-5}$, which is also consistent with a helium WD companion. This indicates that the system has not interacted strongly with other stars in the cluster since recycling. We have not detected any radio eclipses for this system, even at 400 MHz in observations taken near superior conjunction ($\phi \sim 0.25$), so nothing indicates that this is a ‘redback’ binary.

3.3. Position of the system

Its position with respect to NGC 6652A and the cluster centre is shown in Fig. 6; the total offset from the GC centre is 0.038′. The timing position coincides with that of a very bright radio source, which we identify preliminarily as the pulsar (see Sect. 5).

NGC 6652 has a total of 12 known X-ray sources (Stacey et al. 2012). The timing position of NGC 6652B coincides with one of them, a faint source named ‘H’, which has the coordinates $\alpha = 18:35:45.473$ and $\delta = -32:59:25.48$; the positions are consistent within the astrometric precision of the X-ray source. In that study, the authors conclude that, although the faint sources are likely to be cataclysmic variables, some of them could be MSPs.

3.4. Additional candidates

In addition, we found a total of 24 candidates with a significance higher than 6σ in clusters NGC 6440, NGC 6441, NGC 6544, and Terzan 5. These were followed up with additional observations with uGMRT from October to November 2019. However, none of these were re-detected in the follow-up observations. Possible reasons for the non-detection of these candidates could be unfavourable orbital phases (in case of eclipsing binaries) or the flux density subsiding below the detection threshold due to scintillation. Another cause could be the decrease in observed flux density due to varying beam shape when observed at a different elevation to that of the original observation. Nevertheless, a few candidates with high enough significance ($>7\sigma$) and multiple re-detections in different segments of the observations are presented in Appendix A. We encourage future GC pulsar search surveys in these clusters to investigate these candidates for re-detection.

4. Characterising known pulsars

From the available dataset, we re-detected 22 pulsars (out of 55 known) in the eight clusters we observed; their intensity profiles are shown in Fig. 7. These detections include four pulsars that are in eclipsing binary systems, namely, Terzan 5A, Terzan 5O, NGC 6440D, and possibly the ‘black widow’ system NGC 6544A, for which eclipses have not been observed at higher radio frequencies (Lynch et al. 2012). We were only able to detect the ingress and egress of the eclipse in Terzan 5A in our data. No eclipses for the other pulsars occurred during our observations, because none of them coincided with a superior conjunction of those binaries. Table 4 presents the re-detections along with the minimum detection threshold for each of the epochs. These sensitivity thresholds yield an upper limit on the flux density of the pulsars that are not detectable in these observations.

We estimated flux densities for all the re-detected pulsars (of which only Terzan 5A, NGC 6539A, and NGC 1851A had previously reported flux densities at such low frequencies; our estimates are comparable to those values), except for four of these (NGC 6441D, Terzan 5E, I, K) whose S/N were below 6σ ; hence, the flux estimates are not reliable. For these sources as well, we placed the survey detection threshold of their host clusters (see Table 4) as the upper limit on their flux densities. To estimate the flux density, each folded archive of these pulsars was first cleaned with `pazi` to remove any narrow-band RFI and maximise the S/N. Optimised estimates of the spin period and DM were then determined using PSRCHIVE’s `pdmp` for each pulse profile. The radiometer equation given by Dewey et al. (1985) is used to determine the flux densities for all the pulsars at 400 MHz and 650 MHz correspondingly. The calculated flux densities were fit with a power law along with previously known flux values at higher frequencies (taken from the ATNF catalogue) to estimate the spectral indices for each of these pulsars. Expected flux densities at corresponding frequencies are

determined (see Table 4) from the previously known spectral index estimate from ATNF and assuming -1.4 where the spectral index isn’t known.

Using the wide bandwidth of 200 MHz of our observations, we have also estimated the temporal broadening due to the scattering effect of ISM in the pulse profiles of bright pulsars. To estimate this, we modelled the pulse profiles of several sub-bands using the software SCAMP-I¹³. Full details of the method employed by this software can be found in Oswald et al. (2021). For each pulsar, we split the observing band into either two, four, or eight pulse profiles, depending on the signal-to-noise constraints, and modelled the profile in each sub-band independently. The modelling technique uses a Markov-chain Monte Carlo (MCMC) method to fit a single Gaussian, convolved with an isotropic scattering transfer function, to the pulse profile. Five parameters are constrained by the modelling process: the amplitude, mean, and standard deviation of the Gaussian representing the intrinsic pulse profile; any direct current (DC) offset of the profile baseline; and the scattering timescale, τ_{scat} . The MCMC method was run for 10 000 steps for each profile, and the chains were inspected by eye to determine whether they had converged. For the pulsars where the band could be split into a sufficiently large number of sub-bands to obtain multiple scattering timescales at different frequencies, we also obtained a scattering index. This was done by performing a least-squares power-law fit to the variation of scattering timescale with frequency. We report the estimates for scattering timescales, and, where obtainable, scattering indices, in Table 4. We note that for the eclipsing binary pulsar Terzan 5A, we removed time integrations in the folded profile near the eclipsed portion to avoid any phase delays present due to wind emanating from the companion. Table 4 also presents the theoretical prediction of scattering timescales based on the empirical relation by Bhat et al. (2004):

$$\log \tau_{\text{sc}} = -6.46 + 0.154(\log DM) + 1.07(\log DM)^2 - 3.86 \log\left(\frac{\nu_c}{\text{GHz}}\right), \quad (3)$$

where ν_c is the centre frequency of the observing band. We should note that in Bhat et al. (2004) the scatter of fitted data has a variation of around an order of magnitude with regard to this prediction, and hence our scattering estimates lie well within this variation. We note that more recent work, notably that of Lewandowski et al. (2015), has used an increased number of measurements of scattering timescales to undertake deeper investigations of the τ -DM scaling relationship and update its characteristic shape. However, since all of the empirical scaling relationships in the literature are compatible within the spread of scattering timescale measurements collected thus far, the accuracy of the predictions given in Table 4 is sufficient for the purposes for which we are using them. Furthermore, the τ -DM relationships given by Lewandowski et al. (2015) are fixed at 1 GHz, whereas the form of the scaling relationship given in Bhat et al. (2004) makes use of a global frequency-scaling index of $\alpha = 3.86$. This makes it convenient to use it to calculate estimates at our pulsar reference frequencies, even for cases where we do not have a measurement of α .

5. Imaging the globular clusters

Using the visibility data, we created radio maps for each of these clusters. The detection of steep-spectrum radio sources could allow the discovery of bright radio pulsars, which may have been missed by previous time-domain pulsar surveys either due to the

¹³ <https://github.com/pulsarise/SCAMP-I>

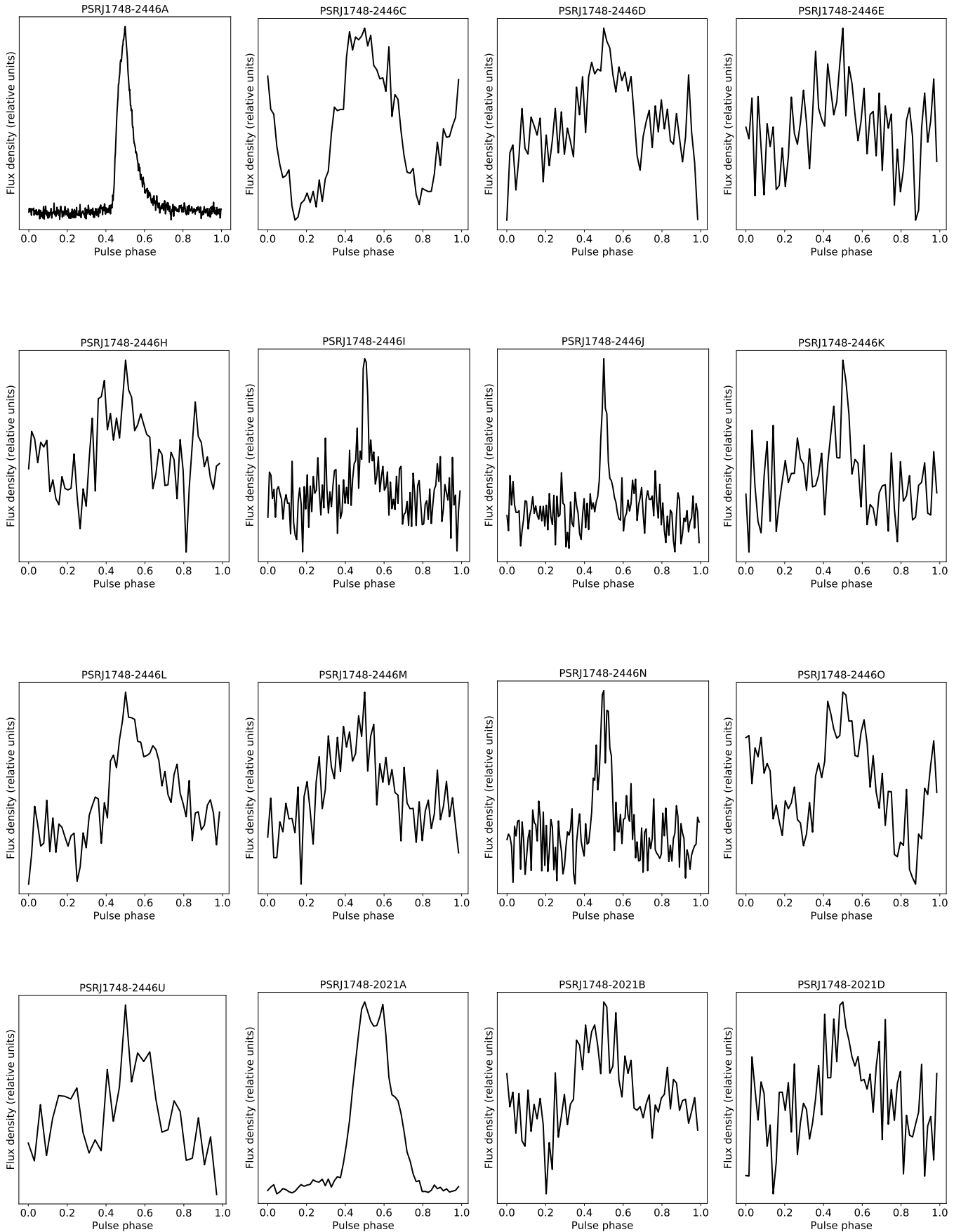


Fig. 7. Intensity profile vs. rotational phase of previously known pulsars visible with uGMRT at sub-GHz frequencies.

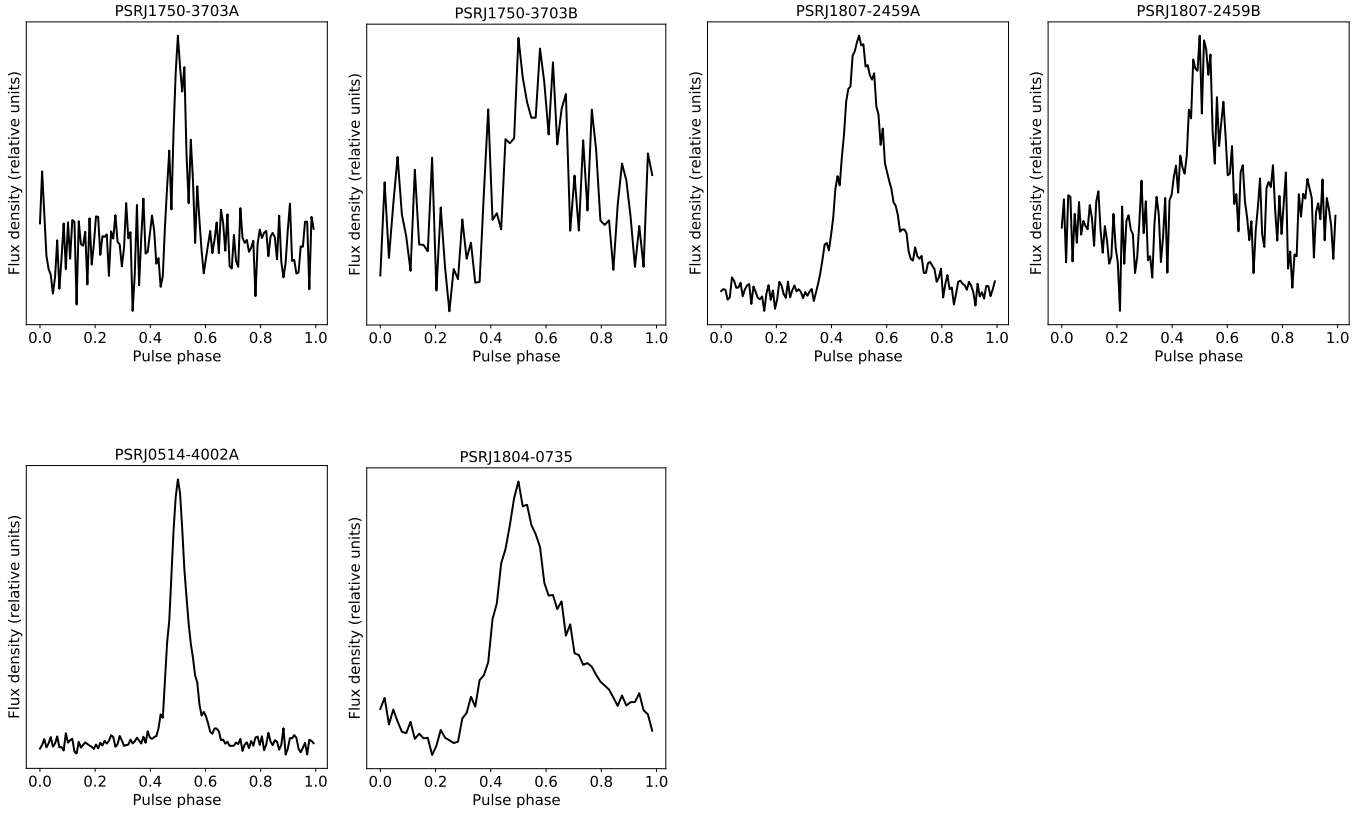


Fig. 7. continued.

Table 4. Properties estimated for re-detected and newly discovered pulsars.

Cluster	F_c (MHz)	S_{\min} (mJy)	Redetections	S/N	S_{obs} (mJy)	S_{exp} (mJy)	Spectral Index	Scattering Index	$\tau_{\text{scat}}, f_{\text{ref}}$ (ms, MHz)	$\tau_{\text{scat}}^{\text{th}}$ (ms)	
NGC 1851	400	0.206	A	126.6	2.717	–	–	–	Not measurably scattered	0.03	
Terzan 5	650	0.143	A	384.2	7.491	4.08	–2.420	–3.2(1)	0.640(9), 640	5.48	
			C	33.4	0.915	–	–	–	–	–	
			D	12.2	0.309	0.19	–1.797	–	–	–	
			F	10.5	0.223	0.17	–1.649	–	–	–	
			H	12.2	0.310	0.07	–2.694	–	–	–	
			I	12.9	0.175	–	–	–	–	0.29(7), 700	3.57
			J	18.9	0.199	0.09	–2.088	–	–	–	–
			L	18.6	0.371	0.19	–3.030	–	–	–	–
			M	15.0	0.503	0.26	–1.407	–	–	–	–
			N	18.2	0.292	0.15	–2.314	–	–	0.56(19), 625	5.49
NGC 6440	650	0.099	O	14.2	0.344	0.57	–1.138	–	–	–	
			U	10.3	0.345	–	–2.732	–	–	–	
			A	178.8	4.234	1.72	–2.197	–	–	Not measurably scattered	3.25
			B	10.9	0.332	0.22	–1.747	–	–	–	
NGC 6441	650	0.105	D	8.2	0.248	0.36	–1.062	–	–	–	
			A	14.6	0.192	0.28	–1.156	–	–	–	
			B	12.9	0.432	0.17	–2.188	–	–	–	
NGC 6539	400	0.099	A	94.1	2.263	3.08	–	–	3.80(83), 412	7.82	
NGC 6544	650	0.099	A	105.9	2.628	4.05	–1.273	–4.0(5)	0.25(2), 662	0.25	
			B	21.2	0.414	0.42	–1.378	–	–	0.37(12), 600	0.41
NGC 6652	400	0.205	B	31.6	1.01	–	–	–	0.174(3), 330	0.142	

Notes. F_c represents the central frequency of observation, S_{\min} is the minimum detection threshold for each cluster, S_{obs} is the observed flux density, S_{exp} is the expected flux density (assuming spectral index of -1.4 if unspecified by ATNF catalogue), τ_{scat} is the measured scattering timescale at reference frequency f_{ref} , and $\tau_{\text{scat}}^{\text{th}}$ is the theoretical estimate of scattering timescale at frequency f_{ref} (calculated from the relation by Bhat et al. 2004).

limited field of view of large telescopes or due to the Doppler smearing of highly accelerated pulsar systems. Imaging known pulsars in these clusters also provide arcsecond localisations that can be used to refine the timing solutions for systems without precisely known positions.

The procedure used standard tasks incorporated in CASA (McMullin et al. 2007) to perform flagging, calibration, and imaging on the dataset. For the observations where a standard flux calibrator was not observed, we calculated a model for the flux density of the phase calibrator from other nearby epochs where a proper flux calibrator was observed and used it for the delay, bandpass, and gain calibrations. This was sufficient to provide reasonable estimates for the flux densities and spectral indices of radio sources.

We used the CASA task `tclean` in the multi-term multi-frequency synthesis (MT-MFS) mode (Rau & Cornwell 2011) to produce radio maps of each cluster with in-band spectral indices calculated for all sources. A few rounds of phase-only self-calibration were also performed for each of the clusters. As the extent of the GCs ($<2'$) is small compared to the FWHM of the primary beam of the GMRT antennas ($69'$ at 400 MHz and $43'$ at 640 MHz), the flux densities of radio sources near clusters were negligibly affected by the beam response. Therefore, we did not correct for this effect in the images. The positions of all radio sources are determined with respect to the well-known positions of the phase calibrators in the International Celestial Reference Frame (ICRF). The pulsar timing uses the planetary ephemerides DE436, which is aligned with the ICRF to within 0.2 milliarcseconds. All the radio images are presented in Fig. 8, and Table 5 summarises the image properties of each of these clusters.

In NGC 6652, we see four bright radio sources (labelled 1–4) near the core of this cluster. Source 1 is the brightest in the cluster and coincides with the timing position of the new pulsar, NGC6652B. This pulsar may be the steep-spectrum source mentioned by Tremou et al. (2018), but without a reported position we cannot be sure. Sources labelled 2, 3, and 4, are not associated with known pulsar positions in this cluster. Since all three sources are within the tidal radius and the two with measurable spectral indices (Table 6) that are relatively steep ($\alpha < -1$), they may be pulsars. Observations to follow up on these sources are ongoing.

In clusters NGC 1851, NGC 6539, NGC 6544, NGC 6440, and Terzan 5, we found five more radio sources not associated with any known pulsar position (one in each of these). The source in NGC 1851 was first noted by Freire et al. (2004), who found no pulsations at 327 MHz. For the other four clusters, there are higher frequency radio maps from the MAVERIC survey (Tremou et al. 2018). Using the 5 and 7 GHz radio point source catalogues of Shishkovsky et al. (2020), we find no matches within 4 arcseconds of our source in NGC 6539. Based on the 5.2 GHz RMS noise of $1.7 \mu\text{Jy beam}^{-1}$ for this cluster, we can set a 5σ upper limit of $\alpha_{0.4-5} = -2.3$ for the spectral index of our source. For NGC 6544, we find that our source matches (within an arcsecond) with one in the Shishkovsky et al. (2020) catalogue. Based on our 650 MHz flux density measurement and the reported 5.0 and 7.4 GHz flux densities, we obtain a spectral index of $\alpha \approx -0.6$, which could be a flat-spectrum pulsar or a background radio galaxy. For NGC 6440, we find a matching MAVERIC source within 0.4 arcseconds of our source. Based on our measured 650 MHz flux density and the reported 5.0 and 7.1 GHz flux densities, we estimate a spectral index of $\alpha \approx -1$. For Terzan 5, we clearly see that our source is a background galaxy in the 3.4 GHz map by Urquhart et al. (2020).

All the pulsar candidate point sources are well within the tidal radii of each of these clusters, indicating they could possibly be part of these clusters. Since these sources are at the outskirts of the clusters, they would have been missed by previous pulsar search surveys, which only observed their central regions. As these sources are now localised in the image, we can point all the GMRT antennas on their locations and achieve higher sensitivity and hopefully clarify their nature.

Estimates of flux density, spectral indices, and positions of all these visible radio sources are listed in Table 6. The statistical 1σ uncertainties from the CASA task `imfit` are presented along with the measured values. To confirm the accuracy of these estimates, we compared the imaging positions with known timing positions for the pulsars with phase-connected solutions. We noticed a positional offset in these images of around 1–2 arcsec in RA and Dec. To verify this, we compared the positions of bright sources in the field of view of each of these clusters with their positions in the NVSS catalogue of Condon et al. (1998). Columns (5) and (6) show the mean systematic shift (along with the uncertainties) in RA and Dec for each of these clusters.

A comparison between the flux density estimates from the radiometer equation (as discussed in Sect. 4) and from the images is shown in Fig. 9. Upper limits on the flux density of pulsars not visible in the image is set to be 3σ , that is, thrice the RMS noise of the respective cluster's image. We see that most of the pulsars follow a linear trend on the plot, except for PSR NGC 6652B, Ter 5C, and Ter 5O, where the flux obtained from imaging is significantly higher than that of folded profiles from the PA data. There are several possible causes for this. First, these pulsars have broad pulse profiles, which could indicate that they have emission at all spin phases, with the varying component of the flux density representing a relatively small amount of the total flux density. Indeed, a large non-varying component should only be detectable in the radio images. Such emission could be studied in detail in polarimetric studies of their pulse profiles by revealing, for instance, large amounts of polarised emission during the full rotation cycle. Second, in the case of an eclipsing binary system such as Ter 5O, the additional flux in the image can also include contributions from the continuum radio emission from the plasma in the interacting binary. In such systems, one could also see suppression of the pulsed emission, further skewing the ratio of continuum to pulsed emission.

In Fig. 9, we highlight which pulsars are in binaries or eclipsing binaries, and which ones have large duty cycles. We can see that the only reliable predictor of an anomalous imaging flux is the large duty cycle, suggesting that the excess imaging flux is caused by emission at all spin phases, and not by interaction with the companion.

A surprising discovery is that one of these pulsars -our newly discovered pulsar, NGC 6652B- is the brightest pulsar identified in all our images, despite its faint pulsations. The position of the pulsar is close to the cluster centre, this means that an additional possible explanation for its large flux could be the overlap of several radio sources at that position. However, this is unlikely given that Source 1 is not at the centre of NGC 6652 (see Fig. 6), but offset from it and centred instead in the timing position of NGC 6652B. If there were additional sources contributing to their flux, they should (statistically) be distributed closer to the centre and shift the position of Source 1 towards the centre of the cluster. Despite that, we cannot exclude the possibility that additional radio sources are contributing to the large flux of NGC 6652B.

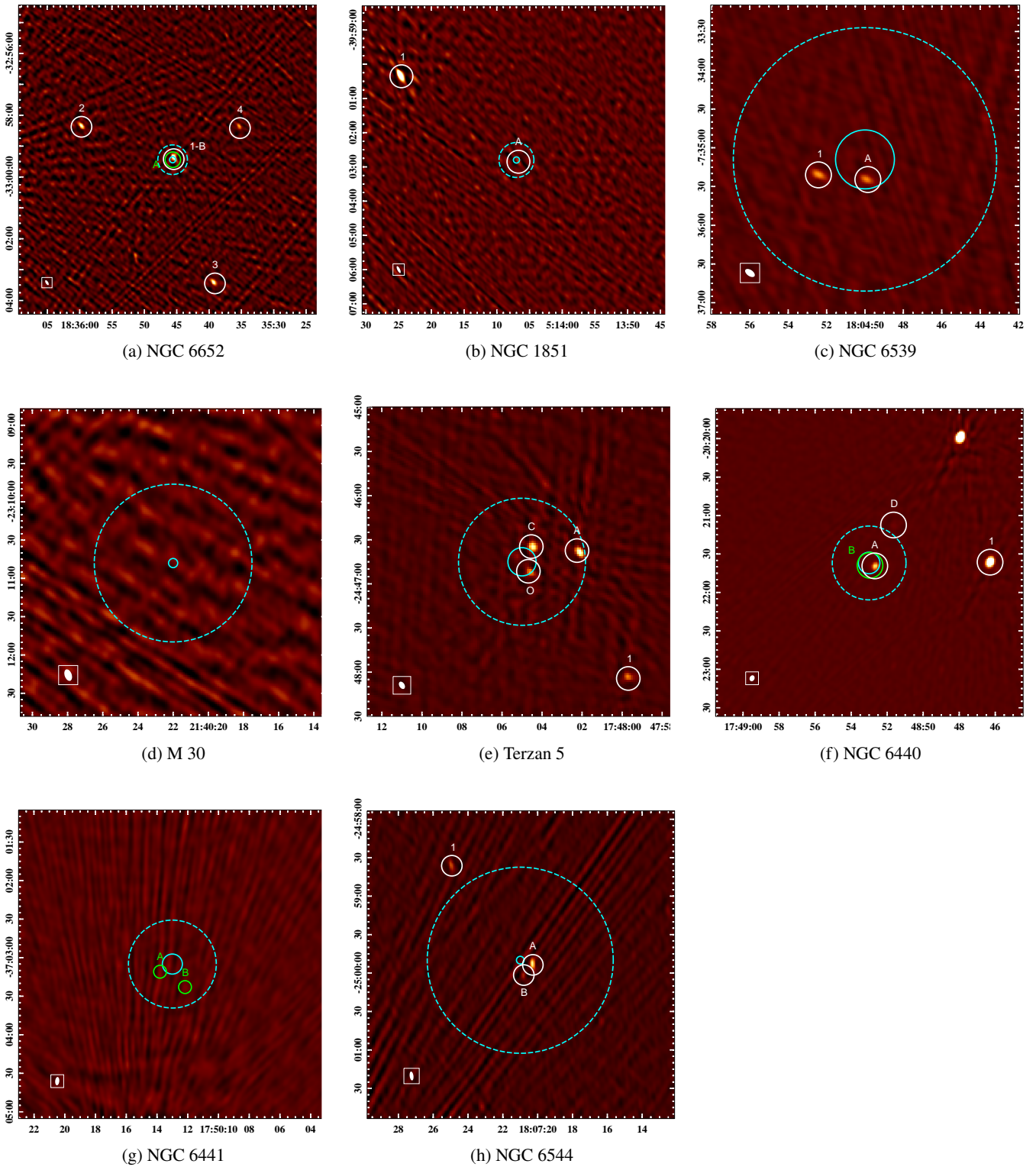


Fig. 8. Radio Images of 8 GCs observed with uGMRT. X and Y axis represent RA (hh:mm:ss) and Dec ($^{\circ}$: $'$: $''$), respectively. The cyan-coloured circle shows the core radius, and the dashed cyan circle shows the half-mass radius. Sources circled in white are the detections in the image, while green-coloured circles show sources visible in the PA data but not in the radio image. In the lower left corner, we display the size and orientation of the imaging beam.

6. Conclusions and discussion

In this paper, we present the results of a GC pulsar survey we performed with the new wide-bandwidth receivers of uGMRT to search for steep-spectrum pulsars at 400 MHz and 650 MHz.

We observed eight GCs and searched each cluster for isolated and binary pulsar systems with segmented and full-length acceleration and jerk search techniques. We discovered a new MSP binary, J1835–3259B in NGC 6652. We presented the timing solution for this system with four years of GMRT observations

Table 5. Properties of the radio images.

Cluster	Epoch (MJD)	Frequency (MHz)	RMS noise (mJy bm ⁻¹)	Synthesized beam (")	Position Angle (°)
NGC 1851	58051	400	0.220	13.30 × 4.69	26.6
Terzan 5	58332	650	0.062	5.48 × 3.58	32.2
NGC 6440	58363	650	0.032	4.87 × 3.72	-23.2
NGC 6441	58332	650	0.049	6.50 × 3.22	-5.4
NGC 6539	57966	400	0.088	8.58 × 4.80	54.8
NGC 6544	58363	650	0.043	6.99 × 2.94	7.5
NGC 6652	58084	400	0.124	10.87 × 4.84	31.6
M30	58102	400	0.220	9.44 × 5.54	19.7

Table 6. Properties of radio sources found in the images.

Cluster	Systematic shift in RA (s)	Systematic shift in Dec (")	Source ID/Name	RA (J2000) (hh:mm:ss)	Dec (J2000) (°:':")	Flux (mJy)	Spectral Index
NGC 1851	0.31(6)	-2.25(73)	J0514-4002A	05:14:06.70 ± 0.11	-40:02:50.87 ± 2.43	1.37 ± 0.58	-
			1	05:14:24.65 ± 0.013	-40:00:19.99 ± 0.29	19.6 ± 1.3	-1.27 ± 0.29
Terzan 5	0.17(10)	-0.82(1.07)	J1748-2446A	17:48:02.11 ± 0.003	-24:46:38.62 ± 0.06	3.35 ± 0.13	-
			J1748-2446C	17:48:04.46 ± 0.008	-24:46:35.06 ± 0.14	3.24 ± 0.32	-
			J1748-2446O	17:48:04.58 ± 0.02	-24:46:52.29 ± 0.21	1.57 ± 0.25	-
			1	17:47:59.68 ± 0.02	-24:48:03.23 ± 0.14	1.52 ± 0.21	-
NGC 6440	0.04(4)	-0.5(6)	J1748-2021A	17:48:52.66 ± 0.002	-20:21:39.64 ± 0.04	3.40 ± 0.11	-2.02 ± 0.01
			J1748-2021D	17:48:51.59 ± 0.03	-20:21:36.08 ± 0.46	0.44 ± 0.12	-
			1	17:48:46.29 ± 0.0008	-20:21:36.41 ± 0.01	18.33 ± 0.20	-0.94 ± 0.01
NGC 6539	-	-	B1802-07	18:04:49.91 ± 0.01	-07:35:24.75 ± 0.12	2.23 ± 0.19	-
			1	18:04:52.41 ± 0.015	-07:35:29.92 ± 0.12	2.94 ± 0.21	-
NGC 6544	0.06(3)	1.0(6)	J1807-2459A	18:07:20.29 ± 0.004	-24:59:52.74 ± 0.23	1.48 ± 0.17	-
			J1807-2459B	18:07:20.81 ± 0.007	-25:00:01.70 ± 0.48	0.28 ± 0.099	-
			1	18:07:24.94 ± 0.01	-24:58:36.14 ± 0.46	0.68 ± 0.12	-
NGC 6652	0.11(13)	1.88 (1.83)	1/J1835-3259B	18:35:45.68 ± 0.01	-32:59:23.46 ± 0.31	5.86 ± 0.60	-3.57 ± 0.25
			2	18:35:59.67 ± 0.02	-32:58:20.95 ± 0.34	3.65 ± 0.28	-2.03 ± 0.38
			3	18:35:39.30 ± 0.01	-33:03:25.01 ± 0.15	3.95 ± 0.22	-1.08 ± 0.09
			4	18:35:35.39 ± 0.02	-32:58:22.23 ± 0.40	1.90 ± 0.19	-

and nine years of GBT observations, for a total time baseline of 10 years. The system is in a wide orbit binary of 1.19 days and has a small eccentricity of 3.5×10^{-5} . Assuming a pulsar mass of $1.4 M_{\odot}$, the median companion mass is $0.21 M_{\odot}$.

The observed orbital and spin period derivatives of the pulsar have contributions from accelerations due to the galactic field (a_{gal}), GCs (a_{gc}), and its composite proper motion (μ):

$$\left(\frac{\dot{P}_b}{P_b}\right)_{\text{obs}} = \left(\frac{\dot{P}_b}{P_b}\right)_{\text{int}} + \frac{a_{\text{gc}}}{c} + \frac{a_{\text{gal}}}{c} + \frac{\mu^2 d}{c}. \quad (4)$$

Assuming no contribution from the intrinsic orbital period derivative due to negligible gravitational wave damping in the system, the GC acceleration can hence be constrained to $3.3 \pm 6.3 \times 10^{-9} \text{ms}^{-2}$; this does not usefully constrain the mass model of the cluster.

Since both the observed spin and orbital period derivatives will be affected by similar accelerations on the system, the following relation can be used to estimate the intrinsic spin period

derivative of the pulsar:

$$\left(\frac{\dot{P}}{P}\right)_{\text{int}} = \left(\frac{\dot{P}}{P}\right)_{\text{obs}} - \left(\frac{\dot{P}_b}{P_b}\right)_{\text{obs}}. \quad (5)$$

From the observed values of \dot{P} and \dot{P}_b , we estimate a 1σ upper limit on the intrinsic spin period derivative, $\dot{P}_{\text{int}} \leq 6.7 \times 10^{-20} \text{ss}^{-1}$. This puts a lower limit of 0.43 Gyr on the characteristic age and an upper limit of 3.5×10^8 G on the surface magnetic field. These values are consistent with MSP systems in the Galactic disc that have helium WD companions, and also some MSP – helium WDs in GCs (Freire et al. 2017).

We find that some of the previously known pulsars in these clusters have steep (< -2) spectra, despite the fact that they were found in surveys at higher frequencies. Comparing the predicted scattering timescales to those measured, we also found the measured values to be considerably smaller than the predictions in most cases (see Table 4). This means it was easier to detect these pulsars than might have been expected. However, it is important to be aware of the uncertainty around the predictions;

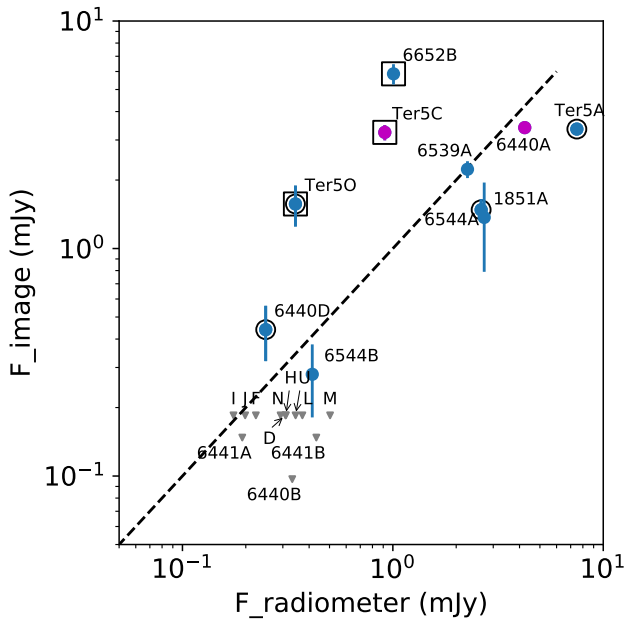


Fig. 9. Comparison of flux density estimates from radio images and folded profiles at 400 MHz for pulsars NGC 1851A, NGC 6544A, NGC 6544B, NGC 6652B, and NGC 6539A, and at 650 MHz for the rest. Blue points represent binary systems, while magenta points represent isolated systems. Pulsars in eclipsing binary systems are marked with black circles, and pulsars with large duty cycles are marked with squares. Points in grey represent the upper limits for pulsars with no measured flux in imaging. The dashed line represents the linear expected trend. The only factor correlating with an imaging flux excess is the large duty cycle.

Lewandowski et al. (2015) found that their estimate of the τ -DM relationship predicted weaker scattering at large DMs than that of Bhat et al. (2004), which we use here for the predicted scattering timescales. We note that the largest differences between predicted and measured scattering timescales in our sample correspond to those pulsars with larger DMs, in agreement with the result of Lewandowski et al. (2015).

With the visibility dataset recorded simultaneously with uGMRT, we created radio images of these eight clusters. From this, we estimated the flux density and spectral indices of all pulsars in these clusters. Interestingly, the newly discovered pulsar NGC 6652B is the brightest of all pulsars among all of our images. This and other pulsars with broad pulse profiles, such as Terzan 5 C and Terzan 5 O, are substantially brighter in the images than they appear in pulsation studies, this shows that they have a large amount of DC radio emission, even at the minimum of their pulse profiles. This raises the possibility that some of the sources in the images might be pulsars that are bright but also have small variability.

These radio images are also useful for looking for bright sources that may have been missed by limited beam size or biases and limitations of the pulsation searches. We identified three radio sources not associated with any known pulsars in NGC 6652 and one each in NGC 6539, Terzan 5, NGC 6440, and NGC 6544. Cross-checking previous surveys shows that the three sources in NGC 6652 and one source in NGC 6539 have not been detected before. The source in Terzan 5 is a background galaxy (Urquhart et al. 2020), and the very bright source in NGC 1851 was detected by (Freire et al. 2004) and has no pulsar counterpart; the other five sources are good pulsar candidates that we will follow up on in future pulsation searches. The

detection of unknown steep sources in the images of GCs allow us to identify undiscovered pulsars that may be present outside the core regions; these outer parts of the clusters are not usually covered when searching for pulsars in GCs. Thus, interferometers such as the GMRT will play a crucial role in a more complete characterisation of the pulsar population in GCs.

Acknowledgements. We thank the referee for the detailed report and many constructive suggestions, which have contributed significantly to the quality of this work. We thank the staff of the GMRT for help with the observations. The GMRT is operated by the National Centre for Radio Astrophysics (NCRA) of the Tata Institute of Fundamental Research (TIFR), India. The Green Bank Observatory is a facility of the National Science Foundation operated under cooperative agreement by Associated Universities, Inc. Data used in this analysis were taken under GBT projects AGBT09B 031, AGBT09C 072, AGBT10A 060, AGBT10A 082, AGBT10B 018, AGBT11B 070, and AGBT12A 388. Part of this research was carried out at the Jet Propulsion Laboratory, California Institute of Technology, under a contract with the National Aeronautics and Space Administration. T.G. thanks Gregory Desvignes and Abhimanyu Susobhanan for useful discussions. A.R. gratefully acknowledges continuing valuable support from the Max-Planck Society, as well as financial support by the research grant “iPeska” (P.I. Andrea Possenti) funded under the INAF national call Prin-SKA/CTA approved with the Presidential Decree 70/2016. M.E.D. acknowledges support from the National Science Foundation (NSF) Physics Frontier Center award 1430284, and from the Naval Research Laboratory by NASA under contract S-15633Y.

References

- Alpar, M. A., Cheng, A. F., Ruderman, M. A., & Shaham, J. 1982, *Nature*, **300**, 728
- Andersen, B. C., & Ransom, S. M. 2018, *ApJ*, **863**, L13
- Bagchi, M., Lorimer, D. R., & Chennamangalam, J. 2011, *MNRAS*, **418**, 477
- Bhat, N. D. R., Cordes, J. M., Camilo, F., Nice, D. J., & Lorimer, D. R. 2004, *ApJ*, **605**, 759
- Bhattacharya, D., & van den Heuvel, E. P. J. 1991, *Phys. Rep.*, **203**, 1
- Bhattacharyya, B., Cooper, S., Malenta, M., et al. 2016, *ApJ*, **817**, 130
- Bhattacharyya, B., Roy, J., Johnson, T. J., et al. 2021, *ApJ*, **910**, 160
- Booth, R. S., & Jonas, J. L. 2012, *African Skies*, **16**, 101
- Camilo, F., Lorimer, D. R., Freire, P., Lyne, A. G., & Manchester, R. N. 2000, *ApJ*, **535**, 975
- Camilo, F., Scholz, P., Serylak, M., et al. 2018, *ApJ*, **856**, 180
- Clark, G. W. 1975, *ApJ*, **199**, L143
- Condon, J. J., Cotton, W. D., Greisen, E. W., et al. 1998, *AJ*, **115**, 1693
- De, K., & Gupta, Y. 2016, *Exp. Astron.*, **41**, 67
- DeCesar, M. E., Ransom, S. M., Kaplan, D. L., Ray, P. S., & Geller, A. M. 2015, *ApJ*, **807**, L23
- Dewey, R. J., Taylor, J. H., Weisberg, J. M., & Stokes, G. H. 1985, *ApJ*, **294**, L25
- Freire, P. C. C., & Ridolfi, A. 2018, *MNRAS*, **476**, 4794
- Freire, P. C., Kramer, M., & Lyne, A. G. 2001, *MNRAS*, **322**, 885
- Freire, P. C., Gupta, Y., Ransom, S. M., & Ishwara-Chandra, C. H. 2004, *ApJ*, **606**, L53
- Freire, P. C. C., Ransom, S. M., Bégin, S., et al. 2008, *ApJ*, **675**, 670
- Freire, P. C. C., Ridolfi, A., Kramer, M., et al. 2017, *MNRAS*, **471**, 857
- Gupta, Y., Ajithkumar, B., Kale, H. S., et al. 2017, *Curr. Sci.*, **113**, 707
- Harris, W. E. 1996, *AJ*, **112**, 1487
- Hessels, J. W. T., Ransom, S. M., Stairs, I. H., Kaspi, V. M., & Freire, P. C. C. 2007, *ApJ*, **670**, 363
- Hessels, J., Possenti, A., Bailes, M., et al. 2015, in *Advancing Astrophysics with the Square Kilometre Array (AASKA14)*, 47
- Hotan, A. W., van Straten, W., & Manchester, R. N. 2004, *PASA*, **21**, 302
- Jacoby, B. A., Cameron, P. B., Jenet, F. A., et al. 2006, *ApJ*, **644**, L113
- Johnston, H. M., & Kulkarni, S. R. 1991, *ApJ*, **368**, 504
- Jonas, J., & MeerKAT Team 2016, in *MeerKAT Science: On the Pathway to the SKA*, 1
- Joshi, B. C., McLaughlin, M. A., Lyne, A. G., et al. 2009, *MNRAS*, **398**, 943
- Lange, C., Camilo, F., Wex, N., et al. 2001, *MNRAS*, **326**, 274
- Lewandowski, W., Kowalińska, M., & Kijak, J. 2015, *MNRAS*, **449**, 1570
- Liu, K., Eatough, R. P., Wex, N., & Kramer, M. 2014, *MNRAS*, **445**, 3115
- Lorimer, D. R. 2011, SIGPROC: Pulsar Signal Processing Programs, Astrophysics Source Code Library [record ascl:1107.016]
- Lorimer, D. R., & Kramer, M. 2012, *Handbook of Pulsar Astronomy* (Cambridge University Press)
- Lyne, A. G., Brinklow, A., Middleditch, J., Kulkarni, S. R., & Backer, D. C. 1987, *Nature*, **328**, 399
- Lynch, R. S., Freire, P. C. C., Ransom, S. M., & Jacoby, B. A. 2012, *ApJ*, **745**, 109

- McMullin, J. P., Waters, B., Schiebel, D., Young, W., & Golap, K. 2007, in *Astronomical Data Analysis Software and Systems XVI*, eds. R. A. Shaw, F. Hill, & D. J. Bell, *ASP Conf. Ser.*, **376**, 127
- Nan, R., & Li, D. 2013, in *Mater. Sci. Eng. Conf. Ser.*, **44**, 012022
- Oswald, L. S., Karastergiou, A., Posselt, B., et al. 2021, *MNRAS*, **504**, 1115
- Pan, Z., Qian, L., Ma, X., et al. 2021, *ApJ*, **915**, L28
- Phinney, E. S. 1992, *Phil. Trans. R. Soc. London, Ser. A*, **341**, 39
- Pooley, D., Lewin, W. H. G., Anderson, S. F., et al. 2003, *ApJ*, **591**, L131
- Possenti, A., D'Amico, N., Corongiu, A., et al. 2005, in *Binary Radio Pulsars*, eds. F. A. Rasio, & I. H. Stairs, *ASP Conf. Ser.*, **328**, 189
- Radhakrishnan, V., & Srinivasan, G. 1982, *Curr. Sci.*, **51**, 1096
- Ransom, S. M., Eikenberry, S. S., & Middleditch, J. 2002, *AJ*, **124**, 1788
- Ransom, S. M., Stairs, I. H., Backer, D. C., et al. 2004, *ApJ*, **604**, 328
- Ransom, S., Hessels, J., Stairs, I., et al. 2005, in *Binary Radio Pulsars*, eds. F. A. Rasio, & I. H. Stairs, *ASP Conf. Ser.*, **328**, 199
- Ransom, S. M., Demorest, P., Ford, J., et al. 2009, in *Am. Astron. Soc. Meeting Abstr.*, **214**, 605.08
- Rau, U., & Cornwell, T. J. 2011, *A&A*, **532**, A71
- Reddy, S. H., Kudale, S., Gokhale, U., et al. 2017, *J. Astron. Instrum.*, **6**, 1641011
- Ridolfi, A., Freire, P. C. C., Torne, P., et al. 2016, *MNRAS*, **462**, 2918
- Ridolfi, A., Freire, P. C. C., Gupta, Y., & Ransom, S. M. 2019, *MNRAS*, **490**, 3860
- Ridolfi, A., Gautam, T., Freire, P. C. C., et al. 2021, *MNRAS*, **504**, 1407
- Shishkovsky, L., Strader, J., Chomiuk, L., et al. 2020, *ApJ*, **903**, 73
- Sigurdsson, S., & Phinney, E. S. 1995, *ApJS*, **99**, 609
- Stacey, W. S., Heinke, C. O., Cohn, H. N., Lugger, P. M., & Bahramian, A. 2012, *ApJ*, **751**, 62
- Tauris, T. M., & Savonije, G. J. 1999, *A&A*, **350**, 928
- Tremou, E., Strader, J., Chomiuk, L., et al. 2018, *ApJ*, **862**, 16
- Urquhart, R., Bahramian, A., Strader, J., et al. 2020, *ApJ*, **904**, 147
- van Straten, W., Demorest, P., & Osłowski, S. 2012, *Astron. Res. Technol.*, **9**, 237
- Vasiliev, E., & Baumgardt, H. 2021, *MNRAS*, **505**, 5978
- Verbunt, F., & Freire, P. C. C. 2014, *A&A*, **561**, A11
- Verbunt, F., & Hut, P. 1987, in *The Origin and Evolution of Neutron Stars*, eds. D. J. Helfand, & J. H. Huang, 125, 187
- Wex, N., & Kopeikin, S. M. 1999, *ApJ*, **514**, 388

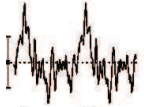
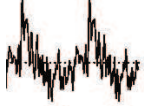
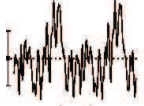
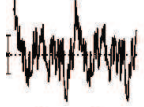
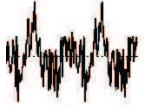
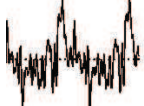
Appendix A:

Table A.1 presents the properties of a few high-significance pulsar candidates found from the GC census presented in this work. Of these, two candidates in GCs NGC 6440 and NGC 6544 were found with exceptionally high acceleration.

In NGC 6440, the pulsar candidate was found in the segmented acceleration search with an extraordinary acceleration of 354 m s^{-2} , rotating at a spin period of 3.35-ms. Its high acceleration could be due to its presence in a tight binary system, hence, if confirmed, it could be one of the few systems that can be used

to test theories of gravity in the strong field regime. The candidate is only found in the first 20-min segment of the observation, which could be because of the failure of the assumption of constant acceleration for the remainder of the orbit. Similarly, in cluster NGC 6544, a 4.43-ms pulsar candidate was detected with an acceleration of $\sim 102 \text{ m s}^{-2}$. Considering the significance of all the candidates presented in Table A.1 and their detections in multiple segments, we encourage future search surveys in these clusters -particularly at low frequencies- to confirm these candidates.

Table A.1. Properties of significant pulsar candidates.

Cluster	Epoch (MJD)	DM (pc cm^{-3})	Period (ms)	Acceleration (m s^{-2})	Segment length (min)	Significance (σ)	Intensity profile
NGC 6441	58332	232.99	2.15	0	full	11.2	
NGC 6440	58363	227.92	3.35	354	20	10.6	
NGC 6440	58363	215.65	2.61	0.1	20, full	11.1	
NGC 6544	58363	130.68	4.43	102	20	9.7	
NGC 6544	58363	132.35	5.17	0	full	7.9	
Terzan 5	58332	219.90	2.93	0	20	9.8	

**Paper titled “Eight new millisecond
pulsars from the first MeerKAT
globular cluster census”**

The paper *Ridolfi, Gautam et al. MNRAS (2021), Volume 504, Issue 1, June 2021, Pages 1407–1426* is reproduced below in its original form with permission by Oxford University Press.



Eight new millisecond pulsars from the first MeerKAT globular cluster census

A. Ridolfi ^{1,2}★, T. Gautam, ²★, P. C. C. Freire ^{1,2}, S. M. Ransom ^{1,3}, S. J. Buchner ^{1,4}, A. Possenti, ^{1,5} V. Venkatraman Krishnan ^{1,2}, M. Bailes, ^{6,7} M. Kramer ^{1,2,8}, B. W. Stappers ^{1,8}, F. Abbate ^{1,2}, E. D. Barr ^{1,2}, M. Burgay ¹, F. Camilo, ⁴ A. Corongiu ¹, A. Jameson, ^{6,7} P. V. Padmanabh ^{1,2}, L. Vleeschower, ⁸ D. J. Champion ^{1,2}, W. Chen, ² M. Geyer ^{1,4}, A. Karastergiou, ^{9,10} R. Karuppusamy, ² A. Parthasarathy ^{1,2}, D. J. Reardon ^{1,6,7}, M. Serylak, ⁴ R. M. Shannon ^{1,6,7} and R. Spiewak ^{1,8,6}

¹INAF – Osservatorio Astronomico di Cagliari, Via della Scienza 5, I-09047 Selargius (CA), Italy

²Max-Planck-Institut für Radioastronomie, Auf dem Hügel 69, D-53121 Bonn, Germany

³National Radio Astronomy Observatory, 520 Edgemont Rd., Charlottesville, VA 22903, USA

⁴South African Radio Astronomy Observatory (SARAO), 2 Fir Street, Black River Park, Observatory, Cape Town 7925, South Africa

⁵Dipartimento di Fisica, Università di Cagliari, S.P. Monserrato-Sestu Km 0,700, I-09042 Monserrato (CA), Italy

⁶Centre for Astrophysics and Supercomputing, Swinburne University of Technology, P.O. Box 218, Hawthorn, VIC 3122, Australia

⁷OzGrav: The ARC Centre of Excellence for Gravitational-wave Discovery, PO Box 218, Hawthorn, VIC 3122, Australia

⁸Jodrell Bank Centre for Astrophysics, Department of Physics and Astronomy, The University of Manchester, Manchester M13 9PL, UK

⁹Department of Astrophysics, University of Oxford, Denys Wilkinson Building, Keble Road, Oxford OX1 3RH, UK

¹⁰Department of Physics and Electronics, Rhodes University, PO Box 94, Grahamstown 6140, South Africa

Accepted 2021 March 5. Received 2021 March 5; in original form 2020 December 22

ABSTRACT

We have used the central 44 antennas of the new 64-dish MeerKAT radio telescope array to conduct a deep search for new pulsars in the core of nine globular clusters (GCs). This has led to the discovery of eight new millisecond pulsars in six different clusters. Two new binaries, 47 Tuc ac and 47 Tuc ad, are eclipsing ‘spiders’, featuring compact orbits ($\lesssim 0.32$ d), very low mass companions, and regular occultations of their pulsed emission. The other three new binary pulsars (NGC 6624G, M62G, and Ter 5 an) are in wider (> 0.7 d) orbits, with companions that are likely to be white dwarfs or neutron stars. NGC 6624G has a large eccentricity of $e \simeq 0.38$, which enabled us to detect the rate of advance of periastron. This suggests that the system is massive, with a total mass of $M_{\text{tot}} = 2.65 \pm 0.07 M_{\odot}$. Likewise, for Ter 5 an, with $e \simeq 0.0066$, we obtain $M_{\text{tot}} = 2.97 \pm 0.52 M_{\odot}$. The other three new discoveries (NGC 6522D, NGC 6624H, and NGC 6752F) are faint isolated pulsars. Finally, we have used the whole MeerKAT array and synthesized 288 beams, covering an area of ~ 2 arcmin in radius around the centre of NGC 6624. This has allowed us to localize many of the pulsars in the cluster, demonstrating the beamforming capabilities of the TRAPUM software backend and paving the way for the upcoming MeerKAT GC pulsar survey.

Key words: pulsars: general – stars: neutron – globular clusters: general – instrumentation: interferometers – surveys.

1 INTRODUCTION

Globular clusters (GCs) are renowned to be among the most fertile grounds for the formation of millisecond pulsars (MSPs). Boasting stellar densities that exceed those found in the Galactic disc by several orders of magnitude, GCs promote two- and three-body gravitational interactions, in the form of tidal captures, exchange encounters, and binary disruptions (Hills 1975; Sigurdsson & Phinney 1995). As a result, isolated neutron stars (NSs) can form binaries with other stars, most often a main sequence or giant star. The latter then evolves and eventually spins the NS up through the transfer of mass and angular momentum (Alpar et al. 1982; Radhakrishnan & Srinivasan 1982;

Bhattacharya & van den Heuvel 1991), a phase in which the system is seen as a ‘low-mass X-ray binary’ (LMXB). This phase can last hundreds of millions to billions of years. At the end of the process, the magnetic field of the NS has been ablated, and the object spins hundreds of times per second.

In the Galactic disc, LMXBs can only evolve from binaries where the NS stays bound to a companion star after the supernova event that forms it. This happens only to a small minority of NSs, all others, seen as isolated rotation-powered NSs, eventually become undetectable as they spin-down over time. In GCs, however, the dominant formation channel for LMXBs is exchange encounters involving such isolated, undetectable NSs. This is the reason why, per unit of stellar mass, GCs have three orders of magnitude more LMXBs than the Galactic disc. These NSs can thus be resurrected through accretion, and when the latter stops, the LMXB becomes a binary MSP. The ultimate proof of this scenario was provided a few years ago by the ‘transitional’

* E-mail: alessandro.ridolfi@inaf.it (AR); tgautam@mpifr-bonn.mpg.de (TG)

binary pulsar PSR J1824–2452I, located in the GC M28, which showed swings between LMXB and radio-MSP phases over time-scales as short as just a few weeks (Papitto et al. 2013).

The dynamic environments of GCs can also create exotic binary pulsars that cannot form in the Galaxy. One of the mechanisms for this is the ‘secondary’ exchange encounters, where the NS involved is an MSP that has already been recycled as a consequence of a previous exchange encounter. These are more likely to occur in the GCs with the densest cores (Verbunt & Freire 2014), which can produce highly eccentric binary MSPs with massive companions, possibly other NSs. Examples are M15C (Prince et al. 1991), NGC 1851A (Freire et al. 2004; Ridolfi et al. 2019), NGC 6544B (Lynch et al. 2012), and NGC 6652A (DeCesar et al. 2015). Such secondary exchange encounters could potentially produce MSP–black hole and even MSP–MSP binaries (e.g. Ransom 2008), which would open up unprecedented possibilities for fundamental physics experiments (e.g. Liu et al. 2014). Some of these secondary exchange encounters could also place an already recycled pulsar in orbit with a main-sequence star, resulting eventually in a new LMXB system, where it undergoes further recycling. This is a possible explanation for the many fast-spinning pulsars in Terzan 5 (henceforth, Ter 5), which include the fastest-spinning pulsar known, Ter 5 ad (Hessels et al. 2006).

Even the usually less exciting isolated pulsars have proven to be extremely valuable, when found in GCs. Timing of single objects (Perera et al. 2017) or of an ensemble of pulsars (Freire et al. 2017; Prager et al. 2017; Abbate et al. 2018, 2019) has been exploited to constrain the gravitational potential of several GCs and can indicate the possible presence of an intermediate-mass black hole at their centre. The measurement of the dispersion measures (DMs) of the pulsars in 47 Tucanae (hereafter, 47 Tuc) has allowed the first detection of an intracluster ionized gas, enabling the three-dimensional localization of the pulsars in the cluster (Freire et al. 2001b; Abbate et al. 2018). Furthermore, the study of the polarimetric properties of the same pulsars has made it possible to study the Galactic magnetic field at arcsecond scales for the very first time, in turn revealing the existence of an extended magnetized outflow from our Galaxy (Abbate et al. 2020a).

Since the discovery of the first pulsar in a GC by Lyne et al. (1987), all of these breakthroughs have nourished interest in GC pulsars, and sustained an ever-increasing effort in the search for these objects. This has led to the discovery of over two hundred pulsars in at least 36 different clusters.¹ However, after a burst of new discoveries made in the early 2000s, only a few new GC pulsars were found in the next several years. Further discoveries were essentially hampered by the sensitivity limit reached at the largest available telescopes, namely Arecibo and the Green Bank Telescope (GBT) for the northern GCs, and the Parkes radio telescope for the southern GCs. New pulsars were mostly found through the reprocessing of archival data using new search techniques, such as the stacking of Fourier spectra from multiple epochs (Pan et al. 2016; Cadelano et al. 2018) or ‘jerk’ searches (Andersen & Ransom 2018). This situation has greatly changed since the mid-2010s. New, wide-bandwidth receivers as well as more modern digital backends have recently been installed at the Upgraded Giant Metrewave Radio Telescope (uGMRT; Gupta et al. 2017) and at Parkes (Hobbs et al. 2020). These have already led to the discovery of a new steep-spectrum MSP in NGC 6652 (Gautam et al., in preparation) as well as five faint MSPs in ω Centauri (Dai

et al. 2020). Moreover, entirely new telescopes have been built in both hemispheres. Since 2016, the new Chinese Five-hundred-meter Aperture Spherical Telescope (FAST; Nan et al. 2011) has been providing a factor of 2–3 times better raw sensitivity than Arecibo in the -15° to $+65^\circ$ declination range of the sky. Early FAST GC observations have resulted, at the time of writing, in the discovery of 32 pulsars.²

The year 2018 also saw the inauguration of the South African 64-dish MeerKAT radio telescope array (Booth & Jonas 2012), the precursor of the Square Kilometer Array – SKA1-mid (Dewdney et al. 2009). As it is located in the Karoo desert at a latitude of -30° , MeerKAT is the only radio telescope, other than Parkes, to have access to high-sensitivity, cm-wavelength observations of pulsars in GCs with declinations of $\delta \lesssim -45^\circ$. When using all the 64 dishes, MeerKAT boasts a gain of 2.8 K Jy^{-1} , four times higher than that of Parkes and 1.4 times higher than that of the GBT. Such an improvement in raw sensitivity represents a major leap for studying pulsars in southern GCs.

Two MeerKAT Large Survey Projects (LSPs) that include science of pulsars in GCs as part of their main scientific goals have already been approved and commenced. The first one to start was MeerTime³ (Bailes et al. 2020), which began collecting data in early 2019. The project has a variety of scientific objectives, one of these is the exploitation of GC pulsars through pulsar timing and polarimetry. Using the Pulsar Timing User Supplied Equipment (PTUSE) machines as the main data acquisition system, MeerTime observations can record the signal from up to four (but only one was available before 2019 December) tied-array beams in either ‘timing’ or ‘search’ mode,⁴ with very high time resolution, full polarimetric information, and real-time coherent de-dispersion. These characteristics are an asset to multiple scientific applications for objects within the diameter of the tied array beam. For example, one cannot only fold one known pulsar in a GC, but also look for giant pulses from other pulsars in the cluster, as well as search for new pulsars in the same data. The search and discovery of new extreme and exotic pulsars in GCs is one of the main objectives of the second LSP, dubbed TRAPUM⁵ (TRAnsients and PULsars with MeerKAT; Stappers & Kramer 2016). Since April 2020, the TRAPUM project has been making use of the full MeerKAT array to observe several GCs. A 60-node computing cluster (APSUSE) utilizes beamforming techniques to synthesize and record incoherently de-dispersed search-mode data for up to ~ 400 beams on the sky. The latter cover an area of $\sim 1\text{--}4$ arcmin in radius, depending on the number of antennas used, the observing frequency, and the beam overlap. This allows the search for pulsars not only in the core, but also in the outskirts of the observed globulars, with full sensitivity. Given the complementary scientific goals and characteristics of their data acquisition systems, MeerTime and TRAPUM LSPs decided to collaborate on a joint endeavour to time and search for pulsars in GCs. This has already resulted in the most detailed study of the giant pulses from PSR J1823–3021A in NGC 6624 (Abbate et al. 2020b).

²See also <https://fast.bao.ac.cn/cms/article/65> (Pan et al. 2020; Wang et al. 2020).

³<http://www.meertime.org>

⁴In ‘search’ mode, the observing band is divided into several small channels and recorded every few μs on to a ‘filterbank’ file type. In ‘timing’ mode, the signal of a particular pulsar is folded in real time according to a model (the ephemeris) that describes its rotational behaviour, resulting in a ‘folded archive’ file.

⁵<http://www.trapum.org>

¹See <https://www3.mpifr-bonn.mpg.de/staff/pfreire/GCpsr.html> for an up-to-date list of the known pulsars in GCs.

Table 1. List of GCs observed in the context of this work, ordered by increasing right ascension, and with their basic parameters as reported by Harris (1996), unless otherwise specified. r_c : core radius; r_{hl} : half-light radius; (DM): median DM of the known pulsars; $N_{p,isol}$: number of isolated pulsars; $N_{p,bin}$: number of binary pulsars.

Cluster name	Centre coordinates (RA, Dec.)	Observed clusters							
		Distance (kpc)	Core collapsed?	r_c (arcmin)	r_{hl} (arcmin)	(DM) (pc cm^{-3})	$N_{p,isol}$ (old/new)	$N_{p,bin}$ (old/new)	
NGC 104 (47 Tuc)	00 ^h 24 ^m 05 ^s .67, −72° 04′ 52 [″] .6	4.69 ^a	No	0.36	3.17	24.4	10/–	15/2	
NGC 6266 (M62)	17 ^h 01 ^m 12 ^s .80, −30° 06′ 49 [″] .4	6.80	No	0.22	0.92	114.0	0/–	6/1	
NGC 6397	17 ^h 40 ^m 42 ^s .09, −53° 40′ 27 [″] .6	2.30	Yes	0.05	2.90	71.8	0/–	1/–	
Terzan 5	17 ^h 48 ^m 04 ^s .80, −24° 46′ 45 [″] .0	6.90	No	0.16	0.72	237.9	19/–	19/1	
NGC 6522	18 ^h 03 ^m 34 ^s .02, −30° 02′ 02 [″] .3	7.70	Yes	0.05	1.00	192.7	3/1	0/–	
NGC 6624	18 ^h 23 ^m 40 ^s .51, −30° 21′ 39 [″] .7	7.90	Yes	0.06	0.82	86.9	5/1	1/1	
NGC 6626 (M28)	18 ^h 24 ^m 32 ^s .81, −24° 52′ 11 [″] .2	5.50	No	0.24	1.97	119.7	4/–	8/–	
NGC 6752	19 ^h 10 ^m 52 ^s .11, −59° 59′ 04 [″] .4	4.00	Yes	0.17	1.91	33.3	4/1	1/–	
NGC 7099 (M30)	21 ^h 40 ^m 22 ^s .12, −23° 10′ 47 [″] .5	8.10	Yes	0.06	1.03	25.1	0/–	2/–	

^aTaken from Woodley et al. (2012).

Here, we report on the results of the first GC census observations conducted with MeerKAT in the framework of the joint MeerTime and TRAPUM activities. They were mostly carried out using the 44 central antennas of the array (although only up to 42 were available at once) and the MeerTime PTUSE data acquisition system, while TRAPUM’s backend has been used to quickly ascertain the positions of some pulsars within their GC. Besides producing new scientific results, the census has served as a benchmark upon which to tune and execute the TRAPUM experiment, which will find pulsars with full sensitivity, both within and beyond the cores of GCs.

In Section 2, we report on the target selection, the instrumental setup, and the observations. In Section 3, we describe the data reduction and analysis methods. The main results are detailed in Section 4, and their implications are discussed in Section 5. Finally, in Section 6, we draw some conclusions and comment on future prospects of GC pulsar observations with MeerKAT.

2 OBSERVATIONS

2.1 Target selection

Among all the GCs visible from the MeerKAT site, we selected a sample of nine. These are listed, along with their main characteristics, in Table 1. The clusters were chosen based on three main criteria:

(i) Each of these clusters hosts at least one previously known pulsar. This requirement had a two-fold purpose: first, the DM of each cluster is constrained within a relatively narrow range, greatly easing the search for new pulsars; secondly, the redetection of the known pulsars allows performance comparisons against other telescopes and serves as a testbed for the data reduction and searching pipelines used.

(ii) Among the GCs with known pulsars, we prioritized those farther south, which had only been searched with the Parkes telescope. For these, the sensitivity gains from MeerKAT searches are larger (see Fig. 1).

(iii) Five of the clusters we targeted – the majority of the sample – are core-collapsed clusters. The reasons for this choice have been highlighted in the Introduction: these are the clusters where exotic binary systems containing MSPs and massive, compact companions (including MSP–black hole or MSP–MSP systems) are likely to form.

However, not all the selected clusters are core collapsed: Ter 5 and 47 Tuc are so rich that they offer a good likelihood of new discoveries

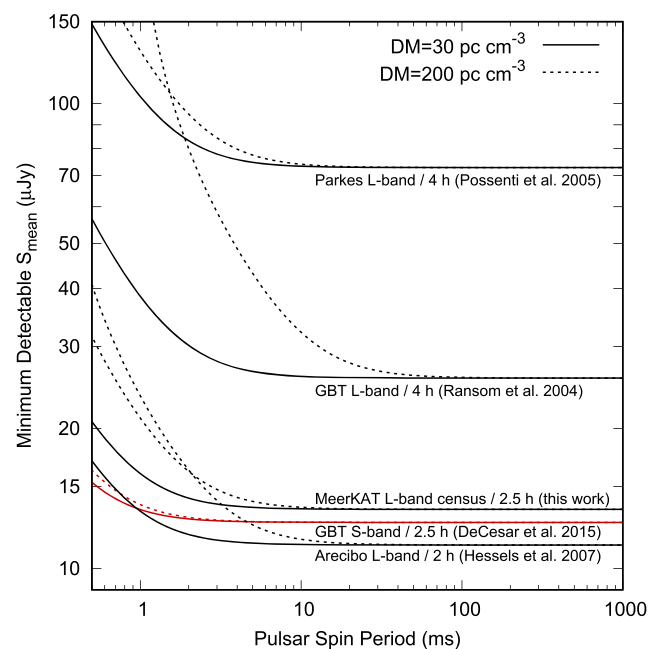


Figure 1. Sensitivity curves of the major L-band (black) and S-band (red) GC pulsar surveys conducted with the Parkes, Arecibo, GBT, and MeerKAT telescopes. The curves are calculated using the survey parameters reported in the references, the typical integration time as indicated in the labels, and assuming an elevation of 45°. Solid lines are relative to a DM = 30 pc cm^{-3} , dashed lines to a DM = 200 pc cm^{-3} . Note (1): The GBT S-band survey appears to be more sensitive because we are not correcting for the spectral index. Its sensitivity to pulsars is very similar to that of the GBT L-band survey, since both surveys detect very similar numbers of pulsars in the same clusters. Note (2): Other GC pulsar surveys, not reported in this plot, are currently being conducted with more modern telescopes and instrumentation (e.g. Dai et al. 2020; Pan et al. 2020).

with improved sensitivity. Furthermore, searching a diversity of types of clusters is important for improving our understanding of the pulsar populations of different GCs, and in particular their differences.

The chosen clusters also have a range of DMs, allowing us to test the telescope performance and the data analysis strategies in a number of different cases. The pulsars in the clusters with a low DM ($<50 \text{ pc cm}^{-3}$) scintillate over time-scales of just a few hours (e.g. 47 Tuc), whereas those in clusters with a high DM ($>150 \text{ pc cm}^{-3}$) show fairly stable flux densities (e.g. NGC 6522). This results in

different search strategies: while the former are targeted with short, but frequent integrations, the latter are targeted with deeper, but less frequent integrations.

2.2 Setup and observing strategy

The nine selected GCs were observed from 2019 March to 2020 August. The full list of observations used for this work is reported in Table 2. For almost all the observations, we used the *L*-band (856–1712 MHz) receivers and up to 42 of the 44 antennas that are located within a radius of 1 km from the nominal phase centre of the array. We will refer to this subset of the MeerKAT antennas as the ‘1-km core’ through the rest of the paper. The choice of using only the 1-km core antennas was dictated by the need to have a large enough beam on the sky: at the central frequency $f_c = 1284$ MHz of the *L* band, each semi-axis of the single tied-array beam has a minimum size of ~ 0.5 arcmin, enough to cover the central regions of most of the observed GCs. With the exception of some data collected at early stages of the experiment, the data were acquired in PSRFITS search-mode format (Hotan, van Straten & Manchester 2004) with the MeerTime PTUSE backend. Initially, we used a nominal bandwidth of 642 MHz, divided into 768 channels. From 2020 February the nominal bandwidth covered the full 856 MHz provided by the *L*-band receivers, and was divided into 1024 channels, hence retaining the same channel width of 0.836 MHz. The band was coherently de-dispersed using the median DM of the known pulsars of the cluster and sampled every 9.57 μ s, retaining all four Stokes parameters.

We observed each cluster at least once with an integration time of 2.5 h. After that, depending on whether one or more potential candidate new pulsars were found, the same cluster was re-observed once or a few more times, with the same setup and integration time whenever possible. The only exception to this strategy was applied to 47 Tuc. In the latter cluster, the observed flux densities of the pulsars are highly dominated by scintillation and show large variations from day to day. Hence, for 47 Tuc, we opted for several, shorter (~ 1 h) observations, regardless of the candidates that they produced each time. This was done to increase the likelihood of discovering pulsars whose signals were by chance boosted by scintillation above our sensitivity limit.

For a few clusters, we also performed additional observations aimed at following up some of the discoveries. These include ‘orbital campaigns’ (see Section 3.4.1), needed to determine the orbital parameters of binary systems, as well as observations made with the *UHF* receivers (544–1088 MHz), needed to assess the best observing band for long-term follow-up timing. Motivated by the discovery of a highly eccentric binary MSP in NGC 6624 (pulsar G, see Section 4.1.5), we also re-observed the latter cluster on two occasions making use of the tiling capabilities of the TRAPUM backend, APSUSE. The main purpose of these observations was the localization of several pulsars (including new discoveries) that were lacking a coherent timing solution, and hence, a known position, in NGC 6624. The TRAPUM backend was used in combination with the full MeerKAT array. This is made by up to 64 antennas (but 60 were available during the observations) that have a maximum baseline of 7.7 km. This translates into a beam diameter at half-power of ~ 12 arcsec at 1.3 GHz. For the NGC 6624 observations, we synthesized 288 coherent beams with a >70 per cent overlap between them. The resulting beam tiling covered an area of ~ 2 arcmin in radius around the cluster’s nominal centre. The data were recorded in search mode, with a 76- μ s time resolution, 856 MHz of bandwidth centred at 1284 MHz divided into 4096 frequency channels with no coherent de-dispersion, and integrated for 4 h. We point out that,

for this work, we focused on the search for new pulsars only in the MeerTime *L*-band observations performed until 2020 July, including those performed for the orbital campaigns. The aforementioned TRAPUM *L*-band and MeerTime *UHF*-band observations are only reported here for their timing implications, whereas the search for new pulsars in those data sets will be discussed elsewhere.

2.3 Sensitivity

The observing setup of the MeerTime *L*-band observations described above translates into a nominal sensitivity that can be estimated with the radiometer equation (Dewey et al. 1985). The latter returns the mean flux density, S_{mean} , that a pulsar must have to be detected with a given signal-to-noise ratio (S/N) as a function of the observing parameters, as

$$S_{\text{mean}} = \frac{S/N \beta T_{\text{sys}}}{G \sqrt{n_{\text{pol}} \text{BW}_{\text{eff}} \Delta t_{\text{obs}}}} \sqrt{\frac{\zeta}{1-\zeta}}. \quad (1)$$

Here, G is the telescope gain, which, when using the 42 antennas of the typical observations made with the MeerKAT 1-km core, is 1.84 K Jy^{-1} . $T_{\text{sys}} = 26 \text{ K}$ is the total system temperature for *L*-band observations, and is the sum of several contributions: the receiver temperature T_{rec} (18 K), the cold sky temperature T_{sky} ($\sim 3.5 \text{ K}$ at 1.3 GHz), and the atmosphere plus the ground spillover temperature $T_{\text{atm+spill}}$ ($\sim 4.5 \text{ K}$ at 45° elevation),⁶ $n_{\text{pol}} = 2$ is the number of orthogonal polarizations summed in the searched signal; β is a factor that accounts for various sensitivity losses due to signal processing and digitization, and we assume it to be 1.1; $\text{BW}_{\text{eff}} \simeq 650 \text{ MHz}$ is the typical effective observing bandwidth, after the removal of frequency channels polluted by radio frequency interference (RFI); Δt_{obs} is the integration time, which we take to be 2.5 h, as for our typical survey observations; ζ is the observed pulse duty cycle, resulting from the convolution of the intrinsic pulse width of the pulsar with both the effects of the interstellar medium and the signal acquisition system. In order to give a value of the S_{mean} for this GC census survey, and to allow a comparison with other pulsar search experiments, we adopt a minimum S/N = 10, and a $\zeta = 8$ per cent. With the above parameters, we are sensitive to slow and mildly recycled pulsars (with spin periods $P \gtrsim 10$ ms) down to a mean flux density of $S_{\text{mean}} \sim 13 \mu\text{Jy}$ at 1.3 GHz, at the beam boresight. For the fastest MSPs ($P \lesssim 10$ ms), the minimum detectable S_{mean} is higher essentially because of scattering broadening, which can become important at the relatively low frequencies of our *L*-band observations. Other effects, such as intrachannel dispersive smearing, are negligible thanks to coherent de-dispersion (see section 2.3 of Hessels et al. 2007 for a detailed discussion of all the effects that can impact ζ). Fig. 1 compares the sensitivity curve of this initial MeerKAT GC census survey, against those of other major GC pulsar surveys, conducted at Parkes (Possenti et al. 2005), Arecibo (Hessels et al. 2007), and the GBT (Ransom et al. 2004; DeCesar et al. 2015), with either their *L*-band ($f_c \sim 1.4 \text{ GHz}$) or *S*-band ($f_c \sim 2 \text{ GHz}$) receivers. For clusters located in the far south ($\delta \lesssim -45^\circ$), we have $\gtrsim 5$ better sensitivity than previous surveys carried out at Parkes. For clusters with higher declinations ($-45^\circ \lesssim \delta \lesssim 0^\circ$) our sensitivity is a factor of ~ 2 better than the GBT *L*-band survey. This can be even higher for those clusters only visible with very low elevations by the GBT (e.g. NGC 6522, NGC 6624, M62), for which atmospheric opacity is significant and increases the total T_{sys} by several K.

⁶<https://skaafrica.atlassian.net/rest/servicedesk/knowledgebase/latest/article/view/277315585>

Table 2. List of MeerKAT observations made in the context of this work. All the observations, with the exception of the TRAPUM ones, were taken using the 1-km core antennas and the search-mode data were acquired using the PTUSE pulsar processor with full-Stokes, a time resolution of 9.57 μ s, and coherently de-dispersing at the nominal cluster DM. TRAPUM observations (marked by ‘-trapum’ in their observation id’s) were taken using 60 antennas and acquiring search-mode data with a 76 μ s time resolution and 4096 frequency channels, without coherent de-dispersion. Observations that were searched for new pulsars as outlined in Section 3 are marked with a star (*); first detections of new pulsars (i.e. discoveries) are highlighted in bold.

Cluster	Obs. id	Start epoch (MJD)	Δt_{obs} (s)	f_c (MHz)	BW (MHz)	Δf_{ch} (MHz)	Redetections of previously known pulsars	Detections of new pulsars
47 Tuc	01L*	58557.386	1008	1177	214	1.672	F, O, Y	–
				1391	214	1.672	O, Y	–
	02L*	58765.918	5427	1284	642	0.836	DEFGHIJLNORTY ab	ac
	03L*	58775.076	9000	1284	642	0.836	CDEFGHIJLORTWYZ ab	–
	04L*	58792.886	5400	1284	642	0.836	DEFGHIJMOQRSTWYZ aa ab	–
	05L*	58831.711	3600	1284	642	0.836	DEFGHIJNORSTWY ab	ad
	06L*	58836.783	3600	1284	642	0.836	DFHILNORSTW ab	–
	07L*	58849.349	3600	1284	642	0.836	CDFGIJMNOQRST ab	–
	08L*	58875.908	3600	1284	642	0.836	CDEFGHIJORTUY ab	–
09U	58928.738	5400	816	544	0.531	CDEFGHIJLNORSTUWYZ aa ab	–	
M62	01L*	58602.820	4538	1122	321	0.836	ABCDEF	G
				1444	321	0.836	ABCDEF	G
	02L*	58769.438	9000	1284	642	0.836	ABCDEF	G
	03L*	58802.451	9000	1284	642	0.836	ABCDEF	G
	04L*	58818.426	9000	1284	642	0.836	ABCDEF	G
	05L-1of2*	58844.331	1450	1284	642	0.836	ABCDEF	G
	05L-2of2*	58844.353	7800	1284	642	0.836	ABCDEF	G
	06L-orb1*	58895.017	7840	1284	856	0.836	ABCDEF	G
	07L-orb2*	58900.996	12600	1284	856	0.836	ABCDEF	G
	08L-orb3*	58901.998	4800	1284	856	0.836	ABCDEF	G
	09L-orb4*	58902.056	7400	1284	856	0.836	ABCDEF	G
	10L-orb5*	58904.023	12600	1284	856	0.836	ABCDEF	G
11L	59074.786	12600	1284	856	0.836	ABCDEF	G	
NGC 6397	01L*	58858.149	9000	1284	642	0.836	A	–
Ter 5	01L*	58630.813	9000	1284	642	0.836	All but P, S, ad, ah, aj, al	an
	02L-orb1*	58905.048	12600	1284	856	0.836	All but J, P, ad, ah, al	an
	03L-orb2*	58906.017	12600	1284	856	0.836	All but P, ad, ah, aj, al	an
	04L-orb3*	58907.022	12600	1284	856	0.836	All but A, P, ad, ah, al	an
	05L-orb4*	58907.326	12600	1284	856	0.836	All but P, ad, ah, al	an
NGC 6522	01L*	58704.596	9000	1284	642	0.836	AC	D
	02L*	58772.653	9000	1284	642	0.836	AC	D
	03U	59046.701	2400	816	544	0.531	A	D
NGC 6624	01L*	58736.715	9000	1284	642	0.836	ABCDF	G, H
	02L*	58771.685	17400	1284	642	0.836	ABCDEF	G
	03L*	58796.566	9000	1284	642	0.836	ABCDEF	G, H
	04L*	58870.134	9000	1284	642	0.836	ABCDEF	G, H
	05L*	58878.113	9000	1284	642	0.836	ABCDEF	G, H
	06L-orb1*	58909.030	7200	1284	856	0.836	ABCDEF	G, H
	07L-orb2*	58909.406	7200	1284	856	0.836	ABCDEF	G, H
	08L-orb3*	58910.023	7200	1284	856	0.836	ABCDEF	G, H
	09L-orb4*	58912.017	7200	1284	856	0.836	ABCDEF	G
	10L-trapum	58990.002	14400	1284	856	0.209	ABCDEF	G, H
	11U	59046.731	2400	816	544	0.531	ABCDF	G
	12L-trapum	59072.807	14400	1284	856	0.209	ABCDEF	G, H
M28	01L*	58683.852	9000	1284	642	0.836	ABCDEFGHIJKL	–
	02L*	58883.106	9000	1284	642	0.836	ABCDEFGHIJKL	–
NGC 6752	01L-1of3*	58666.786	3600	1284	642	0.836	BCDE	F
	01L-2of3*	58666.828	3600	1284	642	0.836	BDE	–
	01L-3of3*	58666.870	1800	1284	642	0.836	BDE	–
	02L*	58850.637	9000	1284	642	0.836	BD	F
M30	01L*	58750.786	11100	1284	642	0.836	A	–
	02L*	58844.526	9000	1284	642	0.836	A	–

3 ANALYSIS

3.1 Data reduction

As a first step in our analysis, we used the `psrfits_subband` routine, part of the `PSRFITS_UTILS`⁷ package, to downsample each observation in both frequency and time, and to sum the two polarizations, thus keeping total intensity only. While doing so, the bandpass was flattened using the proper scale and offset values, which were recorded while acquiring the data. For all the observations we retained a time resolution of 76 μs . The number of frequency channels was chosen to be such that, in the worst case scenario of a new pulsar having a DM that is 5 per cent off the median DM of all the other pulsars known in the cluster, the intrachannel smearing would anyway be less than 76 μs , preventing dispersive smearing from dominating the loss of sensitivity due to pulse broadening. This reduced the size of the data to search from ~ 1100 GB/h for the native-resolution files, to only $\sim 6\text{--}18$ GB/h, depending on the cluster.

3.2 Pulsar searching

The searching analysis was carried out using `PULSAR_MINER`⁸ v1.1, an automated pipeline built upon the `PRESTO`⁹ v2.1 pulsar searching package (Ransom, Eikenberry & Middleditch 2002). All the routines mentioned in this section are part of `PRESTO`, unless otherwise stated.

First, a list of bad frequency channels and time intervals in the observations were flagged as contaminated by RFI and excluded from the rest of the analysis. This was done by generating a mask with the `rfifind` routine. In particular, some of the frequency channels that are notoriously polluted by strong RFI were marked manually. Additional bad channels and time intervals were automatically flagged by `rfifind`, based on statistical analyses.

Ignoring the masked channels, a 0-DM time series was created using `prepdata`. A Fourier transform of the latter led to the detection of prominent periodic RFI (the so-called birdies) still present in the data. The frequencies of such signals were stored in a ‘zaplist’ file, to be later removed from the Fourier spectra where new pulsars are searched. Similarly, for all the previously known isolated pulsars in the cluster, the barycentric spin frequencies and their harmonics (up to eight) were calculated at the epoch of the observation and listed in the same zapfile, to later be also removed from the Fourier spectra. This is especially useful to prevent the re-detection of very bright isolated pulsars, which are likely to produce a large number of candidates, so as to save computational time that would otherwise be needed for their folding.

Using the `DDplan.py` routine, an optimal de-dispersion scheme was generated. This is automatically computed on the basis of the DM range to search for the particular cluster, the DM value at which the data were coherently de-dispersed, as well as on the other observing parameters (see e.g. Lorimer & Kramer 2004). The range of DMs searched for each cluster was chosen to be between ± 5 per cent of the median DM of the known pulsars of that cluster. The mask and the de-dispersion scheme were fed into `prepsubband` to generate a number of (mostly) RFI-free time series, de-dispersed at the different DM trial values within the chosen range, and referred to the Solar system barycentre. The barycentred time series were then Fourier transformed with `realfft` and the resulting power spectra de-reddened using `rednoise`.

⁷https://github.com/scottransom/psrfits_utils

⁸https://github.com/alex88ridolfi/PULSAR_MINER

⁹<https://www.cv.nrao.edu/~sransom/presto/>

The periodicity search was performed using a matched filtering algorithm in the Fourier domain, implemented in `accelsearch`. While an isolated pulsar has its power concentrated in just the Fourier bin associated with its spin frequency and its harmonics, this is not the case for a binary pulsar. In fact, for an observation of length Δt_{obs} , a pulsar with a spin period P that is undergoing a line-of-sight acceleration a_l due to an orbital motion, will see the power associated with its spin frequency shift in the Fourier domain by a number $z = \Delta t_{\text{obs}}^2 a_l / cP$ of Fourier bins, where c is the speed of light. `accelsearch` is capable of recovering such Doppler-shifted periodic signals of binary pulsars, by also considering the Fourier powers spread over up to z_{max} bins around a given frequency, regarded as the fundamental harmonic. For our searches, we used a value of $z_{\text{max}} = 0$ for targeting new isolated pulsars, and a $z_{\text{max}} = 200$ for possible new binary pulsars. In both cases, the powers of the first eight harmonics were summed. It is important to note that the main assumption of the algorithm is that the acceleration along the line of sight undergone by the pulsar during the observation be constant. This assumption is not valid when $\Delta t_{\text{obs}} \gtrsim 0.1P_b$, where P_b is the binary orbital period (Ransom, Cordes & Eikenberry 2003). For this reason, we also performed a so-called segmented search (Johnston & Kulkarni 1991), where the observation is split into shorter sections, each of which is searched individually. This allows for the detections of pulsars in tighter binaries, at the cost of a reduced sensitivity caused by the shorter integration time. Hence, besides searching the full-length observation (which gives the maximum sensitivity to isolated pulsars and wide binaries), we split each observation into sections of 60, 30, 15, and 5 min (with no overlaps) and searched each of them individually. This strategy made our search potentially sensitive to bright pulsars in extremely compact binary systems with orbital periods as short as ~ 50 min.

3.3 Candidate sifting and folding

For each section, all the candidates produced by the acceleration search were grouped according to their harmonic relations and sifted using standard criteria (e.g. the same candidate should be significant in at least three adjacent DM trial values) and kept candidates with a Fourier significance of 4σ or more (see Ransom et al. 2002 for details). This resulted in a number of candidates in the range of 200–3000 for each observation, depending on its length, the number of bright, previously known binary pulsars (whose periodicities were not removed from the Fourier spectra) in that cluster and the residual RFI contamination. All the candidates were automatically folded with `prepfold`, using their nominal period, DM, and possible acceleration, and allowing the software to optimize those parameters and maximize the χ^2 of the folded profile (Leahy et al. 1983). The folds produced diagnostic plots containing, among other things, the integrated pulse profile, and the signal intensity as a function of time and frequency. All the plots were inspected visually. The ones with a high χ^2 , persistent and broad-band signals were marked as ‘good’ candidates, and further investigated.

3.4 Confirmation and characterization

In order to be proclaimed as a newly discovered pulsar, a candidate (i.e. a P –DM pair) was required to be identified in at least two separate observing epochs of the same cluster. For some of the low-DM clusters, where the pulsars scintillate, we also used archival data taken at other radio telescopes to confirm the new discoveries. In that case, we folded the archival data (and then optimized the result) using the P –DM values of the new pulsar; when no detection resulted

from direct folding (as is often the case for binary pulsars) we used `accelesearch` to search for the signal within a narrow range of P and DM around their nominal values.

3.4.1 Orbital determination for binary pulsars

If the observed spin period, P_{obs} , and possibly the associated observed spin period derivative, \dot{P}_{obs} , of a newly found pulsar appeared different from epoch to epoch, we considered that as a sign of binarity of the pulsar. To estimate the orbital parameters, we started following the method of Freire, Kramer & Lyne (2001a). First, we measured the barycentric P_{obs} and \dot{P}_{obs} from all the available detections of the new pulsar. If the detection significance of a particular observation was high, we split that observation into sections, so as to have more P_{obs} and \dot{P}_{obs} measurements. We then converted each \dot{P}_{obs} into the corresponding line-of-sight acceleration, a_l , via the relation $a_l = c(\dot{P}/P)_{\text{obs}}$, and plotted it as a function of P_{obs} . The resulting plot is referred to as ‘period–acceleration’ diagram, where the (P_{obs}, a_l) points will fall on a closed curve, whose position and shape are related to the pulsar’s intrinsic spin period, P_{int} , and to the orbital parameters. In the case of a circular orbit, the points follow an ellipse, which can be fitted to obtain estimates of the orbital period, P_b , and of the semimajor axis of the pulsar orbit, projected along the line of sight, x_p . If the orbit is eccentric, the curve deviates from a perfect ellipse, and its more complex shape embodies information on the eccentricity, e , the longitude of periastron of the pulsar orbit, ω , as well as on P_b and x_p .

For the new binary pulsars that were not affected by scintillation (i.e. their flux density appeared stable in each detection), we performed a few additional observations that were aimed at refining their orbital parameters. We regard these observations as ‘orbital campaigns’ (and label them with ‘-orbX’ in Table 2). These orbital campaigns consisted of 4–5 observations, performed within a time range of a few days, with long enough integration times to guarantee a firm detection of the pulsar in each of them. With these detections, we could fit the observed spin period as a function of time, $P_{\text{obs}}(t)$. We did so using some of the PYTHON scripts included in PRESTO, namely `fit_circular_orbit.py` for the circular binaries, and `fitorb.py` for the eccentric ones. Using the results of period–acceleration diagram as starting estimates, the $P_{\text{obs}}(t)$ fit returned much improved orbital parameters, which could then be further refined by fitting the pulse times-of-arrival (ToAs, see next section).

For two new circular binaries that were affected by scintillation, this strategy was not viable. For them, we used the ‘periodogram’ method (see e.g. Ridolfi et al. 2016) to refine the measurement of P_b . On each observation where the pulsar was detected, we used SPIDER_TWISTER¹⁰ to perform a brute-force search in orbital phase, assuming the initial P_b and x_p estimated through the period–acceleration diagram. The search returned the best times of ascending node, T_{asc} , closest to the epoch of each detection. Exploiting the fact that each T_{asc} pair must accommodate an integer number of orbits, this method allowed us to obtain a much improved estimate of P_b .

3.4.2 Timing

Using the DSPSR¹¹ pulsar software package (van Straten & Bailes 2011), we folded all the MeerKAT observations of the GC where a new pulsar was detected, using the nominal P –DM values. Whenever possible, we also used archival data taken by other telescopes.

We used the PSRCHIVE¹² package (Hotan et al. 2004; van Straten, Demorest & Osłowski 2012) tools to clean the resulting folded archives and to extract topocentric ToAs, using a sensible decimation scheme (i.e. choosing a suitable number of subintegrations and frequency channels) for each individual epoch. We then constructed a starting ephemeris with a basic timing model, which included the nominal host cluster’s centre position, the nominal pulsar barycentric spin frequency, its DM and, if binary, a Keplerian orbital model, with a theory-independent description of relativistic effects, the ‘DD’ model (Damour & Deruelle 1986). The initial Keplerian parameters are derived as described in Section 3.4.1. This ephemeris was fed to the TEMPO¹³ pulsar timing software, which we used to fit the ToAs for the timing model parameters, as well as for arbitrary phase offsets (so-called jumps) between epochs. Following the procedure described in Freire & Ridolfi (2018), we started connecting groups of ToAs, removing the arbitrary jumps whenever possible, and updating the model. For the faintest pulsars, and for those with sparse detections, we did this with the help of DRACULA¹⁴, an automated software for determining the correct rotation counts of pulsars. Depending on the pulsar, the precision of the ToAs and the total time spanned by the data set, we sometimes included additional parameters to the model, such as spin frequency derivatives, the proper motion, and post-Keplerian (PK) effects. The whole procedure was iterated a few times until either all the ToAs were phase-connected or no further improvement of the timing solution was possible.

4 RESULTS

4.1 Discoveries

The search of the MeerKAT L -band data has resulted in the discovery of eight previously unknown MSPs in six different clusters. Five of the discoveries belong to binary systems, with orbital periods ranging from a few hours to several days. The two most compact binaries also show eclipses. The spin periods of the new pulsars are all in the very narrow range of 2.74–8.48 ms. This is not a selection effect, since previously known pulsars with longer periods up to 405 ms were also blindly redetected by our search pipeline. The main characteristics of the new pulsars, including their mean flux densities estimated with the radiometer equation, are reported in Table 3, whereas their integrated pulse profiles are shown in Fig. 2. In the following, we review each discovery in detail.

4.1.1 47 Tuc ac, ad

47 Tuc is one of the most massive GC in the Galaxy, and one of the largest in the sky. It is located at a distance of 4.69 kpc (Woodley et al. 2012), well outside the Galactic plane, not far from the South Celestial Pole. For this reason, deep searches for radio pulsars in 47 Tuc were, until recently, only possible with the Parkes radio telescope. These searches were extremely fruitful, as they allowed the discovery of 25 pulsars in the cluster (Manchester et al. 1990, 1991; Robinson et al. 1995; Camilo et al. 2000; Pan et al. 2016; Freire et al. 2017). 10 of these pulsars are isolated and 15 are part of binary systems, and all are MSPs with rotation periods in the range of 2–8 ms. We have discovered two previously unknown binary MSPs in this cluster, dubbed 47 Tuc ac (PSR J0024–7204ac) and 47 Tuc ad (PSR J0024–7204ad). Both of them, as all the other pulsars in 47

¹⁰https://github.com/alex88ridolfi/SPIDER_TWISTER

¹¹<http://dspsr.sourceforge.net>

¹²<http://psrchive.sourceforge.net>

¹³<http://tempo.sourceforge.net>

¹⁴<https://github.com/pfreire163/Dracula>

Table 3. List of the newly discovered pulsars and their main characteristics. P : spin period; DM: dispersion measure; P_b : binary orbital period; x_p : projected semimajor axis of the pulsar orbit; e : orbital eccentricity; M_c^{\min} : minimum companion mass (estimated from the mass function and assuming a pulsar mass $M_p = 1.4 M_\odot$); S_{1300} : mean flux density at 1300 MHz.

Pulsar name	P (ms)	DM (pc cm^{-3})	Type	Summary of discoveries				S_{1300} (μJy)	Phase-connected solution?
				P_b (d)	x_p (lt-s)	e	M_c^{\min} (M_\odot)		
47 Tuc ac	2.74	24.46	Binary (black widow)	~ 0.18	~ 0.019	0^a	~ 0.0079	152^b	No
47 Tuc ad	3.74	24.41	Binary (redback)	0.32	0.68	0^a	0.205	84^b	No
M62G	4.61	113.68	Binary (pulsar–WD)	0.77	0.62	0.0009	0.099	80(17)	Partial
Ter 5 an	4.80	237.74	Binary (pulsar–WD)	9.62	12.78	0.0066	0.433	31(2)	Yes
NGC 6522D	5.53	192.73	Isolated	–	–	–	–	28(9)	No
NGC 6624G	6.09	86.21	Binary (pulsar–WD/NS)	1.54	3.00	0.3805	0.332	47(10)	Yes
NGC 6624H	5.13	86.85	Isolated	–	–	–	–	31(9)	No
NGC 6752F	8.48	33.20	Isolated	–	–	–	–	55(8) ^b	Yes

^aManually set to zero, not result of fit.

^bLikely biased by scintillation.

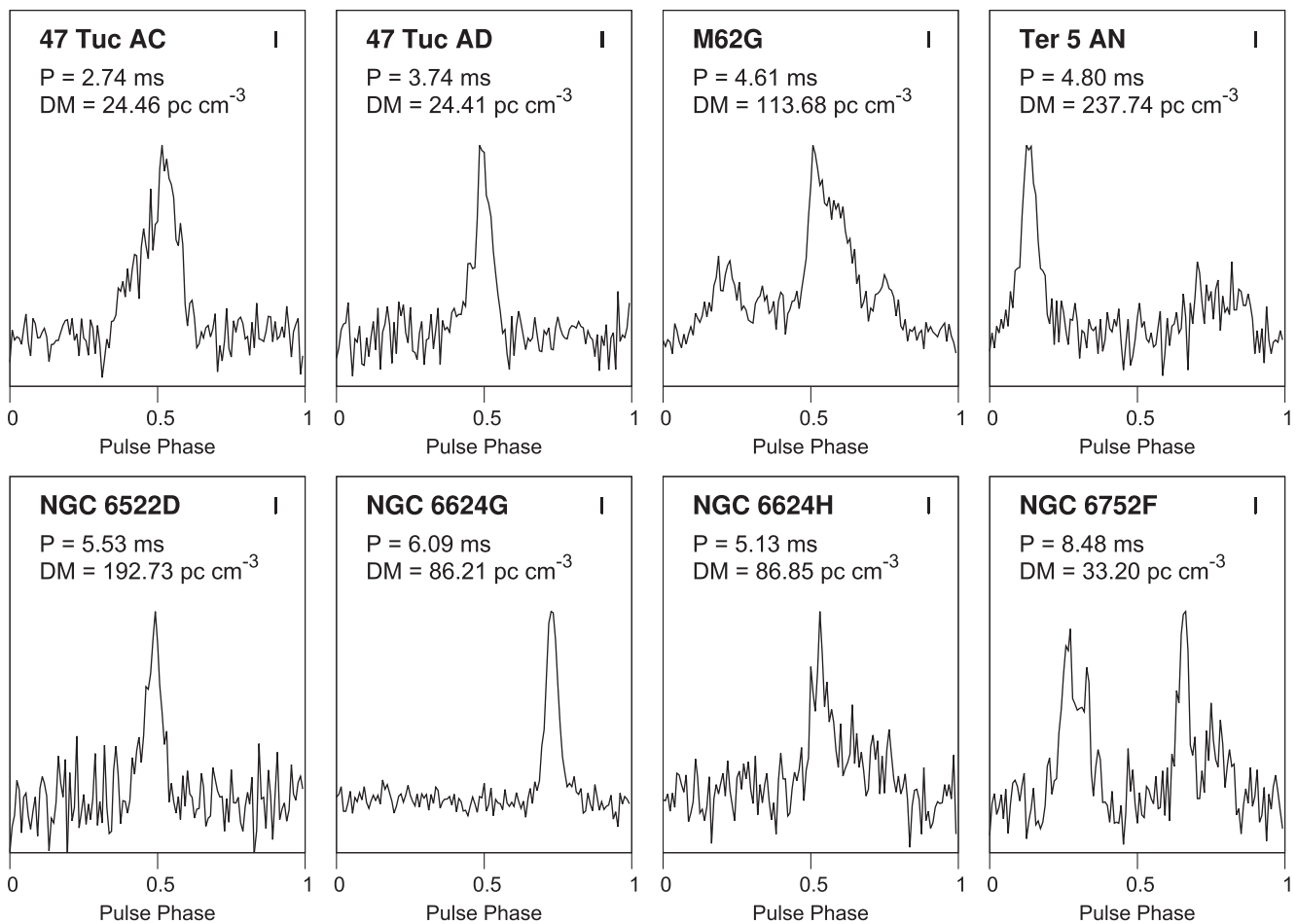


Figure 2. Integrated pulse profiles of the eight MSPs discovered, with their spin period and DM indicated. The horizontal section of the tiny bars on the top right of each panel shows the sampling time of the native-resolution (sampling time of $9.57 \mu\text{s}$) MeerTime search-mode data.

Tuc, are heavily affected by scintillation, which makes their follow-up challenging.

47 Tuc ac was discovered as a 2.74-ms pulsar in the second MeerKAT observation (obs. id 02L) of the cluster, where it appeared extremely bright. It was detected at a DM of 24.46 pc cm^{-3} and with a line-of-sight acceleration of $a_l = -1.1 \text{ m s}^{-2}$ (corresponding to a $z = 4$), indicating the presence of an orbital motion affecting the

observed spin period. Subsequent folding revealed the disappearance of the signal in the last fraction of the observation (rightmost panel of Fig. 3), likely caused by intrabinary material intercepting the pulsar’s radiation, as is typical of many compact ‘spiders’ (Roberts 2013). No further detections of the pulsar were obtained from the other eight MeerKAT observations of 47 Tuc. To confirm the discovery, we analysed the 16-yr 47 Tuc Parkes data set (519 observations taken in

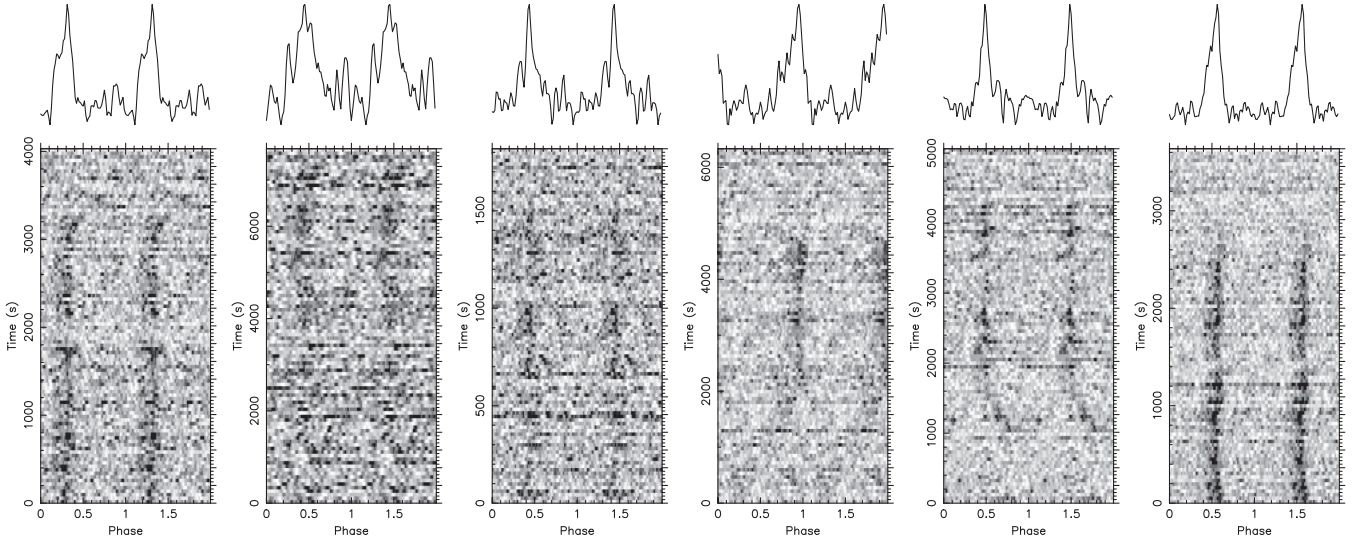


Figure 3. Intensity as a function of time and spin phase for all the six detections obtained for the new eclipsing black widow pulsar 47 Tuc ac. From left to right, the first five panels show the detections obtained from Parkes observations made on 2000-05-17, 2000-10-01, 2001-07-27, 2003-10-04, and 2008-07-01, respectively; the rightmost panel shows the MeerKAT discovery observation (obs. id 02L). The phase drifts shown are likely due to the additional dispersive delay caused by the intrabinary eclipsing material, as well as to some possible residual uncorrected orbital motion due to the poorly determined binary parameters.

the years 1997–2013) described in Ridolfi et al. (2016). Doing a blind search at the DM of 47 Tuc ac, the pulsar was found in three different observations, in all of which the signal was occasionally eclipsed. We used the period–acceleration diagram and the periodogram methods to estimate the orbital parameters and build a first ephemeris. The latter was used to re-fold all the Parkes data, which resulted in a further two faint detections. We then extracted ToAs from all the available detections (excluding the sections near the eclipse ingress and egress) and used TEMPO to fit a simple Keplerian orbital model. However, four orbital period derivatives were needed to fit the ToAs and obtain an incoherent solution that could fold all the six detections. 47 Tuc ac is in an orbit with $P_b \sim 0.18$ d and $x_p \sim 0.019$ lt-s. Notwithstanding, because of the meagre number and quality of the detections obtained over a time span of 20 yr, these parameters are not yet accurate enough to guarantee a correct orbital count. Assuming a pulsar mass of $M_p = 1.4 M_\odot$, the binary mass function implies a minimum companion mass $M_c = 0.0079 M_\odot$, indicating that the pulsar belongs to the class of eclipsing ‘black widows’.

The other newly found MSP, 47 Tuc ad, is a 3.74-ms pulsar, discovered in the fifth MeerKAT observation of the cluster (obs. id 05L) at a DM of 24.41 pc cm^{-3} . It was detected with an acceleration of $a_l = 10.4 \text{ m s}^{-2}$ ($z = -30$) and some residual jerk, as well as evidence of occasional eclipses (right-hand panel of Fig. 4). This is the only detection obtained from all the MeerKAT observations of the cluster. However, following the same procedure as in the case of 47 Tuc ac, we could confirm the discovery by detecting 47 Tuc ad in one of the Parkes observations, taken on 2004 May 27. The latter is a 7.1-h-long pointing in which the pulsar shows up very bright in the first 1.28 h, after which the pulsed signal quickly fades away and disappears for the rest of the observation (left-hand panel of Fig. 4). As for 47 Tuc ac, we used the period–acceleration diagram and periodogram methods. We did so splitting both the MeerKAT and Parkes observations where the pulsar was detected into a few sections, so as to obtain multiple measurements of P_{obs} and a_l , in each of them. For 47 Tuc ad, we find $P_b = 0.3184$ d, $x_p = 0.6819$ lt-s, and $T_{\text{asc}} = 58831.790667$ MJD. The binary mass function implies a minimum companion mass of $M_c = 0.205 M_\odot$, hence 47 Tuc ad is an eclipsing ‘redback’ binary pulsar (e.g. Roberts 2013). The range of

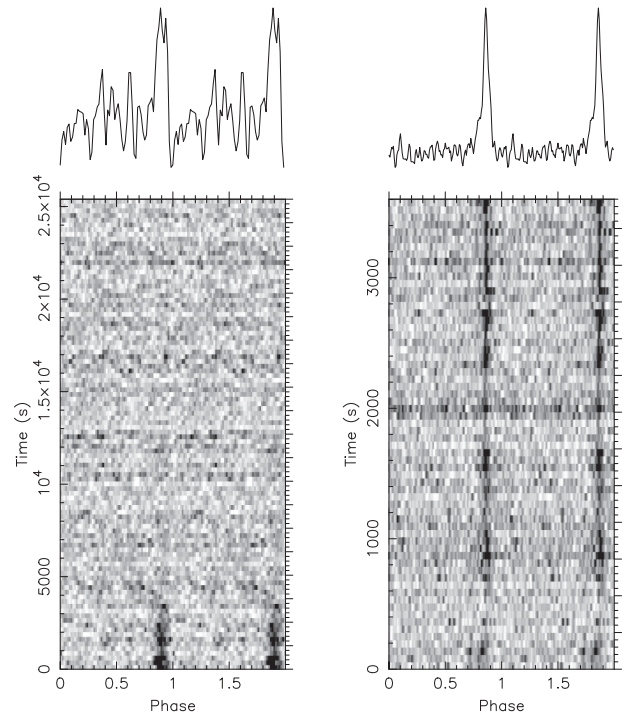


Figure 4. Intensity as a function of time and spin phase for the two detections of the new eclipsing redback pulsar 47 Tuc ad. Left-hand panel: Parkes observation made on 2004-05-27. Right-hand panel: MeerKAT discovery observation (obs. id 05L).

measured values of P_{obs} and a_l was very similar in both observations, indicating that the pulsar was detected in the same orbital phase interval. According to the binary parameters found, both detections fall in the mean anomaly orbital interval $\phi_b \sim 0.7$ – 0.9 . This is not surprising, since it is on the side of the orbit closer to the observer, where pulsars in eclipsing systems are typically most likely to be detected. Using the very long Parkes observation where 47 Tuc ad is detected, we can also estimate the fraction of the orbit in which the

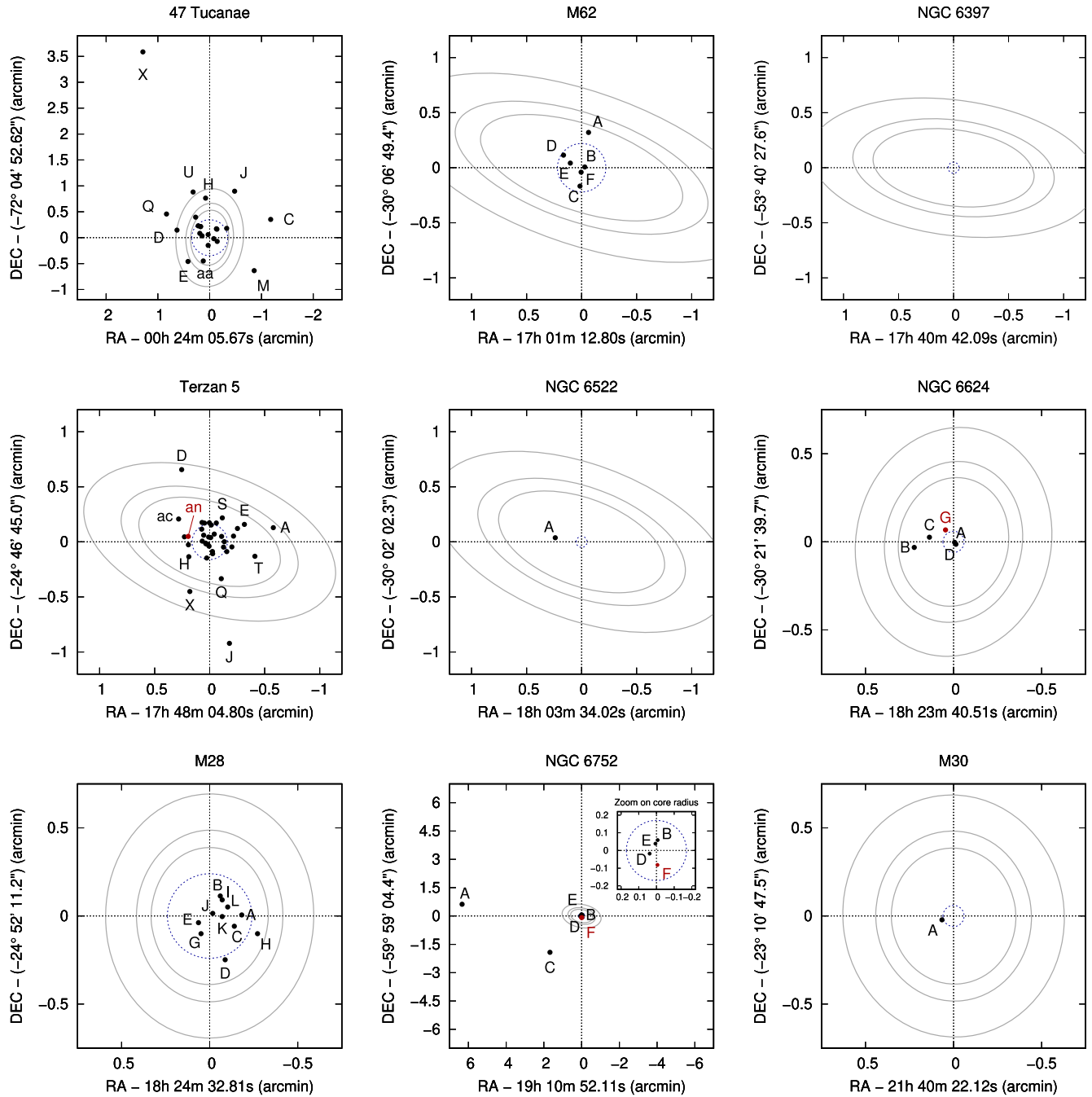


Figure 5. MeerTime L -band tied array beams, shown through their contours as solid grey lines at their 50 per cent level of power, for one sample observation of each of the nine GCs observed. We show the size of the beam for the top edge frequency (inner ellipse), centre frequency (middle ellipse), and bottom edge frequency (outer ellipse). For each cluster, we show the core radius (dashed blue line) as well as all the pulsars with a precisely determined position (black dots for the previously known pulsars, red dots for the discoveries presented here).

pulsar is probably being eclipsed. The derived circular orbit model implies that the 7.1-h Parkes observation started at orbital phase $\phi_b = 0.70$ and ended at $\phi_b = 1.63$. The fact that the pulsar was detected for the first ~ 1.28 h means that the eclipse ingress occurred at $\phi_b \sim 0.87$. If we assume that the eclipse is centred around the pulsar's superior conjunction ($\phi_b = 0.25$), then the pulsar signal would be undetectable for about 76 per cent of the orbit, and the eclipse egress would occur at $\phi_b = 0.63$, i.e. exactly coinciding with when the Parkes observation ends. We remark that the assumption of the eclipse being centred at $\phi_b = 0.25$, although reasonable, is not necessarily true, as observed

for other eclipsing systems. Unfortunately, lacking a detection of 47 Tuc ad in the range $\phi_b = 0.63$ – 0.70 , and scintillation being the dominant factor for the detectability of the pulsar, we cannot currently confirm this hypothesis.

47 Tuc ac and 47 Tuc ad bring the total number of pulsars known in the cluster to 27. Unfortunately, the paucity of their detections due to scintillation prevent us from obtaining phase-connected solutions, so we have no information on their spin period derivatives nor on their exact positions (although future TRAPUM observations may help with the latter). It is likely, however, that both pulsars

are located within ~ 0.5 arcmin from the cluster centre, since this is approximately the radius, at half-power, of the tied-array beam synthesized for those observations (see Fig. 5).

4.1.2 M62G

M62 (also known as NGC 6266) is a massive cluster located at a distance of 6.8 kpc in the direction of the Galactic bulge. Although previous estimates classified this cluster as core collapsed (Djorgovski & Meylan 1993), more recent studies rule out this hypothesis (Beccari et al. 2006). This is supported by the observed pulsar population of M62: all the six known MSPs are circular binaries (D’Amico et al. 2001a; Possenti et al. 2003; Lynch et al. 2012) with characteristics that are typical of unperturbed binary evolution.

We have found a new 4.61-ms binary MSP, named M62G (or PSR J1701–3006G). It was discovered at a DM = 113.68 pc cm⁻³ in the lower half of the band of the first, ~ 1 h MeerKAT observation of the cluster (obs. id 01L), with an acceleration of $\simeq 1.5$ m s⁻² ($z = -23$), hinting at a steep-spectrum binary pulsar (although this could also be an observational bias, if the pulsar is far from the tied-array beam boresight). M62G was redetected in all the subsequent observations of the cluster (which included a dense orbital campaign consisting of five observations taken within 10 d), always with nominal absolute line-of-sight accelerations ranging from 0.5 to 1.6 m s⁻², confirming the binary nature. Using the period–acceleration diagram method first, and the $P_{\text{obs}}(t)$ fitting of the orbital campaign observations, we derive a circular binary orbit with $P_b \sim 0.77$ d and $x_p = 0.62$ lt-s, implying a companion of minimum mass $M_c = 0.099 M_\odot$ (for $M_p = 1.4 M_\odot$). Pulsar G was observed and detected by MeerKAT at all possible orbital phases, without any signs of eclipses. Hence, it is likely that the companion star is a white dwarf (WD). Using all the MeerKAT observations, we computed the ToAs, and fitted the latter with TEMPO. Unfortunately, the detections are too sparse to guarantee a phase-coherent timing solution throughout the data set. However, we could achieve unambiguous phase connection on part of the data. This was enough to reveal that the eccentricity of the system is very low ($e = 9.1 \times 10^{-4}$) but non-zero, leading to a high covariance between the longitude of periastron, ω , and the epoch of periastron passage, T_0 . For this reason, we opted for an ELL1 binary model, which fits for x_p , P_b , and T_{asc} and for the so-called Laplace–Lagrange parameters ($\epsilon_1 = e \sin \omega$ and $\epsilon_2 = e \cos \omega$; Lange et al. 2001). The parameters derived with the partially connected solution for this pulsar are reported in Table 4.

4.1.3 Ter 5 an

Ter 5 is a GC located well within the Galactic bulge. With 38 radio pulsars known (Lyne et al. 1990; Ransom 2001; Ransom et al. 2005; Andersen & Ransom 2018; Cadelano et al. 2018), it holds the record for the highest number of pulsars hosted, and accounts for about one-fifth of the total GC pulsar population.

In this cluster, we have discovered a new 4.80-ms binary MSP, at a DM of 237.74 pc cm⁻³. The pulsar, called Ter 5 an (PSR J1748–2446an), was detected in the first MeerKAT observation of the cluster (obs. id 01L) with a small acceleration of $+0.22$ m s⁻² ($z = -13$). The period and acceleration matched those of a candidate found in the initial set of searches performed in 2005 on the GBT data, thereby instantly confirming it. To determine the binary parameters, a dense orbital campaign of four 3.5-h-long observations was carried out on the pulsar over the course of 3 d.

These observations covered about a quarter of the orbit, enough to fit $P_{\text{obs}}(t)$ and have a first estimate of P_b and x_p . Using this initial orbital model, we could fold and detect the pulsar in a number of archival GBT observations of Ter 5, taken with the Spigot (Kaplan et al. 2005) and GUPPI (DuPlain, Benson & Sessoms 2008) backends with the *L*-band and *S*-band receivers. These were used to further refine the orbital parameters: the pulsar was found to be in a ~ 9.62 -d, slightly eccentric orbit. With more certain binary parameters, the pulsar could then be detected in a large number (63) of observations in the archival data, providing us with a total timing baseline of about 16 yr (2004–2020). Combining the MeerKAT and the GBT detections, we obtained a phase-connected timing solution using the theory-independent DD binary model. Ter 5 an is in a binary orbit with very likely a WD companion of minimum mass of 0.43 M_\odot (for $M_p = 1.4 M_\odot$). The orbital eccentricity is $e = 0.0066$, and it is likely due to the stellar interactions encountered by the system in the dense environment of the cluster. We were also able to measure the rate of advance of the periastron, which is $\dot{\omega} = 0.009 \pm 0.001$ deg yr⁻¹. Assuming that this is fully relativistic, and that General Relativity (GR) is the correct theory of gravity, this translates into a total mass of the system $M_{\text{tot}} = 2.97 \pm 0.52 M_\odot$. Taking the uncertainty of $\dot{\omega}$ into account, and assuming a priori randomly aligned orbits, we made a χ^2 map to constrain the component masses of the system. We find that the pulsar mass is $M_p = 2.13^{+1.01}_{-1.32} M_\odot$ and the companion mass is $M_c = 0.75^{+1.38}_{-0.25} M_\odot$ at the 2σ confidence level. Although the constraints on the masses are very loose, we can at least exclude very high orbital inclinations, given that $i < 83.76^\circ$ at the 2σ level. The resulting mass–mass diagram obtained for Ter 5 an is shown in Fig. 7. We have also measured the orbital period derivative, $\dot{P}_b = (26.8 \pm 3.4) \times 10^{-12}$ which, in the case of GC pulsars, includes contributions from accelerations due to the cluster potential, Galactic potential, and Shklovskii effect (caused by the proper motion of the system; Shklovskii 1970) combined. The long timing baseline has also allowed us to measure the pulsar astrometric and kinematic parameters. Ter 5 an is located ~ 0.2 arcmin (1.26 core radii) east of the cluster centre (Fig. 5). The proper motion is still loosely constrained, with measured values of $\mu_\alpha = -2.2 \pm 0.6$ mas yr⁻¹ and $\mu_\delta = -28 \pm 18$ mas yr⁻¹, consistent with those of the other pulsars in the cluster (S. Ransom, private communication). As for the rotational parameters, we measured up to three spin frequency derivatives for Ter 5 an. The first derivative is due to the intrinsic spin-down, as well as the cluster gravitational potential. The second derivative likely has contributions from both the cluster potential and the presence of nearby stars. Higher derivatives are entirely due to local potentials around the system in the cluster, as has been studied with other known pulsars in Ter 5 (Prager et al. 2017). Since the acceleration contributions to both spin and orbital period derivatives are similar, the intrinsic spin period derivative, \dot{P}_{int} , can be calculated from the relation $\dot{P}_{\text{int}} = \dot{P}_{\text{obs}} - P \dot{P}_{b,\text{obs}}/P_b$ (considering $\dot{P}_{b,\text{int}} \sim 0$, which is the case for wide orbits with negligible gravitational wave damping). We obtain $\dot{P}_{\text{int}} = (8.49 \pm 0.02) \times 10^{-22}$. From this, we can constrain the surface magnetic field, $B_s \leq 3.1 \times 10^8$ G, and characteristic age of the pulsar, $\tau_c \geq 3.75$ Gyr, at the 1σ level.

4.1.4 NGC 6522D

NGC 6522 is a cluster located at a distance of 7.7 kpc, close to the Galactic Centre. It is core collapsed and hosts three previously known MSPs, all of which are isolated (Possenti et al. 2005; Bégin 2006; Zhang et al. 2020). We have discovered a fourth isolated MSP, named NGC 6522D (or PSR J1803–3002D), with a spin period of

Table 4. Timing solutions for four newly discovered MSPs. For all solutions, the time units are TDB, the adopted terrestrial time standard is UTC(NIST), and the Solar System ephemeris used is JPL DE421 (Folkner, Williams & Boggs 2009). All quoted uncertainties and upper/lower limits are 1σ .

Pulsar Alt. pulsar name	M62G J1701–3006G	Ter 5 an J1748–2446an	NGC 6624G J1823–3021G	NGC 6752F J1910–5959F
Phase-connected solution?	Partial	Yes	Yes	Yes
Right ascension, α (J2000)	17:01:14.0(2)	17:48:05.65898(16)	18:23:40.7213(8)	19:10:52.066(3)
Declination, δ (J2000)	–30:06:42(41)	–24:46:42.03(7)	–30:21:35.63(5)	–59:59:09.30(3)
Proper motion in α , μ_α (mas yr ^{–1})	–	–2.12(55)	–	–1.9(1.4)
Proper motion in δ , μ_δ (mas yr ^{–1})	–	–28.4(18.5)	–	–6.5(1.9)
Spin frequency, f (s ^{–1})	217.0090551(6)	208.23191713844(2)	164.168745585(1)	117.8481780116(2)
First spin frequency derivative, \dot{f} (Hz s ^{–1})	–	$-6.7532(26) \times 10^{-15}$	$4.8(6) \times 10^{-16}$	$-1.02942(9) \times 10^{-14}$
Second spin frequency derivative, \ddot{f} (Hz s ^{–2})	–	$-8.83(16) \times 10^{-25}$	–	$-9.37(24) \times 10^{-26}$
Third spin frequency derivative, \dddot{f} (Hz s ^{–3})	–	$-4.586(56) \times 10^{-33}$	–	–
Reference epoch (MJD)	58700.000	56000.000	58700.000	58700.000
Start of timing data (MJD)	58602.827	53204.042	58736.722	51468.265
End of timing data (MJD)	59074.864	58933.449	59072.968	58850.722
Dispersion measure, DM (pc cm ^{–3})	113.679(7)	237.736(8)	86.206(6)	33.20(3)
Number of ToAs	69	198	125	67
Residuals rms (μ s)	19.15	29.17	18.55	38.25
Binary Parameters				
Binary model	ELL1	DD	DD	–
Projected semimajor axis, x_p (lt-s)	0.620316(8)	12.7820385(35)	3.00331(2)	–
Orbital period, P_b (d)	0.77443355(5)	9.6197533(8)	1.54013654(5)	–
Orbital eccentricity, e	–	0.0065856(6)	0.380466(6)	–
Epoch of periastron, T_0 (MJD)	–	56743.6892(1)	58909.681498(8)	–
Longitude of periastron, ω (°)	–	–145.2624(45)	146.721(1)	–
First Laplace–Lagrange parameter, ϵ_1	$6.08(28) \times 10^{-4}$	–	–	–
Second Laplace–Lagrange parameter, ϵ_2	$6.73(24) \times 10^{-4}$	–	–	–
Epoch of ascending node, T_{asc} (MJD)	58894.966321(3)	–	–	–
Rate of periastron advance, $\dot{\omega}$ (deg yr ^{–1})	–	0.0095(11)	0.217(4)	–
Orbital period derivative, \dot{P}_b (s s ^{–1})	–	$26.8(3.4) \times 10^{-12}$	–	–
Derived Parameters				
Spin period, P (ms)	4.60810264(1)	4.8023377671500(4)	6.09129342145(4)	8.48549393697(1)
First spin period derivative, \dot{P} (s s ^{–1})	–	$1.55746(6) \times 10^{-19}$	$-1.8(2) \times 10^{-20}$	$7.4122(6) \times 10^{-19}$
Mass function, $f(M_p)$ (M_\odot)	4.27×10^{-4}	2.42×10^{-2}	1.23×10^{-2}	–
Minimum companion mass, $M_{c, \min}$ (M_\odot)	0.10	0.43	0.33	–
Median companion mass, $M_{c, \text{med}}$ (M_\odot)	0.11	0.52	0.39	–
Total system mass (assuming GR), M_{tot} (M_\odot)	–	2.97(52)	2.65(7)	–
Intrinsic spin-down, \dot{P}_{int} (s s ^{–1})	–	$8.49(2) \times 10^{-22}$	–	–
Surface magnetic field, B_0 (G)	–	$< 3.12 \times 10^8$	–	–
Spin-down luminosity, L_{sd} (erg s ^{–1})	–	$< 7.24 \times 10^{33}$	–	–
Characteristic age, τ_c (Gyr)	–	> 3.75	–	–
Offset from GC centre in α , θ_α	–	0.195	0.046	–0.006
Offset from GC centre in δ , θ_δ	–	0.050	0.068	–0.082
Total offset from GC centre, θ_\perp (arcmin)	–	0.201	0.082	0.082
Proj. distance from GC centre, r_\perp (pc)	–	0.404	0.188	0.095
Proj. distance from GC centre, r_\perp (core radii)	–	1.257	1.363	0.482

5.53 ms and a DM of 192.73 pc cm^{–3}. The pulsar was found in the first *L*-band MeerKAT observation of the cluster (obs. id 01L) with no acceleration. It was then redetected, via direct folding with the nominal barycentric period, in the second *L*-band observation (obs. id 02L) and in a third, 40-min-long follow-up observation made in the *UHF* band (obs. id 03U). We have also searched for NGC 6522D in 154 *L*-band observations taken in the years 2000–2012 with the Parkes telescope in the context of the Parkes Globular Cluster Survey (PKSGC; Possenti et al. 2005). However, we were unable to detect the pulsar in these data. This is not surprising, given the significantly lower sensitivity of the Parkes telescope and the high DM of the cluster, which does not allow scintillation to occasionally boost the pulsar signal over the detectability threshold, as happens for other clusters. Follow-up timing with high-gain telescopes like

MeerKAT or the GBT is therefore required to obtain the astrometric and kinematic parameters of NGC 6522D.

4.1.5 NGC 6624G, H

NGC 6624 is another core-collapsed cluster, known to be the likely host of an intermediate-mass black hole at its centre (Perera et al. 2017). Its radio pulsar population is composed of one binary and five isolated pulsars. Two of the isolated pulsars are unrecycled ones with spin periods > 300 ms, whereas the others are all MSPs (Lynch et al. 2012).

In this cluster, we have found two new MSPs, NGC 6624G (PSR J1823–3021G) and NGC 6624H (PSR J1823–3021H).

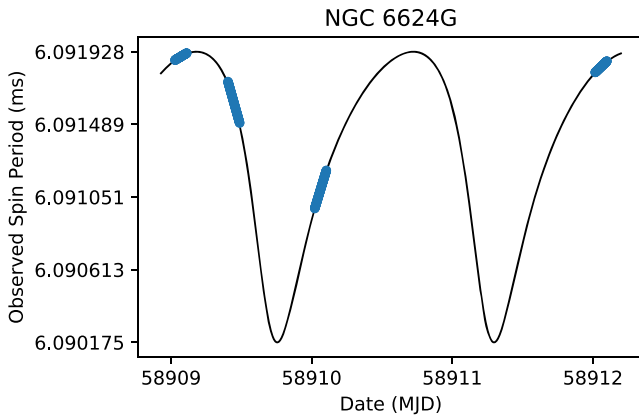


Figure 6. Blue dots: Observed spin period of NGC 6624G as a function of time, as measured during the four orbital campaign observations of the cluster; these clearly show that the pulsar orbit has a significant eccentricity. Black line: Best-fitting orbital model ($P_b = 1.54$ d, $x_p = 3.00$ lt-s, $e = 0.38$, $\omega = 146.7^\circ$).

NGC 6624G is a 6.09-ms pulsar in a highly eccentric binary orbit. The pulsar was discovered in the full-length segment (2.5 h) of the first observation (obs. id 01L) of the cluster, with a line-of-sight acceleration of -0.24 m s $^{-2}$ ($z = 11$) and some leftover jerk in the signal. The pulsar was also redetected in the four successive survey observations, which enabled us to use the period–acceleration diagram method to estimate the orbital parameters. The diagram indicated a relatively wide orbit, with signs of a non-zero eccentricity. To better characterize the orbit, we conducted a dense orbital campaign consisting of four, 2-h-long observations over a time span of about 3 d, in each of which NGC 6624G was easily detected. A fit of $P_{\text{obs}}(t)$ using these observations revealed a 1.54-d orbit with an eccentricity of $e = 0.38$ (Fig. 6). The pulsar orbit has a projected semimajor axis of $x_p = 3.00$ lt-s, and a longitude of periastron $\omega = 146.7^\circ$. The 12 MeerKAT observations of the cluster enabled the determination of a phase-connected timing solution for NGC 6624G, over a time span of ~ 11 months, which is listed in Table 4. For the latter, we used the DD binary model, as in the case of Ter 5 an. The time spanned by the solution allowed us to have first estimates of the pulsar position and its \dot{P} . The timing position places NGC 6624G at ~ 0.08 arcmin, roughly in the north-east direction, from the nominal cluster centre. As we shall see in Section 4.2.2, this position is confirmed by the TRAPUM observations of the cluster. The observed spin period derivative is $\dot{P} = (-1.8 \pm 0.2) \times 10^{-20}$. From the negative value, we deduce that the line-of-sight acceleration caused by the cluster’s gravitational field is significant in NGC 6624G, and the latter must be located on the far side of the cluster. This seems to be at odds with the measured DM of 86.206 ± 0.06 pc cm $^{-3}$, which is the lowest among all the known pulsars in NGC 6624. This means that the DM variations are likely dominated by the Galactic foreground, as in nearly all known GCs, and not by gas within the cluster, as in the case of 47 Tuc (Freire et al. 2001b). Thanks to the high eccentricity of the system, 11 months of timing were also sufficient to measure the rate of advance of periastron to high significance: $\dot{\omega} = 0.217 \pm 0.004$ deg yr $^{-1}$. Assuming that this is purely relativistic and that GR is the correct theory of gravity, this implies that the total mass of the system is $M_{\text{tot}} = 2.65 \pm 0.07 M_\odot$. Also, the $\dot{\omega}$ measurement constrains the minimum mass of the companion to $M_c \gtrsim 0.44 M_\odot$, the maximum pulsar mass $M_p \lesssim 2.4 M_\odot$, and the system inclination $i \gtrsim 9.6^\circ$ (see Fig. 7). As in the case of Ter 5 an, we made a χ^2 map to constrain the component masses of the system, considering

the uncertainty of $\dot{\omega}$, and assuming a priori randomly aligned orbits. For this system, we find that the pulsar mass is $M_p = 2.10^{+0.19}_{-1.23} M_\odot$ and the companion mass is $M_c = 0.53^{+1.30}_{-0.09} M_\odot$ at the 2σ confidence level. Even though the masses are still loosely constrained, the probability that the pulsar has a mass $> 2 M_\odot$ is 69 per cent. The detection of a second relativistic effect will be necessary to have precise measurements of the individual masses, but no such effects have been detected in the timing so far. Finally, we note that the companion star could be either a massive WD or an NS. Regardless of its nature, the current companion is too massive to be the remnant of the star that recycled the pulsar: NGC 6624G is very likely the result of a ‘secondary’ exchange encounter, where the original companion that spun the pulsar up was ejected and replaced by the current companion. Comparing it to the other secondary exchange products mentioned above, we find that contrary to M15C, and similarly to NGC 1851A, NGC 6624G is very close to the cluster centre. This is very likely to be the result of mass segregation: being much more massive than the average stellar population in NGC 6624, dynamical friction caused the system to quickly sink towards the centre.

The second new pulsar in the cluster, NGC 6624H, is isolated and has a spin period of 5.13 ms. It was discovered with no signs of acceleration in the fourth observation of the cluster (obs. id 04L), at a DM of 86.85 pc cm $^{-3}$, and subsequently redetected, through folding, in most of the other observations of NGC 6624. Because of its faintness, we were able to phase connect only a few groups of ToAs, but were unable to derive a coherent solution across all the data. Nevertheless, thanks to the TRAPUM observations of the cluster, we know that pulsar H is most likely located at less than ~ 0.1 arcmin from the centre of NGC 6624 (see Section 4.2.2).

4.1.6 NGC 6752F

NGC 6752 is a core-collapsed cluster hosting five known pulsars. The peculiarity of this cluster is the location of two of these pulsars, namely pulsar A (a relativistic pulsar–WD binary; D’Amico et al. 2001a; Corongiu et al. 2006, 2012) and C (an isolated MSP; D’Amico et al. 2001b), both of which are extremely far from the cluster centre. The other three pulsars (B, D, and E), which are also isolated MSPs, (D’Amico et al. 2001b, 2002) are much closer to the cluster centre, a natural consequence of mass segregation (Ferraro et al. 1997).

We have discovered a new 8.48-ms isolated MSP, dubbed NGC 6752F (or PSR J1910–5959F). The pulsar was found in the second, 2.5-h-long observation (obs id. 02L) of the cluster, at a DM of 33.20 pc cm $^{-3}$ and with no measurable acceleration. We then revisited the preceding observation of NGC 6752 (obs id. 01L) and obtained a second, fainter detection, again with no evidence of acceleration, confirming the isolated nature of the pulsar. Searching for the same periodicity in archival *L*-band data of the cluster taken at Parkes in the years 1999–2016, we were able to redetect pulsar F in 40 other observations. Although in a handful of these NGC 6752F showed up fairly brightly, the vast majority of the detections were extremely faint. The elusiveness of the pulsar in the Parkes data set is due to its intrinsic faintness and to the strong scintillation that affects the pulsars of this cluster, which only occasionally brings the flux density of NGC 6752F above the detection threshold of Parkes. Combining the ToAs obtained from the Parkes and MeerKAT detections, we were able to obtain a phase-connected timing solution spanning ~ 20 yr (1999–2020), listed in Table 4. The pulsar is located within the core radius of the cluster, about 0.1 arcmin south of the nominal cluster centre (Fig. 5). The long time spanned by the data also enabled the detection of two spin frequency derivatives,

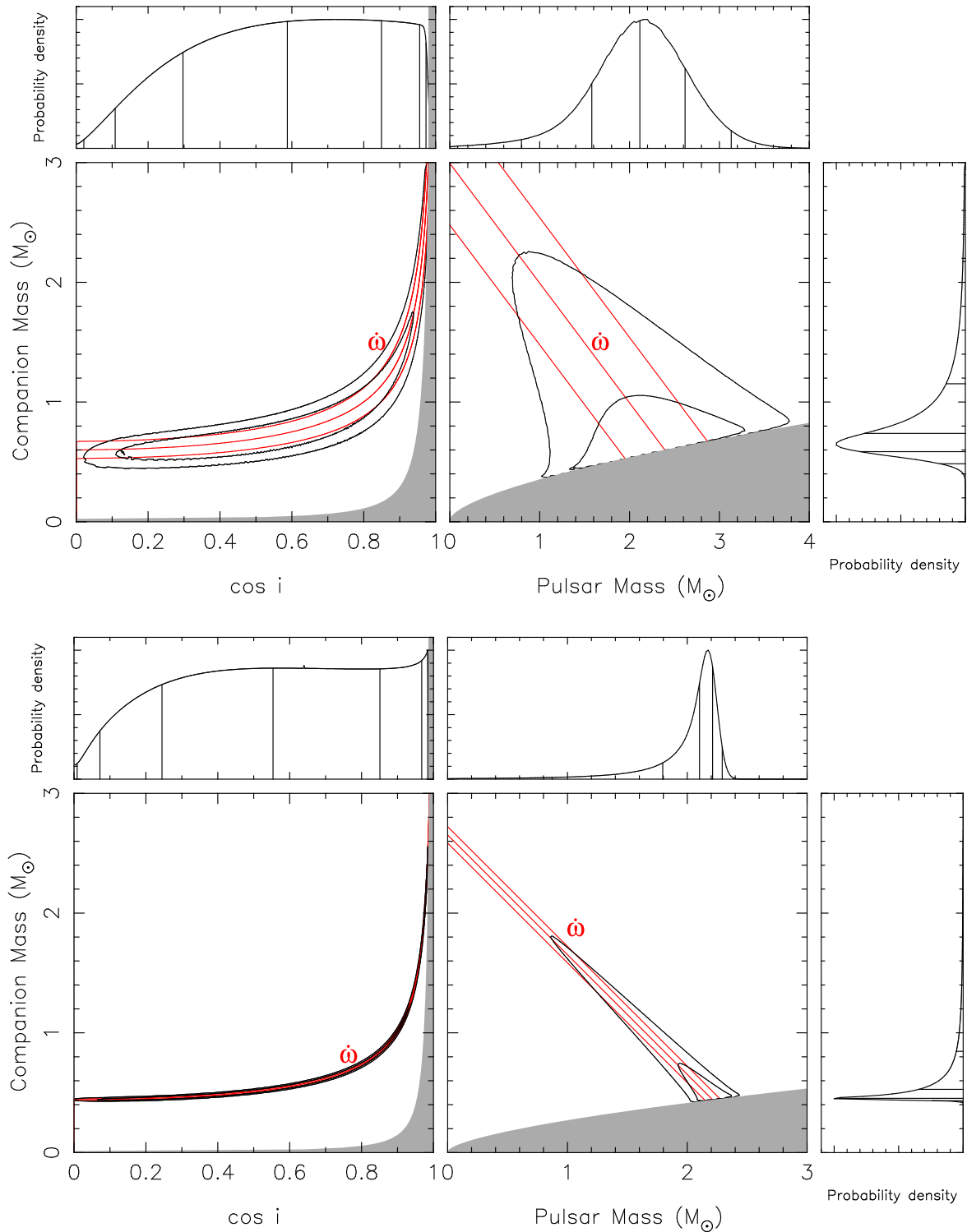


Figure 7. Mass–inclination and mass–mass diagrams for Ter 5 an (top) and NGC 6624G (bottom). The main square panels depict the $\cos i$ – M_c and M_c – M_p planes. The grey areas in the former are excluded by the requirement that the mass of the pulsar is positive, the grey areas in the latter are excluded by the mass function and the requirement that $\sin i \leq 1$. The red lines depict the masses consistent with the measurement of $\dot{\omega}$ and its $\pm 1\sigma$ uncertainties, under the assumption that this effect is dominated by the GR contribution and that GR is the correct theory of gravity. The contours include 68.3 and 95.4 per cent of a 2D probability distribution function (pdf) derived from the χ^2 of TEMPO fits that assumed all GR effects to be according to the masses and orbital inclination at each point. The side panels show the probability density functions for the $\cos i$ (top left), M_p (top right), and M_c (right) derived by marginalizing the aforementioned 2D pdfs. For Ter 5 an, the estimated median pulsar mass is $2.13 M_\odot$ and median companion mass is $0.75 M_\odot$. In the case of NGC 6624G, we obtain a median for the pulsar mass of $2.1 M_\odot$, but with a tail of probability that extends to lower masses: there is a 31 per cent probability of $M_p < 2 M_\odot$ and a 3.8 per cent probability of $M_p < 1.4 M_\odot$. Thus, either the pulsar is very massive or it has a massive companion; the system was likely formed in an exchange encounter. The timing for both systems shows no evidence for the Shapiro delay nor any other relativistic effect that might allow a determination of the individual masses, as we can see from the fact that only high inclinations (near $\cos i = 0$) are excluded by the lack of a detectable Shapiro delay. Apart from these, the pdf is very flat in $\cos i$.

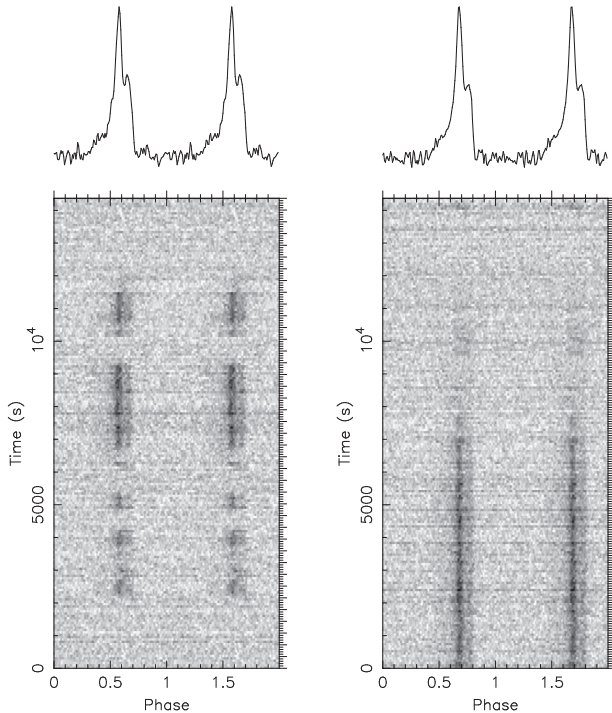


Figure 8. Intensity as a function of time and spin phase for the two strongest detections of the eclipsing redback NGC 6624F, obtained from the two 4-h-long TRAPUM observations of the cluster (left: obs. id 10L-trapum; right: obs. id 12L-trapum).

likely due to the cluster’s and local stellar gravitational potentials experienced by the pulsar. As the first spin period derivative is positive ($\dot{P} = 7.4 \times 10^{-19}$), we cannot say whether NGC 6752F is located on the near or far side of the cluster nor can we use the pulsar to put additional constraints to the mass-to-light ratio of this cluster (D’Amico et al. 2002). We were also able to measure the proper motion of the pulsar in both right ascension and declination, which we find to be $\mu_\alpha = -1.9 \pm 1.4 \text{ mas yr}^{-1}$ and $\mu_\delta = -6.5 \pm 1.9 \text{ mas yr}^{-1}$, respectively. Considering a distance to the cluster of 4.0 kpc (Harris 1996), the total proper motion of $\mu_{\text{tot}} = 6.80 \pm 2.17 \text{ mas yr}^{-1}$ implies that the pulsar is moving with a transverse velocity of $\sim 129 \text{ km s}^{-1}$.

The bulk proper motion of NGC 6752 has recently been measured by Gaia Collaboration (2018): $\mu_\alpha = -3.1908 \pm 0.0018 \text{ mas yr}^{-1}$ and $\mu_\delta = -4.0347 \pm 0.0020 \text{ mas yr}^{-1}$. This implies that the pulsar proper motion relative to the cluster is $\Delta\mu_\alpha \sim 1.3 \pm 1.4 \text{ mas yr}^{-1}$ and $\Delta\mu_\delta \sim -2.5 \pm 1.9 \text{ mas yr}^{-1}$ corresponding to a relative transverse velocity in the range 19–87 km s^{-1} , at the 1σ level. Although the uncertainty is large, this is still consistent with the pulsar being bound to the cluster, as the latter has a central escape velocity of $\sim 30 \text{ km s}^{-1}$ (Colpi, Mapelli & Possenti 2003).

4.2 Characterization of previously known pulsars

Apart from the search and discovery of new pulsars, the first MeerKAT GC census observations are valuable for a number of additional scientific studies. Here, we report a few more results on previously known pulsars, obtained using the collected data.

4.2.1 The orbit and eclipses of NGC 6624F

NGC 6624F (or PSR J1823–3021F) is a 4.85-ms eclipsing binary pulsar discovered by Bégin (2006). A first attempt on characterizing the orbit was made by Lynch et al. (2012), who estimated an orbital

Table 5. List of the NGC 6624 pulsars without a known position and corresponding beams where they were detected with highest S/N in the first TRAPUM observation of the cluster (id 10L-trapum). θ_\perp is the angular distance between the beam boresight and the nominal cluster centre.

Pulsar	Highest-S/N beam (#)	Beam boresight coordinates (RA, Dec.)	θ_\perp (arcsec)
D	004	18 ^h 23 ^m 40 ^s .51, –30° 21′ 39″.70	0
E	056	18 ^h 23 ^m 38 ^s .93, –30° 22′ 22″.30	47.25
F	029	18 ^h 23 ^m 40 ^s .67, –30° 21′ 14″.20	25.58
H	000	18 ^h 23 ^m 40 ^s .48, –30° 21′ 39″.90	0.44

period of $P_b = 0.8827 \text{ d}$ and a projected semimajor axis of $x_p \simeq 4.4 \text{ lt-s}$, assuming a circular orbit. These estimates, however, were based on only three, fairly sparse in time detections, and hence not very robust. The many more, and much more closely spaced MeerKAT detections have allowed us to obtain more precise and reliable measurements of the orbital parameters of NGC 6624F. We did so by starting with the period–acceleration diagram on the early observations, then fitting $P_{\text{obs}}(t)$ from the dense orbital campaign observations, and finally fitting the ToAs obtained from all the detections. We find that the actual orbital period of NGC 6624F is $P_b = 0.220682877(4) \text{ d}$, exactly one-fourth of the value reported by Lynch et al. (2012). The authors likely ended up overestimating P_b because of the sparsity of the three detections that they used. The projected semimajor axis that we measure is $x_p = 0.285389(5) \text{ lt-s}$, also much lower than the previously estimated value. The associated time of passage at the ascending node is $T_{\text{asc}} = 58736.794401(3)$. These orbital parameters imply a minimum companion mass $M_c > 0.105 M_\odot$, hence NGC 6624F belongs to the class of redbacks. As is common for many redbacks, NGC 6624F is always eclipsed for a large fraction (~ 40 per cent) of the orbit, around the pulsar’s superior conjunction (in the range $\phi_b \sim 0.1$ – 0.5). On one occasion (i.e. the first TRAPUM observation, obs. id 10L-trapum, see Fig. 8), the pulsar showed additional, short-lived eclipse events at orbital phases far from the superior conjunction. None of the eclipses observed are accompanied by measurable delays of the pulses. Rather, the radio signal is attenuated fairly abruptly, indicating that the absorbing plasma is very dense or has a small degree of ionization. Despite the many detections obtained with the MeerKAT observations, we were unable to derive an unambiguous phase connection for its ToAs across the ~ 11 months spanned by our data. However, using the tiling of the TRAPUM observations, we could localize it at about 0.4 arcmin north of the cluster centre (see next section).

4.2.2 Localization of five pulsars in NGC 6624

We took advantage of the tiling capabilities offered by the TRAPUM acquisition system to localize the pulsars currently lacking a phase-connected timing solution in NGC 6624 (pulsars D, E, F, and H), as well as to validate the timing position derived for the new eccentric binary MSP (pulsar G). With the observing setup used for the two TRAPUM observations of this cluster (obs. ids 10L-trapum and 12L-trapum) reported in Section 2, the individual beams making up the tiling have elliptic shapes with semi-axes in the range of ~ 8 – 11 arcsec at half power, with the exact values depending on the elevation and other factors. We assume these values as the maximum uncertainty for the positions that we derive for these pulsars. The results are summarized in Table 5, where we list the beams in which each pulsar was detected with highest S/N, and their boresight coordinates. The same is shown graphically in Fig. 9, where the beams with localized pulsars are highlighted in grey. As can be seen,

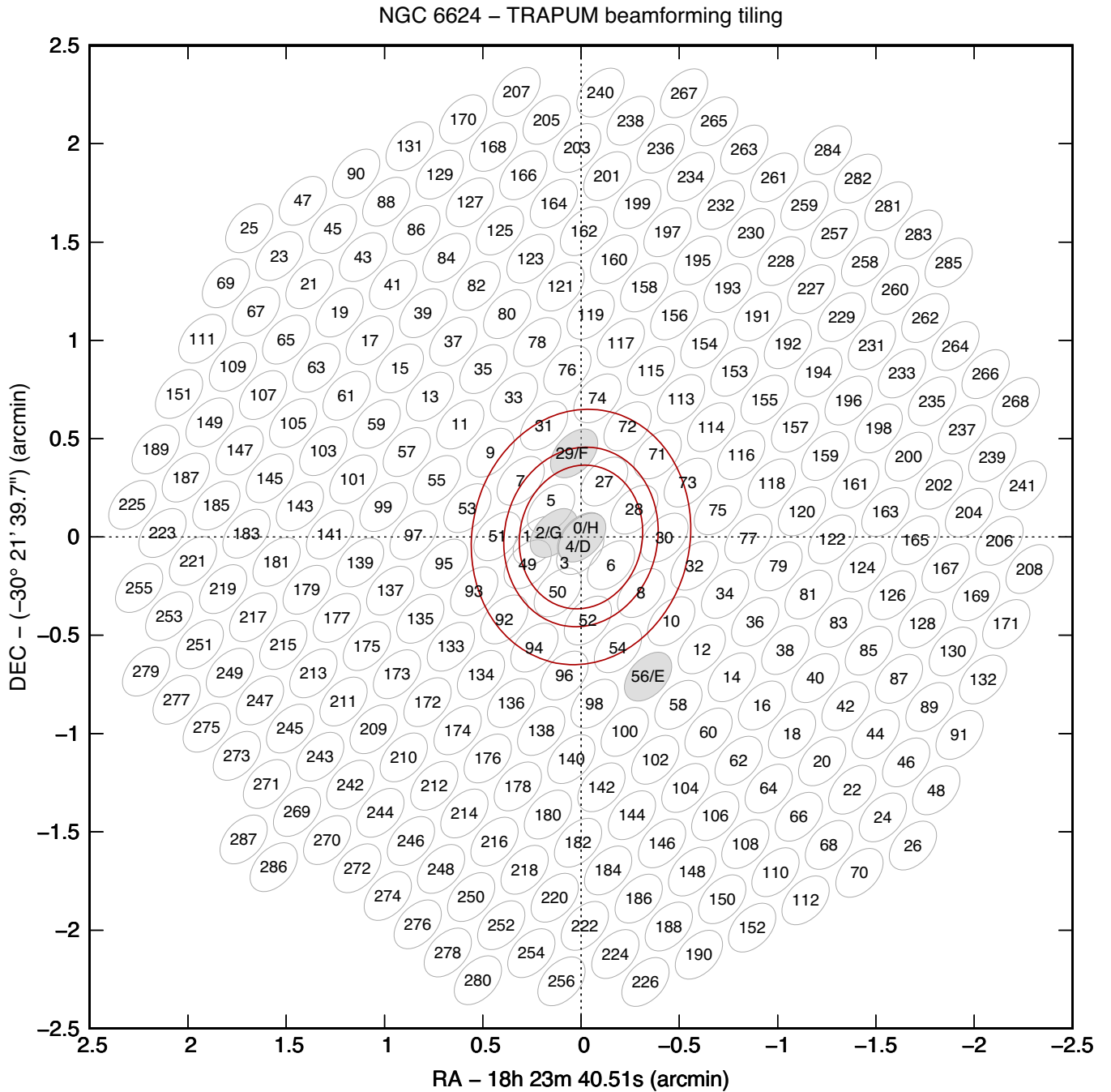


Figure 9. Tiling of the first TRAPUM observation (obs. id 10L-trapum) of NGC 6624. 60 dishes were used to synthesize 288 beams, with an overlap fraction of 80 per cent, around the nominal centre position of the cluster. The light-grey ellipses show the contours of the TRAPUM beams at their 84 per cent level of the power of their boresights, at 1284 MHz. We highlight in solid grey those beams where some of the pulsars show up with the highest S/N: the name of such pulsars are shown next to the beam number. The red ellipses show, for comparison, the *L*-band beam (at half power for top, centre, and bottom of the band) of one of the MeerTime observations of NGC 6624, which used only 42 antennas of the 1-km core of the array.

pulsars D and H are found to be the closest to the cluster centre. The eclipsing redback F and the isolated pulsar E are found at the much larger distances of ~ 0.42 and ~ 0.79 arcmin from the cluster centre, respectively, putting the former near the edge of, and the latter well outside, the half-power of the tied-array beam of the MeerTime observations (which used only the 1-km core antennas) of NGC 6624. This explains why NGC 6624F and E are detected with significantly lower S/N than expected in the MeerTime data as compared to the TRAPUM data, even after accounting for the different number of antennas used. Finally, the eccentric binary pulsar

NGC 6624G showed up with highest S/N in beam #002. This had boresight coordinates of $\alpha = 18^{\text{h}}23^{\text{m}}41^{\text{s}}.150$ and $\delta = -30^{\circ}21'38''.50$. This is just ~ 6.2 arcsec away from, and therefore consistent with, the corresponding timing-derived position of G.

4.2.3 *L*-band detection of the transitional pulsar M28I

M28I (also known as PSR J1824–2452I) is a redback system in M28 belonging to the rare class of *transitional* MSPs (see Jaodand, Hessels & Archibald 2018; Papitto & de Martino 2020 for recent

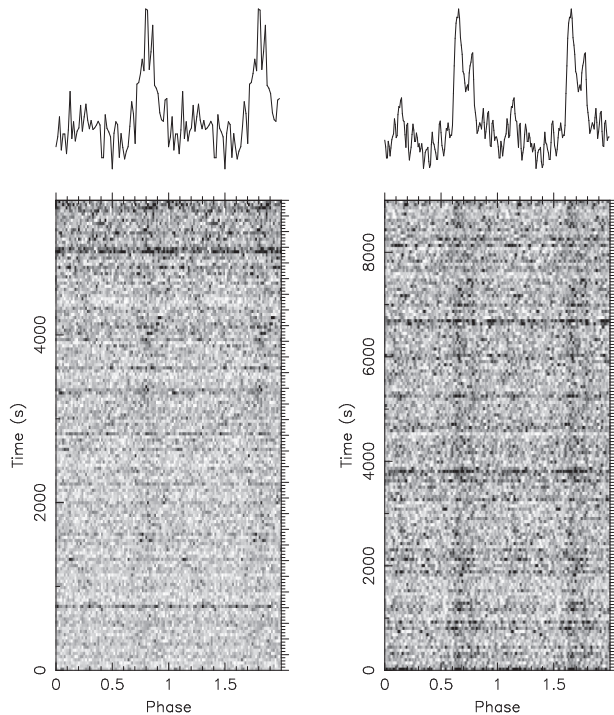


Figure 10. Comparison between the two best detections of M28I obtained in the L band with the GBT on 2015 April 25 by Prager (2017) (left), and with MeerKAT on 2019 July 19 (right). An interpulse is evident in the MeerKAT detection, whereas it is much less obvious in the former.

reviews). Discovered as a radio pulsar by Bégin (2006) with the GBT in the S band (central frequency of 1.95 GHz), it is the first system to be seen swinging between an accreting X-ray MSP state, and a radio MSP state (Papitto et al. 2013; Linares et al. 2014), ultimately confirming the recycling scenario. In the context of our GC census, we have clearly detected M28I in the first (obs id. 01L, dated 2019 July 19) of the two L -band MeerKAT observations of the host cluster made so far (Fig. 10). Hence, we can assert that on 2019 July 19, the pulsar was in a rotation-powered state. In the second MeerKAT observation of M28 (obs id. 02L, dated 2020 February 4), however, we were unable to redetect the pulsar. This is not surprising since the pulsar is known to have a very erratic behaviour: with the GBT, M28I is detected in less than 20 per cent of the observations (S. Ransom, private communication), and always at orbital phases in the range $\phi_b \sim 0.4\text{--}0.9$. What is more interesting and worthy of attention is the marginal detection ($S/N = 6.6$) of an interpulse in the MeerKAT observation, which is not seen in the highest- S/N L -band detection obtained with the GBT (Fig. 10) in 2015. This could potentially have arisen from a rearrangement of the pulsar’s magnetosphere after some short accretion episode. However, the low S/N of the GBT detection and lack of additional information currently prevents us from drawing any firm conclusions.

5 DISCUSSION AND OUTLOOK

5.1 Summary of the findings

In this paper, we have presented the discovery and early follow-up of eight new MSPs in a set of six GCs, out of a total of nine clusters targeted by this survey.

Overall, absent any theoretical interpretation, we find that our results exacerbate the observed differences between the pulsar pop-

ulations of different GCs. In core-collapsed clusters, where isolated pulsars were dominant, three out of four new discoveries (NGC 6522D, NGC 6624H, and NGC 6752F) were isolated MSPs. In the remaining GCs, we have only discovered binaries.

This is very much in line with the expectations of Verbunt & Freire (2014). For clusters with high interaction rate, but a low interaction rate per star, like 47 Tuc, the vast majority of the many LMXBs that form evolve undisturbed, resulting in a population of fully recycled MSPs (all pulsars in 47 Tuc have spin periods between 2 and 8 ms) in circular orbits with WD companions, many compact ‘spider’ systems with very light degenerate or semidegenerate companions (Roberts 2013), and some isolated pulsars; i.e. a population that is nearly identical to the Galactic population of pulsars with these spin periods. With their characteristics, the newly discovered 47 Tuc ac and 47 Tuc ad fit very well within the previously known pulsar population in 47 Tuc, which already had five black widows (47 Tuc I, J, O, P, and R) and two redbacks (47 Tuc V and W). The new binary in M62 also fits well with the other six binaries in that cluster, which, like 47 Tuc, also has a mix of MSP–WD systems, redbacks, and black widows (but thus far no isolated pulsars).

For core-collapsed GCs, which have a large stellar interaction rate per star, most of the binary pulsars (or even LMXBs) have dissociated because of the high rate of interactions. This means that the pulsar populations in such clusters are dominated by isolated pulsars, and some only partially recycled and thus apparently young (like NGC 6624A, B, and C), with some of the latter being quite slow (NGC 6624B and C). NGC 6522 had three isolated MSPs, now it has four, and no known binaries. NGC 6752 had four isolated MSPs and one binary, now it has one more isolated MSP. NGC 6624 had five isolated pulsars and one binary; we discovered one extra isolated pulsar, NGC 6624H, and one binary, NGC 6624G, the only such system we discovered in a core-collapsed cluster. However, and as we have seen, even this system is unusual: it is likely a secondary exchange encounter. As mentioned in Section 2.1 on target selection, finding this sort of systems was precisely the reason why we targeted core-collapsed clusters. The discovery of NGC 6624G confirms that searching core-collapsed GCs is a fruitful strategy.

The GC Ter 5 has intermediate characteristics: although not a core-collapsed cluster, it has a relatively high encounter rate per binary, thanks to its very dense core. It has a few binaries that are very likely secondary exchange encounters. The new binary system discovered there, Ter 5 an, is similar to other binary systems found in that cluster, like Ter 5 N and W: their eccentricities are probably too low for them to have originated in a secondary exchange encounter – they are more likely caused by close flybys of other stars. However, the companion masses are somewhat large compared to the masses of the He WD companions to fast-spinning MSPs we find in the Galactic disc.

5.2 Follow-up of the discoveries

To fully exploit the scientific potential of the discoveries, follow-up observations are highly desirable. For this reason, we have set up a GC pulsar follow-up programme, whose main goals are the confirmation and/or the timing of the new discoveries, which makes use of MeerKAT itself as well as other radio telescopes with comparable sensitivity or complementary characteristics. For example, the Parkes radio telescope, in combination with its Ultra-Wideband Low receiver (Hobbs et al. 2020), may be an asset for confirming discoveries in clusters that are affected by strong scintillation. 100-m class radio telescopes such as the GBT and the Effelsberg telescope will also be important for the long-term timing of some of the discoveries. As of 2020 December, we

already have two proposals approved at two different telescopes: a candidate-confirmation programme using Parkes, and a follow-up timing of NGC 6624G using the GBT with its *S*-band and *L*-band receivers. For the faintest discoveries presented here, such as NGC 6624H, and NGC 6522D, the use of MeerKAT for their follow-up is probably necessary. However, their isolated nature will make it possible to derive their timing solutions conducting observations with a relatively low cadence.

5.3 The future TRAPUM GC pulsar survey

Besides discovering new pulsars, the GC pulsar census served as a testbed and paved the way for the upcoming, fully fledged TRAPUM GC pulsar survey. The latter will take advantage of the whole MeerKAT array, using a minimum of 56 and a maximum of 64 antennas in each observation. This is opposed to the census survey observations, which exploited only the 1-km core of the array, with 38–42 antennas typically used. These numbers imply that the nominal combined telescope gain for the TRAPUM GC survey will be between 33 and 68 per cent higher than that of the census observations, reaching 2.8 KJy^{-1} when using all the 64 antennas. Such an increase in raw sensitivity will be even more pronounced when searching in regions at angular distances $\gtrsim 0.5$ arcmin from the cluster centre, i.e. outside the typical half-power radius of the MeerTime tied-array beam at *L* band for the census observations. This is particularly relevant for nearby and extended clusters, such as NGC 6397, 47 Tuc, or ω Centauri, to mention a few.

6 CONCLUSIONS

We have used the MeerKAT radio telescope to conduct a first census of pulsars in nine selected GCs. As part of this programme, we have carried out a deep search for new pulsars using the 1-km core of the array at *L* band, as well as a few follow-up observations with different configurations, two of which exploited the full array and the tiling capabilities of the TRAPUM backend. We have discovered eight new MSPs in six different clusters. Five of these new pulsars are part of binary systems. One of them, NGC 6624G, is one of the rare MSPs in highly eccentric orbits that resulted from exchange encounters occurring in the extremely dense GC environments. Early timing of this pulsar indicates that the system is massive, with a 69 per cent probability for the NS to exceed $2 M_{\odot}$. Similar (although more uncertain) conclusions apply to another of the discovered binary pulsars, Ter 5 an. Further follow-up timing observations are necessary to constrain the masses of these two systems with higher precision. The same census data were used to better characterize some of the previously known pulsars. These early results demonstrate the exceptional capabilities of the MeerKAT telescope both for the searching and timing of GC pulsars, especially (but not exclusively) for southern sky clusters. We have also shown how the science of pulsars in GCs can greatly benefit from the synergy between the MeerTime and TRAPUM projects, as a result of their complementary goals and characteristics. Notwithstanding, archival data taken at other telescopes have once again proven to be essential for the confirmation and/or characterization of many of the new pulsars, allowing for an instantaneous multiyear timing baseline for a few of them. This is very peculiar to GC pulsar observations, and shows how important it is to keep archival search-mode data. The eight new MSPs presented in this work are the first of several GC pulsar

discoveries so far made by MeerKAT.¹⁵ They represent some of the early examples of a new wave of discoveries of GC pulsars, which have, at the time of writing, reached a total of 221.

ACKNOWLEDGEMENTS

The MeerKAT telescope is operated by the South African Radio Astronomy Observatory (SARAO), which is a facility of the National Research Foundation, an agency of the Department of Science and Innovation. PTUSE was developed with support from the Australian Square Kilometre Array (SKA) Office and Swinburne University of Technology. The Parkes radio telescope (Murriyang) is funded by the Commonwealth of Australia for operation as a National Facility managed by The Commonwealth Scientific and Industrial Research Organisation (CSIRO). The National Radio Astronomy Observatory (NRAO) is a facility of the National Science Foundation (NSF) operated under cooperative agreement by Associated Universities, Inc. The Green Bank Observatory is a facility of the NSF operated under cooperative agreement by Associated Universities, Inc. This work was partly performed on the OzSTAR national facility at Swinburne University of Technology. The OzSTAR program receives funding in part from the Astronomy National Collaborative Research Infrastructure Strategy (NCRIS) allocation provided by the Australian Government. This work is supported by the Max Planck Gesellschaft zur Förderung der Wissenschaften (MPG) Programme “LEGACY”. The authors also acknowledge Max-Planck-Institut für Radioastronomie (MPIfR) funding to contribute to MeerTime infrastructure. MBu and AR thank the Autonomous Region of Sardinia (RAS) for funding computing resources that were used for this work (Regional Law 7 August 2007 n. 7, year 2015, ‘Highly qualified human capital’; project CRP 18 ‘General relativity tests with the Sardinia Radio Telescope’; P.I. Marta Burgay). This research was funded partially by the Australian Government through the Australian Research Council, grants CE170100004 (OzGrav) and FL150100148. AC, APo, AR, and MBu gratefully acknowledge financial support by the research grant ‘iPeska’ (P.I. Andrea Possenti) funded under the Istituto Nazionale di Astrofisica (INAF) national call Prin-SKA/CTA approved with the Presidential Decree 70/2016. APo, AR, and MBu acknowledge support from the Ministero degli Affari Esteri e della Cooperazione Internazionale - Direzione Generale per la Promozione del Sistema Paese - Progetto di Grande Rilevanza ZA18GR02. SMR is a CIFAR Fellow and is supported by the NSF Physics Frontiers Center award 1430284. BWS acknowledges funding from the European Research Council (ERC) under the European Union’s Horizon 2020 research and innovation programme (grant agreement No. 694745). FA, MK, PVP and WC gratefully acknowledge support from ERC Synergy Grant ‘BlackHoleCam’ Grant Agreement Number 610058. AR, TG, PCCF, VVK, MK, FA, EDB, PVP, DJC, WC, RK, and APa acknowledge continuing valuable support from the MPG. LV acknowledges financial support from the Dean’s Doctoral Scholar Award from the University of Manchester. RMS acknowledges support through the Australian Research Council (ARC) Future Fellowship FT190100155. MBa and RMS acknowledge support through ARC grant CE170100004. AK acknowledges support from the UK Science and Technology Facilities Council, grant ST/S000488. We thank Ryan Lynch for providing Green Bank Telescope data that were important to validate and improve some of the timing results presented here. We are

¹⁵See <http://www.trapum.org/discoveries.html> for an up-to-date list.

grateful to the anonymous referee for useful comments, which helped improve the manuscript.

DATA AVAILABILITY

The data underlying this article will be shared on reasonable request to the MeerTime and TRAPUM collaborations.

REFERENCES

- Abbate F., Possenti A., Ridolfi A., Freire P. C. C., Camilo F., Manchester R. N., D'Amico N., 2018, *MNRAS*, 481, 627
- Abbate F., Possenti A., Colpi M., Spera M., 2019, *ApJ*, 884, L9
- Abbate F., Possenti A., Tiburzi C., Barr E., van Straten W., Ridolfi A., Freire P., 2020a, *Nat. Astron.*, 4, 704
- Abbate F. et al., 2020b, *MNRAS*, 498, 875
- Alpar M. A., Cheng A. F., Ruderman M. A., Shaham J., 1982, *Nature*, 300, 728
- Andersen B. C., Ransom S. M., 2018, *ApJ*, 863, L13
- Bailes M. et al., 2020, *Publ. Astron. Soc. Aust.*, 37, e028
- Beccari G., Ferraro F. R., Possenti A., Valenti E., Origlia L., Rood R. T., 2006, *AJ*, 131, 2551
- Bégin S., 2006, Master's thesis, University of British Columbia
- Bhattacharya D., van den Heuvel E. P. J., 1991, *Phys. Rep.*, 203, 1
- Booth R. S., Jonas J. L., 2012, *Afr. Skies*, 16, 101
- Cadelano M., Ransom S. M., Freire P. C. C., Ferraro F. R., Hessels J. W. T., Lanzoni B., Pallanca C., Stairs I. H., 2018, *ApJ*, 855, 125
- Camilo F., Lorimer D. R., Freire P., Lyne A. G., Manchester R. N., 2000, *ApJ*, 535, 975
- Colpi M., Mapelli M., Possenti A., 2003, *ApJ*, 599, 1260
- Corongiu A., Possenti A., Lyne A. G., Manchester R. N., Camilo F., D'Amico N., Sarkissian J. M., 2006, *ApJ*, 653, 1417
- Corongiu A. et al., 2012, *ApJ*, 760, 100
- D'Amico N., Lyne A. G., Manchester R. N., Possenti A., Camilo F., 2001a, *ApJ*, 548, L171
- D'Amico N., Possenti A., Manchester R. N., Sarkissian J., Lyne A. G., Camilo F., 2001b, in Wheeler J. C., Martel H., eds, *AIP Conf. Proc. Vol. 586, 20th Texas Symposium on Relativistic Astrophysics*. Am. Inst. Phys., New York, p. 526
- D'Amico N., Possenti A., Fici L., Manchester R. N., Lyne A. G., Camilo F., Sarkissian J., 2002, *ApJ*, 570, L89
- DeCesar M. E., Ransom S. M., Kaplan D. L., Ray P. S., Geller A. M., 2015, *ApJ*, 807, L23
- Dai S., Johnston S., Kerr M., Camilo F. o., Cameron A., Toomey L., Kumamoto H., 2020, *ApJ*, 888, L18
- Damour T., Deruelle N., 1986, *Ann. Inst. Henri Poincaré Phys. Theor.*, 44, 263
- Dewdney P. E., Hall P. J., Schilizzi R. T., Lazio T. J. L. W., 2009, *IEEE Proc.*, 97, 1482
- Dewey R. J., Taylor J. H., Weisberg J. M., Stokes G. H., 1985, *ApJ*, 294, L25
- Djorgovski S. G., Meylan G., 1993, *Structure and Dynamics of Globular Clusters*. Astronomical Society of the Pacific, San Francisco, U. S.
- DuPlain R., Benson J., Sessoms E., 2008, in Bridger A., Radziwill N. M., eds, *Proc. SPIE Conf. Ser. Vol. 7019, Advanced Software and Control for Astronomy II*. SPIE, Bellingham, p. 70191A
- Ferraro F. R., Carretta E., Bragaglia A., Renzini A., Ortolani S., 1997, *MNRAS*, 286, 1012
- Folkner W. M., Williams J. G., Boggs D. H., 2009, *Interplanetary Network Progress Report*, 42, 1
- Freire P. C. C., Ridolfi A., 2018, *MNRAS*, 476, 4794
- Freire P. C., Kramer M., Lyne A. G., 2001a, *MNRAS*, 322, 885
- Freire P. C., Kramer M., Lyne A. G., Camilo F., Manchester R. N., D'Amico N., 2001b, *ApJ*, 557, L105
- Freire P. C., Gupta Y., Ransom S. M., Ishwara-Chandra C. H., 2004, *ApJ*, 606, L53
- Freire P. C. C. et al., 2017, *MNRAS*, 471, 857
- Gaia Collaboration, 2018, *A&A*, 616, A12
- Gupta Y. et al., 2017, *Curr. Sci.*, 113, 707
- Harris W. E., 1996, *AJ*, 112, 1487 (2010 edition)
- Hessels J. W. T., Ransom S. M., Stairs I. H., Freire P. C. C., Kaspi V. M., Camilo F., 2006, *Science*, 311, 1901
- Hessels J. W. T., Ransom S. M., Stairs I. H., Kaspi V. M., Freire P. C. C., 2007, *ApJ*, 670, 363
- Hills J. G., 1975, *AJ*, 80, 809
- Hobbs G. et al., 2020, *Publ. Astron. Soc. Aust.*, 37, e012
- Hotan A. W., van Straten W., Manchester R. N., 2004, *Publ. Astron. Soc. Aust.*, 21, 302
- Jaodand A., Hessels J. W. T., Archibald A., 2018, in Weltevrede P., Perera B. B. P., Preston L. L., Sanidas S., eds, *Pulsar Astrophysics the Next Fifty Years*, Vol. 337. Cambridge University Press, Cambridge, UK, p. 47
- Johnston H. M., Kulkarni S. R., 1991, *ApJ*, 368, 504
- Kaplan D. L. et al., 2005, *PASP*, 117, 643
- Lange C., Camilo F., Wex N., Kramer M., Backer D. C., Lyne A. G., Doroshenko O., 2001, *MNRAS*, 326, 274
- Leahy D. A., Darbro W., Elsner R. F., Weisskopf M. C., Sutherland P. G., Kahn S., Grindlay J. E., 1983, *ApJ*, 266, 160
- Linares M. et al., 2014, *MNRAS*, 438, 251
- Liu K., Eatough R. P., Wex N., Kramer M., 2014, *MNRAS*, 445, 3115
- Lorimer D. R., Kramer M., 2004, *Handbook of Pulsar Astronomy*. Cambridge University Press, Cambridge, UK
- Lynch R. S., Freire P. C. C., Ransom S. M., Jacoby B. A., 2012, *ApJ*, 745, 109
- Lyne A. G., Brinklow A., Middleditch J., Kulkarni S. R., Backer D. C., 1987, *Nature*, 328, 399
- Lyne A. G. et al., 1990, *Nature*, 347, 650
- Manchester R. N., Lyne A. G., D'Amico N., Johnston S., Lim J., Kniffen D. A., 1990, *Nature*, 345, 598
- Manchester R. N., Lyne A. G., Robinson C., D'Amico N., Bailes M., Lim J., 1991, *Nature*, 352, 219
- Nan R. et al., 2011, *Int. J. Mod. Phys. D*, 20, 989
- Pan Z., Hobbs G., Li D., Ridolfi A., Wang P., Freire P., 2016, *MNRAS*, 459, L26
- Pan Z. et al., 2020, *ApJ*, 892, L6
- Papitto A., de Martino D., 2020, preprint ([arXiv:2010.09060](https://arxiv.org/abs/2010.09060))
- Papitto A. et al., 2013, *Nature*, 501, 517
- Perera B. B. P. et al., 2017, *MNRAS*, 468, 2114
- Possenti A., D'Amico N., Manchester R. N., Camilo F., Lyne A. G., Sarkissian J., Corongiu A., 2003, *ApJ*, 599, 475
- Possenti A., D'Amico N., Corongiu A., Manchester D., Sarkissian J., Camilo F., Lyne A., 2005, in Rasio F. A., Stairs I. H., eds, *ASP Conf. Ser. Vol. 328, Binary Radio Pulsars*. Astron. Soc. Pac., San Francisco, p. 189
- Prager B. J., 2017, PhD thesis, University of Virginia
- Prager B. J., Ransom S. M., Freire P. C. C., Hessels J. W. T., Stairs I. H., Arras P., Cadelano M., 2017, *ApJ*, 845, 148
- Prince T. A., Anderson S. B., Kulkarni S. R., Wolszczan A., 1991, *ApJ*, 374, L41
- Radhakrishnan V., Srinivasan G., 1982, *Curr. Sci.*, 51, 1096
- Ransom S. M., 2001, PhD thesis, Harvard University
- Ransom S. M., 2008, in Bassa C., Wang Z., Cumming A., Kaspi V. M., eds, *AIP Conf. Proc. Vol. 983, 40 Years of Pulsars: Millisecond Pulsars, Magnetars and More*. Am. Inst. Phys., New York, p. 415
- Ransom S. M., Eikenberry S. S., Middleditch J., 2002, *AJ*, 124, 1788
- Ransom S. M., Cordes J. M., Eikenberry S. S., 2003, *ApJ*, 589, 911
- Ransom S. M., Stairs I. H., Backer D. C., Greenhill L. J., Bassa C. G., Hessels J. W. T., Kaspi V. M., 2004, *ApJ*, 604, 328
- Ransom S. M., Hessels J. W. T., Stairs I. H., Freire P. C. C., Camilo F., Kaspi V. M., Kaplan D. L., 2005, *Science*, 307, 892
- Ridolfi A. et al., 2016, *MNRAS*, 462, 2918
- Ridolfi A., Freire P. C. C., Gupta Y., Ransom S. M., 2019, *MNRAS*, 490, 3860
- Roberts M. S. E., 2013, in van Leeuwen J., ed., *Proc. IAU Symp. 291, Neutron Stars and Pulsars: Challenges and Opportunities after 80 years*. Kluwer, Dordrecht, p. 127
- Robinson C., Lyne A. G., Manchester R. N., Bailes M., D'Amico N., Johnston S., 1995, *MNRAS*, 274, 547

1426 *A. Ridolfi et al.*

Shklovskii I. S., 1970, *SvA*, 13, 562

Sigurdsson S., Phinney E. S., 1995, *ApJS*, 99, 609

Stappers B., Kramer M., 2016, *Proc. Sci., MeerKAT Science: On the Pathway to the SKA*. SISSA, Trieste, PoS#9

van Straten W., Bailes M., 2011, *Publ. Astron. Soc. Aust.*, 28, 1

van Straten W., Demorest P., Osłowski S., 2012, *Astron. Res. Tech.*, 9, 237

Verbunt F., Freire P. C. C., 2014, *A&A*, 561, A11

Wang L. et al., 2020, *ApJ*, 892, 43

Woodley K. A. et al., 2012, *AJ*, 143, 50

Zhang L. et al., 2020, *ApJ*, 905, L8

This paper has been typeset from a $\text{\TeX}/\text{\LaTeX}$ file prepared by the author.

Bibliography

- Abbate F., Possenti A., Tiburzi C., Barr E., van Straten W., Ridolfi A., Freire P., 2020, *Nature Astronomy*, 4, 704 (Cited on page 22.)
- Abbate F., Possenti A., Tiburzi C., van Straten W., Barr E., Ridolfi A., Freire P., 2018, in Weltevrede P., Perera B. B. P., Preston L. L., Sanidas S., eds, *Pulsar Astrophysics the Next Fifty Years Vol. 337*, Polarization study of the pulsars in the globular cluster 47 Tucanae. pp 295–298 (Cited on page 29.)
- Allen B., Knispel B., Cordes J. M., Deneva J. S., Hessels J. W. T., Anderson D., Aulbert C., Bock O., Brazier A., Chatterjee S., Demorest P. B., Eggenstein H. B., Fehrmann H., Gotthelf E. V., Hammer D., Kaspi V. M., Kramer M., Lyne A. G., Machenschalk B., McLaughlin M. A., Messenger C., Pletsch H. J., Ransom S. M., Stairs I. H., Stappers B. W., 2013, *ApJ*, 773, 91 (Cited on page 71.)
- Alpar M. A., Anderson P. W., Pines D., Shaham J., 1981, *ApJ*, 249, L29 (Cited on page 11.)
- Alpar M. A., Cheng A. F., Ruderman M. A., Shaham J., 1982, *Nature*, 300, 728 (Cited on pages 15 and 72.)
- Andersen B. C., Ransom S. M., 2018, *ApJ*, 863, L13 (Cited on page 40.)
- Anderson D., Freire P., Yunes N., 2019, *Classical and Quantum Gravity*, 36, 225009 (Cited on pages 71 and 94.)
- Anderson P. W., Itoh N., 1975, *Nature*, 256, 25 (Cited on page 11.)
- Antoniadis J., Freire P. C. C., Wex N., Tauris T. M., Lynch R. S., van Kerkwijk M. H., Kramer M., Bassa C., Dhillon V. S., Driebe T., Hessels J. W. T., Kaspi V. M., Kondratiev V. I., Langer N., Marsh T. R., McLaughlin M. A., Pennucci T. T., Ransom S. M., Stairs I. H., van Leeuwen J., Verbiest J. P. W., Whelan D. G., 2013, *Science*, 340, 448 (Cited on pages 7, 27, 71 and 76.)
- Antoniadis J., van Kerkwijk M. H., Koester D., Freire P. C. C., Wex N., Tauris T. M., Kramer M., Bassa C. G., 2012, *MNRAS*, 423, 3316 (Cited on pages 27 and 95.)
- Archibald A. M., Gusinskaia N. V., Hessels J. W. T., Deller A. T., Kaplan D. L., Lorimer D. R., Lynch R. S., Ransom S. M., Stairs I. H., 2018, *Nature*, 559, 73 (Cited on page 27.)
- Archibald A. M., Stairs I. H., Ransom S. M., Kaspi V. M., Kondratiev V. I., Lorimer D. R., McLaughlin M. A., Boyles J., Hessels J. W. T., Lynch R., van Leeuwen J., Roberts M. S. E., Jenet F., Champion D. J., Rosen R., Barlow B. N., Dunlap B. H., Remillard R. A., 2009, *Science*, 324, 1411 (Cited on page 16.)

- Arfken G. B., Weber H. J., 2005, in *Mathematical methods for physicists* 6th ed. *Mathematical methods for physicists* 6th ed. (Cited on page 38.)
- Asmodelle E., 2017, arXiv e-prints, p. arXiv:1705.04397 (Cited on page 25.)
- Atwood W. B., Abdo A. A., Ackermann M., Althouse W., Anderson B., Axelsson M., Baldini L., Ballet J., Band D. L., Barbiellini G., Bartelt J., Bastieri D., Baughman B. M., Bechtol K., Bédérède D., Bellardi F., Bellazzini R., Berenji B., Bignami G. F., Bisello D., Bissaldi E., Blandford R. D., Bloom E. D., Bogart J. R., Bonamente E., Bonnell J., 2009, *ApJ*, 697, 1071 (Cited on page 100.)
- Baade W., 1942, *ApJ*, 96, 188 (Cited on page 4.)
- Baade W., Zwicky F., 1934a, *Proceedings of the National Academy of Science*, 20, 254 (Cited on page 4.)
- Baade W., Zwicky F., 1934b, *Proceedings of the National Academy of Sciences*, 20, 259 (Cited on page 4.)
- Backer D. C., Kulkarni S. R., Heiles C., Davis M. M., Goss W. M., 1982, *Nature*, 300, 615 (Cited on pages 15 and 42.)
- Bagchi M., Lorimer D. R., Chennamangalam J., 2011, *MNRAS*, 418, 477 (Cited on page 55.)
- Bailes M., Barr E., Bhat N. D. R., Brink J., Buchner S., Burgay M., Camilo F., Champion D., Hessels J., Jameson A., Johnston S., Karastergiou A., Karuppusamy R., Kaspi V., Keith M., Kramer M., McLaughlin M., Moodley K., Osłowski S., Possenti A., Ransom S., Rasio F., Sievers J., Serylak M., Stappers B., Stairs I., Theureau G., van Straten W., Weltevrede P., Wex N., 2016, in *MeerKAT Science: On the Pathway to the SKA MeerTime - the MeerKAT Key Science Program on Pulsar Timing*. p. 11 (Cited on page 100.)
- Bailes M., Jameson A., Abbate F., Barr E. D., Bhat N. D. R., Bondonno L., Burgay M., Buchner S. J., Camilo F., Champion D. J., Cognard I., Demorest P. B., Freire P. C. C., Gautam T., Geyer M., Griessmeier J. M., Guillemot L., Hu H., Jankowski F., Johnston S., Karastergiou A., Karuppusamy R., Kaur D., Keith M. J., Kramer M., van Leeuwen J., Lower M. E., 2020, *PASA*, 37, e028 (Cited on pages 64, 100 and 101.)
- Berti E., Barausse E., Cardoso V., Gualtieri L., Pani P., Sperhake U., Stein L. C., Wex N., Yagi K., Baker T., Burgess C. P., Coelho F. S., Doneva D., Felice A. D., Ferreira P. G., Freire P. C. C., Healy J., Herdeiro C., Horbatsch M., Kleihaus B., Klein A., Kokkotas K., Kunz J., Laguna P., Lang R. N., Li T. G. F., Littenberg T., Matas A., Mirshekari S., Okawa H., Radu E., 2015, *Classical and Quantum Gravity*, 32, 243001 (Cited on page 71.)

- Bhat N. D. R., Cordes J. M., Camilo F., Nice D. J., Lorimer D. R., 2004, *ApJ*, 605, 759 (Cited on page 59.)
- Bhattacharya D., van den Heuvel E. P. J., 1991, *Phys. Rep.*, 203, 1 (Cited on pages 15 and 72.)
- Bhattacharyya B., Cooper S., Malenta M., Roy J., Chengalur J., Keith M., Kudale S., McLaughlin M., Ransom S. M., Ray P. S., Stappers B. W., 2016, *The Astrophysical Journal*, 817, 130 (Cited on page 55.)
- Bhattacharyya B., Roy J., Johnson T. J., Ray P. S., Freire P. C. C., Gupta Y., Bhattacharya D., Kaninghat A., Stappers B. W., Ferrara E. C., Sengupta S., Rathour R. S., Kerr M., Smith D. A., Saz Parkinson P. M., Ransom S. M., Michelson P. F., 2021, *ApJ*, 910, 160 (Cited on pages 55 and 115.)
- Bignami G. F., Caraveo P. A., De Luca A., Mereghetti S., 2003, *Nature*, 423, 725 (Cited on page 10.)
- Bilous A. V., Ransom S. M., Demorest P., 2019, *ApJ*, 877, 125 (Cited on page 120.)
- Booth R. S., Jonas J. L., 2012, *African Skies*, 16, 101 (Cited on page 32.)
- Boyles J., Lorimer D. R., Turk P. J., Mnatsakanov R., Lynch R. S., Ransom S. M., Freire P. C., Belczynski K., 2011, *ApJ*, 742, 51 (Cited on page 6.)
- Brigham E. O., Yuen C. K., 1978, *IEEE Transactions on Systems, Man, and Cybernetics*, 8, 146 (Cited on page 38.)
- Burbidge G. R., Strittmatter P. A., 1968, *Nature*, 218, 1476 (Cited on page 5.)
- Burgay M., D'Amico N., Possenti A., Manchester R. N., Lyne A. G., Joshi B. C., McLaughlin M. A., Kramer M., Sarkissian J. M., Camilo F., Kalogera V., Kim C., Lorimer D. R., 2003, *Nature*, 426, 531 (Cited on pages 16 and 27.)
- Cameron A. D., 2018, PhD thesis, Rheinische Friedrich Wilhelms University of Bonn, Germany (Cited on pages xiv and 33.)
- Cameron A. D., Barr E. D., Champion D. J., Kramer M., Zhu W. W., 2017, *MNRAS*, 468, 1994 (Cited on page 37.)
- Camilo F., Kerr M., Ray P. S., Ransom S. M., Sarkissian J., Cromartie H. T., Johnston S., Reynolds J. E., Wolff M. T., Freire P. C. C., Bhattacharyya B., Ferrara E. C., Keith M., Michelson P. F., Saz Parkinson P. M., Wood K. S., 2015, *ApJ*, 810, 85 (Cited on pages 100, 104 and 112.)
- Camilo F., Lyne A. G., Manchester R. N., Bell J. F., Stairs I. H., D'Amico N., Kaspi V. M., Possenti A., Crawford F., McKay N. P. F., 2001, *ApJ*, 548, L187 (Cited on page 72.)

- Chandrasekhar S., 1935, *Monthly Notices of the Royal Astronomical Society*, 95, 207 (Cited on page 6.)
- Chandrasekhar S., Milne E. A., 1931, *Monthly Notices of the Royal Astronomical Society*, 91, 456 (Cited on page 6.)
- Chen K., Ruderman M., 1993, *ApJ*, 402, 264 (Cited on page 13.)
- Chen S., Sesana A., Conselice C. J., 2019, *MNRAS*, 488, 401 (Cited on page 24.)
- Chen Z.-C., Yuan C., Huang Q.-G., 2020, *Phys. Rev. Lett.*, 124, 251101 (Cited on page 24.)
- Clark G. W., 1975, *ApJ*, 199, L143 (Cited on pages 17, 18 and 29.)
- Cognard I., Freire P. C. C., Guillemot L., Theureau G., Tauris T. M., Wex N., Graikou E., Kramer M., Stappers B., Lyne A. G., Bassa C., Desvignes G., Lazarus P., 2017, *ApJ*, 844, 128 (Cited on page 87.)
- Colpi M., Mapelli M., Possenti A., 2003, *ApJ*, 599, 1260 (Cited on page 68.)
- Comella J. M., Craft H. D., Lovelace R. V. E., Sutton J. M., 1969, *Nature*, 221, 453 (Cited on page 5.)
- Cordes J. M., Freire P. C. C., Lorimer D. R., Camilo F., Champion D. J., Nice D. J., Ramachandran R., Hessels J. W. T., Vlemmings W., van Leeuwen J., Ransom S. M., Bhat N. D. R., Arzoumanian Z., McLaughlin M. A., Kaspi V. M., Kasian L., Deneva J. S., Reid B., Chatterjee S., Han J. L., Backer D. C., Stairs I. H., Deshpande A. A., Faucher-Giguère C. A., 2006, *ApJ*, 637, 446 (Cited on page 71.)
- Cordes J. M., Lazio T. J. W., 2002, arXiv e-prints, pp astro-ph/0207156 (Cited on pages 21, 80 and 110.)
- Dai S., Johnston S., Kerr M., Camilo F., Cameron A., Toomey L., Kumamoto H., 2020, *ApJ*, 888, L18 (Cited on page 115.)
- Damour T., Deruelle N., 1985, *Annales de l'I.H.P. Physique théorique*, 43, 107 (Cited on page 51.)
- Damour T., Deruelle N., 1985, *Ann. Inst. Henri Poincaré Phys. Théor.*, 43, 107 (Cited on page 104.)
- Damour T., Deruelle N., 1986, *Ann. Inst. Henri Poincaré Phys. Théor.*, 44, 263 (Cited on pages 51, 76 and 104.)
- Damour T., Esposito-Farese G., 1993, *Phys. Rev. Lett.*, 70, 2220 (Cited on page 91.)
- Damour T., Esposito-Farèse G., 1996, *Phys. Rev. D*, 54, 1474 (Cited on pages 87 and 91.)

- Damour T., Taylor J. H., 1991, *ApJ*, 366, 501 (Cited on pages 80 and 110.)
- Damour T., Taylor J. H., 1992a, *Phys. Rev. D*, 45, 1840 (Cited on page 51.)
- Damour T., Taylor J. H., 1992b, *Phys. Rev. D*, 45, 1840 (Cited on pages 76 and 99.)
- Davis M. M., Taylor J. H., Weisberg J. M., Backer D. C., 1985, *Nature*, 315, 547 (Cited on page 15.)
- De K., Gupta Y., 2016, *Experimental Astronomy*, 41, 67 (Cited on page 35.)
- DeCesar M. E., Ransom S. M., Kaplan D. L., Ray P. S., Geller A. M., 2015, *ApJ*, 807, L23 (Cited on page 29.)
- Demorest P. B., Ferdman R. D., Gonzalez M. E., Nice D., Ransom S., Stairs I. H., Arzoumanian Z., Brazier A., Burke-Spolaor S., Chamberlin S. J., Cordes J. M., Ellis J., Finn L. S., Freire P., Giampanis S., Jenet F., Kaspi V. M., Lazio J., Lommen A. N., McLaughlin M., Palliyaguru N., Perrodin D., Shannon R. M., Siemens X., Stinebring D., Swiggum J., Zhu W. W., 2013, *ApJ*, 762, 94 (Cited on page 50.)
- Dewdney P. E., Hall P. J., Schilizzi R. T., Lazio T. J. L. W., 2009, *IEEE Proceedings*, 97, 1482 (Cited on page 63.)
- Eardley D. M., 1975, *ApJ*, 196, L59 (Cited on page 87.)
- Eatough R. P., Molkenhain N., Kramer M., Noutsos A., Keith M. J., Stappers B. W., Lyne A. G., 2010, *MNRAS*, 407, 2443 (Cited on page 40.)
- Ebbens A. T., 2020, *European Journal of Physics*, 41, 025601 (Cited on page 10.)
- Edwards P., 2012, arXiv e-prints, p. arXiv:1210.2138 (Cited on page 32.)
- Edwards R. T., Hobbs G. B., Manchester R. N., 2006, *Monthly Notices of the Royal Astronomical Society*, 372, 1549 (Cited on page 49.)
- Espinoza C. M., 2018, in Weltevrede P., Perera B. B. P., Preston L. L., Sanidas S., eds, *Pulsar Astrophysics the Next Fifty Years Vol. 337, Braking indices and spin evolution: something is loose inside neutron stars*. pp 221–224 (Cited on page 9.)
- Espinoza C. M., Lyne A. G., Stappers B. W., 2017, *MNRAS*, 466, 147 (Cited on page 9.)
- Ferdman R. D., Freire P. C. C., Perera B. B. P., Pol N., Camilo F., Chatterjee S., Cordes J. M., Crawford F., Hessels J. W. T., Kaspi V. M., McLaughlin M. A., Parent E., Stairs I. H., van Leeuwen J., 2020, *Nature*, 583, 211 (Cited on page 71.)
- Folkner W. M., Park R., 2016, Tech. Rep. IOM 343R-15-019, Jet Propulsion Laboratory, Pasadena, CA
–2016, JPL planetary and Lunar ephemeris DE436, online, <https://naif.jpl>.

- nasa.gov/pub/naif/JUN0/kernels/spk/de436s.bsp.1b1 (Cited on pages 76 and 104.)
- Fonseca E., Cromartie H. T., Pennucci T. T., Ray P. S., Kirichenko A. Y., Ransom S. M., Demorest P. B., 2021, *ApJ*, 915, L12 (Cited on pages 7, 27, 71 and 76.)
- Foster R. S., Backer D. C., 1990, *ApJ*, 361, 300 (Cited on page 24.)
- Freire P. C., Gupta Y., Ransom S. M., Ishwara-Chandra C. H., 2004a, *ApJ*, 606, L53 (Cited on page 29.)
- Freire P. C., Gupta Y., Ransom S. M., Ishwara-Chandra C. H., 2004b, *ApJ*, 606, L53 (Cited on page 55.)
- Freire P. C., Kramer M., Lyne A. G., 2001, *MNRAS*, 322, 885 (Cited on page 48.)
- Freire P. C., Kramer M., Lyne A. G., Camilo F., Manchester R. N., D'Amico N., 2001, *ApJ*, 557, L105 (Cited on pages [xiv](#), 29 and 47.)
- Freire P. C. C., 2005, in Rasio F. A., Stairs I. H., eds, *Binary Radio Pulsars Vol. 328 of Astronomical Society of the Pacific Conference Series, Eclipsing Binary Pulsars*. p. 405 (Cited on page 16.)
- Freire P. C. C., 2013, in van Leeuwen J., ed., *Neutron Stars and Pulsars: Challenges and Opportunities after 80 years Vol. 291, The pulsar population in Globular Clusters and in the Galaxy*. pp 243–250 (Cited on page 28.)
- Freire P. C. C., Ridolfi A., Kramer M., Jordan C., Manchester R. N., Torne P., Sarkissian J., Heinke C. O., D'Amico N., Camilo F., Lorimer D. R., Lyne A. G., 2017a, *MNRAS*, 471, 857 (Cited on page 29.)
- Freire P. C. C., Ridolfi A., Kramer M., Jordan C., Manchester R. N., Torne P., Sarkissian J., Heinke C. O., D'Amico N., Camilo F., Lorimer D. R., Lyne A. G., 2017b, *MNRAS*, 471, 857 (Cited on page 58.)
- Freire P. C. C., Wex N., 2010, *MNRAS*, 409, 199 (Cited on pages 52, 72, 77 and 104.)
- Freire P. C. C., Wex N., Esposito-Farèse G., Verbiest J. P. W., Bailes M., Jacoby B. A., Kramer M., Stairs I. H., Antoniadis J., Janssen G. H., 2012, *MNRAS*, 423, 3328 (Cited on pages 27, 71, 87 and 95.)
- Gaia Collaboration Helmi A., van Leeuwen F., McMillan P. J., Massari D., Antoja T., Robin A. C., Lindegren L., Bastian U., Arenou F., Babusiaux C., Biermann M., Breddels M. A., Hobbs D., Jordi C., Pancino E., Reylé C., Veljanoski J., Brown A. G. A., Vallenari A., Prusti T., de Bruijne J. H. J., Bailer-Jones C. A. L., Evans D. W., Eyer L., Jansen F., Klioner S. A., Lammers U., Luri X., 2018, *A&A*, 616, A12 (Cited on page 68.)

- Gautam T., Ridolfi A., Freire P. C. C., Wharton R. S., Gupta Y., Ransom S. M., Oswald L. S., Kramer M., DeCesar M. E., 2022, *A&A*, 664, A54 (Cited on pages 55 and 115.)
- Gendreau K., Arzoumanian Z., 2017, *Nature Astronomy*, 1, 895 (Cited on page 27.)
- Gold T., 1969, *Nature*, 221, 25 (Cited on page 5.)
- Graham-Smith F., 2003, *Reports on Progress in Physics*, 66, 173 (Cited on page 8.)
- Gravity Collaboration Abuter R., Amorim A., Bauböck M., Berger J. P., Bonnet H., Brandner W., Clénet Y., Davies R., de Zeeuw P. T., Dexter J., Dallilar Y., Drescher A., Eckart A., Eisenhauer F., Förster Schreiber N. M., Garcia P., Gao F., Gendron E., Genzel R., Gillessen S., Habibi M., Haubois X., Heißel G., 2021, *A&A*, 647, A59 (Cited on pages 80 and 110.)
- Guo Y. J., Freire P. C. C., Guillemot L., Kramer M., Zhu W. W., Wex N., McKee J. W., Deller A., Ding H., Kaplan D. L., Stappers B., Cognard I., Miao X., Haase L., Keith M., Ransom S. M., Theureau G., 2021, *A&A*, 654, A16 (Cited on pages 71, 77, 80, 87, 94 and 95.)
- Gupta Y., Ajithkumar B., Kale H. S., Nayak S., Sabhapathy S., Sureshkumar S., Swami R. V., Chengalur J. N., Ghosh S. K., Ishwara-Chandra C. H., Joshi B. C., Kanekar N., Lal D. V., Roy S., 2017, *Current Science*, 113, 707 (Cited on page 56.)
- Hamaker J. P., 2000, *aaps*, 143, 515 (Cited on page 44.)
- Hamaker J. P., Bregman J. D., Sault R. J., 1996, *aaps*, 117, 137 (Cited on page 44.)
- Hamilton T. T., Helfand D. J., Becker R. H., 1985, *AJ*, 90, 606 (Cited on page 42.)
- Han J. L., Manchester R. N., Lyne A. G., Qiao G. J., van Straten W., 2006, *ApJ*, 642, 868 (Cited on page 22.)
- Han J. L., Manchester R. N., van Straten W., Demorest P., 2018, *ApJS*, 234, 11 (Cited on page 22.)
- Hankins T. H., 1971, *ApJ*, 169, 487 (Cited on page 35.)
- Hankins T. H., Rickett B. J., 1975, *Methods in Computational Physics*, 14, 55 (Cited on page 35.)
- Harding A. K., 2018, in Weltevrede P., Perera B. B. P., Preston L. L., Sanidas S., eds, *Pulsar Astrophysics the Next Fifty Years Vol. 337, Pulsar Emission Physics: The First Fifty Years*. pp 52–57 (Cited on page 8.)
- Harris W. E., 2010, arXiv e-prints, p. arXiv:1012.3224 (Cited on page 68.)

- Harrison B. K., Thorne K. S., Wakano M., Wheeler J. A., 1965, in *Gravitation Theory and Gravitational Collapse* Gravitation Theory and Gravitational Collapse (Cited on page 7.)
- Hellings R. W., Downs G. S., 1983, *ApJ*, 265, L39 (Cited on page 24.)
- Hessels J., Possenti A., Bailes M., Bassa C., Freire P. C. C., Lorimer D. R., Lynch R., Ransom S. M., Stairs I. H., 2015, in *Advancing Astrophysics with the Square Kilometre Array (AASKA14) Pulsars in Globular Clusters with the SKA*. p. 47 (Cited on page 55.)
- Hessels J. W. T., Ransom S. M., Stairs I. H., Freire P. C. C., Kaspi V. M., Camilo F., 2006, *Science*, 311, 1901 (Cited on page 13.)
- Hewish A., Bell S. J., Pilkington J. D. H., Scott P. F., Collins R. A., 1968, *Nature*, 217, 709 (Cited on pages 4 and 20.)
- Hobbs G., Archibald A., Arzoumanian Z., Backer D., Bailes M., Bhat N. D. R., Burgay M., Burke-Spolaor S., Champion D., Cognard I., Coles W., Cordes J., Demorest P., Desvignes G., Ferdman R. D., Finn L., Freire P., Gonzalez M., Hessels J., Hotan A., Janssen G., Jenet F., Jessner A., Jordan C., Kaspi V., Kramer M., Kondratiev V., Lazio J., Lazaridis K., Lee K. J., Levin Y., Lommen A., Lorimer D., Lynch R., Lyne A., Manchester R., McLaughlin M., Nice D., Osłowski S., Pilia M., 2010, *Classical and Quantum Gravity*, 27, 084013 (Cited on page 24.)
- Hobbs G., Lorimer D. R., Lyne A. G., Kramer M., 2005, *MNRAS*, 360, 974 (Cited on page 110.)
- Hobbs G., Manchester R. N., Dunning A., Jameson A., Roberts P., George D., Green J. A., Tuthill J., Toomey L., Kaczmarek J. F., Mader S., Marquarding M., Ahmed A., Amy S. W., Bailes M., Beresford R., Bhat N. D. R., Bock D. C. J., Bourne M., Bowen M., Brothers M., Cameron A. D., Carretti E., Carter N., Castillo S., Chekkala R., Cheng W., Chung Y., Craig D. A., Dai S., Dawson J., Dempsey J., Doherty P., Dong B., Edwards P., Ergesh T., Gao X., Han J., Hayman D., Indermuehle B., Jeganathan K., Johnston S., 2020, *PASA*, 37, e012 (Cited on page 32.)
- Hobbs G. B., Edwards R. T., Manchester R. N., 2006, *MNRAS*, 369, 655 (Cited on page 49.)
- Högbom J. A., 1974, *aaps*, 15, 417 (Cited on page 45.)
- Hotan A. W., van Straten W., Manchester R. N., 2004a, *PASA*, 21, 302 (Cited on pages 49, 74 and 102.)
- Hotan A. W., van Straten W., Manchester R. N., 2004b, *PASA*, 21, 302 (Cited on page 64.)
- Hoyle F., Fowler W. A., 1960, *ApJ*, 132, 565 (Cited on page 6.)

- Hu H., Kramer M., Wex N., Champion D. J., Kehl M. S., 2020, MNRAS, 497, 3118 (Cited on page 28.)
- Hulse R. A., Taylor J. H., 1975, ApJ, 195, L51 (Cited on pages 16 and 25.)
- Hut P., 1983, ApJ, 268, 342 (Cited on page 17.)
- Ivanova N., Heinke C. O., Rasio F. A., Belczynski K., Fregeau J. M., 2008, MNRAS, 386, 553 (Cited on page 18.)
- Jackson J. D., 1962, in Classical Electrodynamics Classical Electrodynamics (Cited on page 9.)
- Johnston H. M., Kulkarni S. R., 1991, ApJ, 368, 504 (Cited on page 40.)
- Johnston S., Karastergiou A., 2017, MNRAS, 467, 3493 (Cited on page 11.)
- Jonas J., MeerKAT Team 2016, in MeerKAT Science: On the Pathway to the SKA The MeerKAT Radio Telescope. p. 1 (Cited on page 100.)
- Joshi B. C., McLaughlin M. A., Lyne A. G., Ludovici D. A., Pawar N. A., Faulkner A. J., Lorimer D. R., Kramer M., Davies M. L., 2009, MNRAS, 398, 943 (Cited on page 55.)
- Kaspi V. M., Beloborodov A. M., 2017, ARA&A, 55, 261 (Cited on page 11.)
- Knispel B., Allen B., Cordes J. M., Deneva J. S., Anderson D., Aulbert C., Bhat N. D. R., Bock O., Bogdanov S., Brazier A., Camilo F., Champion D. J., Chatterjee S., Crawford F., Demorest P. B., Fehrmann H., Freire P. C. C., Gonzalez M. E., Hammer D., Hessels J. W. T., Jenet F. A., Kasian L., Kaspi V. M., Kramer M., Lazarus P., van Leeuwen J., Lorimer D. R., Lyne A. G., Machenschalk B., McLaughlin M. A., Messenger C., Nice D. J., Papa M. A., Pletsch H. J., Prix R., Ransom S. M., Siemens X., Stairs I. H., Stappers B. W., Stovall K., Venkataraman A., 2010, Science, 329, 1305 (Cited on page 71.)
- Knispel B., Lazarus P., Allen B., Anderson D., Aulbert C., Bhat N. D. R., Bock O., Bogdanov S., Brazier A., Camilo F., Chatterjee S., Cordes J. M., Crawford F., Deneva J. S., Desvignes G., Fehrmann H., Freire P. C. C., Hammer D., Hessels J. W. T., Jenet F. A., Kaspi V. M., Kramer M., van Leeuwen J., Lorimer D. R., Lyne A. G., Machenschalk B., McLaughlin M. A., Messenger C., Nice D. J., Papa M. A., Pletsch H. J., Prix R., Ransom S. M., Siemens X., Stairs I. H., Stappers B. W., Stovall K., Venkataraman A., 2011, ApJ, 732, L1 (Cited on page 71.)
- Kopeikin S. M., 1996, ApJ, 467, L93 (Cited on page 96.)
- Kramer M., Stairs I. H., Manchester R. N., Wex N., Deller A. T., Coles W. A., Ali M., Burgay M., Camilo F., Cognard I., Damour T., Desvignes G., Ferdman R. D., Freire P. C. C., Grondin S., Guillemot L., Hobbs G. B., Janssen G., Karuppusamy

- R., Lorimer D. R., Lyne A. G., McKee J. W., McLaughlin M., Münch L. E., Perera B. B. P., Pol N., Possenti A., Sarkissian J., Stappers B. W., Theureau G., 2021, *Physical Review X*, 11, 041050 (Cited on pages [xiii](#), [26](#), [27](#), [28](#), [71](#), [76](#) and [95](#).)
- Kramer M., Stairs I. H., Venkatraman Krishnan V., Freire P. C. C., Abbate F., Bailes M., Burgay M., Buchner S., Champion D. J., Cognard I., Gautam T., Geyer M., Guillemot L., Hu H., Janssen G., Lower M. E., Parthasarathy A., Possenti A., Ransom S., Reardon D. J., Ridolfi A., Serylak M., Shannon R. M., Spiewak R., Theureau G., van Straten W., Wex N., Oswald L. S., Posselt B., Sobey C., Barr E. D., Camilo F., Hugo B., Jameson A., Johnston S., Karastergiou A., Keith M., Osłowski S., 2021, *MNRAS*, 504, 2094 (Cited on page [100](#).)
- Kramer M., Wielebinski R., Jessner A., Gil J., Seiradakis J., 1994, *aaps*, 107, 515 (Cited on page [50](#).)
- Landau L., 1938, *Nature*, 141, 333 (Cited on page [4](#).)
- Lange C., Camilo F., Wex N., Kramer M., Backer D. C., Lyne A. G., Doroshenko O., 2001, *MNRAS*, 326, 274 (Cited on pages [52](#), [77](#) and [104](#).)
- Lazaridis K., Wex N., Jessner A., Kramer M., Stappers B. W., Janssen G. H., Desvignes G., Purver M. B., Cognard I., Theureau G., Lyne A. G., Jordan C. A., Zensus J. A., 2009, *MNRAS*, 400, 805 (Cited on pages [80](#) and [110](#).)
- Lazarus P., Brazier A., Hessels J. W. T., Karako-Argaman C., Kaspi V. M., Lynch R., Madsen E., Patel C., Ransom S. M., Scholz P., Swiggum J., Zhu W. W., Allen B., Bogdanov S., Camilo F., Cardoso F., Chatterjee S., Cordes J. M., Crawford F., Deneva J. S., Ferdman R., Freire P. C. C., Jenet F. A., Knispel B., Lee K. J., van Leeuwen J., Lorimer D. R., Lyne A. G., McLaughlin M. A., Siemens X., Spitler L. G., Stairs I. H., Stovall K., Venkataraman A., 2015, *ApJ*, 812, 81 (Cited on pages [37](#) and [71](#).)
- Lazarus P., Freire P. C. C., Allen B., Aulbert C., Bock O., Bogdanov S., Brazier A., Camilo F., Cardoso F., Chatterjee S., Cordes J. M., Crawford F., Deneva J. S., Eggenstein H. B., Fehrmann H., Ferdman R., Hessels J. W. T., Jenet F. A., Karako-Argaman C., Kaspi V. M., Knispel B., Lynch R., van Leeuwen J., Machenschalk B., Madsen E., McLaughlin M. A., Patel C., Ransom S. M., Scholz P., Seymour A., Siemens X., Spitler L. G., Stairs I. H., Stovall K., Swiggum J., Venkataraman A., Zhu W. W., 2016, *ApJ*, 831, 150 (Cited on page [71](#).)
- Lazarus P., Karuppusamy R., Graikou E., Caballero R. N., Champion D. J., Lee K. J., Verbiest J. P. W., Kramer M., 2016, *MNRAS*, 458, 868 (Cited on pages [74](#) and [102](#).)
- Lazarus P., Tauris T. M., Knispel B., Freire P. C. C., Deneva J. S., Kaspi V. M., Allen B., Bogdanov S., Chatterjee S., Stairs I. H., Zhu W. W., 2014, *MNRAS*, 437, 1485 (Cited on pages [72](#), [73](#), [74](#), [76](#), [80](#) and [82](#).)

- Lee K. J., Stovall K., Jenet F. A., Martinez J., Dartez L. P., Mata A., Lunsford G., Cohen S., Biwer C. M., Rohr M., Flanigan J., Walker A., Banaszak S., Allen B., Barr E. D., Bhat N. D. R., 2013, *MNRAS*, 433, 688 (Cited on page 40.)
- Li D., Lin F. X., Main R., Pen U.-L., van Kerkwijk M. H., Yang I. S., 2019, *MNRAS*, 484, 5723 (Cited on page 120.)
- Lockman F. J., 1998, in Phillips T. G., ed., *Advanced Technology MMW, Radio, and Terahertz Telescopes Vol. 3357 of Society of Photo-Optical Instrumentation Engineers (SPIE) Conference Series, Green Bank Telescope: an overview.* pp 656–665 (Cited on page 32.)
- Lorimer D. R., , 2011, *SIGPROC: Pulsar Signal Processing Programs, Astrophysics Source Code Library*, record ascl:1107.016 (Cited on page 36.)
- Lorimer D. R., Kramer M., 2004, in *Handbook of Pulsar Astronomy Vol. 4, Handbook of Pulsar Astronomy* (Cited on pages 51 and 52.)
- Lorimer D. R., Kramer M., 2012, in *Handbook of Pulsar Astronomy Handbook of Pulsar Astronomy* (Cited on pages xiii, xiv, 9, 10, 20, 21, 22, 24, 39, 53, 82, 110 and 111.)
- Lorimer D. R., Stairs I. H., Freire P. C., Cordes J. M., Camilo F., Faulkner A. J., Lyne A. G., Nice D. J., Ransom S. M., Arzoumanian Z., Manchester R. N., Champion D. J., van Leeuwen J., McLaughlin M. A., Ramachandran R., Hessels J. W., Vlemmings W., Deshpande A. A., Bhat N. D., Chatterjee S., Han J. L., Gaensler B. M., Kasian L., Deneva J. S., Reid B., Lazio T. J., Kaspi V. M., Crawford F., Lommen A. N., Backer D. C., Kramer M., Stappers B. W., Hobbs G. B., Possenti A., D’Amico N., Burgay M., 2006, *ApJ*, 640, 428 (Cited on page 71.)
- Lower M. E., Johnston S., Dunn L., Shannon R. M., Bailes M., Dai S., Kerr M., Manchester R. N., Melatos A., Oswald L. S., Parthasarathy A., Sobey C., Weltevrede P., 2021, *MNRAS*, 508, 3251 (Cited on page 9.)
- Lynch R. S., Freire P. C. C., Ransom S. M., Jacoby B. A., 2012, *ApJ*, 745, 109 (Cited on page 29.)
- Lyne A. G., Brinklow A., Middleditch J., Kulkarni S. R., Backer D. C., 1987, *Nature*, 328, 399 (Cited on pages 42 and 120.)
- Lyne A. G., Burgay M., Kramer M., Possenti A., Manchester R. N., Camilo F., McLaughlin M. A., Lorimer D. R., D’Amico N., Joshi B. C., Reynolds J., Freire P. C. C., 2004, *Science*, 303, 1153 (Cited on page 27.)
- Main R., Yang I. S., Chan V., Li D., Lin F. X., Mahajan N., Pen U.-L., Vanderlinde K., van Kerkwijk M. H., 2018, *Nature*, 557, 522 (Cited on page 120.)

- Manchester R. N., Hobbs G., Bailes M., Coles W. A., van Straten W., Keith M. J., Shannon R. M., Bhat N. D. R., Brown A., Burke-Spolaor S. G., Champion D. J., Chaudhary A., Edwards R. T., Hampson G., Hotan A. W., Jameson A., Jenet F. A., Kesteven M. J., Khoo J., Kocz J., Maciesiak K., Osłowski S., Ravi V., Reynolds J. R., Sarkissian J. M., Verbiest J. P. W., Wen Z. L., Wilson W. E., Yardley D., Yan W. M., You X. P., 2013, *PASA*, 30, e017 (Cited on page 24.)
- Mardling R. A., 1996, in Hut P., Makino J., eds, *Dynamical Evolution of Star Clusters: Confrontation of Theory and Observations Vol. 174, Tidal Capture in Star Clusters*. p. 273 (Cited on pages xiii and 17.)
- Mayall N. U., 1939, *Leaflet of the Astronomical Society of the Pacific*, 3, 145 (Cited on page 4.)
- McLaughlin M. A., 2013, *Classical and Quantum Gravity*, 30, 224008 (Cited on page 24.)
- McMullin J. P., Waters B., Schiebel D., Young W., Golap K., 2007a, in Shaw R. A., Hill F., Bell D. J., eds, *Astronomical Data Analysis Software and Systems XVI Vol. 376 of Astronomical Society of the Pacific Conference Series, CASA Architecture and Applications*. p. 127 (Cited on page 43.)
- McMullin J. P., Waters B., Schiebel D., Young W., Golap K., 2007b, in Shaw R. A., Hill F., Bell D. J., eds, *Astronomical Data Analysis Software and Systems XVI Vol. 376 of Astronomical Society of the Pacific Conference Series, CASA Architecture and Applications*. p. 127 (Cited on page 57.)
- Minter A., O’Neil K., Lockman F., Frayer D., Lynch R., Morgan L., Ghosh T., Armentrout W., Seymour A., Butterfield N., Bublitz J., Salas P., Romero C., Paganelli F., Bonsall A., Gregory B., 2021, in *American Astronomical Society Meeting Abstracts Vol. 53 of American Astronomical Society Meeting Abstracts, The Advanced Green Bank Telescope*. p. 541.01 (Cited on page 32.)
- Morello V., Barr E. D., Bailes M., Flynn C. M., Keane E. F., van Straten W., 2014, *MNRAS*, 443, 1651 (Cited on page 40.)
- Müller J., Murphy T. W., Schreiber U., Shelus P. J., Torre J.-M., Williams J. G., Boggs D. H., Bouquillon S., Bourgoïn A., Hofmann F., 2019, *Journal of Geodesy*, 93, 2195 (Cited on page 25.)
- Müther H., Prakash M., Ainsworth T. L., 1987, *Physics Letters B*, 199, 469 (Cited on page 94.)
- Nan R., Li D., Jin C., Wang Q., Zhu L., Zhu W., Zhang H., Yue Y., Qian L., 2011, *International Journal of Modern Physics D*, 20, 989 (Cited on pages 32 and 72.)
- Nice D. J., Taylor J. H., 1995, *ApJ*, 441, 429 (Cited on pages 80 and 110.)

- Nomoto K., Thielemann F. K., Yokoi K., 1984, *ApJ*, 286, 644 (Cited on page 6.)
- Olausen S. A., Kaspi V. M., 2014, *ApJS*, 212, 6 (Cited on page 11.)
- Oppenheimer J. R., Volkoff G. M., 1939, *Phys. Rev.*, 55, 374 (Cited on pages 4 and 6.)
- Ostriker J. P., Hartwick F. D. A., 1968, *ApJ*, 153, 797 (Cited on page 5.)
- Özel F., Freire P., 2016, *ARA&A*, 54, 401 (Cited on page 71.)
- Pacini F., 1967, *Nature*, 216, 567 (Cited on page 5.)
- Pacini F., 1968, *Nature*, 219, 145 (Cited on page 5.)
- Pan Z., Qian L., Ma X., Liu K., Wang L., Luo J., Yan Z., Ransom S., Lorimer D., Li D., Jiang P., 2021, *ApJ*, 915, L28 (Cited on page 115.)
- Papitto A., Ferrigno C., Bozzo E., Rea N., Pavan L., Burderi L., Burgay M., Campana S., di Salvo T., Falanga M., Filipović M. D., Freire P. C. C., Hessels J. W. T., Possenti A., Ransom S. M., Riggio A., Romano P., Sarkissian J. M., Stairs I. H., Stella L., Torres D. F., Wieringa M. H., Wong G. F., 2013, *Nature*, 501, 517 (Cited on pages 16 and 29.)
- Parent E., Kaspi V. M., Ransom S. M., Krasteva M., Patel C., Scholz P., Brazier A., McLaughlin M. A., Boyce M., Zhu W. W., Pleunis Z., Allen B., Bogdanov S., Caballero K., Camilo F., Camuccio R., Chatterjee S., Cordes J. M., Crawford F., Deneva J. S., Ferdman R., Freire P. C. C., Hessels J. W. T., Jenet F. A., Knispel B., Lazarus P., van Leeuwen J., Lyne A. G., Lynch R., Seymour A., Siemens X., Stairs I. H., Stovall K., Swiggum J., 2018, *ApJ*, 861, 44 (Cited on page 37.)
- Parthasarathy A., Bailes M., Shannon R. M., van Straten W., Osłowski S., Johnston S., Spiewak R., Reardon D. J., Kramer M., Venkatraman Krishnan V., Pennucci T. T., Abbate F., Buchner S., Camilo F., Champion D. J., Geyer M., Hugo B., Jameson A., Karastergiou A., Keith M. J., Serylak M., 2021, *MNRAS*, 502, 407 (Cited on pages 100 and 102.)
- Phinney E. S., 1993, in Djorgovski S. G., Meylan G., eds, *Structure and Dynamics of Globular Clusters Vol. 50 of Astronomical Society of the Pacific Conference Series, Pulsars as Probes of Globular Cluster Dynamics*. p. 141 (Cited on page 29.)
- Phinney E. S., Kulkarni S. R., 1994, *ARA&A*, 32, 591 (Cited on page 105.)
- Pilkington J. D. H., Hewish A., Bell S. J., Cole T. W., 1968, *Nature*, 218, 126 (Cited on page 4.)
- Possenti A., D'Amico N., Manchester R. N., Camilo F., Lyne A. G., Sarkissian J., Corongiu A., 2003, *ApJ*, 599, 475 (Cited on page 117.)

- Prager B. J., Ransom S. M., Freire P. C. C., Hessels J. W. T., Stairs I. H., Arras P., Cadelano M., 2017, *ApJ*, 845, 148 (Cited on page 29.)
- Prša A., Harmanec P., Torres G., Mamajek E., Asplund M., Capitaine N., Christensen-Dalsgaard J., Depagne É., Haberreiter M., Hekker S., Hilton J., Kopp G., Kostov V., Kurtz D. W., Laskar J., Mason B. D., Milone E. F., Montgomery M., Richards M., Schmutz W., Schou J., Stewart S. G., 2016, *AJ*, 152, 41 (Cited on page 77.)
- Qian L., Yao R., Sun J., Xu J., Pan Z., Jiang P., 2020, *The Innovation*, 1, 100053 (Cited on pages 32 and 72.)
- Radhakrishnan V., Cooke D. J., 1969, *Astrophys. Lett.*, 3, 225 (Cited on pages 77 and 78.)
- Radhakrishnan V., Manchester R. N., 1969, *Nature*, 222, 228 (Cited on page 11.)
- Radhakrishnan V., Srinivasan G., 1982, *Current Science*, 51, 1096 (Cited on page 72.)
- Ransom S., , 2011, PRESTO: Pulsar Exploration and Search TOOLKIT, *Astrophysics Source Code Library*, record ascl:1107.017 (Cited on page 36.)
- Ransom S. M., Demorest P., Ford J., McCullough R., Ray J., DuPlain R., Brandt P., 2009, in *American Astronomical Society Meeting Abstracts #214 Vol. 214 of American Astronomical Society Meeting Abstracts*, GUPPI: Green Bank Ultimate Pulsar Processing Instrument. p. 605.08 (Cited on page 57.)
- Ransom S. M., Eikenberry S. S., Middleditch J., 2002, *AJ*, 124, 1788 (Cited on pages 56 and 64.)
- Ransom S. M., Stairs I. H., Archibald A. M., Hessels J. W. T., Kaplan D. L., van Kerkwijk M. H., Boyles J., Deller A. T., Chatterjee S., Schechtman-Rook A., Berndsen A., Lynch R. S., Lorimer D. R., Karako-Argaman C., Kaspi V. M., Kondratiev V. I., McLaughlin M. A., van Leeuwen J., Rosen R., Roberts M. S. E., Stovall K., 2014, *Nature*, 505, 520 (Cited on page 27.)
- Rau U., Cornwell T. J., 2011, *A&A*, 532, A71 (Cited on page 57.)
- Read J. S., Lackey B. D., Owen B. J., Friedman J. L., 2009, *Phys. Rev. D*, 79, 124032 (Cited on page 94.)
- Ridolfi A., Freire P. C. C., Gautam T., Ransom S. M., Barr E. D., Buchner S., Burgay M., Abbate F., Venkatraman Krishnan V., Vleeschower L., Possenti A., Stappers B. W., Kramer M., Chen W., Padmanabh P. V., Champion D. J., Bailes M., Levin L., Keane E. F., Breton R. P., Bezuidenhout M., Grießmeier J. M., Künel L., Men Y., Camilo F., Geyer M., Hugo B. V., Jameson A., Parthasarathy A., Serylak M., 2022b, *A&A*, 664, A27 (Cited on page 119.)

- Ridolfi A., Freire P. C. C., Gautam T., Ransom S. M., Barr E. D., Buchner S., Burgay M., Abbate F., Venkatraman Krishnan V., Vleschower L., Possenti A., Stappers B. W., Kramer M., Chen W., Padmanabh P. V., Champion D. J., Bailes M., Levin L., Keane E. F., Breton R. P., Bezuidenhout M., Griebmeier J. M., Künkel L., Men Y., Camilo F., Geyer M., Hugo B. V., Jameson A., Parthasarathy A., Serylak M., 2022a, arXiv e-prints, p. arXiv:2203.12302 (Cited on page 115.)
- Ridolfi A., Freire P. C. C., Gupta Y., Ransom S. M., 2019, MNRAS, 490, 3860 (Cited on page 96.)
- Ridolfi A., Freire P. C. C., Torne P., Heinke C. O., van den Berg M., Jordan C., Kramer M., Bassa C. G., Sarkissian J., D'Amico N., Lorimer D., Camilo F., Manchester R. N., Lyne A., 2016, MNRAS, 462, 2918 (Cited on page 20.)
- Ridolfi, A., Gautam, T. Freire P. C. C., Ransom S. M., Buchner S. J., Possenti A., Venkatraman Krishnan V., Bailes M., Kramer M., Stappers B. W., Abbate F., Barr E. D., Burgay M., Camilo F., Corongiu A., Jameson A., Padmanabh P. V., Vleschower L., Champion D. J., Chen W., Geyer M., Karastergiou A., Karuppusamy R., Parthasarathy A., Reardon D. J., Serylak M., Shannon R. M., Spiewak R., 2021, MNRAS, 504, 1407 (Cited on pages 63 and 115.)
- Riley T. E., Watts A. L., Ray P. S., Bogdanov S., Guillot S., Morsink S. M., Bilous A. V., Arzoumanian Z., Choudhury D., Deneva J. S., Gendreau K. C., Harding A. K., Ho W. C. G., Lattimer J. M., Loewenstein M., Ludlam R. M., Markwardt C. B., Okajima T., Prescod-Weinstein C., Remillard R. A., Wolff M. T., Fonseca E., Cromartie H. T., Kerr M., Pennucci T. T., Parthasarathy A., Ransom S., Stairs I., Guillemot L., Cognard I., 2021, ApJ, 918, L27 (Cited on pages 7 and 28.)
- Roberts M. S. E., 2013, in van Leeuwen J., ed., Neutron Stars and Pulsars: Challenges and Opportunities after 80 years Vol. 291, Surrounded by spiders! New black widows and redbacks in the Galactic field. pp 127–132 (Cited on page 16.)
- Ruderman M., 1976, ApJ, 203, 213 (Cited on page 11.)
- Ruderman M. A., Sutherland P. G., 1975, ApJ, 196, 51 (Cited on page 13.)
- Russell H. N., 1931, Monthly Notices of the Royal Astronomical Society, 91, 951 (Cited on page 5.)
- Sauls J. A., 2019, arXiv e-prints, p. arXiv:1906.09641 (Cited on page 7.)
- Scheuer P. A. G., 1968, Nature, 218, 920 (Cited on page 22.)
- Shannon C., 1949, Proceedings of the IRE, 37, 10 (Cited on page 34.)
- Shapiro I. I., 1964, Phys. Rev. Lett., 13, 789 (Cited on page 51.)
- Shapiro I. I., 1964, Phys. Rev. Lett., 13, 789 (Cited on pages 76 and 100.)

- Shklovskii I. S., 1970, *Soviet Ast.*, 13, 562 (Cited on page 80.)
- Spiewak R., Bailes M., Miles M. T., Parthasarathy A., Reardon D. J., Shamohammadi M., Shannon R. M., Bhat N. D. R., Buchner S., Cameron A. D., Camilo F., Geyer M., Johnston S., Karastergiou A., Keith M., Kramer M., Serylak M., van Straten W., Theureau G., Venkatraman Krishnan V., 2022, arXiv e-prints, p. arXiv:2204.04115 (Cited on pages 100 and 103.)
- Splaver E. M., Nice D. J., Arzoumanian Z., Camilo F., Lyne A. G., Stairs I. H., 2002, *ApJ*, 581, 509 (Cited on pages 85 and 110.)
- Staelin D. H., 1969, *IEEE Proceedings*, 57, 724 (Cited on page 37.)
- Staelin D. H., Reifenstein E. C., 1968, *Science*, 162, 1481 (Cited on page 5.)
- Stairs I. H., 2004, *Science*, 304, 547 (Cited on pages xiii, 13 and 14.)
- Stappers B., Kramer M., 2016, in *MeerKAT Science: On the Pathway to the SKA An Update on TRAPUM*. p. 9 (Cited on page 64.)
- Stovall K., Freire P. C. C., Chatterjee S., Demorest P. B., Lorimer D. R., McLaughlin M. A., Pol N., van Leeuwen J., Wharton R. S., Allen B., Boyce M., Brazier A., Caballero K., Camilo F., Camuccio R., Cordes J. M., Crawford F., Deneva J. S., Ferdman R. D., Hessels J. W. T., Jenet F. A., Kaspi V. M., Knispel B., Lazarus P., Lynch R., Parent E., Patel C., Pleunis Z., Ransom S. M., Scholz P., Seymour A., Siemens X., Stairs I. H., Swiggum J., Zhu W. W., 2018, *ApJ*, 854, L22 (Cited on page 71.)
- Swarup G., Ananthakrishnan S., Kapahi V. K., Rao A. P., Subrahmanya C. R., Kulkarni V. K., 1991, *Current Science*, 60, 95 (Cited on page 32.)
- Tauris T. M., Langer N., Kramer M., 2011, *MNRAS*, 416, 2130 (Cited on pages 16 and 72.)
- Tauris T. M., Langer N., Kramer M., 2012, *MNRAS*, 425, 1601 (Cited on pages 16 and 72.)
- Tauris T. M., Sanyal D., Yoon S. C., Langer N., 2013, *A&A*, 558, A39 (Cited on page 6.)
- Tauris T. M., Savonije G. J., 1999a, *A&A*, 350, 928 (Cited on page 58.)
- Tauris T. M., Savonije G. J., 1999b, *A&A*, 350, 928 (Cited on pages 105 and 118.)
- Tauris T. M., van den Heuvel E. P. J., 2006, in *Compact stellar X-ray sources Vol. 39, Formation and evolution of compact stellar X-ray sources*. pp 623–665 (Cited on page 16.)
- Tauris T. M., van den Heuvel E. P. J., 2014, *ApJ*, 781, L13 (Cited on page 27.)

- Tauris T. M., van den Heuvel E. P. J., Savonije G. J., 2000, *ApJ*, 530, L93 (Cited on page 16.)
- Taylor C. T., Hutchinson S., Salmon N. A., Wilkinson P. N., Cameron C. D., 2014, in Wikner D. A., Luukanen A. R., eds, *Passive and Active Millimeter-Wave Imaging XVII Vol. 9078 of Society of Photo-Optical Instrumentation Engineers (SPIE) Conference Series*, Investigation of radio astronomy image processing techniques for use in the passive millimetre-wave security screening environment. p. 90780J (Cited on pages xiv and 46.)
- Taylor J. H., 1987, <https://ui.adsabs.harvard.edu/abs/1987grg..conf.....M> (Cited on page 52.)
- Taylor J. H., 1992, *Philosophical Transactions of the Royal Society of London Series A*, 341, 117 (Cited on page 71.)
- Taylor J. H., Huguenin G. R., 1969, *Nature*, 221, 816 (Cited on page 39.)
- Taylor J. H., Weisberg J. M., 1982, *ApJ*, 253, 908 (Cited on page 27.)
- Taylor J. H., Weisberg J. M., 1989, *ApJ*, 345, 434 (Cited on pages 27, 52 and 71.)
- Thompson A. R., 1989, in Perley R. A., Schwab F. R., Bridle A. H., eds, *Synthesis Imaging in Radio Astronomy Vol. 6 of Astronomical Society of the Pacific Conference Series, The Interferometer in Practice*. p. 11 (Cited on page 42.)
- Tolman R. C., 1939, *Phys. Rev.*, 55, 364 (Cited on page 7.)
- Turyshev S. G., 2008, *Annual Review of Nuclear and Particle Science*, 58, 207 (Cited on page 25.)
- Uzan J.-P., 2011, *Living Reviews in Relativity*, 14, 2 (Cited on page 112.)
- van Haasteren R., Levin Y., Janssen G. H., Lazaridis K., Kramer M., Stappers B. W., Desvignes G., Purver M. B., Lyne A. G., Ferdman R. D., Jessner A., Cognard I., Theureau G., D'Amico N., Possenti A., Burgay M., Corongiu A., Hessels J. W. T., Smits R., Verbiest J. P. W., 2011, *MNRAS*, 414, 3117 (Cited on page 24.)
- van Kerkwijk M. H., Kaspi V. M., Klemola A. R., Kulkarni S. R., Lyne A. G., Van Buren D., 2000, *ApJ*, 529, 428 (Cited on page 121.)
- van Leeuwen J., Kasian L., Stairs I. H., Lorimer D. R., Camilo F., Chatterjee S., Cognard I., Desvignes G., Freire P. C. C., Janssen G. H., Kramer M., Lyne A. G., Nice D. J., Ransom S. M., Stappers B. W., Weisberg J. M., 2015, *ApJ*, 798, 118 (Cited on page 71.)
- van Straten W., Demorest P., Osłowski S., 2012a, *Astronomical Research and Technology*, 9, 237 (Cited on pages 49, 74 and 102.)

- van Straten W., Demorest P., Osłowski S., 2012b, *Astronomical Research and Technology*, 9, 237 (Cited on page 64.)
- VandenBerg D. A., Brogaard K., Leaman R., Casagrande L., 2013, *ApJ*, 775, 134 (Cited on page 16.)
- Verbunt F., 1993, *ARA&A*, 31, 93 (Cited on page 72.)
- Verbunt F., Freire P. C. C., 2014, *A&A*, 561, A11 (Cited on page 19.)
- Verbunt F., Hut P., 1987, in Helfand D. J., Huang J. H., eds, *The Origin and Evolution of Neutron Stars Vol. 125, The Globular Cluster Population of X-Ray Binaries*. p. 187 (Cited on page 18.)
- Vogt H., 1926, *Astronomische Nachrichten*, 226, 301 (Cited on page 5.)
- Voisin G., Cognard I., Freire P. C. C., Wex N., Guillemot L., Desvignes G., Kramer M., Theureau G., 2020, *A&A*, 638, A24 (Cited on pages 27 and 71.)
- Wang B., Han Z., 2012, *New A Rev.*, 56, 122 (Cited on page 6.)
- Weisberg J. M., Huang Y., 2016, *ApJ*, 829, 55 (Cited on page 52.)
- Wex N., 2014, arXiv e-prints, p. arXiv:1402.5594 (Cited on page 25.)
- Wielebinski R., 2004, *Naturwissenschaften*, 58, 109 (Cited on page 32.)
- Will C. M., 1993, in *Theory and Experiment in Gravitational Physics Theory and Experiment in Gravitational Physics* (Cited on page 112.)
- Wolszczan A., Frail D. A., 1992, *Nature*, 355, 145 (Cited on page 13.)
- Woltjer L., 1964, *ApJ*, 140, 1309 (Cited on page 4.)
- Yao J. M., Manchester R. N., Wang N., 2017, *ApJ*, 835, 29 (Cited on pages 21, 80 and 110.)
- Zhang B., 2003, *Acta Astronomica Sinica*, 44, 215 (Cited on page 13.)
- Zhang B., Harding A. K., Muslimov A. G., 2000, *ApJ*, 531, L135 (Cited on pages xiii, 12 and 13.)
- Zhang P., Xing Y., Wang Z., 2022, *ApJ*, 935, L36 (Cited on page 59.)
- Zhao J., Freire P. C. C., Kramer M., Shao L., Wex N., 2022, *Classical and Quantum Gravity*, 39, 11LT01 (Cited on pages 71 and 97.)
- Zhu W. W., Berndsen A., Madsen E. C., Tan M., Stairs I. H., Brazier A., Lazarus P., Lynch R., Scholz P., Stovall K., Ransom S. M., Banaszak S., Biwer C. M., Cohen S., Dartez L. P., Flanigan J., Lunsford G., Martinez J. G., Mata A., 2014, *ApJ*, 781, 117 (Cited on page 40.)

Zhu W. W., Desvignes G., Wex N., Caballero R. N., Champion D. J., Demorest P. B., Ellis J. A., Janssen G. H., Kramer M., Krieger A., Lentati L., Nice D. J., Ransom S. M., Stairs I. H., Stappers B. W., Verbiest J. P. W., Arzoumanian Z., Bassa C. G., Burgay M., Cognard I., Crowter K., Dolch T., Ferdman R. D., Fonseca E., Gonzalez M. E., Graikou E., Guillemot L., Hessels J. W. T., Jessner A., Jones G., Jones M. L., Jordan C., Karuppusamy R., Lam M. T., 2019, MNRAS, 482, 3249 (Cited on pages [77](#) and [105](#).)